



Numerical schemes for the hybrid modeling of gas-particle turbulent flows

Kateryna Dorogan

► To cite this version:

Kateryna Dorogan. Numerical schemes for the hybrid modeling of gas-particle turbulent flows. Modeling and Simulation. Aix-Marseille Université; EDF R&D, 2012. English. NNT: . tel-00820978

HAL Id: tel-00820978

<https://theses.hal.science/tel-00820978>

Submitted on 7 May 2013

HAL is a multi-disciplinary open access archive for the deposit and dissemination of scientific research documents, whether they are published or not. The documents may come from teaching and research institutions in France or abroad, or from public or private research centers.

L'archive ouverte pluridisciplinaire **HAL**, est destinée au dépôt et à la diffusion de documents scientifiques de niveau recherche, publiés ou non, émanant des établissements d'enseignement et de recherche français ou étrangers, des laboratoires publics ou privés.

UNIVERSITÉ AIX-MARSEILLE
U.F.R. DE MATHÉMATIQUES, INFORMATIQUE ET MÉCANIQUE

THÈSE

pour obtenir le grade de

DOCTEUR DE L'UNIVERSITÉ AIX-MARSEILLE

DISCIPLINE : MATHÉMATIQUES APPLIQUÉES

ÉCOLE DOCTORALE DE MATHÉMATIQUES ET INFORMATIQUE (ED 184)

présentée et soutenue publiquement par

Kateryna DOROGAN

le 24 mai 2012

**Schémas numériques pour la modélisation hybride
des écoulements turbulents gaz-particules**

DIRECTEUR DE THÈSE : M. JEAN-MARC HÉRARD

devant le jury composé de :

M. Christophe Chalons	Maître de conférences, Université Paris Diderot	Rapporteur
M. Frédéric Coquel	Directeur de recherches CNRS	Rapporteur
M. Thierry Gallouët	Professeur, Université Aix-Marseille	Examinateur
M. Sergey Gavrilyuk	Professeur, Université Aix-Marseille	Examinateur
M. Jean-Marc Hérard	Ingénieur Senior, EDF R&D	Directeur de thèse
M. Frédéric Lagoutière	Professeur, Université Paris-Sud 11	Examinateur
M. Jean-Pierre Minier	Tuteur industriel, EDF R&D	Invité

Abstract

Hybrid Moments/PDF methods have shown to be well suitable for the description of polydispersed turbulent two-phase flows in non-equilibrium which are encountered in some industrial situations involving chemical reactions, combustion or sprays. They allow to obtain a fine enough physical description of the polydispersity, non-linear source terms and convection phenomena. However, their approximations are noised with the statistical error, which in several situations may be a source of a bias. An alternative hybrid Moments-Moments/PDF approach examined in this work consists in coupling the Moments and the PDF descriptions, within the description of the dispersed phase itself. This hybrid method could reduce the statistical error and remove the bias. However, such a coupling is not straightforward in practice and requires the development of accurate and stable numerical schemes. The approaches introduced in this work rely on the combined use of the upwinding and relaxation-type techniques. They allow to obtain stable unsteady approximations for a system of partial differential equations containing non-smooth external data which are provided by the PDF part of the model. A comparison of the results obtained using the present method with those of the “classical” hybrid approach is presented in terms of the numerical errors for a case of a co-current gas-particle wall jet.

Keywords: turbulent two-phase flows, hybrid methods, relaxation techniques, hyperbolic systems, Finite Volume methods, Monte-Carlo methods.

Résumé

Les méthodes hybrides Moments/PDF sont bien adaptées pour la description des écoulements diphasiques turbulents, polydispersés, hors équilibre thermodynamique. Ces méthodes permettent d'avoir une description assez fine de la polydispersion, de la convection et des termes sources non-linéaires. Cependant, les approximations issues de telles simulations sont bruitées ce qui, dans certaines situations, occasionne un biais. L'approche alternative étudiée dans ce travail consiste à coupler une description Eulerienne des moments avec une description stochastique Lagrangienne à l'intérieur de la phase dispersée, permettant de réduire l'erreur statistique et d'éliminer le biais. La mise en œuvre de cette méthode nécessite le développement de schémas numériques robustes. Les approches proposées sont basées sur l'utilisation simultanée des techniques de relaxation et de décentrement, et permettent d'obtenir des approximations stables des solutions instationnaires du système d'équations aux dérivées partielles, avec des données peu régulières provenant du couplage avec le modèle stochastique. Une comparaison des résultats de la méthode hybride Moments-Moments/PDF avec ceux issus de la méthode hybride “classique” est présentée en termes d'analyse des erreurs numériques sur un cas de jet co-courant gaz-particules.

Mots clés: écoulements diphasiques turbulents, méthodes hybrides, techniques de relaxation, systèmes hyperboliques, méthodes Volumes Finis, méthodes Monte-Carlo.

Remerciements

Ce travail a été réalisé au Département Mécanique des Fluides, Énergie et Environnement d'EDF R&D en collaboration avec le Laboratoire d'Analyse, Topologie, Probabilités (LATP) de l'Université Aix-Marseille, dans le cadre de convention CIFRE 203/2009 de l'Agence Nationale pour la Recherche Technique, que je remercie pour son financement.

Je remercie très cordialement Isabelle Flour, chef du groupe "Écoulements Industriels, Réactifs et Polyphasiques", pour son appuis tout au long de ma thèse, pour ses conseils si pertinents, son écoute et sa compréhension.

Je voudrais exprimer toute ma gratitude à Jean-Marc Hérard, mon directeur de thèse, à qui je dois tant que cette page ne saurait suffir: pour sa présence, son soutien, sa gentillesse exceptionnelle, sa patience, mais aussi pour une ambiance de travail de choix et pour son sens de l'humour. Merci de m'avoir accompagnée dans toutes les étapes de ce projet et de ma vie durant ces années, ce fût une grande chance et un honneur pour moi de travailler à ses côtés.

Je tiens à remercier Jean-Pierre Minier, mon responsable EDF, de m'avoir fait confiance pour cette thèse, pour son écoute et ses conseils amicaux et professionnels qui m'ont beaucoup apporté dans les moments difficiles.

Je suis très reconnaissante à Frédéric Coquel et Christophe Chalons pour l'intérêt qu'ils ont porté à mon travail en acceptant de la juger en tant que rapporteurs. Mes remerciements vont également à Sergey Gavrilyuk qui a accepté de faire partie du jury de cette thèse et à Frédéric Lagoutière qui a accepté de présider le jury. Enfin, je remercie sincèrement Thierry Gallouët d'avoir eu la gentillesse de suivre l'évolution de mon travail tout au long de ces trois années et d'avoir accepté de faire partie du jury de thèse.

J'adresse toute ma reconnaissance à Mathieu Guingo pour sa disponibilité, pour le temps qu'il m'a consacré et pour avoir fait de mes problèmes ses problèmes. Un grand merci également à Cyril Baudry pour toute l'aide qu'il a pu m'apporter face aux problèmes informatiques ainsi qu'à Olivier Hurisse pour son esprit rigoureux et ses conseils.

Enfin, je souhaite remercier tous les membres du groupe I81 pour une ambiance de travail agréable et la bonne humeur. Je pense tout particulièrement à mes collègues thésards avec qui j'ai partagé de très bons moments: Sana, Clara, Khaled, Bertrand, Arnaud, Romain, Christophe et Avner.

Mes dernières pensées vont à ma famille, à mes parents, mes grands-parents et mon frère Kirill qui m'ont toujours encouragée et m'ont fait confiance pour tous les choix de la vie, ainsi qu'à Azzedine pour avoir pris soin d'Anthony pendant mes absences et à mon petit Anthony, pour ses chansons et son sourire qui me rendent heureuse tous les jours. Cette thèse leur est dédiée.

Je remercie enfin mes amis proches (ils le savent sans doute) pour leur présence malgré la distance qui nous sépare, mais aussi tous ceux que j'ai eu la chance de connaître et qui ont fait partie de mon univers durant cette période de la vie.

Contents

Introduction	11
Cadre de l'étude et le type d'écoulements étudiés	11
Quelques approches classiques de modélisation des écoulements	12
Classification des descriptions d'une phase continue	12
Quelques approches de description d'une phase dispersée	15
Considérations pour le choix d'une approche numérique diphasique	17
Couplage des descriptions	18
Couplage interfacial	18
Couplage local	21
Positionnement des travaux réalisés	25
Synthèse des travaux	26
Chapitre 1. A Moments/PDF approach to simulation of turbulent two-phase flows	26
Chapitre 2. A one-dimensional relaxation scheme for the hybrid modeling of gaz-particle flows	30
Chapitre 3. A two-dimensional relaxation scheme for the hybrid modelling of two-phase flows	31
Chapitre 4. A hybrid Moments/Moments-PDF approach to simulation of turbulent two-phase flows	32
1 A Moments/PDF approach to turbulent two-phase flows simulation	41
1.1 Introduction	41
1.2 Stochastic modeling of turbulent two-phase flows	42
1.2.1 General formalism of stochastic methods	43

1.2.1.1	Stochastic processes and Langevin equation	43
1.2.1.2	Relationship between stochastic differential equations and Fokker-Planck equation	46
1.2.1.3	Moments equations	47
1.2.1.4	Mean field interactions	47
1.2.2	Probabilistic description of continuous fields	48
1.2.2.1	Eulerian and Lagrangian probability density functions	48
1.2.2.2	Discrete representation and weak approximation of the pdf	49
1.2.3	Stochastic modelling of particle dispersion	50
1.2.3.1	Particle equation of motion	51
1.2.3.2	A Langevin model for inertial particles	52
1.2.3.3	Multiscale character of the stochastic model	55
1.2.3.4	Gas phase moments equations	55
1.3	Moments/PDF numerical approach to description of turbulent two-phase flows . .	57
1.3.1	Main characteristics	57
1.3.2	Numerical approximation and algorithm	59
1.3.2.1	Particle-mesh methods	59
1.3.2.2	General algorithm	60
1.3.2.3	Numerical errors	61
1.3.2.4	Averaging and projection operators	62
1.3.2.5	Time integration of the SDEs	63
1.4	Numerical implementation and results	64
1.4.1	Particle dispersion without mean convective motion	64
1.4.2	Particle convection without turbulent dispersion	68
1.4.3	A more realistic test case: Co-current wall jet	72
1.5	An extension of the Moments/PDF representation	82
1.6	Conclusion	85
2	A one-dimensional relaxation scheme for the hybrid modeling of gas-particle flows	91

2.1	Introduction	94
2.2	Relaxation approach	96
2.2.1	Guidelines	96
2.2.2	System construction	97
2.2.3	Analytical solution of the Riemann problem	99
2.3	Numerical approximation	102
2.3.1	Evolution step: Godunov scheme and interface Riemann solver	104
2.4	Numerical results	105
2.4.1	Algorithm verification	106
2.4.1.1	Supersonic shock tube	106
2.4.1.2	Symmetrical double shock wave	107
2.4.1.3	Symmetrical double rarefaction wave	107
2.4.1.4	Symmetrical double rarefaction wave with vacuum occurrence	108
2.4.1.5	Supersonic rarefaction wave	108
2.4.2	Numerical results for (A2) with a noisy kinetic tensor	109
3	A two-dimensional relaxation scheme for the hybrid modelling of two-phase flows	133
3.1	Introduction	135
3.2	Two distinct relaxation systems	137
3.2.1	A nonlinear interface relaxation system	138
3.2.2	A true interface relaxation system	139
3.3	Main properties of relaxation systems R1 , R2	139
3.3.1	Non-linear relaxation system R1	139
3.3.2	Relaxation system R2	141
3.3.3	Stability properties	144
3.4	Numerical algorithm	145
3.4.1	Algorithm	146
3.4.2	Evolution step	146
3.5	Numerical results	147

3.5.1	A two-dimensional shock tube with noise	147
3.5.2	A two-dimensional collapse over a moving fluid	149
3.5.3	A highly anisotropic case	150
4	A hybrid Moments/Moments-PDF approach to simulation of turbulent two-phase flows	165
4.1	Introduction	165
4.2	A hybrid FV/FV-DSMC algorithm	167
4.2.1	Algorithm	168
4.2.2	Boundary conditions	171
4.3	Numerical experiments and results	172
4.3.1	Co-current gas-particle wall jet	172
4.3.2	Deterministic error	174
4.3.2.1	Convergence of the "classical" Monte-Carlo Solver	174
4.3.2.2	Convergence of the hybrid Monte-Carlo Solver	175
4.3.2.3	Convergence of the Finite Volume Solver	176
4.3.3	Statistical error	176
4.4	Conclusion	177
Conclusion and perspectives		222
Appendix A. Weak first-order Euler numerical scheme for the time integration of SDEs		222

Introduction

Cadre de l'étude et type d'écoulements étudiés

Le terme *écoulement diphasique* désigne un mélange de deux fluides immiscibles, où les phases, séparées par des interfaces, interagissent constamment et sont mises en mouvement par les forces extérieures. En général, une des phases est continue (la phase fluide porteuse) et l'autre apparaît sous forme d'inclusions (la phase dispersée) telles que particules solides, gouttes ou bulles. Dans notre travail, on considère des écoulements diphasiques où la phase fluide porteuse est un écoulement turbulent et la phase des particules est en régime dispersé. Quand la phase dispersée est définie par une distribution de tailles de particules, on parle d'écoulements diphasiques turbulents polydispersés. Le régime dispersé augmente considérablement la surface des interfaces et permet un meilleur échange de la masse et de l'énergie entre les phases. Ce type d'écoulement, souvent associé à d'autres aspects comme la combustion ou la chimie, est rencontré dans de nombreux processus industriels et situations naturelles. A titre d'exemple, on peut évoquer les lits fluidisés denses, la combustion des sprays dans les moteurs et les turbomachines, la synthèse de nanoparticules etc. Dans le domaine des énergies nucléaires, on étudie beaucoup les écoulements dans les réacteurs nucléaires pouvant comporter des particules métalliques (produits de la corrosion) qui sont à l'origine des problèmes de l'enrassement et du colmatage du générateur de vapeur - sujet central du projet MOPHET-C à EDF R&D. En outre, les écoulements polydispersés apparaissent dans les problèmes environnementaux de dispersion des espèces polluantes ou radioactives dans l'atmosphère turbulente. Une meilleure compréhension de l'interaction entre les phases dans ces écoulements permettrait d'améliorer la performance de tels processus, de prévenir des incidents industriels et de prolonger la durée de vie des équipements. Cependant, il reste difficile de prendre en compte tous les processus complexes en jeu: les interactions entre les particules, les interactions entre le fluide et les particules, la turbulence, l'évaporation, la polydispersion et autres phénomènes spécifiques. On est souvent amené à chercher un compromis entre le niveau de description souhaité, les ressources disponibles (mémoire) et les contraintes (le temps de calcul).

Avant de décrire les approches existantes en terme de modélisation, il est important de préciser les caractéristiques des écoulements diphasiques turbulents polydispersés auxquels on se limite dans cette étude. On considère des écoulements turbulents de type gaz-particules instationnaires, chargés en particules dont la densité est beaucoup plus élevée par rapport à la densité du fluide, de sorte que la trainée visqueuse et la gravité sont les forces prédominantes qui agissent sur les

particules. La phase dispersée est supposée suffisamment diluée et les particules de diamètre assez faible pour ne pas prendre en compte les interactions inter-particulaires ainsi que la modulation de la turbulence de la phase continue, et pour ne pas résoudre l'écoulement fluide autour de la surface de la particule (le volume d'une particule est accumulé dans un point).

Quelques approches classiques de modélisation des écoulements

En théorie des milieux continus on a l'habitude de distinguer deux approches théoriques qui décrivent les lois de conservation régissant l'évolution d'un élément fluide. L'approche Lagrangienne, d'une part, qui consiste à suivre les trajectoires des particules discrètes, dont toutes les propriétés moyennes peuvent être extraites à chaque instant par application de la moyenne d'ensemble, et l'approche Eulerienne d'autre part, qui considère le fluide comme un milieu continu et ne décrit qu'un certain nombre des grandeurs statistiques d'intérêt dans chaque point de l'espace-temps. Chacune de ces approches a ses avantages et ses limitations, ce qui les rend plus ou moins adaptées à des problématiques spécifiques.

Le traitement Lagrangien est généralement utilisé pour la simulation des écoulements dilués (dû au fait que le coût calcul de ces méthodes augmente avec le nombre des particules suivies) avec des géométries et des phénomènes physiques complexes, tels que collisions des particules, interactions entre le fluide et les particules, évaporation, polydispersion, conditions aux limites à la paroi etc. En effet, les méthodes Lagrangiennes ne nécessitent pas l'introduction de lois de fermeture macroscopiques. De plus, tous les moments statistiques peuvent en être extraits et sont cohérents (par rapport au principe de réalisabilité généralisé). Cependant, il faut avoir un nombre infini d'échantillons statistiques pour avoir une précision parfaite. Par conséquent, ces méthodes sont susceptibles de devenir gourmandes en terme de mémoire et de temps de calcul, surtout dans les régimes instationnaires. En outre, des erreurs numériques supplémentaires (par exemple, le biais) peuvent être introduites dans les résultats numériques, dûes aux discrétilisations spatiales et temporelles [76].

Pour les écoulements où le fluide est assez dense et/ou un grand nombre de particules doit être traité, l'approche Eulerienne, qui décrit chaque phase comme un fluide continu, a un avantage important devant les méthodes Lagrangiennes. En effet, pour les écoulements turbulents simples mais dans les domaines de calculs étendus, la description Eulerienne se montre beaucoup moins exigeante en termes de temps de calcul et de mémoire CPU, car elle introduit beaucoup moins de degrés de liberté [37]. Néanmoins, elle est moins bien adaptée pour décrire de tels phénomènes comme les interactions entre les particules, la polydispersion, le rebond et la diffusion turbulente.

Classification des descriptions d'une phase continue

Actuellement, il existe une large variété d'approches pour la description d'une phase continue qui sont adaptées à des problématiques (type de l'écoulement, processus physiques prédominants) et besoins particuliers (compromis entre les ressources de calculs disponibles et l'information recherchée). Ces méthodes peuvent être classées par type de description (Eulerienne, décrivant les champs

continus ou Lagrangienne, suivant les trajectoires des particules discrètes) ou par niveau de description (microscopique, décrivant les plus petites échelles physiques et temporelles / macroscopique, décrivant les plus grandes échelles seulement ou les variables moyennées en temps), ou encore peuvent être séparés en modèles proche équilibre (Reynolds-Averaged Navier Stokes equations) ou modèles hors-équilibre (équations de Boltzmann) etc. L'ensemble des descriptions existantes représente une arborescence très développée, c'est pourquoi la classification qui suit ne présente que quelques méthodes les plus classiques dans la littérature et qui sont adaptées au type d'écoulement considéré. Le but de cette classification est d'introduire les caractéristiques générales des méthodes existantes pour éventuellement souligner certaines limitations et perspectives qui motivent le travail continu de modélisation et de simulation, plus particulièrement pour les problèmes de la dispersion des particules engagées dans un écoulement turbulent.

Simulation numérique directe (DNS). La méthode consiste à simuler les équations de Navier-Stokes instationnaires qui décrivent toutes les échelles de la turbulence sans introduire de fermetures macroscopiques. Cette description est très performante pour les écoulements turbulents simples, mais devient très exigeante en terme de coût calcul pour les écoulements industriels à haut nombre de Reynolds et à géométrie complexe, car elle nécessite d'utiliser les discrétisations très fines pour obtenir les solutions convergées [38].

Simulation des grandes échelles (LES). Cette description Eulerienne néglige les détails des petites échelles de la turbulence, leur effet (via le transfert d'énergie) sur les grandes échelles est pris en compte par un modèle dit de sous-maille [43]. Il s'agit de simuler les équations de Navier-Stokes 'filtrées', où la largeur du filtre varie généralement en espace dans la turbulence non-homogène (plus petite en proche paroi). Le coût calcul des méthodes LES se trouve réduit par rapport aux méthodes DNS, ce qui les rend mieux adaptées aux simulations des écoulements complexes à grand nombre de Reynolds [33].

Méthodes PDF (Probability Density Function). Cette approche est originaire de la théorie cinétique, où l'équation de Boltzmann pour la fonction de densité de probabilité décrit la dynamique moléculaire de N particules *discrètes* soumises au mouvement Brownien. La différence de la description pdf d'un écoulement du fluide turbulent consiste à déduire la description probabiliste non pas des échantillons discrets mais des champs *continus* dont l'évolution est donnée par les équations de Navier-Stokes exactes [53, 57]. Donc, on ne donne pas une description statistique du système discret, mais une description probabiliste des champs, où les particules désignent les échantillons des champs fluides dont l'évolution est donnée par les équations Lagrangianes stochastiques. Par conséquent, la description pdf peut être faite du point de vue Lagrangien (l'équation pdf est écrite pour la pdf des variables liées à la particule, où la position en espace est une variable) et du point de vue Eulerien (la pdf est calculée en chaque point de l'espace-temps et la position en espace est un paramètre). L'équation de transport de la *pdf Lagrangienne de transition* est appellée équation de Fokker-Planck. Elle est écrite pour la fonction pdf de transition des variables liées à une particule et supposées être des processus de Markov. Cette équation représente une description mésocopique, entre les équations de Navier-Stokes exactes et les équations pour les moments statistiques, car le modèle est introduit à un niveau de description plus détaillé, ce

qui permet de prendre en compte des phénomènes physiques plus complexes. La simulation de l'équation pdf du point de vue Eulerien avec les méthodes déterministes de type Volumes Finis s'avère cependant coûteuse - le coût calcul étant lié au très grand nombre de degrés de libertés - donc peu adaptée aux problèmes industriels. En pratique, l'équation de Fokker-Planck est souvent "résolue" par les méthodes Lagrangiennes de type DSMC (Direct Simulation Monte-Carlo) via l'écriture des équations stochastiques ou par les méthodes Euleriennes qui consistent à simuler les équations aux dérivées partielles pour un certain nombre de moments statistiques, qui sont obtenues de l'équation pdf par l'application de l'opérateur de moyenne (donc, sans contrainte de convergence statistique). Dans tous les cas, les résultats de l'approche pdf sont des champs fluides même s'ils sont calculés de différentes façons. En fait, l'approche pdf permet d'obtenir une description très détaillée de l'écoulement turbulent sans introduire de modèles macroscopiques. Par conséquent, tous les moments statistiques ainsi que les statistiques conditionnelles sont accessibles.

Méthodes stochastiques. L'idée principale consiste à introduire un grand nombre de particules fluides dont la dynamique est décrite par les équations différentielles stochastiques dans lesquelles la turbulence est modélisée à partir des propriétés statistiques connues. Par ailleurs, il existe une correspondance entre la formulation stochastique et la description PDF qui est souvent utilisée dans les simulations numériques [40, 53, 57]. Les méthodes stochastiques permettent de décrire les écoulements complexes et notamment les écoulements hors-équilibre cinétique. Les limitations principales de ces approches sont liées au coût calcul assez élevé pour les écoulements industriels (un grand nombre de particules doit être traité pour obtenir une bonne convergence des statistiques) et à la possibilité d'introduction du biais lié au nombre fini d'échantillons.

Méthodes des moments (Reynolds-Averaged Navier Stokes equations, RANS). Dans cette approche, on réunit l'ensemble des modèles de turbulence qui décrivent l'évolution temporelle des moments statistiques du premier et deuxième ordres. Les équations de base sont obtenues soit à partir de l'équation pdf soit à partir des équations de Navier-Stokes exactes en décomposant la vitesse du fluide en vitesse moyenne et vitesse fluctuante: $U = \langle U \rangle + u$, ce qui justifie leur nom [12, 40, 56, 59]. Dans ce cas, l'introduction des fermetures macroscopiques pour le tenseur de Reynolds $\langle u_i u_j \rangle$ ou pour les moments d'ordre supérieur est nécessaire. Les modèles de turbulence pour ce type de description sont séparés traditionnellement en modèles à deux équations tels que $k - \varepsilon$, $k - \omega$, $q - \omega$ et autres, où le terme $\langle u_i u_j \rangle$ est exprimé en fonction du gradient de la vitesse moyenne et de la diffusion turbulente moyenne (la seconde variable nécessite également une fermeture), et en modèles plus avancés aux tensions de Reynolds, qui décrivent l'évolution de chaque composante $\langle u_i u_j \rangle$ par une équation de transport supplémentaire [60]. Ces modèles sont bien adaptés aux simulations de la diffusion des particules dans une turbulence anisotrope et sont très utilisés pour les études des processus industriels.

Smoothed-particle hydrodynamics (SPH). SPH est une approche Lagrangienne de plus en plus souvent utilisée pour la simulation numérique des écoulements fluides. Elle représente le fluide comme un ensemble d'éléments discrets (particules) espacés de "distances de lissage" ("smoothing length") qui définit leur contribution aux caractéristiques de l'écoulement dans un point d'intérêt. Ces approches simulent la fonction de densité de probabilité avec les méthodes Monte-Carlo et

ne nécessitent pas de discréétisation spatiale. Par conséquent, c'est la densité qui joue le rôle de paramètre de raffinement numérique. La possibilité de définir "the smoothing length" localement permet de raffiner les calculs dans les zones d'intérêt. Les méthodes SPH sont efficaces pour simuler les écoulements complexes, malgré la tendance à lisser les discontinuités plus fortement que les méthodes basées sur le maillage. Elles ont quelques avantages supplémentaires qui les rendent attractives dans certaines situations: la conservation de la masse dans ces méthodes est garantie par construction; le calcul de la pression s'effectue sur l'ensemble des particules voisines et la solution d'un système linéaire (classique pour les méthodes Euleriennes) n'est plus nécessaire. Cependant, pour atteindre la même précision des approximations, les méthodes SHP nécessitent des ressources de calcul beaucoup plus élevées pas rapport aux méthodes Euleriennes. [36, 44]

Quelques approches de description d'une phase dispersée

Les mêmes méthodes que celles utilisées pour la description d'une phase continue peuvent être adaptées pour décrire une phase dispersée. Cependant, pour une particule inertielle, plus de phénomènes doivent être pris en compte, ce qui change le poids des approches décrites ci-dessus. En effet, les points importants que le modèle de dispersion doit être capable de reproduire pour les particules lourdes, dépendantes essentiellement des forces de trainée et de gravité sont: a) l'effet du nombre de Stokes; b) l'effet de croisement de trajectoires; c) le comportement dans la limite inertielle; d) les lois de conservation. Dans la classification des approches utilisées pour la description d'une phase dispersée, on considère que le volume d'une particule est accumulé dans un point de sorte à négliger l'effet de volume sur l'écoulement fluide. Aussi, toutes les méthodes décrites ci-dessous sont des extensions des méthodes utilisées pour la simulation des écoulements fluides continus. Le choix de la méthode pour la description de la phase dispersée est souvent spécifique au problème et dépend dans une certaine mesure de l'approche retenue pour la simulation de la phase porteuse continue.

Discrete Particle Systems (DPS). Ces méthodes décrivent la dynamique des particules discrètes avec des équations différentielles ordinaires qui traduisent les lois de Newton, soit la conservation de la masse et de la quantité du mouvement. Associées à la description DNS de la phase continue, elles représentent la simulation directe des écoulements diphasiques. Cette configuration s'avère cependant trop "coûteuse" pour les écoulements à nombre de Reynolds un peu élevés [16, 73]. Dans le même esprit, les méthodes LES diphasiques associent la description LES de la phase continue avec les modèles DPS pour les particules et ont l'avantage de décrire l'évolution d'un certain nombre des grandes échelles de turbulence seulement. L'effet des petites échelles de turbulence sur les particules est pris en compte par un modèle [10, 32, 78].

Méthodes PDF (Probability Density Function). Cette approche issue de la théorie cinétique des gaz raréfiés est bien adaptée pour décrire les écoulements diphasiques gaz-particules hors-équilibre cinétique (quand le temps de relaxation de la particule est localement plus grand que le temps caractéristique du fluide turbulent), où les phénomènes physiques complexes tels que les interactions entre les particules, le croisement de jets, les conditions aux limites à la paroi

doivent être traités avec précision. Certains auteurs [9, 63, 68] ont cherché à appliquer la théorie cinétique aux écoulements gaz-particules en écrivant une équation de transport de type Boltzmann sur la fonction de distribution de la vitesse de la phase dispersée. Ensuite, les équations “macroscopiques” Euleriennes pour les moments statistiques en sont extraites [31]. Associée à une description de type RANS pour la phase continue, ce type de modélisation est appellé approche *bi-fluide*, car elle considère les deux phases de l’écoulement comme continues. Cependant, cette approche nécessite la fermeture des corrélations turbulentes fluide-particule. Cela a conduit à une formulation plus générale de l’équation de transport de la fonction de densité de probabilité jointe incluant la vitesse des particules et la vitesse du fluide vu (la vitesse du fluide le long des trajectoires des particules) [42, 62, 70]. Cette formulation repose sur l’analogie entre la description probabiliste admise dans la théorie cinétique et une description stochastique de l’évolution d’une particule fluide proposée dans le cadre des écoulements monophasiques turbulents [53, 57]. L’équation stochastique décrivant l’évolution de la vitesse du fluide vu permet de déduire les équations de transport du tenseur cinétique des particules ainsi que des contraintes fluctuantes fluide-particules [69]. Une approche alternative consiste à écrire l’équation de transport de la fonction de densité de probabilité jointe d’une paire de particules, particule fluide et particule solide, qui porte le nom de “two-point pdf description” et pourrait également fournir toutes les corrélations turbulentes fluide-particule. Cependant, à présent les modèles à deux points ne sont pas assez développés pour être utilisés dans le contexte industriel.

Méthodes stochastiques (SDEs). Les modèles stochastiques Lagrangiens utilisés pour simuler la dispersion des particules dans un écoulement turbulent sont classés selon les exigences en terme de coût calcul: modèles de marche aléatoire discontinue (discontinuous random walk, DRW), modèles de marche aléatoire continue (continuous random walk, CRW), et les modèles aux équations différentielles stochastiques de Langevin (SDE) [37]. Les approches DRW et CRW nécessitent une correction du flux dans les écoulements non-homogènes (spurious mean drift), contrairement aux modèles de Langevin qui sont en plus consistants avec les équations Euleriennes pour les moments statistiques du premier ordre [39, 71]. Les premiers travaux sur la modélisation stochastique aux équations de Langevin de la phase dispersée sont basés sur l’analogie avec la description probabiliste issue de la théorie cinétique, où le choix des variables d’état se limite à la position et la vitesse de la particule [63, 65]. Cependant, dans le cas de l’écoulement turbulent, les effets cinétiques sont associés aux effets de la turbulence de la phase porteuse. Il est donc naturel d’inclure dans le vecteur d’état les variables liées au fluide turbulent. Le choix commun de la plupart des modèles stochastiques de la phase dispersée consiste à rajouter dans le vecteur d’état la vitesse du fluide vue par la particule [42, 61, 62, 70]. Le but de cette démarche est de générer la turbulence artificielle via un modèle basé sur les propriétés statistiques de l’écoulement réel le long des trajectoires des particules. Les modèles stochastiques pour la phase dispersée sont souvent utilisés avec les modèles de type RANS (Reynolds-averaged Navier-Stokes) ou LES (Large-Eddy Simulations) qui fournissent les propriétés statistiques de la phase fluide [51, 72].

Méthodes des moments (RANS). L’idée de ces méthodes Euleriennes consiste à décrire la phase dispersée comme un fluide continu et de résoudre les équations aux dérivées partielles pour les premiers moments statistiques. Ces équations pour la phase dispersée sont obtenues par un

traitement statistique des équations Lagrangiennes locales instantanées qui régissent le mouvement des particules ou en appliquant l'opérateur de moyenne à l'équation pdf. La méthode, comme pour la description de la phase continue, nécessite l'introduction des fermetures macroscopiques ou l'équation de transport pour le tenseur cinétique particulaire [23, 68, 79]. Une telle approche "macroscopique" peut être avantageuse dans certaines situations, par exemple, pour les écoulements denses, quand la phase dispersée est à l'équilibre cinétique ou quand le domaine de calcul est très étendu, mais surtout quand l'information sur les premiers moments statistiques est suffisante pour décrire l'écoulement. Quand la description Eulerienne est utilisée pour les deux phases de l'écoulement, elle porte le nom de modèle bi-fluide [32, 70]. Ces équations sont couplées via l'introduction de termes de transfert aux interfaces et de termes liés aux corrélations des vitesses interfaciales qui nécessitent des fermetures [3, 15, 69]. Les méthodes des moments sont moins exigeantes en terme de ressources de calcul par rapport aux méthodes Lagrangiennes, car elles introduisent beaucoup moins de degrés de liberté. Cependant, elles sont moins bien adaptées pour décrire les phénomènes d'interaction entre les particules, la polydispersion et la diffusion turbulente.

Considérations pour le choix d'une approche numérique diphasique :

Idéalement, on souhaiterait utiliser la méthode la plus précise (comme DNS/DPS) pour décrire un écoulement diphasique turbulent. Malheureusement le coût calcul de ces méthodes s'avère trop élevé pour les problèmes industriels. Il serait donc préférable de trouver un compromis entre la précision recherchée et les ressources disponibles. On peut se référer à une analyse quantitative de l'efficacité des méthodes classiques en termes de mémoire et de temps de calcul présentée dans [37]. En général, les caractéristiques de l'écoulement telles que la compressibilité, la turbulence, l'instationnarité sont déterminantes. Le choix de description de la phase continue de l'écoulement diphasique reflète alors le niveau de précision désiré pour les corrélations fluide-particules. Ensuite, les ressources de calcul sont définies par le raffinement nécessaire pour capter la physique pertinente.

Quelques approches considérées comme les mieux adaptées aux écoulements gaz-particules sont décrites dans [37, 38]. Classiquement, la *phase continue* est modélisée par les méthodes de grandes échelles (RANS ou LES). Ce type d'approche semble le plus approprié pour étudier la dispersion des particules dans un écoulement turbulent: d'une part, les résultats empiriques montrent que ce sont essentiellement les grandes échelles qui gouvernent le mouvement des particules [78]; d'autre part, une telle approche permet de simuler des turbulences à plus grand nombre de Reynolds dans des domaines physiques de dimensions plus importantes, visant les applications industrielles. Dans le travail présent, la phase continue est décrite par les équations "macroscopiques" de type RANS (the Reynolds Averaged Navier-Stokes) instationnaires qui fournissent les champs fluide au modèle de la phase dispersée. *Le choix d'une approche la mieux adaptée pour la description de la phase dispersée est moins évident et va faire l'objet de la section suivante.*

Couplage des descriptions

En raison de la complexité des phénomènes mis en jeu, les méthodes classiques de description de la phase dispersée ne permettent pas toujours de trouver un bon compromis entre le coût calcul et l'information recherchée: les moments statistiques du premier et du second ordre ne sont pas toujours suffisants pour les problèmes industriels, où la connaissance des statistiques conditionnelles dans certaines zones de l'écoulement peut s'avérer nécessaire. D'autre part, le calcul des champs supplémentaires dans tout le domaine exige des ressources de calcul trop élevées. Une solution alternative consiste à recourir à un couplage des descriptions classiques à l'intérieur d'une phase. Il faut souligner que dans la littérature, il existe une grande variété de “méthodes de couplage“ très récentes et que la liste de références citées dans ce chapitre est *totalemen non exhaustive* et ne sert qu'à appuyer la discussion ultérieure. Parmi les types de couplage existants, on se propose dans ce travail d'analyser deux couplages alternatifs (Fig. 1):

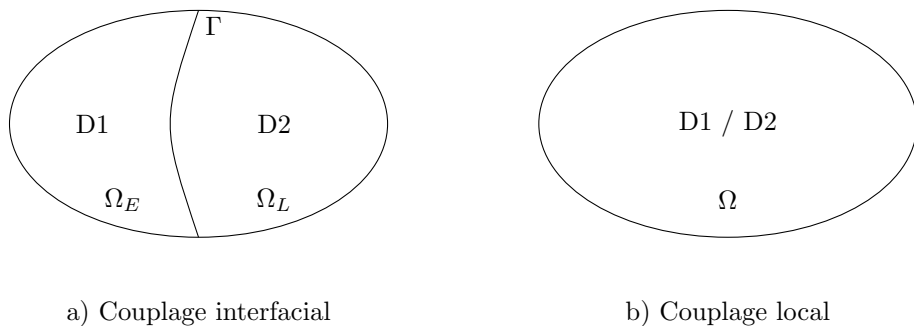


Figure 1: Couplage des approches classiques pour la description d'une phase (D = Description).

- a) **Le couplage interfacial** consiste à découper le domaine de calcul en sous-domaines qui sont séparés par une interface mince (par défaut) et de simuler en chaque point de l'espace-temps un seul modèle; le couplage de différents modèles a lieu sur l'interface de couplage via les conditions aux limites.
- b) **Le couplage local** est basé sur l'utilisation simultanée de deux (ou plusieurs) modèles en chaque point de l'espace-temps. Dans ce cas, les modèles sont conçus pour être complémentaires.

Couplage interfacial

Le couplage interfacial (Fig. 1a) sous-entend l'existence d'une *seule* description de la phase dispersée en chaque point de l'espace-temps, la décomposition du domaine en deux sous-domaines nécessitant le couplage via l'interface *mince* (par défaut, les deux sous-domaines, Ω_E et Ω_L , ne se superposent pas; néanmoins, ci-dessous on va décrire un des cas de couplage avec une interface épaisse, zone où plusieurs modèles coexistent dès lors). Ce type de couplage est utilisé pour raffiner la description de l'écoulement dans certaines zones hors-équilibre, et pour avoir une meilleure

précision des approximations, ou parce que le modèle "macroscopique" utilisé par défaut dans cette situation n'est plus valide. Le couplage interfacial nécessite un certain nombre de *choix* supplémentaires:

- (i) le positionnement de l'interface,
- (ii) le type d'interface (mince ou épais),
- (iii) le choix des modèles à coupler et leur mutuelle consistance.

Dans cette catégorie, on peut citer les travaux sur le couplage de l'équation cinétique [34, 66, 67] ou des équations de la dynamique moléculaire [47, 48, 75] avec un modèle du fluide continu (équations pour les moments statistiques), ou encore le couplage de deux de descriptions du fluide continu [18, 25] etc. Pour plus de références sur les méthodes de couplage interfacial, on invite le lecteur à consulter de nombreux articles cités dans ces papiers. A titre d'exemple, on commente ci-dessous quelques travaux récents, où ces questions sont abordées. Dans le premier papier ¹, les auteurs présentent une technique de couplage de deux systèmes d'équations aux dérivées partielles à dominante convective avec une interface mince (sans aucun recouvrement). Le deuxième article ² traite du couplage d'un modèle issu de l'approche Lagrangienne stochastique et d'un modèle Eulerien pour les moments statistiques via une interface mince. Enfin, le dernier papier ³ décrit une démarche de couplage multi-échelle d'une équation de Boltzmann et d'un modèle hydrodynamique (les équations d'Euler ou de Navier-Stokes) avec une interface épaisse.

Relaxation methods and coupling procedures [1]. Ambroso, A., Chalons, C., Coquel, F., Godlewski, E., Lagoutière, F., Raviart, P.-A., Seguin, N., 2008.

Plusieurs techniques de couplage interfacial instationnaire ont été proposées et explorées par le groupe de travail ⁴ depuis 2005. Ces approches ont été motivées par la nécessité de définir des conditions aux limites instationnaires à fournir à deux codes distincts pour réaliser des couplages de codes synchrones. Les cas considérés par le groupe concernent les codes diphasiques utilisés dans le nucléaire civil par EDF-CEA-AREVA-IRSN. Deux grandes classes d'approches ont été examinées. La première est relative au couplage par flux/état à l'interface de couplage (infiniment mince). La seconde s'appuie sur le formalisme de relaxation, et permet d'éliminer formellement des phénomènes délicats tels que la résonance. L'article [1] donne un aperçu des techniques développées. D'autres techniques ont également été proposées [19], notamment une reposant sur le concept de modèle "père" à l'interface [25, 26].

¹Relaxation methods and coupling procedures. Ambroso, A., Chalons, C., Coquel, F., Godlewski, E., Lagoutière, F., Raviart, P.-A., Seguin, N., Int. J. Num. Meth. Fluids 56(8), 1123-1129, 2008.

²A hybrid Eulerian-Lagrangian method to simulate the dispersed phase in turbulent gaz-particle flows. Pialat, X., Simonin, O., Villedieu, P., Int. J. Multiphase Flow 33, 766–788, 2007.

³A smooth transition model between kinetic and hydrodynamic equations. Degond, P., Jin, S., Mieussens, L., J. Comp. Phys. 209, 665–694, 2005.

⁴<http://www.ljll.math.upmc.fr/groupes/cea>

A hybrid Eulerian-Lagrangian method to simulate the dispersed phase in turbulent gaz-particle flows [52]. Pialat, X., Simonin, O., Villedieu, P., 2007.

Dans le papier [52], les auteurs proposent une méthode hybride de couplage interfacial (sur interface mince) d'un modèle stochastique Lagrangien avec un modèle Eulerien pour les moments statistiques (HELM) dans la description de la phase dispersée de l'écoulement turbulent gaz-particules. Chaque modèle est appliqué dans une des deux parties du domaine qui sont séparées par une *interface mince* et ne se superposent pas. Le couplage consiste à utiliser le modèle Eulerien pour les moments statistiques dans le cœur de l'écoulement et le modèle stochastique Lagrangien dans les zones hors-équilibre, où l'information fournie par la méthode des moments n'est pas suffisante ou n'est plus valide (en proche paroi ou dans les zones avec un faible taux de présence de particules).

L'équation pdf pour la fonction de densité de probabilité jointe des variables $(\mathbf{x}_p, \mathbf{U}_p, \mathbf{U}_s)$ liées à la particule discrète est modélisée suivant les idées présentées dans [69]. Dans ce modèle, U_s est la vitesse du fluide vu par la particule et on suppose que le tenseur de Reynolds lié à la vitesse du fluide vu est équivalent au tenseur de Reynolds lié à la vitesse du fluide. Ensuite, les deux modèles, *le modèle Eulerien aux équations aux dérivées partielles et le modèle Lagrangien aux équations stochastiques*, sont déduits de cette équation pdf. Par conséquent, les pdf correspondantes calculées dans Ω_E et Ω_L sont consistantes a priori (leur consistance est démontrée plus tard dans un cas simplifié). Le modèle Lagrangien stochastique est écrit pour les variables $\mathbf{x}_p(t), \mathbf{U}_p(t), \mathbf{u}'_s(t)$ correspondantes à la position de la particule, la vitesse de la particule et la fluctuation de la vitesse du fluide vu. Les équations aux dérivées partielles Euleriennes pour les moments statistiques décrivent la conservation de la masse, de la quantité du mouvement et de l'énergie cinétique des particules ainsi que de la vitesse de dérive turbulente fluide/particule et du tenseur de corrélations des vitesses fluide/particule. Des deux côtés de l'interface Γ , il existe deux pdfs, $f^{Lag}(\mathbf{x}, t)$ et $f^{Eul}(\mathbf{x}, t)$, calculées par deux modèles différents et le couplage sur l'interface est assuré par les conditions aux limites sur les demi-flux [34]:

$$\begin{aligned} f^{Lag}(\mathbf{x}_\Gamma, t) &= f^{Eul}(\mathbf{x}_\Gamma, t), \quad \text{for } \mathbf{U}_p \cdot \mathbf{n} < 0, \\ f^{Eul}(\mathbf{x}_\Gamma, t) &= f^{Lag}(\mathbf{x}_\Gamma, t), \quad \text{for } \mathbf{U}_p \cdot \mathbf{n} > 0, \end{aligned}$$

où $\mathbf{n}(\mathbf{x})$ est la normale à l'interface Γ dirigée de Ω_L vers Ω_E . La méthode proposée a été validée sur un cas-test de dispersion des particules engagées dans un écoulement turbulent homogène isotrope. Pour les écoulements turbulents non-homogènes, les formules des flux à l'interface doivent être modifiées. La question sur le positionnement de l'interface de couplage Γ n'est pas abordée dans le cas homogène. Dans les écoulements non-homogènes, il dépend directement de la définition des zones de non-équilibre, où les fermetures macroscopiques des corrélations triples de la vitesse des particules dans les équations Euleriennes ne sont plus valables et où le modèle Eulerien doit, par conséquent, être remplacé par le modèle Lagrangien.

A smooth transition model between kinetic and hydrodynamic equations [8]. Degond, P., Jin, S., Mieussens, L., 2005.

L'équation cinétique impliquant plusieurs échelles physiques permet d'obtenir une bonne précision dans la description de la phase dispersée des écoulements complexes, mais sa résolution numérique reste assez exigeante en terme de ressources de calcul (temps, mémoire) à cause du grand nombre de degrés de liberté. En même temps, dans les situations les plus classiques, l'écoulement se trouve à l'équilibre dans la plus grande partie du domaine, à l'exception des zones où les effets microscopiques sont importants (dans les chocs ou en proche paroi). Dans ces cas, il peut être justifié d'utiliser un modèle plus simple, macroscopique, dans les zones de l'écoulement en équilibre et réserver le modèle cinétique pour les zones hors-équilibre. La solution de l'équation cinétique initiale correspond à la combinaison linéaire des solutions des ces équations. En terme de modèle "macroscopique" les auteurs considèrent l'approximation hydrodynamique de l'équation cinétique (équations d'Euler ou de Navier-Stokes). Beaucoup de travaux existants sur le couplage de *l'équation de Boltzmann avec les équations hydrodynamiques* sont basés sur la décomposition du domaine de sorte que les deux modèles sont simulés dans les sous-domaines différents et le couplage est assuré pas les conditions aux limites à l'interface en général épaisse [34, 66]. Les auteurs du papier proposent d'effectuer le couplage entre les sous-domaines via les équations et non via les conditions aux limites. Le couplage est réalisé sur une *interface épaisse* (Fig. 2) où les deux modèles sont simulés, et une fonction de transition assure le passage "continu" entre les deux modèles des deux côtés de l'interface. Quand l'interface épaisse est réduite à l'interface mince, la méthode de couplage correspond à [34, 52]. Cette méthode de décomposition du domaine automatique est basée sur un critère de non-équilibre appliqué à la fontion pdf et peut être facilement adaptée à la détection dynamique des zones hors-équilibre et à la construction dynamique de l'interface [6].

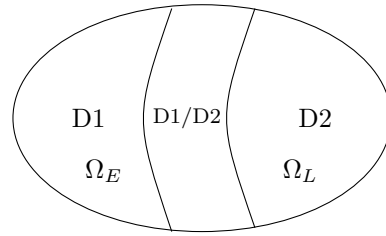


Figure 2: Couplage de modèles avec une interface épaisse.

Couplage local

Le couplage local constitue le point central de notre sujet. Dans chaque point de l'espace-temps, il consiste à définir plusieurs modèles physiques à des échelles éventuellement différentes et avec des discrétilisations différentes. Ce type d'approche apparaît utile lorsque un des modèles, typiquement Eulerien, n'est pas défini ou nécessite localement des fermetures et/ou des termes sources particuliers [13]. Dans le dernier cas, il existe un lien étroit avec le couplage interfacial [6]. Les modèles qui sont susceptibles de fournir les termes inconnus sont souvent issus de la description Lagrangienne et simulés par les méthodes probabilistes de type DSMC (Direct Simulation Monte-

Carlo). Pour ces modèles, une telle approche de couplage joue le rôle d'une technique de réduction de variance (VRT), car elle permet de réduire le biais, l'erreur statistique, et donc d'augmenter la précision des résultats. Par conséquent, le couplage local permet, dans certaines situations, de compenser les défauts des descriptions classiques et de cumuler leurs avantages. Cependant, en pratique, il introduit plusieurs questions complexes qui nécessitent d'être étudiées avec attention:

- le choix du vecteur d'état dans les deux modèles et la méthode de séparation des échelles qui définit le niveau de description,
- la consistance des modèles au niveau continu,
- les discrétisations spatiales et temporelles pour les deux modèles, nécessaires pour satisfaire les contraintes numériques et capter la physique pertinente,
- interpolation / extrapolation des données discrètes (entre les maillages, entre le maillage et les particules),
- les solveurs utilisés doivent être adaptés au traitement des taux de présence des particules très faibles (apparition du vide),
- la stabilité des approximations dans les situations extrêmes qui peuvent survenir dû au couplage,
- le calcul et la gestion des erreurs numériques introduites par les deux méthodes et par le couplage: erreurs de discrétisation spatiale et temporelle, erreur statistique liée au nombre de particules, le biais, les erreurs d'interpolations / extrapolations,
- éventuellement, la consistance numérique (au niveau discret) des champs instationnaires calculés par les deux modèles.

Malheureusement, à présent il existe encore peu de travaux sur le sujet et beaucoup de champs restent inexplorés. Ci-dessous, on présente seulement quelques travaux relatifs, en étant conscient que certaines références ont dû rester oubliées. Le premier papier ⁵ présente une méthode de couplage d'un système d'équations différentielles ordinaires Lagangianes avec un système d'équations Euleriennes pour les moments statistiques, les deux étant issus de la même équation pdf pour la description d'un écoulement turbulent réactif stationnaire. Dans le deuxième article ⁶, les auteurs proposent une technique de correction de la fonction pdf discrète en imposant aux échantillons de suivre les moments statistiques fournis par un modèle Eulerien aux équations aux dérivées partielles. Le dernier papier ⁷ décrit une méthodologie générale de couplage des descriptions multi-échelles.

⁵A consistent hybrid finite-volume / particle method for the pdf equations of turbulent reactive flows. Muradoglu, M., Jenny, P., Pope, S.B., Caughey, D.A., J. Comp. Phys. 154, 342–371, 1999.

⁶The moment-guided Monte Carlo method. Degond, P., Dimarco, G., Pareschi, L., Int. J. for Numerical Methods in Fluids 67 (2), 189–213, 2011.

⁷The heterogeneous multiscale methods. E, W., Engquist, B., Commu. Math. Sci. 1 (1), 87–132, 2003.

A consistent hybrid finite-volume / particle method for the pdf equations of turbulent reactive flows [45, 46]. Muradoglu, M., Jenny, P., Pope, S.B., Caughey, D.A., 1999.

Faisant suite à de nombreux travaux sur les méthodes pdf pour la modélisation et la simulation des écoulements turbulents, ce papier introduit une méthode hybride pour la description des écoulements turbulents réactifs compressibles en régime *stationnaire* (pour un mélange de gaz). L'approche consiste à coupler au même point deux descriptions différentes à l'intérieur du même domaine: *les équations Euleriennes de conservation* de la masse, de la quantité du mouvement et de l'énergie avec une loi d'état thermodynamique d'une part et *les équations Lagrangiennes déterministes* de l'autre. Le modèle Lagrangien est écrit pour les variables liées à la particule fluide: la masse, la position, la vitesse fluctuante, la fraction massique et l'enthalpie. La description Eulerienne est déduite des équations Lagrangiennes de façon *consistante* (via l'équation pdf modélisée). Le but de ce couplage est de faciliter le calcul du champ de pression moyenne et d'éviter les erreurs déterministes dans les simulations Lagrangiennes, qui sont générées quand les coefficients des équations sont dépendants des valeurs moyennes instantanées (le biais). Le module numérique Eulerien, basé sur une méthode de Volumes Finis, fournit explicitement la pression et la vitesse moyenne au module Lagrangien, qui lui renvoie le tenseur de Reynolds, les flux scalaires et les termes sources réactifs. Pour préserver la consistance des descriptions au niveau discret sur maillage donné, deux conditions sont imposées sur les variables Lagrangiennes: la vitesse fluctuante moyenne doit être nulle et l'énergie interne calculée par les deux approches, Eulerienne et Lagrangienne, doit être identique.

Les équations différentielles ordinaires Lagrangiennes sont à leur tour intégrées en temps avec un schéma d'Euler explicite du second ordre. L'erreur statistique de ces simulations est réduite grâce à l'utilisation des solutions moyennées en temps - une technique admise dans les régimes stationnaires. Les équations Euleriennes sont résolues par une méthode de Volumes Finis souvent utilisée pour les équations d'Euler compressibles sans les termes sources (toutes les données fournies par la partie Lagrangienne du modèle sont traitées comme tels):

$$\begin{aligned} \frac{\partial \bar{\rho}}{\partial t} + \frac{\partial}{\partial x_i} (\bar{\rho} \tilde{U}_i) &= 0, \\ \frac{\partial}{\partial t} (\bar{\rho} \tilde{U}_j) + \frac{\partial}{\partial x_i} [\bar{\rho} \tilde{U}_i \tilde{U}_j + p \delta_{ij}] &= - \frac{\partial}{\partial x_i} [\bar{\rho} \langle u_i^* u_j^* | \mathbf{x} \rangle], \\ \frac{\partial \tilde{e}_s}{\partial t} + \frac{\partial}{\partial x_i} [\tilde{U}_i (\tilde{e}_s + p)] &= -\bar{\rho} \sum_{\alpha} \epsilon_{\alpha}^{so} \left\langle \frac{dY_{\alpha}^*}{dt} | \mathbf{x} \right\rangle + p \frac{\partial \check{U}_i}{\partial x_i} - \frac{\partial}{\partial x_i} [\bar{\rho} \langle u_i^* \epsilon_s^* | \mathbf{x} \rangle] - \tilde{U}_i \frac{\partial}{\partial x_k} [\bar{\rho} \langle u_i^* u_k^* | \mathbf{x} \rangle], \\ \tilde{e}_s &= \bar{\rho} \left(\tilde{\epsilon}_s + \frac{1}{2} \tilde{U}_i \tilde{U}_i \right), \quad p = \check{\kappa} \left(\tilde{e}_s - \frac{1}{2} \bar{\rho} \tilde{U}_i \tilde{U}_i \right), \quad \check{\kappa} = \frac{\langle \kappa^* \epsilon_s^* | \mathbf{x} \rangle}{\langle \epsilon_s^* | \mathbf{x} \rangle}, \quad \forall i, j, k \in \mathbb{Z}, \end{aligned}$$

avec la densité moyenne $\bar{\rho}(\mathbf{x}, t)$, la vitesse moyenne $\tilde{\mathbf{U}}(\mathbf{x}, t)$, l'énergie interne $\tilde{e}_s(\mathbf{x}, t)$ et l'énergie totale $\tilde{e}_s(\mathbf{x}, t)$. Une technique numérique différente pour stabiliser les approximations des termes sources dans ce système a été proposée ensuite dans [24]. Finalement, une étude détaillée des erreurs numériques est présentée pour un écoulement stochastique réactif d'un gaz parfait en espace monodimensionnel.

The moment-guided Monte Carlo method [7]. Degond, P., Dimarco, G., Pareschi, L., 2011.

Les auteurs proposent une méthode hybride de résolution numérique des équations pdf en considérant l'exemple de *l'équation de Boltzmann*. L'idée de la méthode consiste à réduire la variance des méthodes Monte-Carlo (DSMC), utilisées pour l'approximation des solutions de l'équation pdf, en imposant aux échantillons les moments statistiques calculés par les équations aux dérivées partielles déduites de l'équation pdf. En effet, ces moments ne contiennent pas d'erreur statistique ni de biais par définition. L'équation pdf et les équations aux dérivées partielles sont couplées via le terme de correction cinétique pour prendre en compte la perte de l'équilibre thermodynamique. Les équations pour les moments statistiques correspondent aux *équations d'Euler compressibles* pour la conservation de la masse, de la quantité du mouvement et de l'énergie, qui sont simulées par une méthode de Volumes / Différences Finis. La discrétisation est réalisée par décomposition des flux en partie "moyenne" et partie fluctuante, fournie par la simulation Monte-Carlo. Un schéma explicite du premier ordre, construit par composition d'un schéma centré de type Lax-Friedrichs, d'un schéma MUSCL, et d'une technique de type NGP (Nearest Grid Point) qui permet de "lisser" les fluctuations, en résulte. A la fin de chaque pas de temps, les positions, les vitesses et les corrélations des vitesses fluctuantes des particules discrètes sont corrigées pour s'identifier aux moyennes imposées par les équations Euleriennes. En considérant plusieurs cas tests, les auteurs constatent une réduction importante des fluctuations dues à l'erreur statistique et concluent donc que les résultats de la simulation couplée sont plus précis. Les résultats quantitatifs sont présentés en comparant les solutions obtenues par l'approche hybride et par l'approche DSMC classique à nombre de particules fixe avec la solution de référence obtenue avec un très grand nombre de particules.

The heterogeneous multiscale methods [13]. E, W., Engquist, B., 2003.

Cet article décrit la méthodologie générale de couplage des modèles macroscopiques avec les modèles microscopiques pour les problèmes impliquant plusieurs échelles physiques, spatiales et temporelles (Heterogeneous Multiscale Methods, HMM). Cette approche est motivée par l'invalidité des fermetures empiriques pour les modèles marcoscopiques dans les zones hors-équilibre, où les phénomènes physiques à petite échelle tels que la combustion, les réactions chimiques, la destruction ou la turbulence sont importants. Les variables d'intérêt restent les variables macroscopiques, mais le fait d'introduire localement un modèle microscopique (provenant, par exemple, de la dynamique moléculaire (MD)) permet d'éviter les fermetures empiriques et d'augmenter la précision des résultats. Le modèle microscopique peut être introduit sur plusieurs mailles du maillage macroscopique ou à l'intérieur d'une seule maille (dans ce cas, le modèle microscopique fournit les flux à travers les bords de cette maille) et nécessite sa propre discrétisation spatiale et temporelle (raffinement local) ainsi que le traitement numérique particulier. Pour cette raison, les méthodes sont appelées hétérogènes, contrairement aux techniques multigrid classiques, qui utilisent le même modèle physique avec des discrétisations différentes. Les méthodes HMM se distinguent également des méthodes de décomposition de domaine avec une interface épaisse. Par exemple, lors du couplage d'un modèle du fluide continu avec des équations de la dynamique moléculaire à l'aide de la méthode de Schwartz [21, 22, 35], les deux sous-domaines se superposent et sur l'interface la

consistance des modèles est imposée. Dans les méthodes HMM, le modèle macroscopique est défini sur tout le domaine, tandis que le modèle microscopique est introduit comme un raffinement local et utilise l'approche de séparation des échelles, en évitant le couplage des échelles temporelles entre les deux modèles. Par conséquent, le nombre de degrés de liberté se trouve considérablement réduit dans les modèles microscopiques, ce qui contribue au succès de ces méthodes.

Les auteurs du papier se concentrent sur deux types de problèmes multi-échelle:

Type-A Le modèle macroscopique est connu mais n'est pas valide dans certaines zones de l'écoulement, où la description microscopique vient le remplacer. Les conditions aux limites à l'interface pour le modèle marcoscopique sont obtenues à partir des données microscopiques (par exemple, la dynamique moléculaire, MD). Ce type de problème est rencontré sur les fronts des flammes turbulentes, dans la dynamique de la ligne de contact, dans les interactions fluide-structure ou dans les systèmes avec les réactions chimiques localisées.

Type-B Dans ce cas, le modèle macroscopique n'est pas explicitement connu et les contraintes, les flux ou les lois d'état sont déduits du modèle microscopique (MD) dans les zones où ils sont inconnus pour le solveur macroscopique, par exemple, dans les écoulements en milieu poreux, des fluides complexes, les polymères et les problèmes de plasticité.

Plusieurs exemples de descriptions couplées pour les problèmes de la mécanique des fluides et du solide sont présentés avec les opérateurs de projection / reconstruction et les relations de consistance assurant le couplage ainsi que les schémas numériques adaptés.

Après avoir dressé ce panorama rapide et non exhaustif décrivant quelques techniques utilisées pour la simulation des écoulements fluides, et faisant appel à la notion de couplage interfacial instationnaire ou de couplage local instantané, nous allons présenter une synthèse des travaux réalisés.

Position des travaux réalisés

Le présent travail de thèse vise à développer une nouvelle description de la *phase dispersée* proposée initialement dans [4, 24, 27] et basée sur le *couplage local de descriptions classiques Eulerienne et Lagrangienne*, où les deux modèles sont déduits de la même équation pdf. Dans une certaine mesure, les travaux réalisés sont par nature et au niveau des objectifs assez voisins de ceux décrits dans les articles présentés ci-dessus pour le cas de la combustion turbulente [45] et pour la résolution numérique de l'équation de Boltzmann [7].

Le modèle stochastique Lagrangien, et le modèle Eulerien représenté par un système d'équations aux dérivées partielles qui décrit la conservation de la masse et de la quantité du mouvement, sont couplés via des termes d'échange. Le modèle Lagrangien fournit au modèle Eulerien le tenseur cinétique particulaire calculé sur l'ensemble des particules traitées (les fermetures empiriques ne sont donc plus nécessaires) ; à son tour, le modèle Eulerien calcule la vitesse moyenne des particules

qui ne contient pas de biais par définition. Son utilisation dans les coefficients des équations stochastiques Lagrangiennes présente une technique de réduction de la variance (VRT) et devrait permettre d'augmenter la précision des approximations. Faisant suite à des travaux récents sur ce sujet [4, 27], on va se concentrer sur le développement de la méthodologie de couplage et des méthodes numériques dédiées à la simulation de ces modèles. Le but principal consistera dans un premier temps à développer un schéma Volumes Finis pour la partie Eulerienne du modèle de la phase dispersée, qui soit adapté aux écoulements dilués en particules, et aussi capable de fournir des approximations stables des solutions même en présence de données Lagrangiennes peu régulières. Dans un second temps, on s'intéressera à l'efficacité d'une telle méthode de couplage pour la réduction de l'erreur numérique globale.

Synthèse des travaux

Le manuscrit de la thèse est organisé comme suit. Le premier chapitre présente une synthèse des aspects théoriques des méthodes PDF dans le cadre des simulations des écoulements turbulents gaz-particules, où la phase fluide est simulée avec un modèle de grandes échelles (RANS). Il rappelle brièvement le modèle stochastique Lagrangien, le schéma numérique pour son intégration temporelle et décrit plus en détail la vérification du module Lagrangien implémenté. Le deuxième chapitre introduit le modèle Eulerien de la phase dispersée, consistant avec le modèle Lagrangien du chapitre précédent, ainsi qu'un schéma de relaxation pour la simulation de ce modèle en espace mono-dimensionnel. De nombreux cas-tests provenant de la dynamique des gaz valident le schéma dans un cas particulier où le tenseur cinétique est une fonction de la variable principale. Quelques résultats de simulations avec un tenseur cinétique bruité sont analysés en termes de stabilité, et pour évaluer la diffusion numérique du schéma. Le troisième chapitre est consacré à l'extension de ce schéma dans un espace bi-dimensionnel. La difficulté principale ici est liée à la structure fortement anisotrope du tenseur cinétique qui n'apparaît pas dans le cas 1D. Enfin, le dernier chapitre décrit l'algorithme de couplage des deux descriptions, Lagrangienne et Eulerienne, et aborde les questions de discrétisation, interpolation et échange des données entre les modèles. Finalement, une tentative de mesure des erreurs numériques du modèle couplé de la phase dispersée est réalisée sur un cas test de jet co-courant gaz-particules et les résultats sont comparés aux approximations des méthodes Lagrangiennes “classiques” décrites dans le chapitre 1.

Chapitre 1. A Moments/PDF approach to simulation of turbulent two-phase flows

Ce chapitre décrit une méthode classique de couplage pour la simulation numérique des écoulements gaz-particules où le gaz est une phase fluide porteuse et les particules apparaissent comme inclusions transportées par le fluide. Le régime dispersé augmente considérablement les échanges entre les phases et paraît préférable dans de nombreux processus industriels. En même temps, la simulation numérique de ces écoulements s'avère difficile, car elle nécessite de prendre en compte

la polydispersion de certaines propriétés et les phénomènes hors-équilibre thermodynamique (liés par exemple aux réactions chimiques, à la combustion, etc). Pour ces raisons, l'approche bi-fluide n'est pas toujours adaptée car elle ne fournit que quelques moments statistiques, ou parce que ses fermetures empiriques dans certaines zones ne sont pas pertinentes. C'est notamment le cas dans les écoulements dilués en particules auxquels on va désormais se limiter. Or, quand le nombre de particules discrètes à traiter reste limité, on peut s'intéresser aux méthodes de description plus fines. Une approche classique basée sur le couplage d'un modèle RANS pour la phase fluide et d'une équation PDF pour une particule discrète a été implementée (voir notamment les références [51, 72]). Le modèle R_{ij} retenu pour le fluide incompressible s'écrit [56]:

$$\begin{aligned} \frac{\partial \langle U_{g,i} \rangle}{\partial x_i} &= 0 \\ \frac{\partial \langle U_{g,i} \rangle}{\partial t} + \langle U_{g,j} \rangle \frac{\partial \langle U_{g,i} \rangle}{\partial x_j} + \frac{\partial \langle u_{g,i} u_{g,j} \rangle}{\partial x_j} &= -\frac{1}{\rho_f} \frac{\partial \langle P_g \rangle}{\partial x_i} \\ \frac{\partial \langle u_{g,i} u_{g,j} \rangle}{\partial t} + \langle U_{g,k} \rangle \frac{\partial \langle u_{g,i} u_{g,j} \rangle}{\partial x_k} + \frac{\partial \langle u_{g,i} u_{g,j} u_{g,k} \rangle}{\partial x_k} + \langle u_{g,i} u_{g,k} \rangle \frac{\partial \langle U_{g,j} \rangle}{\partial x_k} + \langle u_{g,j} u_{g,k} \rangle \frac{\partial \langle U_{g,i} \rangle}{\partial x_k} & \\ = G_{ik} \langle u_{g,j} u_{g,k} \rangle + G_{jk} \langle u_{g,i} u_{g,k} \rangle + C_0 \langle \varepsilon \rangle \delta_{ij}, & \end{aligned} \quad (1)$$

où $\langle \mathbf{U}_g \rangle$ dénote la vitesse moyenne du fluide, $\mathbf{u}_g = \mathbf{U}_g - \langle \mathbf{U}_g \rangle$ la vitesse fluctuante qui apparaît dans la décomposition de Reynolds et $\langle P_g \rangle$ la pression moyenne. Dans les simulations pratiques, le système (1) nécessite une équation supplémentaire pour le taux de dissipation de l'énergie cinétique turbulente, $\langle \varepsilon \rangle$ [60].

La phase dispersée est décrite par un système d'équations Lagrangiennes stochastiques qui simulent les trajectoires d'un certain (grand) nombre de particules:

$$d\mathbf{Z}(t) = \mathbf{A}(t, \mathbf{Z}(t), p(t; \mathbf{z}), \mathbf{Y}(t))dt + \mathbf{B}(t, \mathbf{Z}(t), p(t; \mathbf{z}), \mathbf{Y}(t))d\mathbf{W}(t), \quad (2)$$

où $p(t; \mathbf{z})$ est une fonction de densité de probabilité (pdf) du vecteur d'état $\mathbf{Z}(t)$ lié à une particule [17]; $\mathbf{Y}(t)$ désigne des champs moyens externes, par exemple liés au fluide, définis à la position de la particule et $\mathbf{W}(t)$ est un processus de Wiener [49]. Une fois que ces équations sont intégrées en temps, tous les moments statistiques peuvent en être extraits par application de l'opérateur de moyenne d'ensemble. Cette procédure est caractéristique des méthodes de Monte-Carlo et permet d'approcher la fonction pdf par une approximation discrète. Cependant, en pratique, les équations SDE_p^{Lag} (2) sont difficiles à simuler, puisque il existe une dépendance non-linéaire de la pdf: à chaque instant une particule nécessite la connaissance des statistiques non-locales calculées sur tous les échantillons suivis.

L'algorithme de couplage peut donc se résumer ainsi: le modèle (1) de la phase fluide, PDE_g^{Eul} , est simulé par une méthode de type Volumes Finis et fournit les approximations des champs moyens au solveur Lagrangien de la phase dispersée, SDE_p^{Lag} , Fig. 3. Ces champs moyens permettent de recréer une turbulence synthétique dans le modèle stochastique (2).

Ce chapitre présente une synthèse des travaux réalisés dans [40, 51] sur le couplage Moments/PDF, en se concentrant sur la **description de la phase dispersée**. Il comporte notamment les rappels de notions liés aux méthodes PDF et aux modèles stochastiques, des explications sur l'équivalence

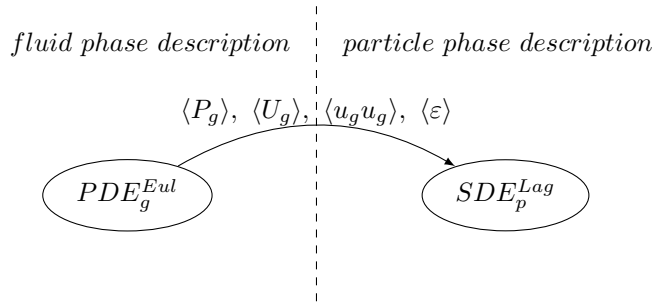


Figure 3: Représentation classique Moments/PDF des écoulements turbulents (dilués) gaz-particles.

entre les différentes descriptions des écoulements, les erreurs numériques générées par les méthodes stochastiques et les opérateurs de moyenne/projection. Le schéma d'Euler du premier ordre retenu pour l'intégration temporelle des équations stochastiques (2) proposé dans [41] est rapidement rappelé.

La vérification de l'implémentation numérique du module Lagrangien qui simule SDE_p^{Lag} est réalisée sur plusieurs cas-tests:

- un cas de dispersion d'un point source dans la turbulence homogène isotrope stationnaire qui permet de vérifier entre autres la convergence correcte de l'erreur statistique;
- un cas de convection pure, sans dispersion turbulente, pour vérifier la convergence de l'erreur de discrétisation temporelle (pour un schéma du 1er ordre en temps);
- un cas test de jet diphasique pariétal avec une turbulence stationnaire non-homogène: on présente une comparaison des statistiques de la phase dispersée du module développé avec les résultats de simulations provenant de *Code-Saturne*⁸, où l'approche Moments/PDF a été implementée précédemment. Il faut noter que les champs fluides utilisés par les deux codes sont les mêmes, ils sont fournis par une simulation monophasique préliminaire avec *Code-Saturne*.

Enfin, une méthode de couplage alternative est proposée, faisant suite aux travaux [4, 24, 27]. Cette nouvelle méthode est dérivée de la méthode Moments/PDF et introduit un couplage supplémentaire, à l'intérieur de la phase dispersee - ce qui justifie l'appellation "Moments/Moments-PDF", Fig. 4. Elle est motivée par la volonté de réduire, à nombre de particules donné, le bruit statistique propre aux méthodes Lagrangiennes et, éventuellement, le biais dû au caractère non-linéaire du système (2).

Le nouveau modèle de la phase dispersée comprend donc la même description stochastique Lagrangienne (2) à laquelle se rajoute un système d'équations aux dérivées partielles pour la densité et la vitesse moyennes qui sont déduites de (2):

⁸Computational fluid dynamics free software developed at EDF R&D, <http://www.code-saturne.org>.

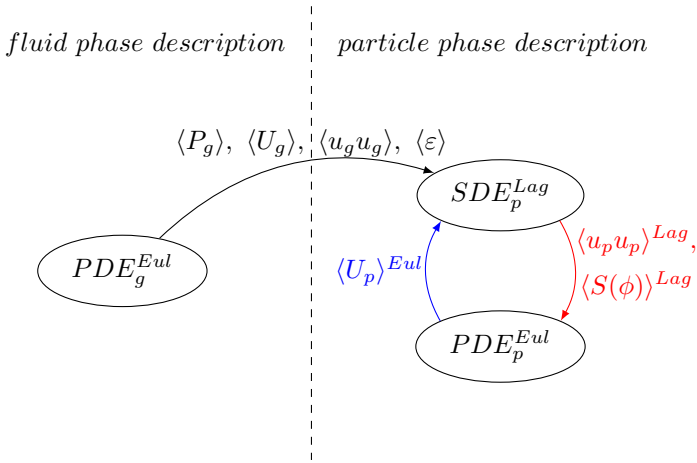


Figure 4: Extension de la méthode classique - description hybride Moments/Moments-PDF.

- **Équations stochastiques Lagrangiennes SDE_p^{Lag} :**

$$\begin{aligned}
 dx_{p,i} &= U_{p,i} dt \\
 d\mathbf{U}_{p,i} &= \frac{1}{\tau_p} (U_{s,i} - U_{p,i}) dt + g_i dt \\
 dU_{s,i} &= -\frac{1}{\rho_g} \frac{\partial \langle P_g \rangle}{\partial x_i} dt + (\langle \mathbf{U}_{p,j}^E \rangle - \langle U_{g,j} \rangle) \frac{\partial \langle U_{g,i} \rangle}{\partial x_j} dt - \frac{(U_{s,i} - \langle U_{g,i} \rangle)}{\mathbf{T}_{L,i}^{E*}} dt + \\
 &\quad \sqrt{\langle \varepsilon \rangle \left(C_0 b_i \tilde{k}/k + \frac{2}{3} (b_i \tilde{k}/k - 1) \right)} dW_{t,i}, \quad i, j \in \mathbb{Z}
 \end{aligned} \tag{3}$$

où les statistiques de la phase fluide portent l'indice “ g “ et sont calculées par un solveur Volumes Finis, PDE_g^{Eul} . Les termes fournis par le solveur Eulerien de la phase dispersée sont notés par l'exposant ” E “.

- **Équations aux dérivées partielles Euleriennes PDE_p^{Eul} - équations de conservation - déduites de (3):**

$$\begin{aligned}
 \frac{\partial \alpha_p^E \rho_p}{\partial t} + \frac{\partial}{\partial x_i} (\alpha_p^E \rho_p \langle U_{p,i}^E \rangle) &= 0, \quad i \in \mathbb{Z} \\
 \frac{\partial \alpha_p^E \rho_p \langle \mathbf{U}_{p,i}^E \rangle}{\partial t} + \frac{\partial}{\partial x_j} (\alpha_p^E \rho_p (\langle U_{p,i}^E \rangle \langle U_{p,j}^E \rangle + \langle \mathbf{u}_{p,i} \mathbf{u}_{p,j} \rangle^L)) &= \alpha_p^E \rho_p g_i + \left\langle \frac{\alpha_p^E \rho_p \mathbf{U}_{r,i}^L}{\tau_p^L} \right\rangle,
 \end{aligned} \tag{4}$$

où $\alpha_p(t, \mathbf{x})$ est le taux de présence des particules, ρ_p la densité constante, $\langle \mathbf{U}_p \rangle(t, \mathbf{x})$ la vitesse moyenne de la phase dispersée et $\langle \mathbf{u}_p \mathbf{u}_p \rangle(t, \mathbf{x})$ le tenseur cinétique particulaire. Les variables calculées par le module Lagrangien (3) sont marquées par l'exposant ” L “. Les termes sources au second membre représentent les forces de gravité et de traînée.

Pour la mise en œuvre de cette technique de couplage, les questions algorithmiques et les problèmes numériques, liés notamment aux échanges des données entre les descriptions différentes, vont être abordés dans les chapitres suivants.

Chapitre 2. A one-dimensional relaxation scheme for the hybrid modeling of gaz-particle flows

Le modèle Eulerien de la phase dispersée décrit l'évolution des moments statistiques du premier ordre par un système d'équations de conservation de la masse et de la quantité du mouvement qui sont déduites des équations stochastiques Lagrangiennes présentées dans le chapitre 1. Dans l'espace d -dimensionnel, pour le vecteur d'état composé par la densité moyenne $\rho(t, \mathbf{x}) = \rho_p^0 \alpha_p(t, \mathbf{x})$ et le flux moyen $(\rho \mathbf{U})(t, \mathbf{x}) = (\rho \langle \mathbf{U}_p \rangle)(t, \mathbf{x}) \in \mathbb{R}^d$, le système Eulerien (4) peut être réécrit comme:

$$\begin{cases} \partial_t \rho + \partial_{x_j} (\rho U_j) = 0, & t > 0, \quad \mathbf{x} \in \mathbb{R}^d, \\ \partial_t (\rho U_i) + \partial_{x_j} (\rho U_i U_j) + \partial_{x_j} (\rho R_{ij}^L) = \rho g_i + \rho \langle U_{r,i} / \tau_p \rangle^L, \end{cases} \quad (5)$$

où l'exposant “ L ” désigne les variables calculées via la description Lagrangienne: $R_{ij}^L(t, \mathbf{x}) = \langle u'_i u'_j \rangle^L$, $i, j = 1, \dots, d$ est le tenseur cinétique particulaire avec $\mathbf{u}'(t, \mathbf{x}) \in \mathbb{R}^d$ la vitesse fluctuante des particules provenant de la décomposition de Reynolds de la vitesse instantanée; les termes sources dans la deuxième équation de (5) décrivent les forces de gravité et de traînée exercées sur les particules, où $\mathbf{U}_r(t, \mathbf{x})$ désigne la vitesse relative entre le fluide et la particule et τ_p le temps nécessaire à la particule pour s'adapter à la vitesse du fluide. Par conséquent, ce système est fermé par les termes provenant du module Lagrangien - la méthodologie du couplage est décrite dans le chapitre 1, sec. 1.5. Ces termes ne dépendent pas des variables du système (5) et sont potentiellement peu régulières, car issus des simulations Lagrangiennes. Un détail important doit être souligné: le terme $R_{ij}^L(t, \mathbf{x})$ qui apparaît dans l'opérateur de divergence spatiale ne représente pas le terme de pression, mais un tenseur anisotrope provenant de la décomposition de Reynolds de la vitesse. L'enjeu principal de ce volet consistera donc à développer une technique de simulation de ce système qui assurerait des *approximations stables* même avec des *données extérieures bruitées*.

L'approche proposée dans ce chapitre dans le cadre monodimensionnel sera basée sur les techniques de relaxation [30] et de décentrement global [20]. La propagation des ondes acoustiques est correctement prise en compte en simulant un sursystème qui comporte une équation supplémentaire d'évolution du tenseur cinétique et qui coïncide avec le système original quand le paramètre de relaxation τ_p^R tend vers zéro. Le système de relaxation généralisé s'écrit:

$$\begin{cases} \partial_t \rho + \partial_x (\rho U) = 0, & t > 0, \quad x \in \mathbb{R}, \\ \partial_t (\rho U) + \partial_x (\rho U^2 + \rho R) = \rho g + \rho \langle U_r / \tau_p \rangle^L, \\ \partial_t (\rho R) + \mathcal{A}(W, \partial_x W) = \rho(R^L - R) / \tau_p^R. \end{cases} \quad (6)$$

Deux formes d'opérateur $\mathcal{A}(W, \partial_x W)$ ont été proposées [11, 28] et résultent en deux sursystèmes non-conservatifs, **A1** et **A2**. Le premier est “naturel”, car il correspond au modèle R_{ij} “classique”; cependant, il admet deux champs vraiment non-linéaires et nécessite donc l'introduction de relations de saut approchées. Le deuxième est déduit de A1 de sorte qu'il ne contient que des champs linéairement dégénérés, pour lesquels les relations de saut sont définies de façon unique.

L'algorithme numérique pour l'approche A1 est détaillé dans [28]. L'algorithme correspondant à la

méthode A2 est proposé dans ce chapitre, il est basé sur la méthode de splitting d'opérateurs et le schéma de Godunov.

La vérification et la comparaison des deux approches, A1 et A2, sont réalisées dans le cadre où le tenseur cinétique est une fonction de la densité: $\rho R^L = \pi(\rho)$. Pour tester la stabilité des deux schémas correspondant à A1 et A2, des cas tests ont été réalisés dans les situations extrêmes: doubles chocs forts, détentes supersoniques avec apparition du vide et présentant des rapports de pression importants. Les résultats permettent de conclure que les deux méthodes assurent la stabilité des approximations, et convergent vers les bonnes solutions (ce qui est dû à la forme conservative des deux premières équations). Par ailleurs, on obtient les vitesses de convergence correctes (vitesse 1 correspondant aux ondes vraiment non-linéaires du système (5) avec $\rho R^L = \pi(\rho)$).

Quelques résultats de simulations avec un tenseur cinétique $R^L(t, x)$ bruité sont analysés en termes de stabilité et de la diffusion numérique du schéma A2. Les résultats similaires pour l'approche A1 sont présentés dans [28]. Ici encore, les deux méthodes permettent d'obtenir des approximations stables et ont tendance à lisser les non-régularités en dehors du domaine bruité.

Finalement, une des annexes présente des estimations d'énergie pour les systèmes homogènes correspondant à A1 et A2, dans le cadre continu.

Chapitre 3. A two-dimensional relaxation scheme for the hybrid modelling of two-phase flows

Le troisième chapitre étend le problématique du chapitre 2 au cadre bi-dimensionnel. La partie Eulerienne du modèle hybride pour la phase dispersée engagée dans un écoulement du fluide turbulent décrit l'évolution des quantités moyennes liées aux particules - de la densité et de la vitesse moyennes - qui est régie par les lois de conservation (4):

$$\begin{cases} \partial_t \rho + \partial_{x_j} (\rho U_j) = 0, & t > 0, \quad \mathbf{x} \in \mathbb{R}^d, \\ \partial_t (\rho U_i) + \partial_{x_j} (\rho U_i U_j) + \partial_{x_j} (\rho R_{ij}^L) = \rho g_i + \rho \langle U_{r,i} / \tau_p \rangle^L. \end{cases} \quad (7)$$

Il est important de rappeler que le terme $\mathbf{R}^L(t, \mathbf{x})$ n'est pas une fonction des variables du système $(\rho, \rho \mathbf{U})$, mais une donnée extérieure comportant le bruit statistique qui caractérise les approximations instationnaires issues des simulations Monte-Carlo. Par conséquent, l'objectif principal reste le même : trouver une approche numérique de simulation de ce système qui permet obtenir des approximations stables, même avec des données fortement bruitées, et sans introduire d'excès de diffusion numérique. Cependant, dans le cadre bi-dimensionnel on est en outre confronté à une autre particularité du système (7): le tenseur cinétique étant fortement anisotrope, $R_{ij}^L \neq \frac{1}{2} \text{tr}(R) \delta_{ij}$, les techniques de relaxation utilisées dans le cas 1D nécessitent d'être étendues pour correctement prendre en compte la structure des ondes multi-D. Aucune confusion avec les techniques de relaxation utilisées dans la dynamique des gaz pour la simulation des équations d'Euler barotropes [2] ne peut plus survenir, contrairement au cas 1D, où ρR_{ij}^L pourrait correspondre au terme de

pression dû à la structure sphérique.

Suivant la procédure décrite dans le chapitre 2, on introduit le modèle de relaxation :

$$\begin{cases} \partial_t \rho + \partial_{x_j} (\rho U_j) = 0, & t > 0, \quad \mathbf{x} \in \mathbb{R}^d, \\ \partial_t (\rho U_i) + \partial_{x_j} (\rho U_i U_j) + \partial_{x_j} (\rho R_{ij}) = \rho g_i + \rho \langle U_{r,i} / \tau_p \rangle^L, \\ \partial_t (\rho R_{ij}) + \partial_{x_k} (\rho U_k R_{ij}) + \rho (R_{ik} \partial_{x_k} U_j + R_{jk} \partial_{x_k} U_i) = \rho \phi_{ij} / \tau_p^R. \end{cases} \quad (8)$$

En effet, par analogie avec le cas monodimensionnel, ce système reproduit le modèle de turbulence R_{ij} et introduit un décentrement des termes convectifs dits "de production". L'association des techniques de relaxation avec des techniques de décentrement permet de stabiliser les approximations, le critère de stabilité étant prioritaire dans les simulations hybrides.

L'algorithme de simulation est basé sur la méthode de splitting d'opérateurs et sur le schéma Volumes Finis construit suivant le formalisme du problème de Riemann. Sur l'interface entre deux mailles, le sursystème est approché par deux systèmes de relaxation **R1** et **R2** correspondant aux approches A1 et A2 du chapitre 2 respectivement. Le système R1 est naturellement déduit du modèle de turbulence R_{ij} et admet des champs vraiment non-linéaires. L'introduction des relations de saut approchées s'avère nécessaire. R2 est introduit en tant que "linéarisation" du système R1, et n'admet que des champs linéairement dégénérés.

Une rapide analyse de stabilité non-linéaire des sursystèmes homogènes correspondant à R1 et R2 est donnée en se basant sur les estimations d'énergie totale de la phase dispersée.

Le chapitre présente les résultats numériques de simulations 2D avec la méthode R2 uniquement, qui est désormais retenue pour réaliser les simulations couplées. L'implémentation de cette méthode a été validée par des cas-tests monodimensionnels dans chaque direction d'espace. Quelques résultats de simulations avec un tenseur cinétique bruité qui reproduit la turbulence synthétique sont illustrés. Finalement, la méthode développée permet d'obtenir des approximations stables et permet de prendre en compte l'anisotropie du tenseur cinétique. L'extension de cette approche dans le cadre 3D serait directe.

Chapitre 4. A hybrid Moments/Moments-PDF approach to simulation of turbulent two-phase flows

Le chapitre est consacré à la mise en œuvre numérique de la méthode hybride Moments/Moments-PDF. Il décrit l'algorithme numérique FV/FV-PDF basé sur l'extension de l'algorithme des méthodes classiques du chapitre 1. Les points qui sont mis en évidence concernent les échanges des données entre les particules et le maillage ainsi que la correspondance entre les discrétisations spatiales du module Lagrangien et du module Eulerien. Le choix des conditions aux limites de façon consistante pour les deux descriptions Eulerienne et Lagrangienne est également proposé.

Le premier objectif poursuivi dans cette partie consiste à vérifier que le solveur Eulerien développé dans les chapitres 2 et 3 permet d'obtenir les approximations stables dans la configuration hybride

où le tenseur cinétique et les termes sources contenant de l'erreur statistique sont introduits dans le système.

Dans un second temps, l'analyse de l'erreur numérique totale doit permettre de conclure quant à l'efficacité de cette méthode hybride en termes de précision/coût calcul. Plus précisément, on veut comparer l'erreur numérique des approximations issues des calculs hybrides avec celle des calculs dits "classiques" suivant l'approche Moments/PDF du chapitre 1. Il est important de rappeler que l'erreur numérique totale est composée par l'erreur de discrétisation spatiale, temporelle, l'erreur statistique et le biais, ce dernier ayant lieu pour le modèle non-linéaire en pdf uniquement. Pour pouvoir dissocier les différentes erreurs et notamment pour déterminer l'erreur prédominante dans les calculs hybrides, on est amené à choisir une situation-test avec une turbulence non-homogène anisotrope stationnaire où on peut trouver une solution de référence grâce à l'homogénéisation en temps. On reprend donc le cas test de jet diphasique cocourant le long d'une paroi rigide, qui a été étudié dans le chapitre 1, et on choisit des approximations obtenues avec la méthode Lagrangienne "classique" Moments/PDF à convergence en pas d'espace, pas de temps et en nombre de particules par maille comme la solution de référence.

Finalement, on analyse la convergence de l'erreur déterministe et de l'erreur statistique des approximations "hybrides" en fonction des paramètres numériques: le pas de maillage, le pas de temps et le nombre de particules par maille N_{pc} . Les questions auxquelles on souhaite répondre sont :

- Le solveur Eulerien développé permet-t-il d'obtenir des approximations stables dans la configuration hybride Moments/Moments-PDF?
- Les approximations du schéma Volumes Finis pour la phase dispersée convergent-elles vers la solution de référence?
- Les approximations Lagagiennes obtenues avec le schéma d'Euler dans la configuration hybride convergent-elles vers la solution de référence?
- Quelle erreur est prédominante dans la méthode classique Moments/PDF et dans la méthode hybride Moments/Moments-PDF?
- Observe-t-on la réduction de l'erreur statistique et du biais pour le même nombre de particules par maille, N_{pc} entre les simulations "classiques" et les simulations "hybrides" ?

Enfin, on présente quelques extensions numériques possibles du présent algorithme.

Valorisation

Le chapitre 2 est accepté pour publication à la revue "Computers and Fluids". Une version préliminaire de ce chapitre est parue en tant que rapport EDF H-i81-2010-02352-EN. Le chapitre 3 est paru comme rapport EDF H-i81-2012-00646-EN, et est soumis à publication.

Deux communications de congrès ont été rédigées:

- "A hybrid method for two-phase flows simulations", K. Dorogan, J.-M. Hérard, J.-P. Minier, International Conference on Computational Fluid Dynamics, St. Petersbourg, 12-16 juillet 2010. Publié dans les proceedings "Computational Fluid Dynamics 2010", Springer-Verlag, 2011, ISBN 978-3-642-17883-2. Rapport EDF H-i81-2010-1581-EN.
- "A two-dimensional relaxation scheme for the hybrid modelling of two phase flows", K. Dorogan, J.-M. Hérard, J.-P. Minier, Congrès Finite Volumes for Complex Applications 6, Prague, 6-10 juin 2011. Publié dans les proceedings "Finite Volumes for Complex Applications. Problems and Perspectives", Springer-Verlag, 2011. ISBN 978-3-642-20670-2, ISSN 2190-5614. Rapport EDF H-i81-2011-00691-EN.

Bibliography

- [1] Ambroso, A., Chalons, C., Coquel, F., Godlewski, E., Lagoutière, F., Raviart, P.-A., Seguin, N.: Relaxation methods and coupling procedures. *Int. J. Num. Meth. Fluids*, **56**(8), 1123–1129 (2008).
- [2] Chalons, C., Coulombel, J.F.: Relaxation approximation of the Euler equations. *J. Math. Anal. Appl.*, **348**, pp. 872–893 (2008)
- [3] Chen, C.P., Wood, P.E.: Turbulence closure modeling of dilute gas-particle axisymmetric jet. *AICHE J.*, **32** (1) 163–166 (1986)
- [4] Chibbaro, S., Hérard, J.M., Minier, J.P.: A novel Hybrid Moments/Moments-PDF method for turbulent two-phase flows. Final Technical Report Activity Marie Curie Project. TOK project Lange Contract MTKD-CT-2004 509849 (2006)
- [5] Csanady, G.T.: Turbulent diffusion for heavy particles in the atmosphere. *Journal of Atmospheric Sciences*, 20:201-8 (1963)
- [6] Degond, P., Dimarco, G., Mieussens, L.: A multiscale kinetic-fluid solver with dynamic localization of kinetic effects. *J. Comp. Phys.*, **229** 4907–4933 (2010)
- [7] Degond, P., Dimarco, G., Pareschi, L.: The moment-guided Monte Carlo method. *Int. J. for Numerical Methods in Fluids*, **67** (2) 189–213 (2011)
- [8] Degond, P., Jin, S., Mieussens, L.: A smooth transition model between kinetic and hydrodynamic equations. *J. Comp. Phys.*, **209** 665–694 (2005)
- [9] Derevich, I., Zaichik, L.: Precipitation of particles from a turbulent flow. *Mekhanika Zhidkosti i Gaza*, **5** 96–104 (1988)
- [10] Deutsch, E., Simonin, O.: Large eddy simulation applied to the motion of particles in stationary homogeneous fluid turbulence. Turbulence modification in multiphase flows, *FED* **110**, ASME 255–60 (1991)
- [11] Dorogan, K., Guingo, M., Hérard, J.M., Minier, J.P.: A relaxation scheme for hybrid modelling of gas-particle flows. Accepted for publication in *Computers and Fluids* (2012)
- [12] Drew, D.A.: Mathematical modeling of two-phase flow. *Annu. Rev. Fluid Mech.*, 15:261–91 (1983)

- [13] E, W., Engquist, B.: The heterogeneous multiscale methods. *Commun. Math. Sci.*, **1** (1), 87–132 (2003)
- [14] E, W., Liu, D., Vanden-Eijnden, E.: Analysis of multiscale methods for stochastic differential equations. *Communications on Pure and Applied Mathematics*, John Wiley & Sons, Inc. (2003)
- [15] Elghobashi, S.E., Abou-Arab, T.W.: A two-equation turbulence model for two-phase flows. *Phys. Fluids*, **26** (4), 931–938 (1983)
- [16] Elghobashi, S.E., Truesdell, G.C.: Direct simulation of particle dispersion in a decaying isotropic turbulence. *J. Fluid Mech.*, **242**, 655–700 (1992)
- [17] Gardiner, C.W.: *Handbook of stochastic methods for physics, chemistry and natural sciences*. Springer, Berlin (1990)
- [18] Girault, L., Hérard, J.M.: A two-fluid model in a porous medium. *Math. Mod. Numer. Anal.*, **44** (6), 1319–1348 (2010)
- [19] Godlewski, E.: Coupling fluid models. Proceedings of the International Conference Finite Volumes for Complex Applications 5, ISTE-Wiley, London **118**, 87–102 (2008)
- [20] Godlewski, E., Raviart, P.A.: *Numerical approximation of hyperbolic systems of conservation laws*. AMS, **118**, Springer (1996)
- [21] Hadjiconstantinou, N., Patera, A.T.: Heterogeneous atomistic-continuum representation for dense fluid systems. *Int. J. Modern Phys., C* **8** 967 (1997)
- [22] Hadjiconstantinou, N.: Hybrid atomistic-continuum formulations and the moving contact-line problems. *J. Comp. Phys.*, **154** 245–265 (1999)
- [23] He, J., Simonin, O.: Non-equilibrium prediction of the particle-phase stress tensor in vertical pneumatic conveying. In: *Gas-Solid Flows*, ASME FED **166** 253–263 (1993)
- [24] Hérard, J.M.: A relaxation tool to compute hybrid Euler-Lagrange compressible models. AIAA paper 2006-2872 (2006) <http://aiaa.org>
- [25] Hérard, J.M., Hurisse, O.: Coupling of two and one dimensional unsteady Euler equations through a thin interface. *Computers and Fluids*, **36** (4), 651–666 (2007)
- [26] Hérard, J.M., Hurisse, O.: Some attempts to couple distinct fluid models. *Networks and Heterogeneous Media*, **5** (3), 649–660 (2010)
- [27] Hérard, J.M., Minier, J.P., Chibbaro, S.: A Finite Volume scheme for hybrid turbulent two-phase flow models. AIAA paper 2007-4587, <http://aiaa.org>
- [28] Hérard, J.M., Uhlmann, M., Van der Velden, D.: Numerical techniques for solving hybrid Eulerian Lagrangian models for particulate flows. EDF report H-I81-2009-3961-EN, pp. 1-50, (2009)

- [29] Hockney, R.W., Eastwood, J.W.: Computer simulation using particles. Adam Hilger, New York (1988)
- [30] Jin, S., Xin, Z.: The relaxation schemes for systems of conservation laws in arbitrary space dimensions. *Comm. Pure Appl. Math.*, **48**, pp. 235–276 (1995)
- [31] Kartushinsky, A.I., Michaelides, E.E., Zaichik, L.: Comparison of the RANS and PDF methods for air-particle flows. *Int. J. Multiphase Flow*, **35**, 914–923 (2009)
- [32] Laviéville, J.: Simulations numériques et modélisation des interactions entre l’entraînement pas la turbulence et les collisions interparticulaires en écoulement gas-solide. Ph.D. thesis, Université de Rouen (1997)
- [33] Lesieur, M., Métais, O.: New trends in large-eddy simulations of turbulence. *Annu. Rev. Fluid Mech.*, **28**, 45–82 (1996)
- [34] Le Tallec, P., Mallinger, F.: Coupling Boltzmann and Navier-Stokes equations by half-fluxes. *J. Comput. Phys.*, **136** (1), 51–67 (1997)
- [35] Li, J., Liao, D., Yip, S.: Nearly exact solution for coupled continuum/MD fluid simulation. *Journal of Computer-Aided Material Design*, **6**, 95–102 (1999)
- [36] Liu, G.R., Liu, M.B.: Smoothed Particle Hydrodynamics: a meshfree particle method. Singapore: World Scientific (2003).
- [37] Loth, E.: Numerical approaches for motion of dispersed particles, droplets and bubbles. *Prog. Energy Combust. Sci.*, **26**, 161–223 (2000)
- [38] Mashayek, F., Pandya, R.V.R.: Analytical description of particle/droplet-laden turbulent flows. *Prog. Energy Combust. Sci.*, **29**, 329–378 (2003)
- [39] Mc Innes, J.M., Bracco, F.V.: Stochastic particle dispersion modeling and the tracer-particle limit. *Phys. Fluid A*, **4**, 2809 (1992)
- [40] Minier, J.P., Peirano, E.: The pdf approach to polydispersed turbulent two-phase flows. *Physics reports*, **352**, 1–214 (2001)
- [41] Minier, J.P., Peirano, E., Chibbaro, S.: Weak first- and second-order numerical schemes for stochastic differential equations appearing in Lagrangian two-phase flow modelling. *Monte Carlo Methods and Appl.*, **9**, 93–133 (2003)
- [42] Minier, J.P., Pozorski, J.: Derivation of a pdf model for turbulent flows based on principles from statistical physics. *Physics of Fluids*, **9**, 1748–1753 (1997)
- [43] Moin, P.: Progress in large eddy simulation of turbulent flows. *AIAA Aerospace Sciences Meeting*, Reno, NV, AIAA-97-0749 (1997)
- [44] Monaghan, J.: An introduction to SPH, *Computer Physics Communications*, **48**, 88–96 (1988)

- [45] Muradoglu, M., Jenny, P., Pope, S.B., Caughey, D.A.: A consistent hybrid finite-volume/particle method for the pdf equations of turbulent reactive flows. *J. Comp. Phys.*, **154**, 342–371 (1999)
- [46] Muradoglu, M., Pope, S.B., Caughey, D.A.: The hybrid method for the pdf equations of turbulent reactive flows: consistency and correction algorithms. *J. Comp. Phys.*, **172**, 841–878 (2001)
- [47] Nie, X.B., Chen, S.Y., Robbins, M.O.: Hybrid continuum-atomistic simulation of singular corner flow. *Phys. Fluids* **16** (10), 3579–3591 (2004)
- [48] O’Connell, S.T., Thompson, P.A.: Molecular dynamics-continuum hybrid computations: a tool for studying complex fluid flows. *Phys. Rev. E* **52**, R5792–R5795 (1995)
- [49] Øksendal, B.: Stochastic differential equations. An introduction with applications. Springer, Berlin (1995)
- [50] Onsager, L., Machlup, S.: *Phys. Rev.* **91**, 1505, 1512 (1953)
- [51] Peirano, E., Chibbaro, S., Pozorski, J., Minier, J.P.: Mean-field/PDF numerical approach for polydispersed turbulent two-phase flows. *Prog. Ene. Comb. Sci.*, **32**, 315–371 (2006)
- [52] Pialat, X., Simonin, O., Villedieu, P.: A hybrid Eulerian-Lagrangian method to simulate the dispersed phase in turbulent gas-particle flows. *Int. J. Multiphase Flow*, **33**, 766–788 (2007)
- [53] Pope, S.B.: PDF methods for turbulent reactive flows. *Prog. Energy Combust. Sci.*, **11**, 119–92 (1985)
- [54] Pope, S.B., Chen, Y.L.: The velocity-dissipation probability density function model for turbulent flows. *Phys. Fluids A*, **2**, 1437 (1990)
- [55] Pope, S.B.: Application of the velocity-dissipation probability density function model to inhomogeneous turbulent flows. *Phys. Fluids A*, **3**, 1947 (1991)
- [56] Pope, S.B.: On the relationship between stochastic Lagrangian models of turbulence and second moment closures. *Phys. Fluids* **6**, 973–985 (1994)
- [57] Pope, S.B.: Lagrangian PDF methods for turbulent flows. *Annu. Rev. Fluid Mech.*, 23–63 (1994)
- [58] Pope, S.B.: Particle method for turbulent flows: integration of stochastic model equations. *J. Comput. Phys.*, 117:332–49 (1995)
- [59] Pope, S.B.: Mean Field Equations in PDF Particle Methods for Turbulent Reactive Flows, Technical Report FDA 97-06. Cornell University (1997)
- [60] Pope, S.B.: Turbulent flows. Cambridge University Press, Cambridge (2000)
- [61] Pozorski, J., Minier, J.P.: On the lagrangian turbulent dispersion models based on the Langevin equation. *Int. J. Multiphase Flow*, **24**, 913–945 (1998)

- [62] Pozorski, J., Minier, J.P.: Probability density function modelling of dispersed two-phase turbulent flows. *Phys. Rev. E*, **59** (1), 855–863 (1998)
- [63] Reeks, M.W.: On a kinetic equation for the transport of particles in turbulent flows. *Phys. Fluids A*, **3**, 446–456 (1991)
- [64] Reeks, M.W.: On the continuum equations for dispersed particles in nonuniform flows. *Phys. Fluids A*, **4** (6), 1290–1303 (1992)
- [65] Reeks, M.W.: On the constitutive relations for dispersed particles in nonuniform flows, I dispersion in a simple shear flow. *Phys. Fluids A*, **5** (3), 750–761 (1992)
- [66] Schneider, J.: Direct coupling of fluid and kinetic equations. *Transport Theory Stat. Phys.*, **25** (6), 681–698 (1996)
- [67] Schwartzentruber, T.E., Boyd, I.D.: A hybrid particle-continuum method applied to shock waves. *J. Comp. Phys.*, **215** (2), 402–416 (2006)
- [68] Simonin, O.: Prediction of the dispersed phase turbulence in particle-laden jets. In: *Gas-Solid Flows 1991*, ASME FED 121, 197–206 (1991)
- [69] Simonin, O., Deutsch, E., Minier, J.P.: Eulerian prediction of the fluid/particle correlated motion in turbulent two-phase flows. *Appl. Sci. Res.*, 51:275–83 (1993)
- [70] Simonin, O.: Combustion and turbulence in two-phase flows. Von Karman Institute for Fluid Dynamics, Lecture Series (1996)
- [71] Sommerfeld, M., Kohnen, G., Rüger, M.: Some open questions and inconsistencies of Lagrangian particle dispersion models. In: *Proceedings of the Ninth Symposium on Turbulent Shear Flows*, Kyoto, Paper 15.1, (1993)
- [72] Sommerfeld, M.: Modeling and calculation of turbulent gas-solid flows with the Euler/Lagrange approach. *KONA (Powder and Particles)*, **16**, 194–206 (1999)
- [73] Squires, K.D., Eaton, J.K.: Measurements of particle dispersion obtained from direct numerical simulations of isotropic turbulence . *J. Fluid Mech.*, **226**, 1–35 (1991)
- [74] Talay, D.: in Kree, P., Wedig, W, editors. *Simulation of stochastic differential equations, in probabilistic methods in applied physics*. Springer, Berlin (1995)
- [75] Werder, T., Walther, J.H., Koumoutsakos, P.: Hybrid atomistic continuum method for the simulation of dense fluid flows. *J. Comp. Phys.* **205**, 373–390 (2005)
- [76] Xu, J., Pope, S.B.: Source of Bias in Particle-Mesh Methods for PDF Models for Turbulent Flows, Technical Report FDA 97-06. Cornell University (1997)
- [77] Xu, J., Pope, S.B.: Assessment of numerical accuracy of PDF/Monte-Carlo methods for turbulent reacting flows. *J. Comput. Phys.*, 152–192 (1999)
- [78] Yeh, F., Lei, U.: On the motion of small particles in a homogeneous isotropic turbulent flow. *Phys. Fluids*, **3** (11) 2571–86 (1991)

- [79] Zaichik, L.I.: A statistical model of particle transport and heat transfer in turbulent shear flows. *Phys. Fluids*, **11** (6) 1521–1534 (1999)

Chapter 1

A Moments/PDF approach to turbulent two-phase flows simulation

1.1 Introduction

This chapter deals with the modelling and the numerical simulation of polydispersed turbulent two-phase flows, where one phase is a turbulent flow (considered to be a continuum) and the other appears as separate inclusions carried by the turbulent fluid (solid particles, droplets or bubbles). Such flows can be encountered in several industrial situations (combustion, water sprays, smokes) as well as in various environmental problems (pollutant dispersion). In spite of a need for their accurate prediction, the physical complexity of these processes is so broad that existing methods are either too expensive, for example, DNS/DPS, or do not provide all the necessary information: the first two statistical moments computed by RANS equations are not always sufficient for engineering problems. An alternative solution consists in resorting to a coupling of classic descriptions, where a different description is used for each phase. Such a coupling method, proposed in [23] and developed in [30] and referred to as the Moments/PDF approach, enables to reach an acceptable compromise between the level of accessible information and a tractable numerical treatment. **The main concern of the present chapter consists in numerical implementation of this approach following [30], which will serve a basis for the derivation of a new coupling method in chapter 4.**

For two-phase flows, the Moments/PDF approach consists in coupling the Eulerian description for the fluid phase, which will be referred to as PDE_g (from Partial Differential Equations for the gas phase) with the Lagrangian stochastic (or PDF) description for the particle phase (SDE_p , Stochastic Differential Equations for particles). The fluid and the particle models are consistent in the particle-tracer limit, that is when particle inertia tends to zero and when discrete particles

behave as fluid particles¹. The fluid phase is modeled by the Reynolds Averaged Navier-Stokes (RANS) equations, which are solved numerically with an arbitrary Finite Volume method that provides the fluid statistics to the particle stochastic model. Attention is focused on the *one-point PDF description of the dispersed phase*. PDF modeling of particles embedded in a turbulent flow allows to take into account the polydispersity in some particle properties and to obtain a high-level description of the fields without introducing complicated macroscopic closures. In practice, it is accomplished by following in time the trajectories of a large number of statistical samples. As a result, all N -order one-point particle statistics are accessible. However, our concern is not only to show the advantages of this approach in some situations, but also to demonstrate its limitations (related, for example, to computational costs and to occurrence of bias error), and eventually suggest possible ways to overcome it. In this work, we will limit ourselves to *incompressible* turbulent flows laden with *heavy particles* ($\rho_p \gg \rho_g$, with ρ_g, ρ_p - the fluid and the particle densities respectively), and *dilute* enough, so that particle-particle interactions and two-way coupling effects (the influence of the particle phase on the fluid phase) can be neglected without loss of generality.

The present chapter is organized as follows. In section 2, we present the mathematical background of the PDF methods and underline the relation between the PDF and the Lagrangian stochastic descriptions. The basic concepts of the PDF approach to the simulation of turbulent flows are summarized. Section 3 describes the complete Moments/PDF approach and the numerical treatment of such a class of coupled descriptions focusing on the simulation of the dispersed phase with dynamic Monte-Carlo method. **These two sections represent an overview of what has been proposed in [23, 30].** Some numerical results are given in section 4, which aims at the "verification" of the present numerical implementation. A realistic example of a two-phase co-current wall jet simulation is presented in order to provide a comparison of results with those provided by *Code_Saturne*² in a non-homogeneous configuration. Finally, section 5 introduces an alternative approach to simulation of turbulent two-phase flows, which is derived from the Moments/PDF approach using a new coupling strategy. This method, referred to as a hybrid Moments/Moments-PDF approach, will present the main subject of the present work.

1.2 Stochastic modeling of turbulent two-phase flows

The basic equations describing turbulent flows - the Navier-Stokes equations - are deterministic but involve a very large number of degrees of freedom as well as a wide range of scales. Moreover, at large enough scales we are hardly interested in the full description of the flow but rather in some contracted description of its fields. For these reasons, in some situations, a statistical point of view is more suitable. However, the classical RANS equations for some, usually small, number of statistical moments appear to be too restricted. The pdf description considered in this work is a mesoscopic representation coming from deterministic Navier-Stokes equations (as the finest description) and based on the field of probability density functions (pdf). Some information is of course lost in the pdf description and the modeling step consists in expressing it using a stochastic description for the remaining degrees of freedom. The turbulent closure is achieved through a mod-

¹Fluid particle is a point moving with the local fluid velocity [31]

²Computational fluid dynamics free software developed at EDF R&D, <http://www.code-saturne.org>.

eled transport equation for the joint pdf of some chosen variables, which constitute the state vector of the process. The main advantage of the PDF approach over the moment-closure methods is its ability to reproduce convection and local non-linear source terms without introducing macroscopic closures. Moreover, the information available is the complete pdf (though modeled) and, thus, all the statistical moments which are calculated from it.

Before introducing stochastic models used to describe the turbulent flows in fluid dynamics, we recall below some basic notions and definitions coming from the probability theory and stochastic formalism [28].

1.2.1 General formalism of stochastic methods

1.2.1.1 Stochastic processes and Langevin equation

Definition 2.1. If Ω is a given set, then a σ -algebra \mathcal{A} on Ω is a family of subsets of Ω with the following properties: (i) $\emptyset \in \mathcal{A}$; (ii) $A \in \mathcal{A} \Rightarrow A^C \in \mathcal{A}$, where $A^C = \Omega \setminus A$; (iii) $A_1, A_2, \dots \in \mathcal{A} \Rightarrow A := \bigcup_{i=1}^{\infty} A_i \in \mathcal{A}$. The pair (Ω, \mathcal{A}) is called a *measurable space*.

Definition 2.2. A probability measure P on a measurable space (Ω, \mathcal{A}) is a function $P : \mathcal{A} \rightarrow [0, 1]$ such that (i) $P(\emptyset) = 0$, $P(\Omega) = 1$; (ii) if $A_1, A_2, \dots \in \mathcal{A}$ and $\{A_i\}_{i=1}^{\infty}$ is disjoint ($A_i \cap A_j = \emptyset$ if $i \neq j$) then $P(\bigcup_{i=1}^{\infty} A_i) = \sum_{i=1}^{\infty} P(A_i)$. The triple (Ω, \mathcal{A}, P) is called a *probability space*.

Definition 2.3. A *random variable* X is an \mathcal{A} -measurable function $X : \Omega \rightarrow \mathbb{R}^d$, where the probability measure on \mathbb{R}^d is the *distribution* of X .

Definition 2.4. A *stochastic process* is a parameterized collection of random variables $X = (X_t)_{t \in \mathbb{T}}$ from a probability space (Ω, \mathcal{A}, P) into $(\mathbb{R}^d, \mathcal{B})$, where \mathcal{B} is a *Borel* σ -algebra on \mathbb{R}^d . The (*finite-dimensional*) *distributions* of the process X are measures defined on $\mathbb{R}^{d \times k}$ by

$$\bar{P}_{t_1 \dots t_k}(B_1 \times \dots \times B_k) := P(X_{t_1} \in B_1, \dots, X_{t_k} \in B_k), \quad (1.2.1)$$

for all $B_1, \dots, B_k \in \mathcal{B}$ and for all $t_1, \dots, t_k \in \mathbb{T}$, $\forall k \in \mathbb{N}$.

The family of all finite-dimensional distributions determines the most important properties of the process X . The parameter space \mathbb{T} is an interval $[0, t_{max}]$. For each fixed $t \in \mathbb{T}$, we have a random variable $\omega \rightarrow X_t(\omega)$ defined on (Ω, \mathcal{A}, P) . For each fixed $\omega \in \Omega$, the function $t \rightarrow X_t(\omega)$ is a real-valued function defined on \mathbb{T} . Such a time-dependent function for given ω is called a *trajectory* or *sample path* of the process X .

The probability that the stochastic process X takes a value in the interval $[x, x + \Delta x]$ at time t is given by the *probability density function* (pdf) $p(t, x)$:

$$P_t(x \leq X_t \leq x + \Delta x) = \int p(t, x) dx. \quad (1.2.2)$$

Based on these notions, below we present two main classes of “tractable” stochastic processes we are dealing with: the Markov processes and the Gaussian processes.

Markov processes. The manipulation of general stochastic processes is difficult since it requires to handle the family of n -point joint distributions

$$p(t_1, x_1; t_2, x_2; \dots; t_n, x_n), \forall n \in \mathbb{N}. \quad (1.2.3)$$

An important simplification can be obtained for the class of Markov processes. A stochastic process satisfies the *Markov property* if the future state of the system at any time $t' > t$ is "independent" of the past behavior of the system at times $t'' < t$, given the present state at time t . In other words, the further evolution of the process depends on its history only through the current state of the process. It can be shown that the Markov processes are completely determined by their initial distribution $p(t_0, x_0)$ and their *transitional pdf* $p(t, x|t_0, x_0)$. This transitional pdf represents the probability that X takes a value x at time t conditioned on the fact that at time t_0 its value was x_0 . For Markov processes, the Chapman-Kolmogorov formula is verified

$$p(t, x|t_0, x_0) = \int p(t, x|t_1, x_1)p(t_1, x_1|t_0, x_0)dx_1. \quad (1.2.4)$$

This equation states that the probability to go from (t_0, x_0) to (t, x) is the sum over all intermediate locations x_1 at an intermediate time t_1 . The factorization inside the integral reflects the "independence" of the past and the future at t_1 when the present is known. Thus, if the family of transition probabilities $p(t, x|t', x')$ for $t, t' \in \mathbb{T}$ with $t' < t$ is given, for $t_1, \dots, t_n \in \mathbb{T}$, $0 = t_0 < t_1 < \dots < t_n$ and for a given probability density $p(t_0, x_0)$, we can deduce a family of continuous finite-dimensional measures:

$$p(t_1, x_1; t_2, x_2; \dots; t_n, x_n) = p(t_n, x_n|t_{n-1}, x_{n-1}) \dots p(t_2, x_2|t_1, x_1)p(t_1, x_1|t_0, x_0)p(t_0, x_0). \quad (1.2.5)$$

Gaussian processes. Gaussian stochastic processes arise naturally in many applications and can be easily handled. All finite-dimensional Gaussian distributions are characterized by their first and second moments

$$\begin{aligned} M(t) &= \langle X_t \rangle, \\ C(t, t') &= \langle X_t X_{t'} \rangle - \langle X_t \rangle \langle X_{t'} \rangle, \end{aligned} \quad (1.2.6)$$

or by the probability density function

$$p(t, x; M(t), C(t, t)) = \frac{1}{\sqrt{2\pi C(t, t)}} e^{-\frac{(x-M(t))^2}{2C(t, t)}}. \quad (1.2.7)$$

For an arbitrary function $M(t) : \mathbb{T} \rightarrow \mathbb{R}$, if the covariance matrices $C(t, t')$ of all finite-dimensional marginal distributions are symmetric and positive-semidefinite, it can be shown that there exists a Gaussian process X for which (1.2.6) holds. Using this statement, Gaussian processes can be constructed in a simple manner [29].

An example of a stochastic process that belongs to both classes of Gaussian and Markov processes is the *Wiener process* $W = (W_t)_{t \in \mathbb{T}}$ [29, 28]. More precisely, it is a *Markov process with independent Gaussian increments*, which is of great importance for the stochastic modeling and is characterized by a number of related properties:

- if for all $T > 0$ there exists positive constants α, β, D such that $\langle |W_t - W_{t'}|^\alpha \rangle \leq D \cdot |t - t'|^\beta$ for $0 \leq t, t' \leq T$, there exists a version of W with continuous trajectories (*Kolmogorov's continuity theorem*),

- the trajectories of the Wiener process are of unbounded variation in every finite interval, thus are nowhere differentiable,
- $\langle W_t \rangle = 0$, $\langle W_t W_{t'} \rangle = \min(t, t')$, $\forall t, t' \in \mathbb{T}$,
- each increment dW_t , $t \in \mathbb{T}$ is a Gaussian random variable. Increments over small time steps are stationary and independent, $\langle W_t - W_{t'} \rangle = 0$, $\langle (W_t - W_{t'})^2 \rangle = |t - t'|$, and $\langle dW_t dW_{t'} \rangle = 0$ with $t' \neq t$, $t' \in \mathbb{T}$,
- the Wiener process is an example of a non-stationary Markov process that is homogeneous with respect to time (the transition probability $P(W_t \in B | W_{t'} = w')$ for $t' < t$ depends only on the difference $t - t'$ rather than on t and t' separately).

The fact that the mean-square increment increases linearly with time suggests that the Wiener process is closely related to the diffusive motion. For this reason, the version of the Wiener process with continuous trajectories is referred to as a *diffusion process*, to which we limit ourselves from now on. A more general real-valued diffusion stochastic process X is said to possess the stochastic differential

$$dX_t := A_t dt + B_t dW_t, \quad (1.2.8)$$

where the processes $(A_t)_{t \in \mathbb{T}}$ and $(B_t)_{t \in \mathbb{T}}$ are non-anticipating (their history up to some time t is independent of the future evolution of the Wiener process W after the time t) and such that the following equations hold for almost all $\omega \in \Omega$:

$$\int_{\mathbb{T}} |A_t(\omega)| dt < \infty, \quad (1.2.9)$$

$$\int_{\mathbb{T}} B_t(\omega)^2 dt < \infty, \quad (1.2.10)$$

$$X_t(\omega) = X_0(\omega) + \int_0^t A_{t'}(\omega) dt' + \left(\int_0^t B_{t'} dW_{t'} \right)(\omega), \quad \forall t \in \mathbb{T}. \quad (1.2.11)$$

In Eq. (1.2.11), the stochastic B-integral, written in the Itô sense [28], is the random variable obtained by stochastic integration, evaluated at $\omega \in \Omega$, where the integration is performed with a measure $dW(t)$. A process X satisfying (1.2.11) is also referred to as an *Itô process*. Moreover, for Itô process X and for any twice continuously differentiable function $g(t, X_t)$ on \mathbb{R} , the *Itô's formula* states:

$$dg(t, X_t) = \frac{\partial g}{\partial t}(t, X_t) dt + A(t, X_t) \frac{\partial g}{\partial x}(t, X_t) dt + B(t, X_t) \frac{\partial g}{\partial x}(t, X_t) dW_t + \frac{1}{2} B^2(t, X_t) \frac{\partial^2 g}{\partial x^2}(t, X_t) dt. \quad (1.2.12)$$

This formula is the fundamental differentiation rule of the stochastic calculus and will be used in the following sections for the derivation of the stochastic differential equations.

Existence and uniqueness of solutions to stochastic differential equations (SDEs)

Let us consider a stochastic differential equation often referred to as *Langevin equation*:

$$dX_t = A(t, X_t) dt + B(t, X_t) dW_t, \quad (1.2.13)$$

where $A(t, X_t)$ and $B(t, X_t)$ is the drift and the diffusion terms respectively. The process X , solution to (1.2.13), and the Wiener process W are defined on the same probability space (Ω, \mathcal{A}, P) . Such a solution is referred as a *strong solution*. A strong solution is called *unique* if, and only if, for any two solutions almost all trajectories are identical with a possible exception of a null set. If X is a non-anticipating process, it is sufficient to assume that $A(t, x)$ and $B(t, x)$ are measurable real-valued functions on $\mathbb{T} \times \mathbb{R}$ in order to guarantee that $A(t, X_t)$ and $B(t, X_t)$ are non-anticipating processes [29]. Then, the conditions for the existence and uniqueness of the solution to (1.2.13) are given by the following theorem [29]:

Theorem 2.1 Suppose that the measurable functions $A(t, x)$ and $B(t, x)$ $\forall t \in \mathbb{T}$ and $\forall x, y \in \mathbb{R}$ satisfy the Lipschitz conditions

$$\begin{aligned}|A(t, x) - A(t, y)| &\leq c|x - y|, \\ |B(t, x) - B(t, y)| &\leq c|x - y|,\end{aligned}\tag{1.2.14}$$

and the linear growth conditions

$$\begin{aligned}|A(t, x)| &\leq c(1 + |x|), \\ |B(t, x)| &\leq c(1 + |x|),\end{aligned}\tag{1.2.15}$$

for some constant $c \in \mathbb{R}$. If the real-valued random variable X_0 is independent of the Wiener process W , there exists a unique solution of the stochastic differential equation (1.2.13) with initial condition $X(t = t_0) = X_0$ on the entire time interval \mathbb{T} .

The proof is classical and can be found in [12] for instance. If $A(t, x)$ and $B(t, x)$ are general continuous functions of t and x , the existence of a solution can still be established, however, the solution is in general not unique. Theorem 2.1 is easily generalized to the multi-dimensional case.

1.2.1.2 Relationship between stochastic differential equations and Fokker-Planck equation

The relationship between stochastic differential equations for stochastic diffusion processes and pdf equations for their transition probability densities is extremely important and facilitates the numerical treatment of the pdf equations. Let $X = (X_t)_{t \in \mathbb{T}}$ be a diffusion process, solution of the SDEs (1.2.13) with the initial condition $X_{t_0} = x_0$. If the initial state (t_0, x_0) is fixed and if the coefficients $A(t, x)$ and $B(t, x)$ in (1.2.13) are continuous functions on $\mathbb{T} \times \mathbb{R}^d$, the evolution of the transitional probability density function $p(t, x|t_0, x_0)$, as well as of the joint probability density function $p(t, x)$, which characterizes the continuous distribution of X_t , is governed by a partial differential equation which is known as the Fokker-Planck equation associated with the solution of the stochastic differential equation (1.2.13) [13]:

$$\frac{\partial p}{\partial t} = -\frac{\partial}{\partial x} [A(t, x)p] + \frac{1}{2} \frac{\partial^2}{\partial x^2} [D(t, x)p],\tag{1.2.16}$$

where $D = B \cdot B^T$, though such a decomposition in a multidimensional space ($d > 1$) is not unique. However, even if a decomposition $D = B \cdot B^T$ is specified, the correspondence between Fokker-Planck equation and stochastic differential equations (SDEs) is not one-to-one. The Fokker-Planck equation (written for *transitional* or *joint* pdf) specifies the distribution of the stochastic process

and contains a large number of degrees of freedom, whereas a stochastic differential equation determines the actual trajectories of a fixed number of particles (samples of the complete pdf) from which a “reduced” pdf is reconstructed (however, the complete pdf given by the Fokker-Planck equation remains inaccessible). In fact, given a Fokker-Planck equation for the transition probabilities one has the freedom of choosing a probability space, a Wiener process, and a random variable with an initial distribution before the trajectories of the process can be determined by solving the stochastic differential equations (1.2.13) in the strong sense. Thus, a Fokker-Planck equation dealing only with the distribution of the process provides what is defined as a *weak solution* to stochastic differential equations. Although, in most engineering problems, one is mainly interested by different statistics and thus, by the distribution of the solution, much more advantages are gained in numerical treatment by reformulating Fokker-Planck equations in terms of stochastic differential equations.

1.2.1.3 Moments equations

Given a stochastic diffusion process $X = (X_t)_{t \in \mathbb{T}}$ with the probability density $p(t, x)$ and given any function $\mathcal{H}(t, x)$, we assume the following averaging operator:

$$\langle \mathcal{H} \rangle(t) = \langle \mathcal{H}(t, x) \rangle = \int \mathcal{H}(t, x) p(t, x) dx. \quad (1.2.17)$$

By multiplying equation (1.2.16) by $\mathcal{H}(t, x)$ and applying the previously defined operator, after integration by parts with the assumptions

$$\mathcal{H} A p, \mathcal{H} \frac{\partial p}{\partial x}, \frac{\partial \mathcal{H}}{\partial x} p \rightarrow 0, \text{ when } x \rightarrow \pm\infty, \quad (1.2.18)$$

we obtain the following moment equation:

$$\frac{\partial \langle \mathcal{H} \rangle}{\partial t} = - \left\langle A(t, x) \frac{\partial \mathcal{H}}{\partial x} \right\rangle + \frac{1}{2} \left\langle D(t, x) \frac{\partial^2 \mathcal{H}}{\partial x^2} \right\rangle. \quad (1.2.19)$$

It is important to note here that the same moment equation can be derived directly from the Lagrangian stochastic equations (1.2.13) by following the formalism of the stochastic calculus. An example of a practical derivation will be given in the following sections on example of equations coming from fluid dynamics.

1.2.1.4 Mean field interactions

When the Fokker-Planck equation is nonlinear with respect to the probability density p , because its coefficients depend on averages evaluated with p , the processes solutions of such nonlinear equations are referred to as nonlinear diffusions or processes with mean field interactions. These processes rise many difficult theoretical questions that at present are not studied enough [29]. To detail some of issues, let us rewrite system (1.2.13) in the following generalized form:

$$dX(t) = A(t, X(t), \langle f_A(X_t) \rangle) dt + B(t, X(t), \langle f_B(X_t) \rangle) dW(t), \quad (1.2.20)$$

where the drift vector $A(t, X(t), \langle f_A(X_t) \rangle)$ and the diffusion matrix $B(t, X(t), \langle f_B(X_t) \rangle)$ depend on expectations of one or several real-valued functions. Provided that the functions A, B, f_A and f_B satisfy Lipschitz conditions (1.2.14) and suitable growth conditions (1.2.15), the existence of a unique solution to this stochastic differential equation can be established.

From the discrete point of view, it is a *law of large numbers* that ensures the convergence of ensemble averages to the mathematical expectations. Precisely, for the system of n SDEs

$$dX_t^{(j)} = A \left(t, X_t^{(j)}, \frac{1}{n} \sum_{k=1}^n f_A \left(X_t^{(j)}, X_t^{(k)} \right) \right) dt + B \left(t, X_t^{(j)}, \frac{1}{n} \sum_{k=1}^n f_A \left(X_t^{(j)}, X_t^{(k)} \right) \right) dW_t^{(j)}, \quad (1.2.21)$$

with $j = 1, 2, \dots, n$, where the processes $W^{(j)}$ are independent Wiener processes and where the expectations are replaced by ensemble averages, the law of large numbers states the following: if X_t is the solution of the SDEs with mean-field interactions, if the initial conditions $X_0^{(j)}$ are independent, identically distributed random variables, if moreover, the coefficient functions satisfy Lipschitz and suitable growth conditions, then we have a mean-square convergence:

$$ms - \lim_{n \rightarrow \infty} \frac{1}{n} \sum_{j=1}^n f \left(X_t^{(j)} \right) = \langle f(X_t) \rangle, \quad (1.2.22)$$

for all bounded functions $f : \mathbb{R}^d \rightarrow \mathbb{R}$. The fluctuations for finite n are expected to be of the order of $n^{-1/2}$. It has been also shown in [22] that under suitable smoothness conditions an almost sure convergence can be obtained, so that a strong law of large numbers is verified. The processes $X^{(j)}$ are often referred to as *weakly interacting stochastic processes*: the weakness of the interaction is coming from the factor $1/n$ in front of the interaction terms in (1.2.21). For large n , any finite number of processes becomes essentially independent [29].

1.2.2 Probabilistic description of continuous fields

1.2.2.1 Eulerian and Lagrangian probability density functions

The PDF approach in fluid dynamics involves the notions of both particles and fields. The particles are in fact statistical samples of the fields and they are used to introduce a probabilistic description. Thus, the system can be described either from a Lagrangian or from an Eulerian probabilistic point of view. Yet, the resulting macroscopic quantities will always be fields (the local moments). Only, when a Lagrangian description is used, the particle state vector includes the particle position, and the simulation consists in following the particle trajectory in time, whereas from an Eulerian point of view, the particle position is a parameter and we look at the particle properties at a fixed node.

Further explanations are related to the choice of the particle state vector. We assume the particle density and the particle volume to be constant, and consider a one-particle state vector which includes the particle location and the particle velocity $\mathbf{Z} = (x, U)$, which in sample space is written as $\mathbf{Z} = (y, V)$. 'One-particle' means that we look at a reduced system which includes one particle. The probability to find a particle in the state $[y, y + dy]$, $[V, V + dV]$ is given by $p^L(t; y, V) dy dV$ in a Lagrangian formulation. The *exact* pdf equation satisfied by $p^L(t; y, V)$ can be derived by writing the Navier-Stokes equations in a Lagrangian formulation.

If the *Eulerian pdf* description is used, the space coordinates are not variables but parameters, because this point of view consists in monitoring the fields values at a fixed point of time and space. Therefore, we define the Eulerian pdf $p^E(t, x; V)$ with $p^E(t, x; V)dV$ the probability to observe in the flow field a state in the range $[V, V + dV]$ at time t and position x . By doing so, we have defined a field of distribution function since for each point (t, x) a distribution function of the velocity has been associated.

In the *incompressible* case, the relation between the Eulerian and the Lagrangian pdfs is given by:

$$p^E(t, x; V) = p^L(t; y = x, V) = \int p^L(t; y, V) \delta(x - y) dy. \quad (1.2.23)$$

Thus, the Eulerian pdf is the Lagrangian one conditioned on the local position:

$$p^L(t; V|x) = \frac{p^L(t; x, V)}{p^L(t; x)} = p^E(t, x; V), \quad (1.2.24)$$

where

$$p^L(t; x) = \int p^L(t; x, \tilde{V}) d\tilde{V}. \quad (1.2.25)$$

Using the definition of the Lagrangian pdf via the transitional pdf, which translates the probability to find a particle in the state $[x, x + dx]$, $[V, V + dV]$ at time t conditioned on the fact that at time t_0 it was in the state $[x_0, x_0 + dx_0]$, $[V_0, V_0 + dV_0]$:

$$p^L(t; x, V) = \int p^L(t; x, V|t_0; x_0, V_0) p^L(t_0; x_0, V_0) dx_0 dV_0, \quad (1.2.26)$$

we can find the following important relation:

$$p^E(t, x; V) = \int p^L(t; x, V|t_0; x_0, V_0) p^E(t_0, x_0; V_0) dx_0 dV_0, \quad (1.2.27)$$

which shows that the Eulerian probability density function is propagated by the transitional Lagrangian pdf.

Henceforth, as a key notion we will consider the *one-particle Lagrangian transitional pdf*, $p^L(t; x, V|t_0; x_0, V_0)$, which is the solution of the PDF transport equation. The approximate solution of the PDF equation using classical numerical techniques, such as finite-volume methods, is difficult in practice, since the computational cost increases exponentially with the number of dimensions. On the other hand, in the previous sections it has been shown that the PDF equations are equivalent, in a weak sense, to a set of stochastic differential equations (SDEs). In this case, the pdf is represented by an ensemble of Lagrangian stochastic particles whose properties are driven by the modeled stochastic differential equations. The stochastic particles can be regarded as samples of the pdf and following these particles in time represents a dynamical Monte-Carlo method, whose computational cost increases only linearly with the number of particles. Therefore, the remainder of this section is devoted to the notions related to stochastic differential equations and to the relations between different statistical descriptions.

1.2.2.2 Discrete representation and weak approximation of the pdf

In practical simulations, a finite number of particles is followed in time. Each particle has its values of $x(t)$ and $U(t)$. The discrete approximation of the Lagrangian probability density function with

N particles is therefore given by

$$p_N^L(t; y, V) = \sum_{i=1}^N \delta(y - x^i(t)) \otimes \delta(V - U^i(t)). \quad (1.2.28)$$

The approximation of a mean Eulerian quantity at a given point in space x and at time t , $\tilde{\mathcal{H}}(t, x)$:

$$\tilde{\mathcal{H}}(t, x) = \langle \mathcal{H}(U(t, x)) \rangle = \int \mathcal{H}(V) p^E(t, x; V) dV \quad (1.2.29)$$

can be obtained from the above discrete expression p_N^L . Using equation (1.2.23), where the delta function in space is replaced by $\delta(y - x) \simeq 1/\delta\mathcal{V}_x$ when $y \in \delta\mathcal{V}_x$, $\delta\mathcal{V}_x$ being a small volume around each point x , we obtain

$$\tilde{\mathcal{H}}(t, x) \simeq \frac{1}{\delta\mathcal{V}_x} \sum_{i=1}^{N_x} \mathcal{H}(U^i(t)). \quad (1.2.30)$$

Then, it can be seen that the discrete approximation, through the ensemble average over N_x particles present in the small volume $\delta\mathcal{V}_x$ around x , approximates the mean quantity $\tilde{\mathcal{H}}$:

$$\tilde{\mathcal{H}} \simeq \mathcal{H}_N = \frac{\sum_{i=1}^{N_x} \mathcal{H}(U^i(t))}{N_x}. \quad (1.2.31)$$

This procedure is valid in the general non-stationary and non-homogeneous case, but is actually based on a *local homogeneity hypothesis*. A small volume $\delta\mathcal{V}_x$ is introduced around point x , and the N_x particles located in this small volume are regarded as independent realizations and samples of the probability density function at point x . This amounts to assuming spatial homogeneity within the small volume $\delta\mathcal{V}_x$.

The *law of large numbers* states that $\langle \mathcal{H}_N \rangle$ is an unbiased estimation of $\langle \mathcal{H} \rangle$. The rate of convergence of the discrete approximation is given by the *Central Limit Theorem* which shows that there exists a constant C such that:

$$\langle \mathcal{H}_N \rangle = \tilde{\mathcal{H}} \quad \text{and} \quad \langle (\tilde{\mathcal{H}} - \mathcal{H}_N)^2 \rangle \leq \frac{C}{N}. \quad (1.2.32)$$

It is a convergence in the sense of distributions, or weak convergence, since it is the mean value which converges as $N \rightarrow +\infty$:

$$\langle \mathcal{H}_N \rangle \xrightarrow{N \rightarrow \infty} \langle \mathcal{H} \rangle. \quad (1.2.33)$$

This notion of weak convergence and of weak approximation is fully consistent with the overall aim of the pdf methods, where the interest is to obtain information on various statistics of the flow. In practice, the challenge of Monte-Carlo methods is to reach a satisfactory compromise between spatial errors (governed by the size of $\delta\mathcal{V}_x$), time discretization errors (time step is used to integrate the trajectories of the process) and statistical errors (governed by $N^{1/2}$) for a tractable total number of particles.

1.2.3 Stochastic modelling of particle dispersion

Once the theoretical framework of the PDF modeling is recalled, let us introduce a stochastic model for the dispersion of discrete inertial particles engaged in a turbulent fluid flow. The turbulent

fluid phase is described by the density ρ_g , the dynamic viscosity ν_g , the mean velocity $\langle \mathbf{U}_g \rangle(t, \mathbf{x})$, the mean pressure $\langle P_g \rangle(t, \mathbf{x})$, the Reynolds stress tensor $\mathbf{R}_g = \langle \mathbf{u}_g \mathbf{u}_g \rangle(t, \mathbf{x})$ or the turbulent kinetic energy $k = \frac{1}{2} \text{tr}(\mathbf{R}_g)$, and the mean dissipation rate of the turbulent energy $\langle \varepsilon \rangle(t, \mathbf{x})$. Thus, these fields are provided by the model of the turbulent fluid phase. The subscript “ g ” is used because the fluid phase is supposed to be a gas.

1.2.3.1 Particle equation of motion

A physical inertial particle we are dealing with is characterized by its diameter d_p , density ρ_p , constant volume \mathcal{V}_p , position in space $\mathbf{x}_p(t)$ and velocity $\mathbf{U}_p(t)$. When the diameter of particles varies in space and/or time, we speak of the polydispersity in the particle size. The exact equations of the particle motion, derived for instance by Gatignol in [14] for small particle-related Reynolds numbers,

$$Re_p = \frac{d_p |\mathbf{U}_r|}{\nu_g} \ll 1,$$

take into account the pressure-gradient, buoyancy, drag, added-mass and Basset forces. The first two are fluid-related forces that would exist if the particle was not present. The drag, added-mass and Basset forces arise from the presence of the relative velocity $\mathbf{U}_r = \mathbf{U}_s - \mathbf{U}_p$. Yet, for heavy particles where $\rho_p \gg \rho_g$, the drag and the gravity forces are the dominant forces and the *particle equation of motion* is reduced to

$$\begin{aligned} \frac{dx_{p,i}}{dt} &= U_{p,i}, \\ \frac{dU_{p,i}}{dt} &= \frac{1}{\tau_p} (U_{s,i} - U_{p,i}) + g_i, \quad i \in \mathbb{Z} \end{aligned} \tag{1.2.34}$$

where $\mathbf{U}_s = \mathbf{U}_s(\mathbf{x}_p(t), t)$ is the fluid velocity seen, i.e. the fluid velocity (undisturbed by the presence of a particle) sampled along the particle trajectory $\mathbf{x}_p(t)$. The particle relaxation time scale, τ_p , represents the time necessary for a particle to adjust to the fluid velocity and is defined as:

$$\tau_p = \frac{\rho_p}{\rho_g} \frac{4d_p}{3C_D |\mathbf{U}_r|}. \tag{1.2.35}$$

Here, the drag coefficient C_D is a non-linear function of the particle Reynolds number, Re_p . One of the most often used empirical expressions for C_D is [4]:

$$C_D = \begin{cases} \frac{24}{Re_p} [1 + 0.15 Re_p^{0.687}] & \text{if } Re_p \leq 1000, \\ 0.44 & \text{if } Re_p \geq 1000. \end{cases} \tag{1.2.36}$$

When $Re_p \ll 1$, one can use a simpler expression obtained from (1.2.35):

$$\tau_p = \frac{\rho_p}{\rho_g} \frac{d_p^2}{18\nu_g}. \tag{1.2.37}$$

The choice of the particle time scale is very important, because it defines the character of the flow and thus the hypotheses which can be valid for the particle motion. For instance, we suppose here $\rho_p \gg \rho_g$, then τ_p is very large with respect to the viscous time scale, $\tau_p \gg d_p^2/\nu_g$, see (1.2.37).

Consequently, the assumption that the unsteady added-mass and Basset forces can be neglected is confirmed. In the following, we limit ourselves to such a defined case of *heavy particles*. Moreover, we study the flows *dilute enough* not to consider particle interactions and collisions; otherwise, the drag coefficient would have to be modified in order to take into account the underlying phenomena.

1.2.3.2 A Langevin model for inertial particles

Since the transitional Lagrangian pdf appears to be the key notion and since both the Lagrangian and the Eulerian probability density functions (and thus the equations for statistical moments) can be expressed from it using (1.2.27) or (1.2.26), we turn henceforth to the *Lagrangian stochastic description* using the *trajectory point of view*. The next step consists in the choice of the appropriate model for the *exact one-point transitional pdf* p^L , which actually amounts to replacing the *exact instantaneous* particle trajectories by the *modeled* ones. The model which will be used in the present work has been derived in [26] and we only recall here some important modeling assumptions.

First, it is important to note that the choice of the state vector for an inertial particle in two-phase flow is less obvious than in the case of single-phase flows. The first works in this direction have adopted the description common to kinetic theory of gases by including the particle position and the particle velocity to the state vector [6, 40, 41]. Later, this approach has been extended to account for the turbulence effects on particle motion via fluid-particle correlations by adding the fluid velocity seen at the particle position, \mathbf{U}_s , in the particle state vector [26, 39, 42, 44]. This choice is related to a specific form of the covariance matrix $\langle dU_{s,i}(t)dU_{s,j}(t+dt) \rangle$, $\forall i, j \in \mathbb{Z}$, which is characterizing the diffusion processes (see sec. 1.2.1.1) [23]. Thus, the dynamic motion of a discrete particle is described by the particle position, by the particle velocity and by the fluid velocity seen at particle position: $\mathbf{Z}(t) = (\mathbf{x}_p(t), \mathbf{U}_p(t), \mathbf{U}_s(t))$.

Before writing the stochastic model for increments $d\mathbf{Z}(t)$, it is important to note that the *particle dispersion* phenomenon is more complicated than the phenomenon of the fluid-particle diffusion in single-phase turbulent flows, since we have to account in addition for *particle inertia* (the drag force) and for *external forces* (here, the gravity). Moreover, since we consider the flows *dilute enough* in particles not to describe the turbulence modulation, $\mathbf{U}_s(t)$ is not disturbed by the presence of particles and does not depend explicitly on $\mathbf{U}_p(t)$. One possible *Langevin model* of the particle dispersion was proposed in [23]:

$$\begin{aligned} dx_{p,i} &= U_{p,i} dt, \\ dU_{p,i} &= \frac{1}{\tau_p} (U_{s,i} - U_{p,i}) dt + g_i dt, \\ dU_{s,i} &= -\frac{1}{\rho_g} \frac{\partial \langle P_g \rangle}{\partial x_i} dt + (\langle U_{p,j} \rangle - \langle U_{g,j} \rangle) \frac{\partial \langle U_{g,i} \rangle}{\partial x_j} dt - \frac{(U_{s,i} - \langle U_{g,i} \rangle)}{T_{L,i}^*} dt \\ &\quad + \sqrt{\langle \varepsilon \rangle \left(C_0 b_i \tilde{k}/k + \frac{2}{3} (b_i \tilde{k}/k - 1) \right)} dW_i. \end{aligned} \tag{1.2.38}$$

Here, the *drift term*

$$C_i(\mathbf{x}_p, \mathbf{U}_p, \mathbf{U}_s) = -\frac{1}{\rho_g} \frac{\partial \langle P_g \rangle}{\partial x_i} + (\langle U_{p,j} \rangle - \langle U_{g,j} \rangle) \frac{\partial \langle U_{g,i} \rangle}{\partial x_j} - \frac{(U_{s,i} - \langle U_{g,i} \rangle)}{T_{L,i}^*}, \quad i = 1, \dots, d \quad (1.2.39)$$

reproduces the mean drift and the return-to-equilibrium phenomena, where the mean fluid velocity at particle locations is acting as the local equilibrium value. $B_{ij} = \sqrt{\langle \varepsilon \rangle \left(C_0 b_i \tilde{k}/k + \frac{2}{3} (b_i \tilde{k}/k - 1) \right)} \delta_{ij}$ is diagonal but non-isotropic *diffusion matrix* which ensures the correct decrease of turbulent kinetic energy, $\mathbf{W}(t) = (W_1(t), \dots, W_d(t))$ is a set of independent Wiener processes (with d - the space dimension) and C_0 is the Kolmogorov constant.

The timescales $T_{L,i}^*$, $i = 1, \dots, d$ are functions of the particle inertia and represent the Lagrangian timescales of the velocity of the fluid seen derived from the fluid integral timescale T_L :

$$T_L = \frac{1}{\left(\frac{1}{2} + \frac{3}{4} C_0 \right) \langle \varepsilon \rangle} \quad (1.2.40)$$

according to Csanady's analysis, in order to take into account the particle inertia and the *crossing-trajectory effect* [42], which is due to the presence of external forces. Assuming, for the sake of simplicity, that the mean drift is aligned with the first coordinate axis, the modeled expressions for the time scales are, in the longitudinal direction:

$$T_{L,1}^* = \frac{T_L}{\sqrt{1 + \beta^2 \frac{|\langle \mathbf{U}_r \rangle|^2}{2k/3}}}, \quad (1.2.41)$$

and in the transversal directions:

$$T_{L,2}^* = T_{L,3}^* = \frac{T_L}{\sqrt{1 + 4\beta^2 \frac{|\langle \mathbf{U}_r \rangle|^2}{2k/3}}}. \quad (1.2.42)$$

In these expressions, β is the ratio of the Lagrangian and the Eulerian time scales of the fluid $\beta = T_L/T_E$, assumed to be constant. Thus, the discrete particles with negligible inertia ($\tau_p \rightarrow 0$) tend to follow their surrounding fluid elements and therefore 'see' velocities which are correlated in a time interval T_L . On the contrary, the particles with very high inertia ($\tau_p \gg 1$) are moving very slowly with reference to the fluid elements and will 'see' the fluid velocities at about the same point (thus, essentially correlated) whose integral time scale is T_E . Actually, the influence of the particle inertia on the time scale T_L^* is often left out for the sake of simplicity ($\beta = 1$). However, there is still the instantaneous drift, $(\mathbf{U}_s - \mathbf{U}_p)dt$, and thus the separation of the fluid and the discrete particle trajectories related to the particle inertia.

The presence of external forces that are acting on the particles induces a *mean relative velocity*, $\langle \mathbf{U}_r \rangle$, between the discrete particles and the surrounding fluid, and therefore the separation of the average trajectories of the discrete and of the fluid elements. This results in a decorrelation of the velocity of the fluid seen with respect to the velocity of fluid particles, and is called the *crossing-trajectory effect*. This phenomenon is not to be confused with the existence of the instantaneous drift, $(\mathbf{U}_s - \mathbf{U}_p)dt$, related to the discrete particle inertia. It can be seen from expressions (1.2.41),

(1.2.42) that when there is no mean relative velocity, the crossing-trajectory effect is neglected, and the time scale of the fluid velocity seen is given by T_L .

In the diffusion matrix \mathbf{B} a new kinetic energy is introduced with respect to the *anisotropy* of diffusion vector:

$$b_i = \frac{T_L}{T_{L,i}^*}; \quad \tilde{k} = \frac{3}{2} \frac{\sum_{i=1}^3 b_i \langle u_{g,i}^2 \rangle}{\sum_{i=1}^3 b_i}, \quad (1.2.43)$$

where $\mathbf{u}_g(t, \mathbf{x}) = \mathbf{U}_g(t, \mathbf{x}) - \langle \mathbf{U}_g(t, \mathbf{x}) \rangle$ is the fluctuating fluid velocity. The case of general axis is discussed elsewhere [23].

Finally, the *modeled pdf* equation for pdf $p^L(t; \mathbf{y}_p, \mathbf{V}_p, \mathbf{V}_s)$ corresponding to (1.2.38) is the Fokker-Planck equation:

$$\begin{aligned} \frac{\partial p^L}{\partial t} + V_{p,i} \frac{\partial p^L}{\partial y_{p,i}} &= -\frac{\partial}{\partial V_{p,i}} \left(\frac{V_{s,i} - V_{p,i}}{\tau_p} p^L \right) - \frac{\partial(g_i p^L)}{\partial V_{p,i}} + \frac{1}{\rho_g} \frac{\partial \langle P_g \rangle}{\partial y_i} \frac{\partial p^L}{\partial V_{s,i}} - (\langle U_{p,j} \rangle - \langle U_{g,j} \rangle) \frac{\partial \langle U_{g,i} \rangle}{\partial x_j} \frac{\partial p^L}{\partial V_{s,i}} \\ &+ \frac{\partial}{\partial V_{s,i}} \left(\frac{(V_{s,i} - \langle U_{g,i} \rangle)}{T_{L,i}^*} p^L \right) + \frac{1}{2} \frac{\partial^2}{\partial V_{s,i} \partial V_{s,j}} ([\mathbf{B} \mathbf{B}^\mathbf{T}]_{ij} p^L). \end{aligned} \quad (1.2.44)$$

It is important to note that in this equation, the non-local terms (the pressure gradient and the molecular transport coefficient), which represent the forces exerted on a particle by the fluid, are modeled since the one-point pdf provides no information on space correlations. Moreover, the coefficients in the pdf equation depend not only on the variables of the state vector $\mathbf{Z}(t)$ but also on the expected values of functionals $f(\mathbf{Z})$ (here $\langle \mathbf{U}_p \rangle$), which are computed directly from particles in a cell. This dependence is characterizing the so-called *McKean equations* [22] and brings to the formation of the *Bias error* that has important consequences for the numerical algorithm. Thus, writing this model amounts to replacing the real problem of N interacting particles (1.2.34) by a ‘weak-interaction’ approximation, where the particles do not interact directly but create a mean field and interact with it.

On the other hand, such a pdf description has two main advantages related to the Lagrangian point of view. In fact, following the particles allows to treat the convection without any modeling assumption. As a result, in the mean moment equations, any term coming from the convection term will be in closed form. Thus, the problem of closures for $\langle u_i u_j \rangle$, $\langle u_i u_j u_k \rangle$ etc. disappears in the PDF methods. Moreover, comparing to the “macroscopic” Eulerian approaches, the PDF description allows to compute any *local* non-linear source terms “without approximation”:

$$\langle S(\phi) \rangle \neq F(\langle \phi \rangle, \langle \phi^2 \rangle, \dots) \quad \text{but} \quad \langle S(\phi) \rangle = \int S(\psi) p^E(t, \mathbf{x}; \psi) d\psi. \quad (1.2.45)$$

Some other interesting properties of the present model are detailed in [23], Chapter 7.5.

Finally, the present Langevin model (1.2.38) proposes only one possible form of equation for $\mathbf{dU}_s(t)$. Slightly different approaches can be found in [42, 44] and their comparison with the present model is discussed in [21, 23]. It must be emphasized that the derivation of the model for the velocity of the fluid seen describing the particle dispersion remains a very complicated issue.

1.2.3.3 Multiscale character of the stochastic model

There are three different timescales describing the dynamics of discrete particles: the timescale at which the process is observed, dt , the integral timescale of the fluid velocity seen, $T_{L,i}^*$, and the particle relaxation timescale, τ_p . System (1.2.38) has a physical meaning only in the case where $dt \ll T_{L,i}^*, \tau_p$. However, when this condition is not satisfied, it is possible to show that, in the continuous sense, the system converges towards several limit systems. More details on the fast variable elimination technique and limit cases can be found in [24], [30]. Here, we present only two of the limit systems, when both variables $T_{L,i}^*, \tau_p$ are continuous functions of time.

Case 1. Following [30], when $\tau_p \rightarrow 0$, the discrete particles behave like fluid particles without inertia and the crossing-trajectory effect may be neglected. Then, system (1.2.38) is consistent with the **fluid-particle model** also known as the Simple Langevin Model (SLM) **for the gas phase** [32]:

$$\begin{aligned} dx_{p,i} &= U_{p,i} dt \\ U_{p,i} &= U_{s,i} \\ dU_{s,i} &= -\frac{1}{\rho_g} \frac{\partial \langle P_g \rangle}{\partial x_i} dt - \frac{(U_{s,i} - \langle U_{g,i} \rangle)}{T_L} dt + \sqrt{C_0 \langle \varepsilon \rangle} dW_i \end{aligned} \quad (1.2.46)$$

and may be rewritten as:

$$\begin{aligned} dx_{g,i} &= U_{g,i} dt \\ dU_{g,i} &= -\frac{1}{\rho_g} \frac{\partial \langle P_g \rangle}{\partial x_i} dt - \frac{(U_{g,i} - \langle U_{g,i} \rangle)}{T_L} dt + \sqrt{C_0 \langle \varepsilon \rangle} dW_i. \end{aligned} \quad (1.2.47)$$

This model of the gas phase will be used in the following section for the derivation of the gas phase moments equations.

Case 2. When $T_{L,i}^* \rightarrow 0$ and $B_{ij} T_{L,i}^* \rightarrow cst$, the fluid velocity seen becomes a fast variable (Gaussian white noise) and is eliminated from the system of equations:

$$\begin{aligned} dx_{p,i} &= U_{p,i} dt \\ dU_{p,i} &= \frac{1}{\tau_p} (\langle U_{g,i} \rangle - U_{p,i}) dt + g_i dt + \sum_j \frac{B_{ij} T_{L,i}^*}{\tau_p} dW_j, \end{aligned} \quad (1.2.48)$$

where B_{ij} is the diffusion matrix in (1.2.38).

The multiscale character of model (1.2.38) reflects that it is able to capture interesting physics of particle dispersion in general turbulent flows. Finally, since it is not possible to control dt in the general case, the numerical scheme that will be used must also be consistent with the limit cases.

1.2.3.4 Gas phase moments equations

As it was emphasized in the previous section, there exists a strong connection between the class of the Lagrangian stochastic models considered here and the moments equations. This relation can be demonstrated on the example of the **fluid-particle stochastic model for the gas phase**

(1.2.47). In order to show how the the equations for statistical moments - which in this case will be Reynolds-Averaged Navier-Stokes equations - are deduced from the pdf formulation, we need to introduce an averaging operator. In the case of **incompressible** flows, where we deal with the Eulerian probability density function p^E , for any function $\mathcal{H}(\mathbf{V}_g)$, the averaging operator can be defined as:

$$\langle \mathcal{H} \rangle(t, \mathbf{x}) = \langle \mathcal{H}(\mathbf{U}_g(t, \mathbf{x})) \rangle = \int \mathcal{H}(\mathbf{V}_g) p^E(t, \mathbf{x}; \mathbf{V}_g) d\mathbf{V}_g. \quad (1.2.49)$$

The first-order moment equations are obtained following the standard procedure when the pdf equation for $p^E(t, \mathbf{x}; \mathbf{V}_g)$ is first multiplied by $\mathcal{H}(\mathbf{V}_g)$ and then the averaging operator (1.2.49) is applied (sec. 1.2.1.3). In order to obtain higher-order moment equations using this procedure, a change of coordinates in phase space is necessary, and the reader is referred to [23] for further details. Another way to derive the equations for statistical moments consists in applying the stochastic calculus formalism to the stochastic differential equations. In the trajectory point of view, the condition of mass conservation implies that the gas mean velocity is divergence free [31]:

$$\frac{\partial \langle U_{g,i} \rangle}{\partial x_i} = 0. \quad (1.2.50)$$

We assume moreover that $\partial u_{g,i} / \partial x_i = 0$.

The mean momentum equation is derived from (1.2.47) by applying the averaging operator to the particle velocity equation:

$$\langle dU_{g,i} \rangle = -\frac{1}{\rho_g} \frac{\partial \langle P_g \rangle}{\partial x_i} dt. \quad (1.2.51)$$

Replacing the instantaneous substantial derivative by its Eulerian expression:

$$\begin{aligned} \frac{\langle dU_{g,i} \rangle}{dt} &= \frac{\partial \langle U_{g,i} \rangle}{\partial t} + \left\langle U_{g,j} \frac{\partial U_{g,i}}{\partial x_j} \right\rangle = \frac{\partial \langle U_{g,i} \rangle}{\partial t} + \frac{\partial \langle U_{g,j} U_{g,i} \rangle}{\partial x_j} = \\ &= \frac{\partial \langle U_{g,i} \rangle}{\partial t} + \langle U_{g,j} \rangle \frac{\partial \langle U_{g,i} \rangle}{\partial x_j} + \langle U_{g,i} \rangle \frac{\partial \langle U_{g,j} \rangle}{\partial x_j} + \frac{\partial \langle u_{g,i} u_{g,j} \rangle}{\partial x_j}, \end{aligned} \quad (1.2.52)$$

we obtain the high-Reynolds form of the mean Navier-Stokes equation which governs the mean velocity field:

$$\frac{\partial \langle U_{g,i} \rangle}{\partial t} + \langle U_{g,j} \rangle \frac{\partial \langle U_{g,i} \rangle}{\partial x_j} + \frac{\partial \langle u_{g,i} u_{g,j} \rangle}{\partial x_j} = -\frac{1}{\rho_g} \frac{\partial \langle P_g \rangle}{\partial x_i}, \quad (1.2.53)$$

where $u_{g,i} = U_{g,i} - \langle U_{g,i} \rangle$. These first two mean equations are exact and no closures are needed because all the terms coming from convection in the pdf models are treated without approximation. The model is for the first time introduced in the second order mean equations (through the matrix G corresponding to the pressure rate of strain correlation). Actually, in the stochastic model (1.2.47), the forces which were modeled are the fluctuating pressure gradient and the fluctuating viscous force that appear for the first time in the second-order mean equation. By rewriting $u_{g,i} = U_{g,i} - \langle U_{g,i} \rangle$, we deduce:

$$\frac{du_{g,i}}{dt} = \frac{dU_{g,i}}{dt} - \frac{d\langle U_{g,i} \rangle}{dt} = \frac{dU_{g,i}}{dt} - \frac{\partial \langle U_{g,i} \rangle}{\partial t} - U_{g,j} \frac{\partial \langle U_{g,i} \rangle}{\partial x_j} \quad (1.2.54)$$

or

$$\frac{du_{g,i}}{dt} = \frac{dU_{g,i}}{dt} - \left\{ \frac{\partial \langle U_{g,i} \rangle}{\partial t} + \langle U_{g,j} \rangle \frac{\partial \langle U_{g,i} \rangle}{\partial x_j} \right\} - u_{g,j} \frac{\partial \langle U_{g,i} \rangle}{\partial x_j}. \quad (1.2.55)$$

In incremental form, using (1.2.47) and (1.2.53), it is equivalent to:

$$du_{g,i} = -\frac{1}{\rho_g} \frac{\partial \langle P_g \rangle}{\partial x_i} dt + G_{ij} u_{g,j} dt + \sqrt{C_0 \langle \varepsilon \rangle} dW_i + \frac{\partial \langle u_{g,i} u_{g,j} \rangle}{\partial x_j} dt + \frac{1}{\rho_g} \frac{\partial \langle P_g \rangle}{\partial x_i} - u_{g,j} \frac{\partial \langle U_{g,i} \rangle}{\partial x_j} \quad (1.2.56)$$

or

$$du_{g,i} = \frac{\partial \langle u_{g,i} u_{g,j} \rangle}{\partial x_j} dt - u_{g,j} \frac{\partial \langle U_{g,i} \rangle}{\partial x_j} dt + G_{ij} u_{g,j} dt + \sqrt{C_0 \langle \varepsilon \rangle} dW_i \quad (1.2.57)$$

with the return-to-equilibrium matrix:

$$G_{ij} = -\frac{\delta_{ij}}{T_L} + G_{ij}^a. \quad (1.2.58)$$

From Itô's formula, the derivative of the product $u_{g,i} u_{g,j}$ is given by the following expression [29]:

$$d(u_{g,i} u_{g,j}) = u_{g,i} du_{g,j} + u_{g,j} du_{g,i} + C_0 \langle \varepsilon \rangle dt \delta_{ij}. \quad (1.2.59)$$

Finally, the mean second-order equation can be derived by applying the averaging operator:

$$\begin{aligned} \frac{\partial \langle u_{g,i} u_{g,j} \rangle}{\partial t} &= \left\langle u_{g,i} \frac{\partial \langle u_{g,j} u_{g,k} \rangle}{\partial x_k} \right\rangle + \left\langle u_{g,j} \frac{\partial \langle u_{g,i} u_{g,k} \rangle}{\partial x_k} \right\rangle - \langle u_{g,i} u_{g,k} \rangle \frac{\partial \langle U_{g,j} \rangle}{\partial x_k} - \langle u_{g,j} u_{g,k} \rangle \frac{\partial \langle U_{g,i} \rangle}{\partial x_k} + \\ &\quad G_{jk} \langle u_{g,i} u_{g,k} \rangle + G_{ik} \langle u_{g,j} u_{g,k} \rangle + C_0 \langle \varepsilon \rangle \delta_{ij}. \end{aligned} \quad (1.2.60)$$

Thus, we obtain

$$\begin{aligned} \frac{\partial \langle u_{g,i} u_{g,j} \rangle}{\partial t} + \langle U_{g,k} \rangle \frac{\partial \langle u_{g,i} u_{g,j} \rangle}{\partial x_k} + \frac{\partial \langle u_{g,i} u_{g,j} u_{g,k} \rangle}{\partial x_k} + \langle u_{g,i} u_{g,k} \rangle \frac{\partial \langle U_{g,j} \rangle}{\partial x_k} + \langle u_{g,j} u_{g,k} \rangle \frac{\partial \langle U_{g,i} \rangle}{\partial x_k} = \\ G_{ik} \langle u_{g,j} u_{g,k} \rangle + G_{jk} \langle u_{g,i} u_{g,k} \rangle + C_0 \langle \varepsilon \rangle \delta_{ij}. \end{aligned} \quad (1.2.61)$$

The anisotropy matrix G_{ij}^a depends on mean fields only and can take different forms. When $G_{ij}^a = 0$, the Rotta model (simple return-to-isotropy) is retrieved [31, 36].

Eventually, moments equations (1.2.50), (1.2.53), (1.2.61) may be completed by the equation for the mean frequency rate $\langle \omega \rangle$ or for the mean dissipation rate $\langle \varepsilon \rangle$ derived in a similar way [23].

1.3 Moments/PDF numerical approach to description of turbulent two-phase flows

1.3.1 Main characteristics

The present section will be devoted to a discussion of a Moments/PDF approach to simulation of turbulent two-phase flows, which is based on the coupling of two different descriptions. A detailed presentation can be found elsewhere [30, 45]. Here, we only recall the main features allowing the correct treatment of results presented in the numerical part. The Moments/PDF method we

are dealing with is composed by a system of partial differential equations for statistical moments characterizing the fluid phase and a set of stochastic differential equations for the particle phase, Fig. 1.1. Moments (RANS) equations for the **gas phase** have been derived in sec. 1.2.3.4 from the stochastic model of the fluid-particle motion (1.2.47):

$$\begin{aligned} \frac{\partial \langle U_{g,i} \rangle}{\partial x_i} &= 0 \\ \frac{\partial \langle U_{g,i} \rangle}{\partial t} + \langle U_{g,j} \rangle \frac{\partial \langle U_{g,i} \rangle}{\partial x_j} + \frac{\partial \langle u_{g,i} u_{g,j} \rangle}{\partial x_j} &= -\frac{1}{\rho_g} \frac{\partial \langle P_g \rangle}{\partial x_i} \\ \frac{\partial \langle u_{g,i} u_{g,j} \rangle}{\partial t} + \langle U_{g,k} \rangle \frac{\partial \langle u_{g,i} u_{g,j} \rangle}{\partial x_k} + \frac{\partial \langle u_{g,i} u_{g,j} u_{g,k} \rangle}{\partial x_k} &+ \langle u_{g,i} u_{g,k} \rangle \frac{\partial \langle U_{g,j} \rangle}{\partial x_k} + \langle u_{g,j} u_{g,k} \rangle \frac{\partial \langle U_{g,i} \rangle}{\partial x_k} \\ &= G_{ik} \langle u_{g,j} u_{g,k} \rangle + G_{jk} \langle u_{g,i} u_{g,k} \rangle + C_0 \langle \varepsilon \rangle \delta_{ij}, \end{aligned} \quad (1.3.1)$$

where $\langle \mathbf{U}_g \rangle$ is the mean fluid velocity and $\mathbf{u}_g = \mathbf{U}_g - \langle \mathbf{U}_g \rangle$ is the fluctuating fluid velocity following Reynolds decomposition. The matrix \mathbf{G} is chosen so that the fluid and the particle models are consistent in the particle tracer limit ($\tau_p \rightarrow 0$). For instance, the simple Langevin model (SLM) with $G_{ij} = -\delta_{ij}/T_L$ corresponds to a classical $R_{ij} - \varepsilon$ Rotta model [36]. In practical computations, system (1.3.1) is supplemented with an equation for the mean dissipation rate of turbulent energy $\langle \varepsilon \rangle$:

$$\frac{\partial \langle \varepsilon \rangle}{\partial t} + \frac{\partial}{\partial x_i} (\langle U_{g,i} \rangle \langle \varepsilon \rangle) = d + C_{\varepsilon_1} \mathcal{P} \frac{\langle \varepsilon \rangle}{k} - C_{\varepsilon_2} \frac{\langle \varepsilon \rangle^2}{k}, \quad (1.3.2)$$

where if we denote by $R_{g,ij} = \langle u_{g,i} u_{g,j} \rangle$, $i, j \in \mathbb{Z}$ the Reynolds stress tensor, then

$$d = C_\varepsilon \frac{\partial}{\partial x_k} \left(\frac{k}{\langle \varepsilon \rangle} R_{g,ik} \frac{\partial \langle \varepsilon \rangle}{\partial x_i} \right), \quad (1.3.3)$$

$$\mathcal{P} = - \left(R_{g,ik} \frac{\partial \langle U_{g,i} \rangle}{\partial x_k} \right), \quad (1.3.4)$$

and C_ε , C_{ε_1} , C_{ε_2} are constants of the model [31, 35]. System (1.3.1)-(1.3.4) can be simulated by an Eulerian solver, for example, based on the Finite Volume Methods.

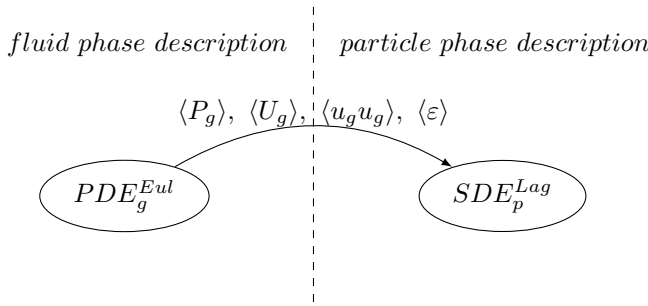


Figure 1.1: Classical Moments/PDF representation of dilute gas-particle turbulent flows.

The stochastic model of the **particle dispersion** introduced in the previous section describes the

time evolution of particle variables $\mathbf{Z}(t) = (\mathbf{x}_p, \mathbf{U}_p, \mathbf{U}_s)$:

$$\begin{aligned} dx_{p,i} &= U_{p,i} dt \\ dU_{p,i} &= \frac{1}{\tau_p} (U_{s,i} - U_{p,i}) dt + g_i dt \\ dU_{s,i} &= -\frac{1}{\rho_f} \frac{\partial \langle P \rangle}{\partial x_i} dt + (\langle U_{p,j} \rangle - \langle U_{g,j} \rangle) \frac{\partial \langle U_{g,i} \rangle}{\partial x_j} dt - \frac{(U_{s,i} - \langle U_{g,i} \rangle)}{T_{L,i}^*} dt \\ &\quad + \sqrt{\langle \varepsilon \rangle} \left(C_0 b_i \tilde{k}/k + \frac{2}{3} (b_i \tilde{k}/k - 1) \right) dW_i, \end{aligned} \quad (1.3.5)$$

with definitions given by (1.2.39) - (1.2.43) and values of $\langle P_g \rangle$, $\langle \mathbf{U}_g \rangle$, k , $\langle \varepsilon \rangle$ provided by numerical approximation of solutions to (1.3.1)-(1.3.4). System (1.3.5) is simulated by integrating the stochastic differential equations in time and resorting to Monte-Carlo methods. The model is anisotropic due to the crossing-trajectory effect. In the particle-tracer limit this effect is neglected since the discrete particle behaves like a fluid particle. Thus, when $\tau_p \rightarrow 0$ the model of the particle dispersion is consistent with the model for the fluid-particle motion and, consequently, with the moments equations (1.3.1) which are derived from it.

In practice, the present Moments/PDF approach shows to be more efficient in terms of computational cost than the stand-alone PDF approach. However, one of the main drawbacks of the current method is that even though the mean fields of the fluid are known by solving RANS equations, the last equation in (1.3.5) remains a McKean-type SDE. Indeed, it is still necessary to compute the mean velocity $\langle U_p \rangle$ using a given (finite) number of particles that implies that a bias error may be introduced.

1.3.2 Numerical approximation and algorithm

1.3.2.1 Particle-mesh methods

The purpose of this section is to describe the numerical approach used to solve the whole system of equations modeling dispersed turbulent two-phase flows (1.3.1) - (1.3.5). The solutions of the Moments (RANS) equations are given by a numerical method based on a Finite Volume scheme, thus are defined on the mesh. On the other hand, the dispersed phase is represented by a large number of discrete particles moving in the mesh (generated for the solution of the moments equations). Thus, the method that has been called Moments/PDF approach in the previous section, can also be referred to as an Eulerian/Lagrangian method or Finite Volumes/Monte-Carlo simulation since there is an exchange of data between particles and mesh points.

To solve the SDEs (1.3.5) describing the particle motion, a Monte-Carlo method is used, where the particle statistics are obtained after the time integration of stochastic differential equations and application of the averaging operator. Yet, the knowledge of fluid and even particle statistical moments at particle locations is required to compute the time evolution of particles. This property makes the system of SDEs difficult to solve. Seen in this way, system (1.3.5) can be rewritten in the form:

$$d\mathbf{Z}(t) = \mathbf{A}(t, \mathbf{Z}(t), p(t; \mathbf{z}), \mathbf{Y}(t)) dt + \mathbf{B}(t, \mathbf{Z}(t), p(t; \mathbf{z}), \mathbf{Y}(t)) d\mathbf{W}(t), \quad (1.3.6)$$

where $p(t; \mathbf{z})$ stands for the pdf of $\mathbf{Z}(t)$ and $\mathbf{Y}(t)$ for external mean fields, i.e. the fluid mean fields defined at particle locations. Since the one-point pdf $p(t; \mathbf{z})$ is computed at each t using all tracked particles (which are samples of the pdf), the non-local information is needed. In practice, necessary particle statistics are evaluated at cell centers of the mesh using a given *averaging operator*, here approximated by a spatial averaging. Then, these moments can be computed at particle location by interpolation or *projection*. The same projection operator is used to compute the statistics of the fluid at the locations of the stochastic particles. Moreover, the way to transfer the data from the particles to the mesh (averaging operator) and from the mesh to the particles (projection operator) must be consistent. Such an approximation allows to reduce the CPU time but is often the reason of additional numerical errors due to averaging, projection and definition of the particle location in the mesh.

1.3.2.2 General algorithm

Let $\{\mathbf{Y}^{[\mathbf{x}]}\}$ denote the set of the fluid mean fields at the mesh points and let $\{\mathbf{Y}^{(N)}\}$ be the fluid mean fields interpolated at particle locations. Let $\{\mathbf{Z}^{(N)}\}$ denote the set of variables attached to the stochastic particles and $\{\mathbf{Z}^{[\mathbf{x}]}\}$ the set of statistics, defined at cell centers, extracted from $\{\mathbf{Z}^{(N)}\}$. Time is discretized with a constant time step $\Delta t = t_{n+1} - t_n$ and space with a uniform mesh of cell size Δx .

The first step (operator F) of the algorithm is to solve the partial differential equations (PDEs) describing the fluid,

$$\{\mathbf{Y}^{[\mathbf{x}]}\}(t_n) \text{ and } \{\mathbf{Z}^{[\mathbf{x}]}\}(t_n) \xrightarrow{F} \{\mathbf{Y}^{[\mathbf{x}]}\}(t_{n+1}). \quad (1.3.7)$$

The F operator corresponds to a finite volume solver for system (1.3.1)-(1.3.4), which gives the instantaneous values of the fluid related statistical moments: the mean pressure $\langle P_g \rangle$ (or its gradient), the mean velocity $\langle \mathbf{U}_g \rangle$, the Reynolds stress tensor \mathbf{R}_g , the mean dissipation rate $\langle \varepsilon \rangle$ and additional fields depending on applications.

Then, using projection operator P , mean-particle properties and mean-fluid properties are transferred to the particle locations,

$$\{\mathbf{Z}^{[\mathbf{x}]}\}(t_n) \text{ and } \{\mathbf{Y}^{[\mathbf{x}]}\}(t_n) \xrightarrow{P} \{\mathbf{Z}^{(N)}\}(t_n) \text{ and } \{\mathbf{Y}^{(N)}\}(t_n). \quad (1.3.8)$$

After that, the system of stochastic differential equations (1.3.5) can be integrated in time (this stage is denoted by operator T):

$$\{\mathbf{Z}^{(N)}\}(t_n) \text{ and } \{\mathbf{Y}^{(N)}\}(t_n) \xrightarrow{T} \{\mathbf{Z}^{(N)}\}(t_{n+1}). \quad (1.3.9)$$

Finally, from the new computed set of variables at particle locations, new statistical moments are evaluated at cell centers using averaging operator A ,

$$\{\mathbf{Z}^{(N)}\}(t_{n+1}) \xrightarrow{A} \{\mathbf{Z}^{[\mathbf{x}]}\}(t_{n+1}). \quad (1.3.10)$$

A general particle-mesh algorithm within a time step is therefore defined by iterating the four operators, $F \rightarrow P \rightarrow T \rightarrow A$. The nature of operator F is not discussed here. The purpose of the

present section is to outline the implementation aspects related to the averaging and projection operators as well as to the time integration of SDEs following the developments [24, 30]. In particular, the questions on the numerical errors generated by the present particle/mesh algorithm, on the consistency and the convergence of the weak numerical scheme will be discussed.

1.3.2.3 Numerical errors

Following [48], an expected value of a functional of \mathbf{Z} , $\langle f(\mathbf{Z}) \rangle$, computed with the particle/mesh algorithm $P \rightarrow T \rightarrow A$ contains several kinds of errors. The total error at $t = T$ is given by the difference:

$$\epsilon(T) = \langle f(\mathbf{Z}_T) \rangle - \{f(\bar{\mathbf{Z}}_T)\}_{N_{pc}, \Delta x}, \quad (1.3.11)$$

where $\bar{\mathbf{Z}}_T$ is the approximation of \mathbf{Z}_T after time integration (operator T) and $\{\cdot\}_{N_{pc}, \Delta x}$ is the approximation of the mathematical expectation $\langle \cdot \rangle$:

$$\{f(\bar{\mathbf{Z}}_T)\}_{N_{pc}, \Delta x} = \frac{1}{N_{pc}} \sum_{n=1}^{N_{pc}} f(\bar{\mathbf{Z}}_T^n). \quad (1.3.12)$$

The total error can be decomposed into a deterministic and a random part, the former involving the bias, spatial and temporal discretization errors:

$$\epsilon(T) = \epsilon_\infty(T) + \epsilon_{\Delta t}(T) + \epsilon_{\Delta x}(T) + \epsilon_{N_{pc}}(T). \quad (1.3.13)$$

- The *bias* error is a deterministic error typical of non-linear stochastic differential equations:

$$\epsilon_\infty(T) = \{f(\bar{\mathbf{Z}}_T)\}_{\infty, \Delta x} - \left\langle \{f(\bar{\mathbf{Z}}_T)\}_{N_{pc}, \Delta x} \right\rangle, \quad (1.3.14)$$

which expresses the difference between the mean value of a quantity for a finite number N_{pc} of particles and the mean value for infinitely many particles (all other parameters being unchanged) and scales as (N_{pc}^{-1}) [47].

- The *temporal discretization* error is a deterministic error due to the numerical integration in time of the stochastic differential equations (operator T):

$$\epsilon_{\Delta t}(T) = \langle f(\mathbf{Z}_T) \rangle - \langle f(\bar{\mathbf{Z}}_T) \rangle. \quad (1.3.15)$$

- Depending on the mesh size, the *spatial discretization* error is due to the exchange of the information between the mesh and the particles (operators A, P):

$$\epsilon_{\Delta x}(T) = \langle f(\bar{\mathbf{Z}}_T) \rangle - \{f(\bar{\mathbf{Z}}_T)\}_{\infty, \Delta x} \quad (1.3.16)$$

This error is not involved when the coefficients of SDEs depend only on local values of the state vector $\mathbf{Z}(t)$ (thus not for McKean SDEs) [30], [48].

- The *statistical* error is a random variable of zero average:

$$\epsilon_{N_{pc}}(T) = \left\langle \{f(\bar{\mathbf{Z}}_T)\}_{N_{pc}, \Delta x} \right\rangle - \{f(\bar{\mathbf{Z}}_T)\}_{N_{pc}, \Delta x} \quad (1.3.17)$$

This kind of error is inherent to all Monte-Carlo methods, where the spatial averaging operator (A) is used with a finite number of particles N_{pc} . The asymptotic behavior of the statistical error is given by the Central Limit Theorem. The latter states that the statistical error of a mean quantity $\{f(\bar{\mathbf{Z}}_T)\}_{N_{pc}, \Delta x}$ is a random variable that tends in distribution towards the Gaussian random variable of zero mean and known variance:

$$\epsilon_{N_{pc}}(T) \xrightarrow{d} \frac{\sigma[f(\bar{\mathbf{Z}}_T)]}{\sqrt{N_{pc}}} \mathcal{N}(0, 1), \quad (1.3.18)$$

where $\sigma[f(\bar{\mathbf{Z}}_T)]$ is the root mean square of $f(\bar{\mathbf{Z}}_T)$. There exist specific procedures, referred to as variance reduction techniques (VRT) [34], that allow to reduce considerably the statistical error. An example of such a technique will be presented in conclusion.

1.3.2.4 Averaging and projection operators

As it was stated earlier, averaging and projection operators ensure the exchange of data between the particles and the mesh. Averaging consists in computation of particle mean fields at the cell centers, and projection - in the interpolation of these values at particle locations. The main difference with classical particle-in-cell methods (PIC) [19] is due to the fact that we deal with non-deterministic models (that are moreover of McKean type), where complex boundary conditions are often imposed. However, it has been shown in [30] that classical techniques that are used in PIC methods are also suitable for the present particle-mesh problems if some additional hypotheses are made. Below, we present the main lines of this study.

For the seek of clarity, let us denote with the superscript (n) particle-related quantities and with $[i]$ those that refer to the mesh. Then, some definitions can be given.

For a *deterministic function* $\Phi(\mathbf{x})$, the *spatial average* $\langle \cdot \rangle_\Delta$ (with a characteristic smoothing length Δ) in the cell centered at $\mathbf{x}^{[i]}$, can be written as the integral:

$$\langle \Phi^{[i]} \rangle_\Delta = \int \Phi(\mathbf{x}) \tilde{w}(\mathbf{x} - \mathbf{x}^{[i]}) d\mathbf{x}, \quad (1.3.19)$$

where $\Phi^{[i]} = \Phi(\mathbf{x}^{[i]})$, \tilde{w} is a given weighting function satisfying $\int \tilde{w}(\mathbf{x}) d\mathbf{x} = 1$.

For a *random field* $\Phi(t, \mathbf{x})$ with a pdf $f_\Phi(t, \mathbf{x}; \Psi)$, the mean at $\mathbf{x}^{[i]}$ corresponds to the mathematical expectation,

$$\langle \Phi^{[i]} \rangle = \int_{-\infty}^{+\infty} \Psi f_\Phi(t, \mathbf{x}^{[i]}; \Psi) d\Psi, \quad (1.3.20)$$

where Ψ is a sample-space variable of Φ . In classical Monte-Carlo methods, the pdf $f_\Phi(t, \mathbf{x}^{[i]}; \Psi)$ at each point $\mathbf{x}^{[i]}$ is approximated by using a finite number N_{pc} of independent samples of the random variable, $\Phi^{(n)}$, $n = 1, \dots, N_{pc}$. Thus, under a local homogeneity hypotheses, expectations $\langle \Phi^{[i]} \rangle$ can be approximated by (local) spatial averages $\langle \Phi^{[i]} \rangle_{N_{pc}, \Delta}$ based on a discrete particle set:

$$\langle \Phi^{[i]} \rangle \simeq \langle \Phi^{[i]} \rangle_{N_{pc}, \Delta} = \sum_{n=1}^{N_{pc}} \Phi^{(n)} w(\mathbf{x}^{(n)} - \mathbf{x}^{[i]}). \quad (1.3.21)$$

This expression, also known as kernel estimate, is derived from Eq. (1.3.19) as a quadrature formula [31]; the weights w are the discrete equivalents of \tilde{w} ,

$$\sum_{n=1}^{N_{pc}} w(\mathbf{x}^{(n)} - \mathbf{x}^{[i]}) = 1. \quad (1.3.22)$$

By analogy, the local value of the variance σ_Φ^2 of the random field $\Phi(t, \mathbf{x})$

$$(\sigma_\Phi^2)^{[i]} = \int_{-\infty}^{+\infty} \left(\Psi - \langle \Phi^{[i]} \rangle \right)^2 f_\Phi(t, \mathbf{x}^{[i]}; \Psi) d\Psi. \quad (1.3.23)$$

can be approximated by the expression for σ_Φ^2 with the use of spatial averaging:

$$(\sigma_\Phi^2)^{[i]} \simeq (\sigma_\Phi^2)_{N_{pc}, \Delta}^{[i]} = \sum_{n=1}^{N_{pc}} \left(\Phi^{(n)} - \langle \Phi \rangle \right)^2 w(\mathbf{x}^{(n)} - \mathbf{x}^{[i]}), \quad (1.3.24)$$

where $\langle \Phi \rangle$ stands either for a cell average $\langle \Phi^{[i]} \rangle$ or is interpolated at $\mathbf{x}^{(n)}$.

Finally, the choice of the weighting function is not obvious [19], [30]. In computations of particle-related statistics presented below, the NGP (Nearest-Grid-Point) method will be used, which consists in associating the particle properties with the center of the cell containing the particle. Then, the weighting function is piecewise constant, i.e.

$$w(\mathbf{x}^{(n)} - \mathbf{x}^{[i]}) = \begin{cases} 1/N_{pc}^i, & \text{for particle } n \text{ in cell } i \\ 0, & \text{otherwise} \end{cases}$$

A local average is then given by the sum over all N_{pc}^i particles in a given cell i :

$$\langle \Phi^{[i]} \rangle = \frac{1}{N_{pc}^i} \sum_{n=1}^{N_{pc}^i} \Phi^{(n)}. \quad (1.3.25)$$

However, it is important to note that this choice of the averaging operator may result in spurious variances or bias which decrease linearly with the number of particles.

The *projection* of averaged cell values onto the particle locations is an interpolation procedure, which must be consistent with the choice of the averaging operator, otherwise non-physical effects may be generated during the simulations. Here, for a particle (n), which is located at the cell $[i]$, we assume:

$$\langle \Phi \rangle^{(n)} = \langle \Phi^{[i]} \rangle.$$

1.3.2.5 Time integration of the SDEs

Once averaging and projection operators are chosen, the remaining task consists in numerical time integration of stochastic differential equations (1.3.5) describing the dynamics of discrete particles (definition of operator T). In the present work, we implement the *weak first-order Euler scheme* which has been derived in [24] and is recalled in Appendix A. The scheme is *consistent* with the mathematical definition of the stochastic integral in the *Ito's sense*, *explicit* and *unconditionally*

stable. Moreover, it is consistent with all limit systems by construction [30]. The term “weak” underlines the weak mode of convergence, that is at time $t = T$, for all sufficiently smooth functions f , there exists a constant C such that:

$$\sup_{t \leq T} |\langle f[\mathbf{Z}(t)] - f[\mathbf{Z}^{\Delta t}(t)] \rangle| \leq C(T) (\Delta t), \quad (1.3.26)$$

where $\mathbf{Z}^{\Delta t}(t)$ is a numerical approximation of the process $\mathbf{Z}(t)$ obtained with a uniform time discretization Δt . Other convergence modes are possible [20, 29], for example *strong convergence* in the mean-square sense, if one is interested in the exact trajectories of the process. However, it is not often the case in engineering problems, where we are mainly interested in the expected values (statistics).

1.4 Numerical implementation and results

In this section we focus on the numerical simulations of the particle phase in the turbulent two-phase flow using the Moments/PDF approach. The mean fields related to the fluid carrier phase are given by either analytical expressions or preliminary computations. The particles are statistical models of real particles and their evolution is described by stochastic differential equations. On the other hand, the particles are samples of the one-point pdf and represent different realizations of the flow. The outcome of the method is statistical averages that correspond to a weak approximation of the underlying one-point pdf. Thus, the present subsection aims at the verification of the numerical implementation for the particle stochastic model (1.2.38).

1.4.1 Particle dispersion without mean convective motion

Let us study the case of the particle dispersion from a source point when at $t = 0$ the particles are placed into a box filled with an isotropic homogeneous stationary turbulent flow such that there is no mean convective motion, $\langle U_g \rangle = 0$. The initial conditions for system (1.3.5) are:

$$x_p^0 = 0, \quad U_p^0 = 0, \quad U_s^0 = 0. \quad (1.4.1)$$

After some transient period, the statistics of particle velocities reach equilibrium values, which are functions of constant statistics of the fluid. The relations giving the equilibrium values in terms of the fluid statistics are called the Tchen’s formulas. More precisely, it relates particle and fluid kinetic energies:

$$\langle U_p^2 \rangle = \langle U_p U_s \rangle = \langle U_s^2 \rangle \frac{1}{1 + \tau_p/T_L}. \quad (1.4.2)$$

These relations are formulated under an assumption that the statistics of the fluid seen are constant or that the particle driving force is a stationary process, which refers to the case of homogeneous turbulence and amounts to neglecting the convective phenomena.

PDF model and analytical solution

Taking into account the isotropy of turbulence, we can consider a one-dimensional state vector $\mathbf{Z}_t = (x_p(t), U_p(t), U_s(t))$ whose evolution on $[0, t]$ is given by a simplified system of stochastic differential equations with constant coefficients:

$$\begin{cases} dx_p = U_p dt, \\ dU_p = \frac{U_s - U_p}{\tau_p} dt, & x_p \in [-L, L], t > 0, \\ dU_s = -\frac{U_s}{T_L} dt + BdW_t, \end{cases} \quad (1.4.3)$$

where the mean drift term and the gravity force are omitted with reference to the complete model (1.2.38). Time scales τ_p, T_L are assumed to be constant together with the diffusion coefficient B . In this case, system (1.4.3) enables analytical solutions that are written in terms of stochastic integrals. Denoting $\theta = T_L/(T_L - \tau_p)$, we have:

$$U_s(t) = U_s^0 e^{-\frac{t}{T_L}} + Be^{-\frac{t}{T_L}} \int_0^t e^{\frac{s}{T_L}} dW_s, \quad (1.4.4)$$

$$U_p(t) = U_p^0 e^{-\frac{t}{\tau_p}} + U_s^0 \theta \left(e^{-\frac{t}{T_L}} - e^{-\frac{t}{\tau_p}} \right) + \frac{B}{\tau_p} e^{-\frac{t}{\tau_p}} \int_0^t e^{\frac{t'}{\theta\tau_p}} \left(\int_0^{t'} e^{\frac{s}{T_L}} dW_s \right) dt', \quad (1.4.5)$$

$$\begin{aligned} x_p(t) = & x_p^0 + U_p^0 \tau_p \left(1 - e^{-\frac{t}{\tau_p}} \right) + U_s^0 \theta \left[T_L \left(1 - e^{-\frac{t}{T_L}} \right) + \tau_p \left(e^{-\frac{t}{\tau_p}} - 1 \right) \right] + \\ & BT_L \times W_t - B\theta T_L e^{-\frac{t}{T_L}} \int_0^t e^{\frac{s}{T_L}} dW_s + B\theta \tau_p e^{-\frac{t}{\tau_p}} \int_0^t e^{\frac{s}{\tau_p}} dW_s. \end{aligned} \quad (1.4.6)$$

Taking homogeneous initial conditions (1.4.1) we can derive the expressions for $\langle U_s^2 \rangle, \langle U_p U_s \rangle, \langle U_p^2 \rangle, \langle X_p^2 \rangle$ that are more relevant:

$$\langle U_s^2 \rangle(t) = \frac{B^2 T_L}{2} \left(1 - e^{-\frac{2t}{T_L}} \right), \quad (1.4.7)$$

$$\langle U_p U_s \rangle(t) = \frac{(BT_L)^2}{2} \left(\frac{1}{T_L + \tau_p} + \frac{2\tau_p}{T_L^2 - \tau_p^2} e^{-\left(\frac{1}{T_L} + \frac{1}{\tau_p}\right)t} - \frac{1}{T_L - \tau_p} e^{-\frac{2t}{T_L}} \right), \quad (1.4.8)$$

$$\begin{aligned} \langle U_p^2 \rangle(t) = & \frac{(BT_L)^2}{2} \cdot \frac{1}{T_L + \tau_p} \left(1 - e^{-\frac{2t}{\tau_p}} \right) + \frac{(BT_L)^2}{2} \cdot \frac{4T_L \tau_p}{(T_L^2 - \tau_p^2)(T_L - \tau_p)} \left(e^{-\left(\frac{1}{T_L} + \frac{1}{\tau_p}\right)t} - e^{-\frac{2t}{\tau_p}} \right) - \\ & \frac{(BT_L)^2}{2} \cdot \frac{T_L}{(T_L - \tau_p)^2} \left(e^{-\frac{2t}{T_L}} - e^{-\frac{2t}{\tau_p}} \right), \end{aligned} \quad (1.4.9)$$

$$\begin{aligned} \langle X_p^2 \rangle(t) = & (BT_L)^2 \times t + \frac{B^2 T_L^5}{2(\tau_p - T_L)^2} \left(1 - e^{-\frac{2t}{T_L}} \right) + \frac{B^2 T_L^2 \tau_p^3}{2(\tau_p - T_L)^2} \left(1 - e^{-\frac{2t}{\tau_p}} \right) + \\ & \frac{2B^2 T_L^4}{\tau_p - T_L} \left(1 - e^{-\frac{t}{T_L}} \right) - \frac{2B^2 T_L^2 \tau_p^2}{\tau_p - T_L} \left(1 - e^{-\frac{t}{\tau_p}} \right) - \frac{2B^2 T_L^4 \tau_p^2}{(\tau_p - T_L)^2 (\tau_p + T_L)} \left(1 - e^{-\frac{t}{\tau_p}} e^{-\frac{t}{T_L}} \right). \end{aligned} \quad (1.4.10)$$

Numerical results

We present a comparison of numerical approximations obtained using the first order numerical scheme (Appendix A) with $N_{pc} = 10^4$ samples during 4000 iterations (the stationary state is reached before 1000 iterations) and analytical solutions (1.4.7)-(1.4.10). We show that the Tchen's relations (1.4.2) are verified and present an analysis of the statistical error.

Physical time scales T_L, τ_p being constant, it would be reasonable to take $\Delta t \ll T_L, \tau_p$ to allow a physically meaningful solution. The failure of this condition (when some time scale goes to zero continuously in time) leads to several limit cases detailed in section 1.2.3.3. In order to demonstrate the multiscale character of the scheme, two of the limit cases are considered:

- the 1st limit case: when $\tau_p \rightarrow 0$ a discrete particle behaves like a fluid particle. This limit case appears when the following inequalities are verified: $\tau_p \ll \Delta t \ll T_L$;
- the 2nd limit case: when $T_L \rightarrow 0$ and, at the same time, $BT_L = cst$, the fluid velocity seen becomes a fast variable and is eliminated from system of equations (1.4.3), corresponding to flows with large high-inertia particles: $T_L \ll \Delta t \ll \tau_p$.

(i) **General case:** $\Delta t \ll T_L, \tau_p$. We set $\Delta t = 10^{-3}s, T_L = 2.10^{-1}s, \tau_p = 10^{-1}s$ and the value of the diffusion coefficient $B = 10 m/s^{3/2}$. Taking the limit at $t \rightarrow \infty$ in analytical expressions (1.4.7)-(1.4.10) gives us the equilibrium values for the second order statistics:

$$\lim_{t \rightarrow \infty} \langle U_s^2 \rangle(t) = \frac{B^2 T_L}{2} = 10 m^2/s^2, \quad (1.4.11)$$

$$\lim_{t \rightarrow \infty} \langle U_p^2 \rangle(t) = \lim_{t \rightarrow \infty} \langle U_p U_s \rangle(t) = \frac{B^2 T_L}{2} \cdot \frac{T_L}{T_L + \tau_p} = 6.6 m^2/s^2, \quad (1.4.12)$$

$$\lim_{t \rightarrow \infty} \frac{d \langle X_p^2 \rangle(t)}{dt} = (BT_L)^2 = 4 m^2/s. \quad (1.4.13)$$

We can see that Tchen's relations (1.4.2) are verified for both analytical and numerical solutions (Fig. 1.2) and that the slope of $\langle X_p^2 \rangle(t)$ is consistent with (1.4.10). Moreover, the shape of $\langle X_p^2 \rangle(t)$ reveals the diffusive behavior of the discrete particles, quadratic in dt for small times and linear in time for long observation times.

(ii) **1st limit case:** $\tau_p \ll \Delta t \ll T_L$. Let us take $\Delta t = 10^{-3}s, T_L = 10^{-1}s, \tau_p = 10^{-5}s$ and $B = 10 m/s^{3/2}$. In this case, the discrete particles are characterized by a very low inertia and thus reproduce the behavior of fluid particles. Then, $U_p(t) = U_s(t)$ is instantaneously verified. Actually, when $\tau_p \ll T_L$ and $t \rightarrow \infty$ we have:

$$\lim_{t \rightarrow \infty} \langle U_p^2 \rangle(t) = \lim_{t \rightarrow \infty} \langle U_p U_s \rangle(t) = \lim_{t \rightarrow \infty} \langle U_s^2 \rangle(t) = \frac{B^2 T_L}{2} = 5 m^2/s^2. \quad (1.4.14)$$

The slope of $\langle X_p^2 \rangle(t)$ is approximately $(BT_L)^2 = 1$, as can be noted in Fig. 1.4.

(iii) 2nd limit case: $T_L \ll \Delta t \ll \tau_p$. When, for example, $\Delta t = 10^{-3}s, T_L = 10^{-5}s, \tau_p = 10^{-1}s$ and $B = 10^3\text{ m/s}^{3/2}$, the velocity of the fluid seen becomes a fast variable and is eliminated from system of equations (1.4.3):

$$U_s(t) \xrightarrow{d} \mathcal{N}\left(0, \frac{B^2 T_L}{2}\right). \quad (1.4.15)$$

Moreover, Tchen's relations are still valid here (Fig. 1.5):

$$\lim_{t \rightarrow \infty} \langle U_s^2 \rangle(t) = \frac{B^2 T_L}{2} = 5\text{ m}^2/\text{s}^2, \quad (1.4.16)$$

$$\lim_{t \rightarrow \infty} \langle U_p^2 \rangle(t) = \lim_{t \rightarrow \infty} \langle U_p U_s \rangle(t) = \frac{B^2 T_L}{2} \cdot \frac{T_L}{T_L + \tau_p} \xrightarrow{T_L \rightarrow 0} \frac{(BT_L)^2}{2\tau_p} = 5.10^{-4}\text{ m}^2/\text{s}^2, \quad (1.4.17)$$

and

$$\lim_{t \rightarrow \infty} \frac{d \langle X_p^2 \rangle(t)}{dt} = (BT_L)^2 = 10^{-4}\text{ m}^2/\text{s}. \quad (1.4.18)$$

It is important to note that when the coefficients of system (1.4.3) are constant, there is no discretization error because the numerical scheme corresponds exactly to the analytical solution. Moreover, since the system of equations is linear, the bias error is eliminated too. Therefore, the **statistical error** analysis can be properly made for $\langle U_p \rangle, \langle U_s \rangle, \langle U_p^2 \rangle$ and $\langle U_s^2 \rangle$ in the general case. For $Z_T = U_p(T), U_s(T)$, the central limit theorem states that the statistical error of a mean quantity $\{f(Z_T)\}_{N_{pc}, \Delta x}$ is a random variable that tends in distribution towards the Gaussian random variable of zero mean and known variance:

$$\epsilon_{N_{pc}}(T) = \left\langle \{f(\bar{Z}_T)\}_{N_{pc}, \Delta x} \right\rangle - \{f(\bar{Z}_T)\}_{N_{pc}, \Delta x}, \quad \epsilon_{N_{pc}}(T) \xrightarrow{d} \frac{\sigma[f(\bar{Z}_T)]}{\sqrt{N_{pc}}} \mathcal{N}(0, 1), \quad (1.4.19)$$

where $\sigma[f(\bar{Z}_T)]$ is the root mean square of $f(\bar{Z}_T)$, \bar{Z}_T is the approximation of Z_T after the time integration and $\{\cdot\}_{N_{pc}, \Delta x}$ is the approximation of the expected value $\langle \cdot \rangle$ with N_{pc} samples:

$$\{f(\bar{Z}_T)\}_{N_{pc}, \Delta x} = \frac{1}{N_{pc}} \sum_{n=1}^{N_{pc}} f(\bar{Z}_T^n). \quad (1.4.20)$$

Here, $\bar{Z}_T = Z_T$ since there is no discretization error. In order to verify the statement (1.4.19) numerically, we study the variance of the statistical error that is equivalent to:

$$\mathcal{V}_{N_{pc}}[f(Z_T)] = \left\langle \left(\{f(Z_T)\}_{N_{pc}, \Delta x} - \left\langle \{f(Z_T)\}_{N_{pc}, \Delta x} \right\rangle \right)^2 \right\rangle. \quad (1.4.21)$$

In practice, to estimate the variance (1.4.21) for each value of N_{pc} , we perform a large number M of simulations so that $\mathcal{V}_{N_{pc}}$ becomes roughly independent of M . These simulations, with different values of N_{pc} , are going to give $\mathcal{V}_{N_{pc}}[f(Z_T)]$ as a function of N_{pc} . This will be performed for the first- and second-order moments, $f(Z_T) = Z_T$ and $f(Z_T) = Z_T^2$, respectively. For $f(Z_T) = Z_T$, the quantity to evaluate is :

$$\mathcal{V}_{N_{pc}}[Z_T] = \frac{1}{M} \sum_{i=1}^M \left(\{Z_T\}_{N_{pc}}^i - \frac{1}{M} \sum_{i=1}^M \{Z_T\}_{N_{pc}}^i \right)^2, \quad (1.4.22)$$

and it must be shown that

$$\sqrt{\mathcal{V}_{N_{pc}}[Z_T]} \simeq \sigma(Z_T)/\sqrt{N_{pc}}, \quad (1.4.23)$$

where $\sigma(Z_T)$ is the root mean square value of Z_T . In the same way, for $f(Z_T) = Z_T^2$ the expression

$$\mathcal{V}_{N_{pc}}[Z_T^2] = \frac{1}{M} \sum_{i=1}^M \left(\{Z_T^2\}_{N_{pc}}^i - \frac{1}{M} \sum_{i=1}^M \{Z_T^2\}_{N_{pc}}^i \right)^2 \quad (1.4.24)$$

is computed to show that the expected behavior is obtained:

$$\sqrt{\mathcal{V}_{N_{pc}}[Z_T^2]} \simeq \sigma(Z_T^2)/\sqrt{N_{pc}}. \quad (1.4.25)$$

The exact values of $\sigma(Z_T)$ for $Z_T = U_p(T), U_s(T)$ are given by $\sqrt{\langle U_p^2 \rangle(T)}$ and $\sqrt{\langle U_s^2 \rangle(T)}$. Since Z_T is a Gaussian random variable (it is a stochastic integral of a deterministic function) [29], one has $\langle Z_T^4 \rangle = 3 \langle Z_T^2 \rangle^2$ and therefore

$$\sigma(Z_T^2) = \sqrt{2} [\sigma(Z_T)]^2.$$

Convergence curves presented in Fig. 1.3 show that the error $\epsilon_{N_{pc}}(T)$ for $\langle U_p \rangle, \langle U_s \rangle, \langle U_p^2 \rangle$ and $\langle U_s^2 \rangle$ is indeed decreasing as $1/\sqrt{N_{pc}}$ with a correct slope.

1.4.2 Particle convection without turbulent dispersion

We focus on a verification of the part of the numerical scheme that approximates the convective terms of the complete PDF model (1.2.38). In fact, these terms were not involved in the model of particle dispersion (1.4.3), thus their influence was not studied yet. Here, the deterministic terms modeling the convection phenomena in (1.2.38) are taken as functions of time, which introduce a temporal discretization error. Analysis of the convergence has been made for vanishing Δt .

PDF model and analytical solution

Keeping the one-dimensional state vector $Z_t = (x_p(t), U_p(t), U_s(t))$, we solve the following system of ordinary differential equations on $[t_0, t]$ for $t_0 > 0$:

$$\begin{cases} dx_p = U_p dt \\ dU_p = \frac{U_s - U_p}{\tau_p} dt, & x_p \in [-L, L], t > t_0, \\ dU_s = -\frac{U_s}{T_L} dt + F(t) dt, \end{cases} \quad (1.4.26)$$

corresponding to system (1.2.38) without stochastic terms. For $T_L = cst, \tau_p = \tau_p(t) = t$ and $F(t) = t$, analytical solutions to (1.4.26) can be derived:

$$U_s(t) = C_0 e^{-\frac{(t-t_0)}{T_L}} + T_L(t - T_L) \quad \text{with} \quad C_0 = U_s(t_0) - T_L t_0 + T_L^2, \quad (1.4.27)$$

$$U_p(t) = \frac{1}{t} \left(t_0 U_p(t_0) + C_0 T_L - \frac{T_L(t_0 - T_L)^2}{2} + \frac{T_L(t - T_L)^2}{2} - C_0 T_L e^{-\frac{(t-t_0)}{T_L}} \right). \quad (1.4.28)$$

Numerical results

Approximations displayed in Fig. 1.6 allow to conclude that the scheme provides a quite good approximation for analytical solution (1.4.27) - (1.4.28). Moreover, the slope of the convergence curves for the temporal discretization error is 0.99, that is very close to 1.

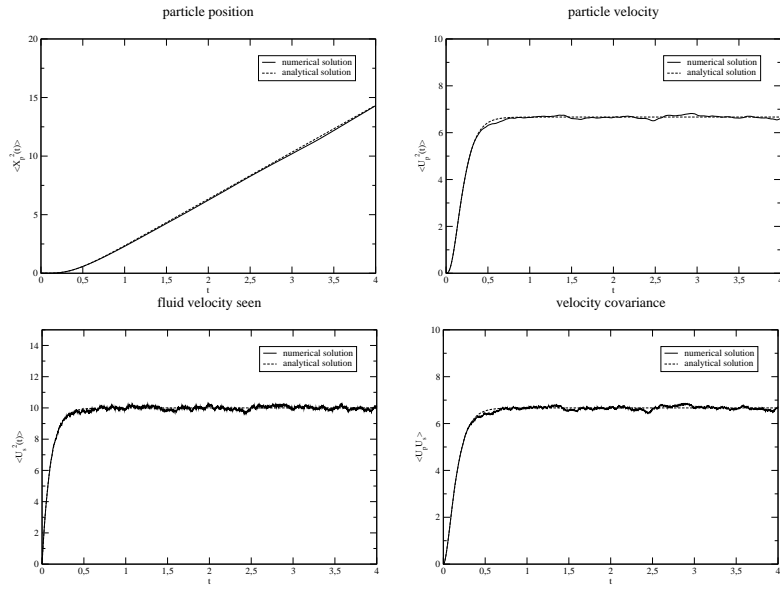


Figure 1.2: Numerical simulation with $N_{pc} = 10^4$ for system (1.4.3). General case: $\Delta t \ll T_L, \tau_p$ with $\Delta t = 10^{-3}s$, $T_L = 2.10^{-1}s$, $\tau_p = 10^{-1}s$ and $B = 10 m/s^{3/2}$.

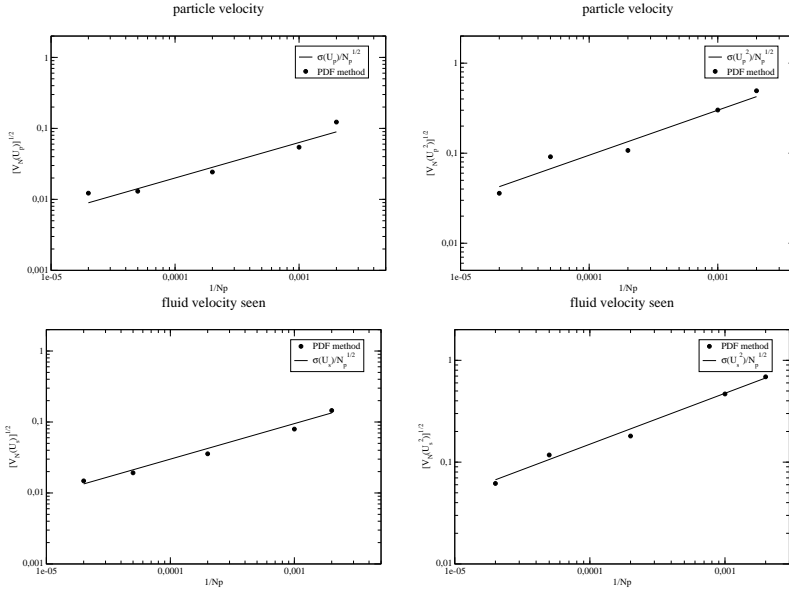


Figure 1.3: Study of the statistical error for system (1.4.3) in the general case: $\Delta t = 10^{-3}s$, $T_L = 2.10^{-1}s$, $\tau_p = 10^{-1}s$ and $B = 10 m/s^{3/2}$. L^2 convergence curves for $\sqrt{\mathcal{V}_N(Z_T)}$ and $\sqrt{\mathcal{V}_N(Z_T^2)}$ as a function of the number of samples N_p .

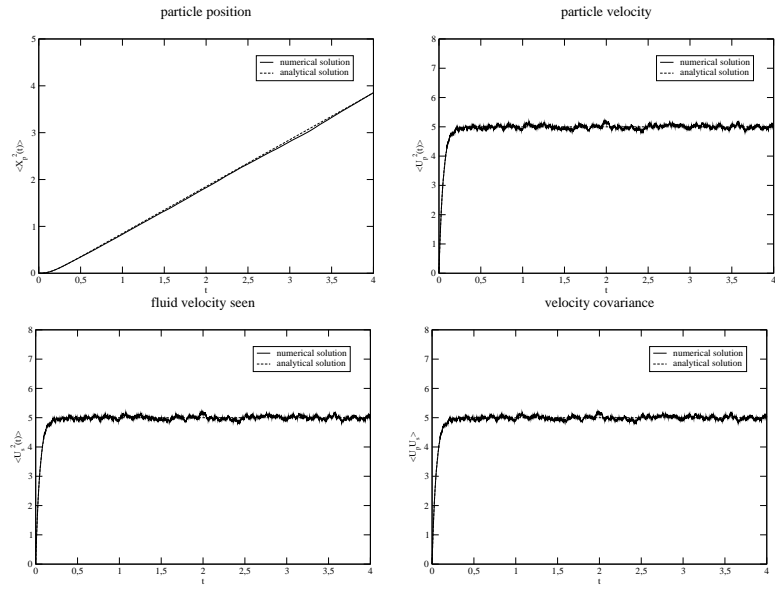


Figure 1.4: Numerical simulation with $N_{pc} = 10^4$ for system (1.4.3). 1st limit case: $\tau_p \ll \Delta t \ll T_L$ with $\Delta t = 10^{-3}s$, $T_L = 10^{-1}s$, $\tau_p = 10^{-5}s$ and $B = 10 m/s^{3/2}$.

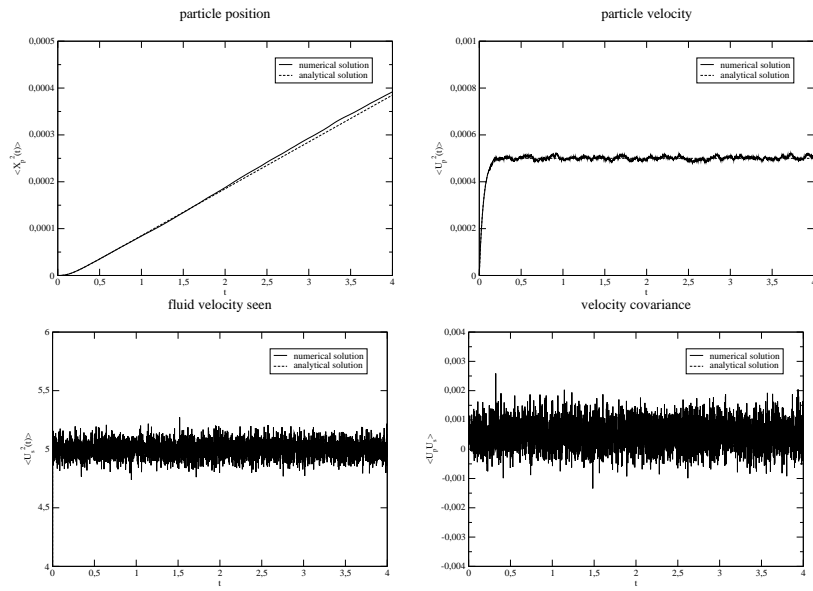


Figure 1.5: Numerical simulation with $N_{pc} = 10^4$ for system (1.4.3). 2nd limit case: $T_L \ll \Delta t \ll \tau_p$ with $\Delta t = 10^{-3}s$, $T_L = 10^{-5}s$, $\tau_p = 10^{-1}s$ and $B = 10^3 m/s^{3/2}$.

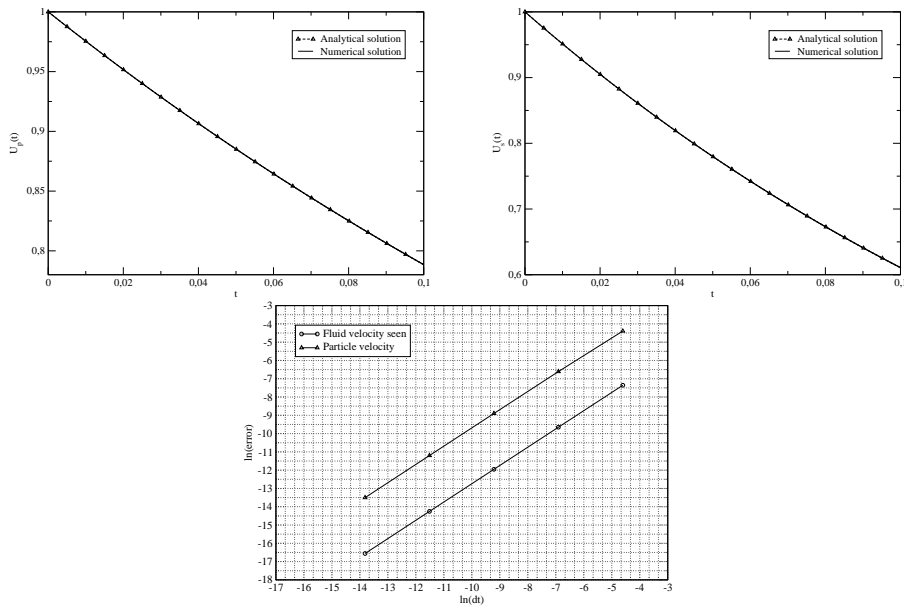


Figure 1.6: Numerical simulation for system (1.4.26) with $\Delta t = 10^{-3}$ s. Study of the discretization error, L^1 convergence curves for $U_p(t)$ and $U_s(t)$ as functions of the time step Δt .

1.4.3 A more realistic test case: Co-current wall jet

In this section, we aim at studying a more realistic case of two-dimensional turbulent two-phase wall jet, where solid particles are involved in a turbulent air flow, which is characterized by the non-homogeneous anisotropic stationary turbulence. Still, only the particle PDF model is solved, while the fluid mean fields are provided by a preliminary single-phase computation using *Code-Saturne* [1]. Thus, we intend to compare the particle statistics given by the present code with those provided by *Code-Saturne* using the same flow configurations. *Code-Saturne* has been chosen as a reference both because we need a solver that provides the fluid fields to make the computations of the particle fields, particles being agitated by the fluid turbulence, and because it contains a module allowing the Lagrangian simulations of the particle dispersion. It is important to emphasize that both codes simulate the same stochastic model of the particle dispersion (1.3.5) using the same numerical scheme (see Appendix A) and the same fluid-related mean fields.

PDF model and experimental setup

We consider a 2D rectangular domain of dimensions $Lx \times Ly$. A sketch of the geometry is given in Fig.2.16, where edge AE is a wall boundary. Air at ambient temperature and atmospheric pressure is injected both in AB and BC regions. The ratio between the gas velocity in the region AB and the gas velocity in the region BC is low enough so that there is no recirculation in the flow. Solid particles are injected in AB region of diameter d and after some time leave the domain by outlets CD and DE. A stationary turbulent two-phase flow is then obtained.

The PDF description of the dispersed phase is given by the Simple Langevin Model (SLM):

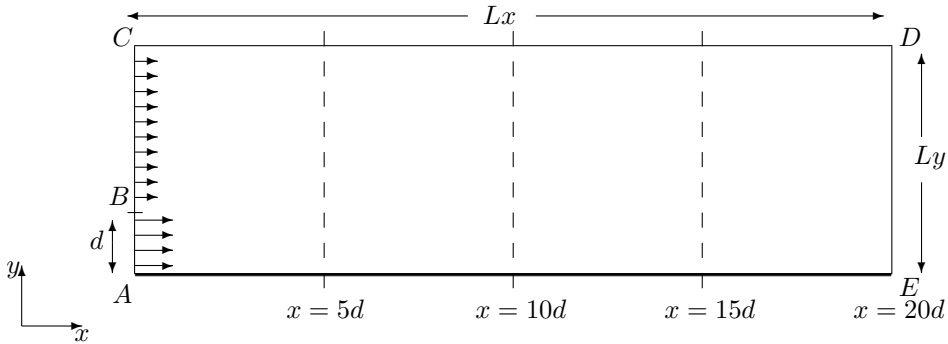


Figure 1.7: Computational domain, definition of the geometry of a wall jet of diameter d .

$$\begin{cases} dx_{p,i} = U_{p,i} dt \\ dU_{p,i} = \frac{U_{s,i} - U_{p,i}}{\tau_p} dt \\ dU_{s,i} = -\frac{1}{\rho_g} \frac{\partial \langle P_g \rangle}{\partial x_i} dt - \frac{U_{s,i} - \langle U_{g,i} \rangle}{T_L} dt + \sqrt{C_0 \langle \varepsilon \rangle} dW_{t,i}, \end{cases} \quad (1.4.29)$$

with $T_L = \frac{1}{(1/2+3/4C_0)} \frac{k}{\langle \varepsilon \rangle}$, where the fluid mean fields $\langle P_g \rangle$, $\langle \mathbf{U}_g \rangle$, k , $\langle \varepsilon \rangle$ are external data computed in advance with $k - \varepsilon$ model using *Code-Saturne* and then used as frozen fields. Further, the mean pressure gradient reconstruction is necessary. It is worth noting that taking an isotropic closure T_L in system (2.4.61) does not affect the general anisotropy of the model.

Numerical simulation

In present computations we assume the following dimensions: $Lx = 1.0 \text{ m}$, $Ly = 0.2 \text{ m}$, $d = 0.05 \text{ m}$. The fluid is characterized by the density $\rho_g = 2.1 \text{ kg/m}^3$, the dynamical viscosity $\mu_g = 1.85 \times 10^{-5} \text{ Pa.s}$ and $C_0 = 2.1$. The gas is injected in the normal to the inlet direction with a constant velocity 1.5 m/s in region AB and 1.0 m/s in BC. The dispersed phase is described by the particle density $\rho_p = 2000 \text{ kg/m}^3$ and the diameter $d_p = 10^{-5} \text{ m}$. The computations are made on a uniform mesh of the size $Nx \times Ny = 100 \times 20$ with $\Delta t = 10^{-3} \text{ s}$, where at the beginning of each time step particles are injected in the domain with the fluid velocity. For a particle (n) injected in the cell $[i]$ of the domain, we assume the following initial conditions:

$$\begin{aligned} \mathbf{U}_p^{(n)} &= \langle \mathbf{U}_g \rangle^{[i]}, \\ \mathbf{U}_s^{(n)} &= \langle \mathbf{U}_g \rangle^{[i]} + \sqrt{\frac{2}{3} k^{[i]}} \zeta, \end{aligned} \quad (1.4.30)$$

where $\zeta = (\zeta_x, \zeta_y)$ is a vector of independent $\mathcal{N}(0, 1)$ random variables. For such a configuration, τ_p is equal approximately $6 \times 10^{-4} \text{ s}$. Moreover, looking at the mean drift direction only, we note that if a particle moves with the fluid velocity 1.5 m/s , it stays in a cell of the length $\Delta x = 10^{-3} \text{ m}$ during almost 7 time iterations. Thus, it might leave the domain in 0.7 s (or 700 time iterations) and the stationary state may be reached soon after. All relevant characteristics of the flow are

summarized in Table 1. Below, we compare two computations in terms of statistical error as a function of number of particles per cell, N_{pc} .

Characteristic	Value
Domain length	1.0 m
Domain width	0.2 m
Jet width	0.05 m
Fluid density	1.2 kg/m ³
Fluid dynamical viscosity	1.85×10^{-5} Pa.s
Maximum velocity in the jet	1.5 m/s
Velocity of the co-current stream	1.0 m/s
Particle diameter	10 ⁻⁵ m
Particle density	2000 kg/m ³

Table 1.1: Characteristics of the flow.

Wall boundary conditions

We consider an elastic wall-particle collision, so that when a particle reaches the wall boundary during a time iteration the following correction is made at the end of the time step (see Fig. 1.8):

$$\begin{aligned} x_p^{n+1} &= \tilde{x}_p^{n+1}, & y_p^{n+1} &= -\tilde{y}_p^{n+1} \\ U_{p,x}^{n+1} &= \tilde{U}_{p,x}^{n+1}, & U_{p,y}^{n+1} &= -\tilde{U}_{p,y}^{n+1} \\ U_{s,x}^{n+1} &= \tilde{U}_{s,x}^{n+1}, & U_{s,y}^{n+1} &= -\tilde{U}_{s,y}^{n+1} \end{aligned} \quad (1.4.31)$$

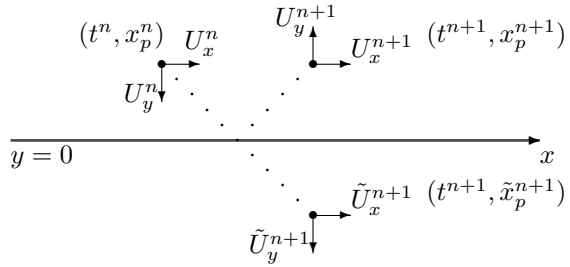


Figure 1.8: The treatment of the wall boundary conditions in the Lagrangian particle simulations.

Results and comparison with *Code-Saturne*

In both examples A and B present below, the fluid related mean-fields $\langle P_g \rangle, \langle \mathbf{U}_g \rangle, k, \langle \varepsilon \rangle$ are provided to the model of the particle dispersion (2.4.61) by a preliminary computation using $k - \varepsilon$ model with *Code-Saturne*. For each set of parameters, the particle statistics obtained with the present code are compared to the numerical results obtained with *Code-Saturne* when simulating the same model of the particle dispersion (2.4.61) in the same configuration and with the same

numerical scheme. Therefore, it is only a matter of verification of the numerical code, and not of the validation of the physical modeling (it has been done for example in [23]). Then, both cases are compared to each other in order to demonstrate the decrease of the statistical error according to the central limit theorem. We look at the particle volumetric fraction α_p , the mean particle velocity $\langle \mathbf{U}_p \rangle$ and the particle related kinetic tensor $\mathbf{R}_p = \langle \mathbf{u}_p \mathbf{u}_p \rangle$ considered to be symmetric. Here, at each cell i (with the cell center \mathbf{x}_i) containing $N_{pc}^{[i]}$ particles at time t , the following approximations are used:

$$\alpha_p(t, \mathbf{x}_i) = \frac{\sum_{n=1}^{N_{pc}^{[i]}} v^{(n)}}{\mathcal{V}_i}, \quad (1.4.32)$$

where $v^{(n)}$ is the volume occupied by a particle and \mathcal{V}_i - the volume of the cell i . For other mean particle quantities we obtain the numerical approximations as ensemble averages:

$$\langle \mathcal{H}_p \rangle(t, \mathbf{x}_i) \simeq \langle \mathcal{H}_p \rangle_{N_{pc}}(t, \mathbf{x}_i) = \frac{\sum_{n=1}^{N_{pc}^{[i]}} \mathcal{H}_p^{(n)}(t)}{N_{pc}^{[i]}}. \quad (1.4.33)$$

Case A: Simulation consists of 5000 time iterations. The equilibrium value of the number of particles in the domain is about $N_{p,A} = 710$. Since after some transient period (which covers 2000 iterations) the flow becomes stationary, we compute the time averaged mean quantities. Actually, this amounts to make the computations with $3000 \cdot N_{p,A} = 2.13 \times 10^6$ particles or approximately $N_{pc} = 10^3$ particles per cell. The profiles of the solution corresponding to the cross-stream sections $x = 5d, 10d, 15d, 20d$ are shown in Fig. 2.17 - 2.19.

Case B: The way to make the computations is very similar to the previous one: during 3000 time iterations in the stationary state we compute the time averaged statistics for $N_{p,B} = 7100$ particles (2.13×10^7 samples) or $N_{pc} = 10^4$ particles per cell. The comparisons of results with approximations of *Code_Saturne* for the same number of particles are displayed in Fig. 1.14 - 1.18.

We can see that in both examples the comparisons are rather fair. The differences between the two codes appear in the cells, where there is a very small number of particles in one of the codes (thus, there is statistics computation) and there is no any in the other (all statistics are zero). It is also worth noting that there are some differences between the present implementation and that of the *Code_Saturne*. For instance, the pseudo-random number generators used in the both codes are not the same (in the present code, the Box-Muller transform has been implemented). The pressure-gradient reconstruction may be another source of gaps. However, one can see that these differences tend to disappear when N_{pc} is increased. Moreover, when comparing two cases with different numbers of particles per cell:

$$\frac{N_{pc,B}}{N_{pc,A}} = 10,$$

we note that the results are in agreement with the central limit theorem. For a random vector process $\mathbf{Z}(t)$, the latter states that the statistical error of the expected value of a functional of \mathbf{Z} at $t = T$:

$$\epsilon_{N_{pc}}(T) = \left\langle \{f(\bar{\mathbf{Z}}_T)\}_{N_{pc}, \Delta x} \right\rangle - \{f(\bar{\mathbf{Z}}_T)\}_{N_{pc}, \Delta x} \quad (1.4.34)$$

is approximatively a normally distributed random variable:

$$\epsilon_{N_{pc}}(T) \xrightarrow{d} \frac{\sigma[f(\bar{\mathbf{Z}}_T)]}{\sqrt{N_{pc}}} \mathcal{N}(0, 1), \quad (1.4.35)$$

where $\sigma[f(\bar{\mathbf{Z}}_T)]$ is the root mean square of $f(\bar{\mathbf{Z}}_T)$, $\bar{\mathbf{Z}}_T$ is the approximation of \mathbf{Z}_T after time integration and $\{\cdot\}_{N_{pc}, \Delta x}$ is the approximation of the expected value $\langle \cdot \rangle$:

$$\{f(\bar{\mathbf{Z}}_T)\}_{N_{pc}, \Delta x} = \frac{1}{N_{pc}} \sum_{n=1}^{N_{pc}} f(\bar{\mathbf{Z}}_T^n). \quad (1.4.36)$$

We can define the confidence intervals that allow to frame this error when replacing $\langle \cdot \rangle$ by $\{\cdot\}_{N_{pc}, \Delta x}$:

$$|\epsilon_{N_p}(T)| \leq 1.96 \frac{\sigma_f}{\sqrt{N_{pc}}}, \quad (1.4.37)$$

Here, σ_f in practice is not known and is replaced by its empirical value. This estimate corresponds to the 5% risk level. For example, analyzing in this way the statistical error for $\langle U_{p,x} \rangle$ in Case A, we find the following approximation of the confidence interval:

$$|\epsilon_{N_{pc,A}}| \leq 1.96 \frac{\sqrt{R_{p,xx}}}{\sqrt{N_{pc,A}}} \simeq 0.4 \text{ m/s}, \quad (1.4.38)$$

whereas the corresponding interval in Case B with $N_{pc,B} = 10 \times N_{pc,A} = 10^4$ is given by:

$$|\epsilon_{N_{pc,B}}| \leq 1.96 \frac{\sqrt{R_{p,xx}}}{\sqrt{N_{pc,B}}} \simeq 0.125 \text{ m/s}. \quad (1.4.39)$$

Actually, the statistical error is decreasing as $1/\sqrt{N_{pc}}$:

$$\frac{\max |\epsilon_{N_{pc,A}}|}{\max |\epsilon_{N_{pc,B}}|} = \sqrt{\left(\frac{N_{pc,A}}{N_{pc,B}}\right)^{-1}} = \frac{0.4}{0.125} \simeq \sqrt{10}, \quad (1.4.40)$$

that is, multiplying N_{pc} by 10 reduces the error by $\sqrt{10}$.

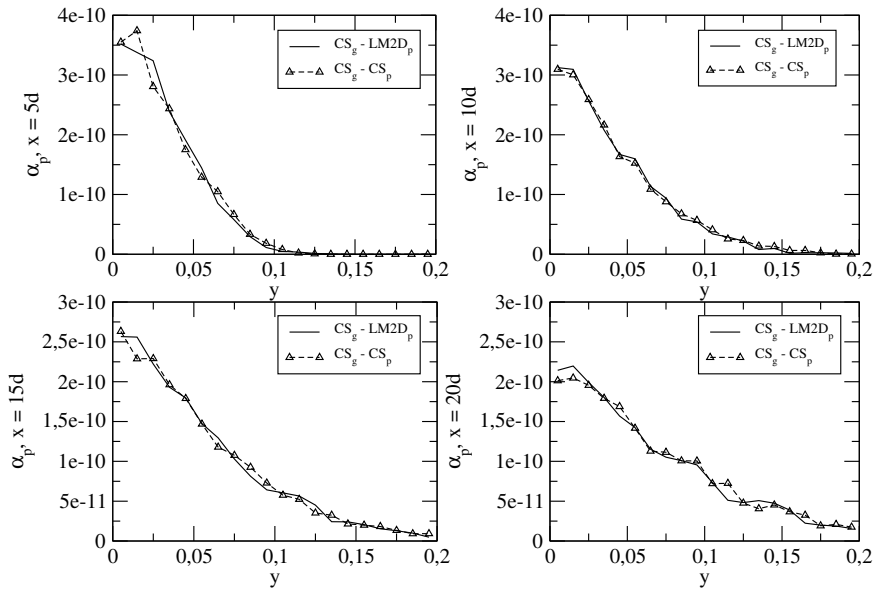


Figure 1.9: Case A: particle volumetric fraction. Numerical simulation for system (2.4.61) on the mesh of 100×20 cells with 10^3 particles per cell and $\Delta t = 10^{-3}s$: $CS_g - LM2D_p$ - approximations obtained when using *Code_Saturne* for the fluid phase and the present code for the dispersed phase, $CS_g - CS_p$ - approximations obtained when using *Code_Saturne* for both fluid and particle phases.

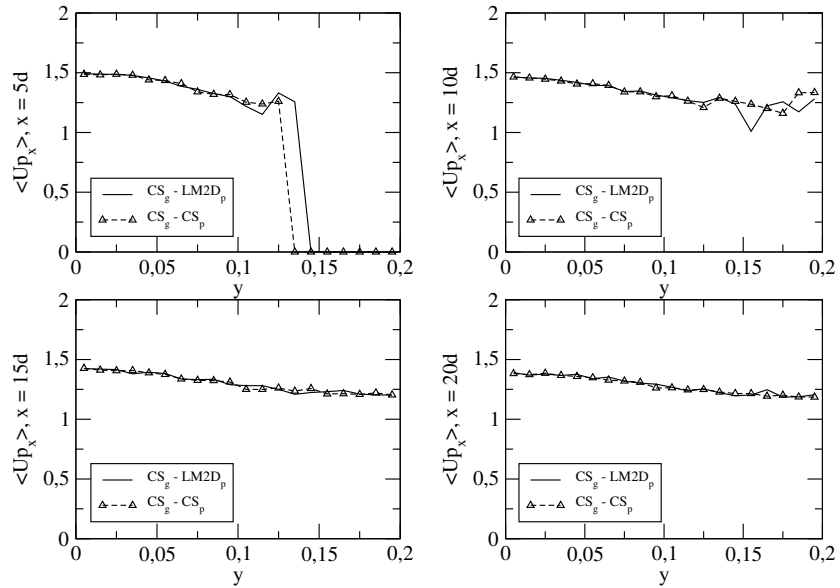


Figure 1.10: Case A: mean particle velocity in the longitudinal direction. Numerical simulation for system (2.4.61) on the mesh of 100×20 cells with 10^3 particles per cell and $\Delta t = 10^{-3}s$: $CS_g - LM2D_p$ - approximations obtained when using *Code_Saturne* for the fluid phase and the present code for the dispersed phase, $CS_g - CS_p$ - approximations obtained when using *Code_Saturne* for both fluid and particle phases.

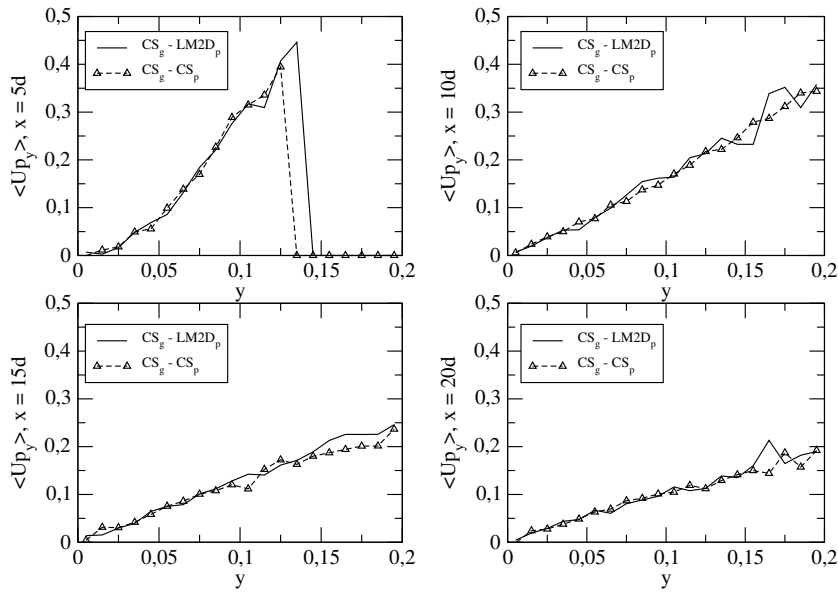


Figure 1.11: Case A: mean particle velocity in the transversal direction. Numerical simulation for system (2.4.61) on the mesh of 100×20 cells with 10^3 particles per cell and $\Delta t = 10^{-3}s$: $CS_g - LM2D_p$ - approximations obtained when using *Code-Saturne* for the fluid phase and the present code for the dispersed phase, $CS_g - CS_p$ - approximations obtained when using *Code-Saturne* for both fluid and particle phases.

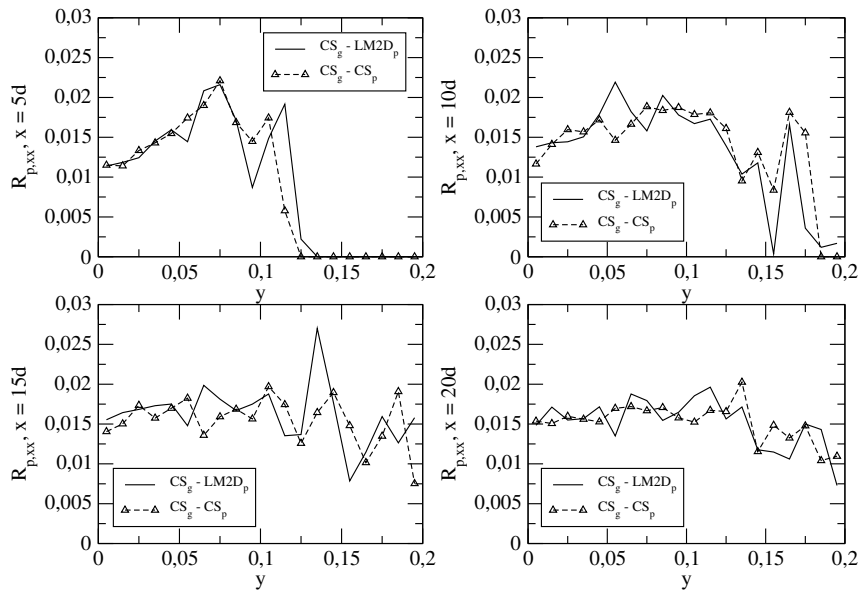


Figure 1.12: Case A: variance of the particle velocity in the longitudinal direction. Numerical simulation for system (2.4.61) on the mesh of 100×20 cells with 10^3 particles per cell and $\Delta t = 10^{-3}s$: $CS_g - LM2D_p$ - approximations obtained when using *Code-Saturne* for the fluid phase and the present code for the dispersed phase, $CS_g - CS_p$ - approximations obtained when using *Code-Saturne* for both fluid and particle phases.

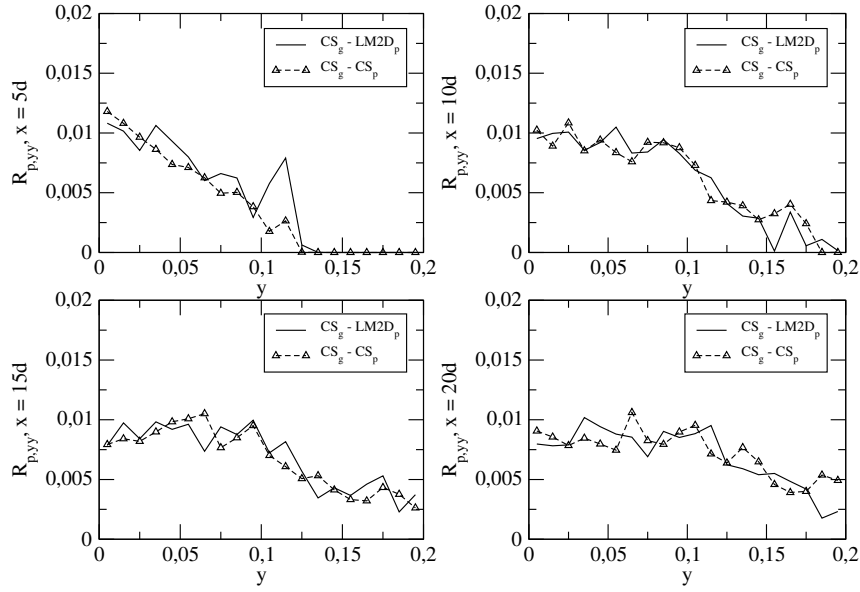


Figure 1.13: Case A: variance of the particle velocity in the transversal direction. Numerical simulation for system (2.4.61) on the mesh of 100×20 cells with 10^3 particles per cell and $\Delta t = 10^{-3}$ s: $CS_g - LM2D_p$ - approximations obtained when using *Code_Saturne* for the fluid phase and the present code for the dispersed phase, $CS_g - CS_p$ - approximations obtained when using *Code_Saturne* for both fluid and particle phases.

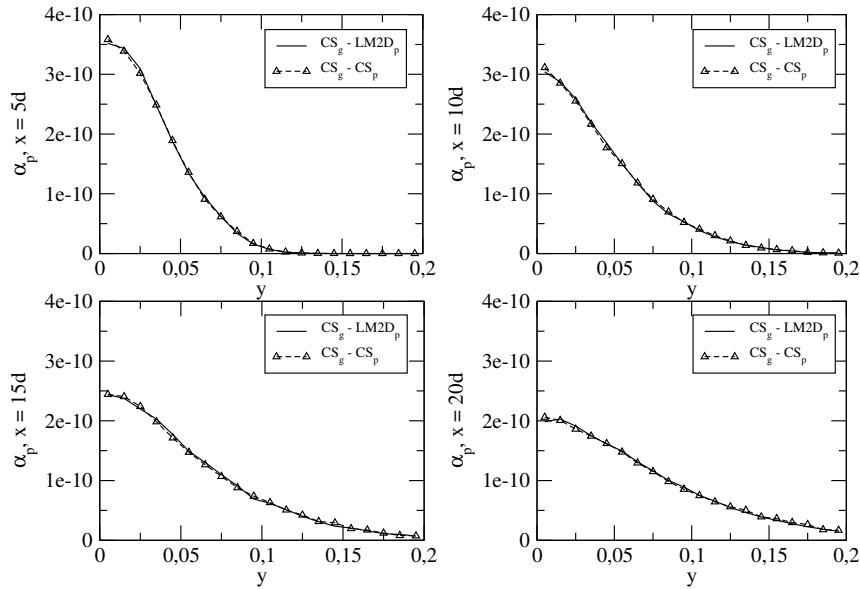


Figure 1.14: Case B: particle volumetric fraction. Numerical simulation for system (2.4.61) on the mesh of 100×20 cells with 10^4 particles per cell and $\Delta t = 10^{-3}$ s: $CS_g - LM2D_p$ - approximations obtained when using *Code_Saturne* for the fluid phase and the present code for the dispersed phase, $CS_g - CS_p$ - approximations obtained when using *Code_Saturne* for both fluid and particle phases.

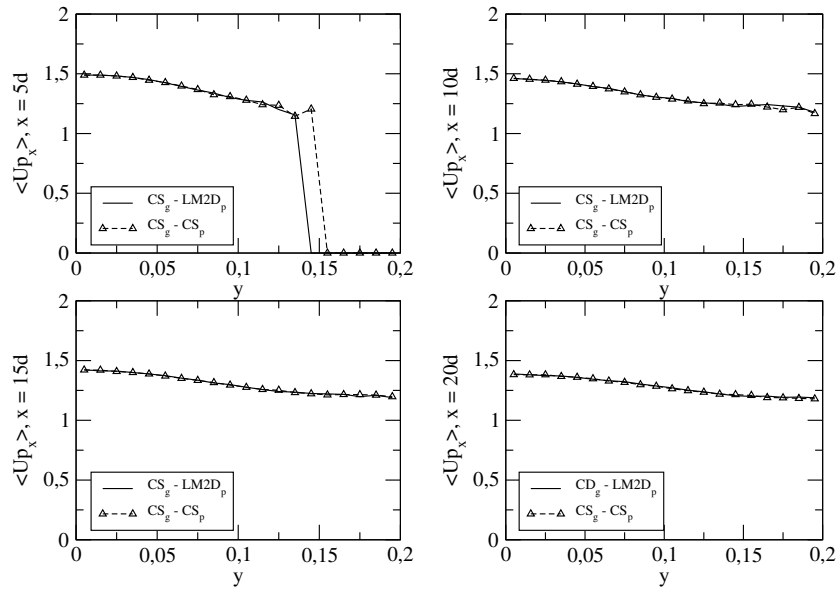


Figure 1.15: Case B: mean particle velocity in the longitudinal direction. Numerical simulation for system (2.4.61) on the mesh of 100×20 cells with 10^4 particles per cell and $\Delta t = 10^{-3}$ s: $CS_g - LM2D_p$ - approximations obtained when using *Code_Saturne* for the fluid phase and the present code for the dispersed phase, $CS_g - CS_p$ - approximations obtained when using *Code_Saturne* for both fluid and particle phases.

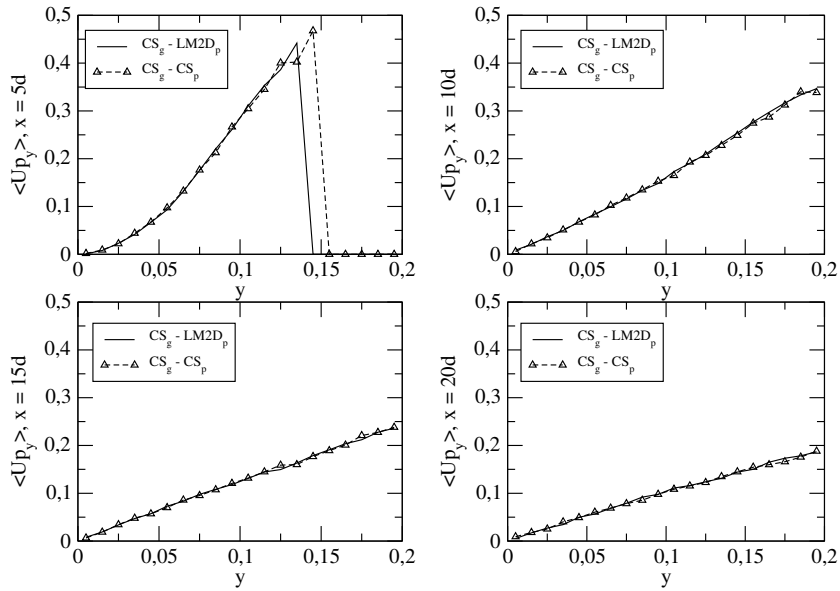


Figure 1.16: Case B: mean particle velocity in the transversal direction. Numerical simulation for system (2.4.61) on the mesh of 100×20 cells with 10^4 particles per cell and $\Delta t = 10^{-3}$ s: $CS_g - LM2D_p$ - approximations obtained when using *Code_Saturne* for the fluid phase and the present code for the dispersed phase, $CS_g - CS_p$ - approximations obtained when using *Code_Saturne* for both fluid and particle phases.

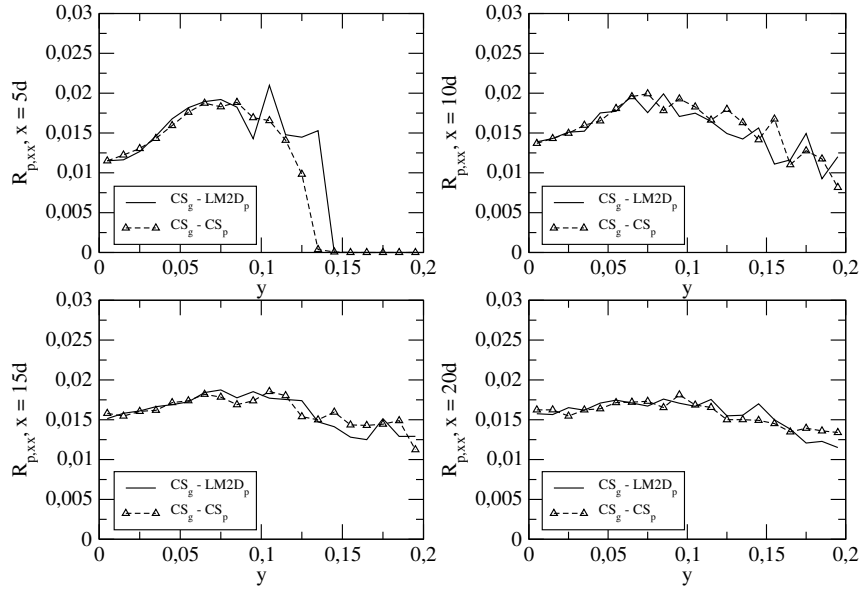


Figure 1.17: Case B: variance of the particle velocity in the longitudinal direction. Numerical simulation for system (2.4.61) on the mesh of 100×20 cells with 10^4 particles per cell and $\Delta t = 10^{-3}$ s: $CS_g - LM2D_p$ - approximations obtained when using *Code_Saturne* for the fluid phase and the present code for the dispersed phase, $CS_g - CS_p$ - approximations obtained when using *Code_Saturne* for both fluid and particle phases.

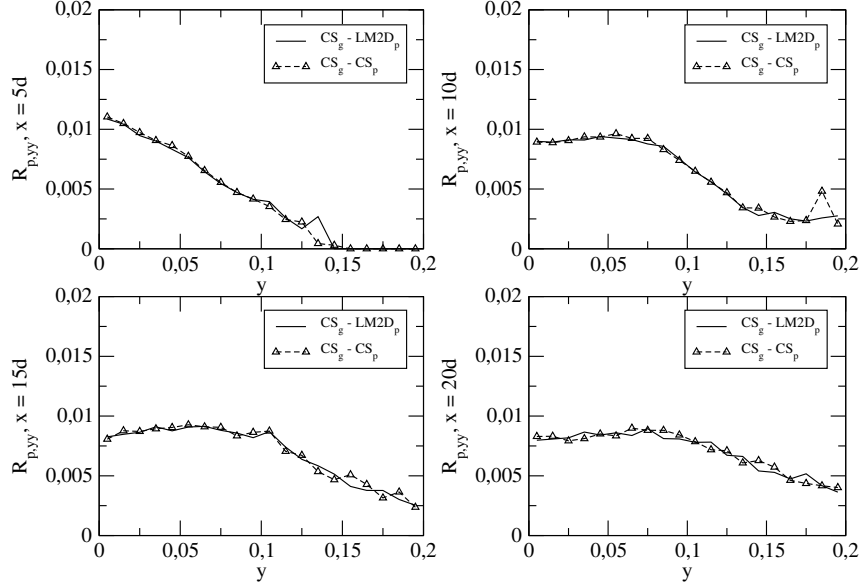


Figure 1.18: Case B: variance of the particle velocity in the transversal direction. Numerical simulation for system (2.4.61) on the mesh of 100×20 cells with 10^4 particles per cell and $\Delta t = 10^{-3}$ s: $CS_g - LM2D_p$ - approximations obtained when using *Code_Saturne* for the fluid phase and the present code for the dispersed phase, $CS_g - CS_p$ - approximations obtained when using *Code_Saturne* for both fluid and particle phases.

1.5 An extension of the Moments/PDF representation

The Moments/PDF approach presented and implemented in the previous sections (Fig. 1.1) is a classical way to describe polydispersed turbulent two-phase flows in non-equilibrium. It allows to obtain a high level of physical description and, in particular, to treat correctly polydispersity, convection and local nonlinear source terms. Moreover, all one-particle statistical moments are available. In this method, the mean fields related to the fluid phase are computed via an Eulerian approach, as solutions of partial differential equations (PDE_g^{Eul}) on a mesh, whereas particle properties evolve within a Lagrangian framework according to a system of stochastic differential equations (SDE_p^{Lag}) from which the particle mean fields are extracted. However, some features of this method and, in particular, the stochastic model of the particle dispersion, which takes into account the crossing-trajectory effect and related mean drift, result in the following limitations during the numerical implementation:

- The modeled PDF equation to be solved is nonlinear since some mean particle quantities computed using the pdf are involved in the coefficients. In this case, the uniqueness of the solution is difficult to establish.
- The use of mean particle fields in the particle equations induces an important distinction between different PDF solution algorithms [32, 37, 42]. For instance, the use of the mean particle velocity in the particle equations (1.3.5) has been found to lead to a deterministic error called *bias* [47, 48]. This error is generated when a mean value containing non-null statistical error (which is caused by the number of particles per cell N_{pc} being finite) is introduced in the coefficients of the SDEs. In this case, the nonlinear dependence on N_{pc} results in a bias, which scales as N_{pc}^{-1} and appears to be one of the dominant errors in the self-contained particle methods [47].
- The approximations obtained using a direct Monte-Carlo simulation are affected by a *statistical error* and an attempt to reduce the variance can result in high computational costs, which are related to the small rate of convergence of Monte-Carlo methods and are even more important in unsteady situations.

In order to overcome these difficulties, an alternative approach to the simulation of the solutions of the pdf equations has been proposed recently [3], based on a new coupling strategy. The underlying idea consists in solving simultaneously the Lagrangian stochastic equations and the Eulerian deterministic equations for some mean particle quantities, corresponding to the same PDF equation. Both systems are coupled in a way to allow some numerical improvements with reference to classical Moments/PDF method. For instance, the variables which are biased in the classical Moments/PDF method, will be computed by an Eulerian approach (thus become unbiased) and provided to the Lagrangian stochastic method. First, this method should reduce the number of particles needed for a given precision, and in this case, would play a role of a Variance Reduction Technique (VRT). Since we are not dealing any more with a McKean pdf equation but now with a linear pdf equation, this method moreover allows to reduce the bias of the approximations. Analogous ideas have been followed for the case of turbulent combustion [27] and later, for the numerical solution of the Boltzmann equation [5].

The hybrid approach developed in the present work follows the description proposed in [3]. In the Eulerian part of the particle model, two state variables are retained from the Lagrangian state vector $\mathbf{Z}(t) = (\mathbf{x}_p, \mathbf{U}_p, \mathbf{U}_s)$, the particle volumetric fraction $\alpha_p(t, \mathbf{x})$ and the mean particle velocity $\langle \mathbf{U}_p \rangle(t, \mathbf{x})$. The exact equations for these variables can be extracted from the exact instantaneous equations (1.2.34) or, in a closed form, from the modeled PDF equation (1.2.44). The latter way to construct the Eulerian mean equations ensures the consistency with the Lagrangian stochastic model (1.3.5).

The moments equations corresponding to the PDF model are :

$$\begin{aligned} \frac{\partial \alpha_p^E \rho_p}{\partial t} + \frac{\partial}{\partial x_i} (\alpha_p^E \rho_p \langle U_{p,i}^E \rangle) &= 0, \quad i, j \in \mathbb{Z}, \\ \frac{\partial \alpha_p^E \rho_p \langle U_{p,i}^E \rangle}{\partial t} + \frac{\partial}{\partial x_j} (\alpha_p^E \rho_p (\langle U_{p,i}^E \rangle \langle U_{p,j}^E \rangle + \langle u_{p,i} u_{p,j} \rangle)) &= \alpha_p^E \rho_p g_i + \left\langle \frac{\alpha_p^E \rho_p U_{r,i}}{\tau_p} \right\rangle, \end{aligned} \quad (1.5.1)$$

where the superscript “ E “ refers to the particle properties computed with the Eulerian approach and ρ_p is the constant particle density. The right-hand-side terms account for the gravity and the drag forces. Once the particle mean velocity has been computed, it can be used as a not-biased averaged quantity in the set of SDEs (1.3.5). The Lagrangian equations (SDE_p^{Lag}), in turn, will provide the Eulerian part of the particle model (PDE_p^{Eul}) with the particle kinetic tensor $\mathbf{R}_p = \langle \mathbf{u}_p \mathbf{u}_p \rangle$ and possibly with local nonlinear source terms, enabling physically meaningful closures in the Eulerian equations. The sketch of the new coupling algorithm presented in Fig. 1.19 can be compared with the one used in the classical Moments/PDF method, Fig. 1.1.

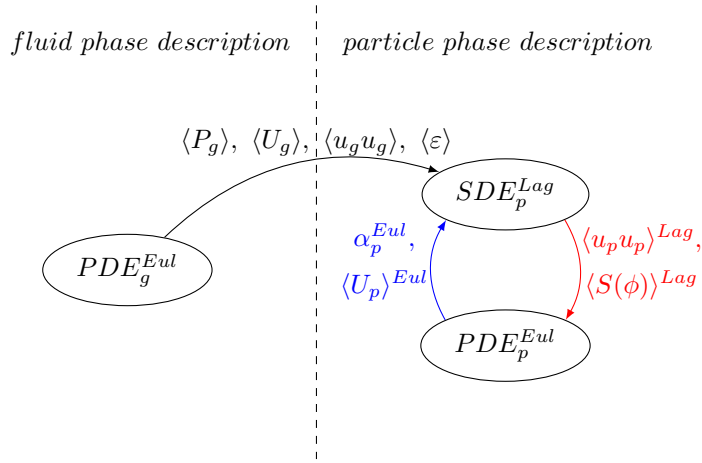


Figure 1.19: An extension of the classical representation - a hybrid Moments/Moments-PDF description.

From now on, the governing equations describing turbulent gas-particle flows can be summarized. Following the notations given in the previous sections, the **Eulerian description of the turbulent gas phase** corresponding to $R_{ij} - \varepsilon$ model with gas volumetric fraction $\alpha_g \approx 1$ is given by the system of partial differential equations PDE_g^{Eul} :

$$\begin{aligned}
 \frac{\partial \langle U_{g,i} \rangle}{\partial x_i} &= 0 \\
 \frac{\partial \langle U_{g,i} \rangle}{\partial t} + \langle U_{g,j} \rangle \frac{\partial \langle U_{g,i} \rangle}{\partial x_j} + \frac{\partial \langle u_{g,i} u_{g,j} \rangle}{\partial x_j} &= -\frac{1}{\rho_f} \frac{\partial \langle P_g \rangle}{\partial x_i} \\
 \frac{\partial \langle u_{g,i} u_{g,j} \rangle}{\partial t} + \langle U_{g,k} \rangle \frac{\partial \langle u_{g,i} u_{g,j} \rangle}{\partial x_k} + \frac{\partial \langle u_{g,i} u_{g,j} u_{g,k} \rangle}{\partial x_k} &+ \langle u_{g,i} u_{g,k} \rangle \frac{\partial \langle U_{g,j} \rangle}{\partial x_k} + \langle u_{g,j} u_{g,k} \rangle \frac{\partial \langle U_{g,i} \rangle}{\partial x_k} \\
 &= G_{ik} \langle u_{g,j} u_{g,k} \rangle + G_{jk} \langle u_{g,i} u_{g,k} \rangle + C_0 \langle \varepsilon \rangle \delta_{ij},
 \end{aligned} \tag{1.5.2}$$

with $G_{ij} = -\left(\frac{1}{2} + \frac{3}{4}C_0\right) \frac{\langle \varepsilon \rangle}{k} \delta_{ij} + G_{ij}^a$ and with the corresponding equation for the mean dissipation rate of turbulent energy:

$$\frac{\partial \langle \varepsilon \rangle}{\partial t} + \frac{\partial}{\partial x_i} (\langle U_{g,i} \rangle \langle \varepsilon \rangle) = d + C_{\varepsilon_1} \mathcal{P} \frac{\langle \varepsilon \rangle}{k} - C_{\varepsilon_2} \frac{\langle \varepsilon \rangle^2}{k}, \tag{1.5.3}$$

where if we denote by $R_{g,ij} = \langle u_{g,i} u_{g,j} \rangle$, $i, j \in \mathbb{Z}$ the Reynolds stress tensor, then

$$d = C_{\varepsilon} \frac{\partial}{\partial x_k} \left(\frac{k}{\langle \varepsilon \rangle} R_{g,ik} \frac{\partial \langle \varepsilon \rangle}{\partial x_i} \right), \tag{1.5.4}$$

$$\mathcal{P} = - \left(R_{g,ik} \frac{\partial \langle U_{g,i} \rangle}{\partial x_k} \right), \tag{1.5.5}$$

and C_{ε} , C_{ε_1} , C_{ε_2} are constants of the model [31, 35].

The particle phase description is given by a coupled Moments/PDF representation:

- **Lagrangian description of the particle phase.** Stochastic differential equations SDE_p^{Lag} :

$$\begin{aligned}
 dx_{p,i} &= U_{p,i} dt, \\
 d\mathbf{U}_{p,i} &= \frac{1}{\tau_p} (U_{s,i} - U_{p,i}) dt + g_i dt, \\
 dU_{s,i} &= -\frac{1}{\rho_g} \frac{\partial \langle P_g \rangle}{\partial x_i} dt + (\langle \mathbf{U}_{p,i}^E \rangle - \langle U_{g,j} \rangle) \frac{\partial \langle U_{g,i} \rangle}{\partial x_j} dt - \frac{(U_{s,i} - \langle U_{g,i} \rangle)}{\mathbf{T}_{L,i}^{E*}} dt + \\
 &\quad \sqrt{\langle \varepsilon \rangle \left(C_0 b_i \tilde{k}/k + \frac{2}{3} (b_i \tilde{k}/k - 1) \right)} dW_{t,i},
 \end{aligned} \tag{1.5.6}$$

where the superscript “ E “ indicates the terms provided by the Eulerian particle solver.

- **Eulerian description of the particle phase.** Mass and momentum conservation equations deduced from (1.5.6) for particle statistical quantities, PDE_p^{Eul} :

$$\begin{aligned}
 \frac{\partial \alpha_p^E \rho_p}{\partial t} + \frac{\partial}{\partial x_i} (\alpha_p^E \rho_p \langle U_{p,i}^E \rangle) &= 0, \\
 \frac{\partial \alpha_p^E \rho_p \langle \mathbf{U}_{p,i}^E \rangle}{\partial t} + \frac{\partial}{\partial x_j} (\alpha_p^E \rho_p (\langle U_{p,i}^E \rangle \langle U_{p,j}^E \rangle + \langle \mathbf{u}_{p,i} \mathbf{u}_{p,j} \rangle^L)) &= \alpha_p^E \rho_p g_i + \left\langle \frac{\alpha_p^E \rho_p \mathbf{U}_{r,i}^L}{\tau_p^L} \right\rangle,
 \end{aligned} \tag{1.5.7}$$

where the variables computed by the Lagrangian solver are denoted with the script ” L “.

For this description, the equivalence of duplicate fields must be verified:

$$\alpha_p^L(t, \mathbf{x}) = \alpha_p^E(t, \mathbf{x}), \quad \langle \mathbf{U}_p \rangle^L(t, \mathbf{x}) = \langle \mathbf{U}_p \rangle^E(t, \mathbf{x}). \quad (1.5.8)$$

Since the mean velocity $\langle \mathbf{U}_p \rangle$ is now provided to the Lagrangian stochastic method by the Eulerian moments method, it becomes an external variable and, therefore, the pdf equation is no longer a McKean equation and becomes a classical Fokker-Planck one. It is important to emphasize that the Eulerian approximations in this case contain some statistical error provided to the system with the Lagrangian kinetic tensor $\langle u_p u_p \rangle^L$. Thus, the bias may still be present, but it should be substantially diminished.

Another point worth noting is that, in the new method, a set of PDEs is added to the set of SDEs with respect to the classical Moments/PDF formulation. However, by reducing the bias error, the number of particles required for a given accuracy should be diminished and thus, the global computational efficiency should be improved.

Apart from its interesting features, this coupling technique raises several difficult issues related to the numerical implementation. The purpose of this work is therefore to address the following algorithmic and numerical questions associated with the present hybrid method:

- The feasibility of the hybrid approach. It has been found that the use in the Eulerian moments equations of noisy particle quantities provided by the Lagrangian particle solver causes important *instabilities and convergence problems* in Finite Volume methods [2, 5, 27]. These issues will be addressed in Chapter 2 in 1D framework and in Chapter 3 in two space dimensions.
- Monte-Carlo convergence of the Lagrangian approximations in coupled computations and the influence of the new coupling strategy on *the statistical and the bias errors* (Chapter 4).
- Consistency of duplicate fields. In fact, since the particle volumetric fraction $\alpha_p(t, \mathbf{x})$ and the mean particle velocity $\langle \mathbf{U}_p \rangle(t, \mathbf{x})$ are computed by both, Eulerian and Lagrangian, parts of the hybrid method, they can be defined as "duplicate fields". The global method is said to be consistent if and only if the duplicate fields computed from the two different descriptions are *consistent, within the numerical errors*.

Eventually, in the present work both spatial and temporal discretizations related to the Lagrangian and Eulerian parts of the method are assumed to coincide.

1.6 Conclusion

In the present chapter, a *Moments/PDF approach* to simulation of polydispersed turbulent two-phase flows has been presented. It consists in an Eulerian/Lagrangian coupled description, where the fluid phase is modeled by mean moments (RANS) equations and is solved in the Eulerian framework, whereas the particle related statistics are obtained by solving numerically the PDF equation from the Lagrangian stochastic point of view. This is an example of a hybrid model,

since the two descriptions have different information content: for the fluid phase we compute a limited number of statistical moments on a mesh whereas for the description of the dispersed phase we simulate the pdf function, from which all moments that can be derived. However, both descriptions, of fluid and particle phases, are consistent in the particle-tracer limit: the fluid moments equations can be derived from the particle stochastic equations when the discrete particle inertia goes to zero as a continuous function of time.

It is important to recall that the terms “Eulerian” and “Lagrangian” refer to the adopted point of view and not to the kind of model: for example, the PDF equation could also be solved using a mesh and an Eulerian description in phase space. Thus, the numerical treatment of such models can be referred to as hybrid Finite-Volume/Monte-Carlo simulations or, in terms of discrete variables, as Mesh/Particle methods. In the framework of this coupling algorithm, attention is mainly focused on the particle statistics computed with the dynamic Monte-Carlo method from the system of stochastic differential equations (1.2.38). The first-order Euler numerical scheme proposed in [24] was implemented in order to compute the approximations of the solution to this - highly nonlinear - system of SDEs, where the multiscale character of the particle related stochastic model plays a crucial role. The numerical verification of the present implementation is made by comparison with analytical results and with the approximations obtained by *Code_Saturne* in the same configurations.

The pdf method used for the particle phase description is well suited for the treatment of the polydispersity in particle properties or for the non-equilibrium situations, where it allows to capture the small-scale phenomena. Yet, it suffers from two main drawbacks: the occurrence of a possible bias error that is due to the number of statistical particles per cell being finite and to the choice of averaging/projection operators; relatively high computational costs required to reduce the statistical error. These issues are the main object of further developments. In particular, a *new hybrid method* trying to go further into a mixed Moments/PDF approach within the description of the particle phase itself has been proposed in [3]. It consists in computing some particle statistics by a Moments method so that they are not biased by construction. Providing these statistics to the stochastic model plays the role of a Variance Reduction Technique (VRT). Yet, the consistency of the different particle phase descriptions needs to be ensured. Actually, this approach is of the main concern in the present work and will be detailed further.

One can find in [23], [30] a broad discussion on possible extensions of the present Moments/PDF method to more complex problems of particle-particle interactions, bubbly flows, combustion, ..., together with propositions on other types of coupling (i.e. particle-based LES methods).

Bibliography

- [1] Archambeau, F., Mechitoua, N., Sakiz, M.: Code_Saturne: a Finite Volume Code for the Computation of Turbulent Incompressible Flows à Industrial Applications. International Journal on Finite Volumes (2004)
- [2] Chang, G.C.: A Monte-Carlo PDF/Finite-Volume study of turbulent flames. PhD thesis, Cornell University (1996)
- [3] Chibbaro, S., Hérard, J.M., Minier, J.P.: A novel Hybrid Moments/Moments-PDF method for turbulent two-phase flows. Final Technical Report Activity Marie Curie Project. TOK project Lange Contract MTKD-CT-2004 509849 (2006)
- [4] Clift, R., Grace, J.R., Weber, M.E.: Bubbles, Drops and Particles. Academic Press, New York (1978)
- [5] Degond, P., Dimarco, G., Pareschi, L.: The moment-guided Monte Carlo method. Int. J. for Numerical Methods in Fluids, **67** (2) 189–213 (2011)
- [6] Derevich, I., Zaichik, L.: Precipitation of particles from a turbulent flow. Mekhanika Zhidkosti i Gaza, **5** 96–104 (1988)
- [7] Dorogan, K., Hérard, J.M., Minier, J.P.: Development of a new scheme for hybrid modelling of gas-particle two-phase flows. EDF report H-I81-2010-2352-EN, unpublished, 1–50 (2010)
- [8] Dorogan, K., Guingo, M., Hérard, J.M., Minier, J.P.: A relaxation scheme for hybrid modelling of gas-particle flows. Accepted for publication in Computers and Fluids (2012)
- [9] Dorogan, K., Hérard, J.M., Minier, J.P.: A two-dimensional relaxation scheme for the hybrid modelling of two phase flows. International Conference Finite Volumes for Complex Applications 6, Prague, 6-10 juin 2011. Published in proceedings “Finite Volumes for Complex Applications. Problems and Perspectives”, Springer-Verlag (2011).
- [10] Dreeben, T.D., Pope, S.B.: Probability density function/Monte-Carlo simulation of near-wall turbulent flows. J. Fluid Mech. 357:141-66 (1998)
- [11] E, W., Liu, D., Vanden-Eijnden, E.: Analysis of multiscale methods for stochastic differential equations. Communications on Pure and Applied Mathematics, John Wiley & Sons, Inc. (2003)

- [12] Gard, T.C.: *Introduction to Stochastic Differential Equations*. Marcel Dekker, New York Basel (Monographs and Textbooks in Pure and Applied Mathematics, **114**) (1988)
- [13] Gardiner, C.W.: *Handbook of stochastic methods for physics, chemistry and natural sciences*. Springer, Berlin (1990)
- [14] Gatignol, R.: The Fax n formulae for a rigid particle in an unsteady non-uniform Stokes flow. *J. Mec. Th or. Appl.*, **1(2)**, 143–160 (1983)
- [15] Golse, F., Saint-Raymond, L.: The incompressible Navier-Stokes limit of the Boltzmann equation for hard cutoff potentials. *J. Math. Pure Appl.*, **91**, 508–552 (2009)
- [16] H rard, J.M.: A relaxation tool to compute hybrid Euler-Lagrange compressible models. AIAA paper 2006-2872 (2006) <http://aiaa.org>
- [17] H rard, J.M., Minier, J.P., Chibbaro, S.: A Finite Volume scheme for hybrid turbulent two-phase flow models. AIAA paper 2007-4587, <http://aiaa.org>
- [18] H rard, J.M., Uhlmann, M., Van der Velden, D.: Numerical techniques for solving hybrid Eulerian Lagrangian models for particulate flows. EDF report H-I81-2009-3961-EN (2009)
- [19] Hockney, R.W., Eastwood, J.W.: *Computer simulation using particles*. Adam Hilger, New York (1988)
- [20] Kloeden, P.E., Platen, E.: *Numerical solution of stochastic differential equations*. Springer-Verlag, Berlin (1992)
- [21] La n, S., Grillo, C.A.: Comparison of turbulent particle dispersion models in turbulent shear flows. *Brazilian Journal of Chemical Engineering*, **24 (3)**, 351–363 (2007)
- [22] McKean, H.P.: Lecture Series in Differential Equations 7. Catholic University, Washington D.C. **41** (1967)
- [23] Minier, J.P., Peirano, E.: The pdf approach to polydispersed turbulent two-phase flows. *Physics reports*, **352**, 1–214 (2001)
- [24] Minier, J.P., Peirano, E., Chibbaro, S.: Weak first- and second-order numerical schemes for stochastic differential equations appearing in Lagrangian two-phase flow modelling. *Monte Carlo Methods and Appl.*, **9**, 93–133 (2003)
- [25] Minier, J.P., Pozorski, J.: Wall-boundary conditions in probability density function methods and application to a turbulent channel flow. *Physics of Fluids*, **11**, 2632–2644 (1999)
- [26] Minier, J.P., Pozorski, J.: Derivation of a pdf model for turbulent flows based on principles from statistical physics. *Physics of Fluids*, **9**, 1748–1753 (1997)
- [27] Muradoglu, M., Jenny, P., Pope, S.B., Caughey, D.A.: A consistent hybrid finite-volume/particle method for the pdf equations of turbulent reactive flows. *J. Comp. Phys.*, **154**, 342–371 (1999)

- [28] Øksendal, B.: Stochastic differential equations. An introduction with applications. Springer, Berlin (1995)
- [29] Öttinger, HC.: Stochastic processes in polymeric fluids. Tools and examples for developing simulation algorithms. Springer, Berlin (1996)
- [30] Peirano, E., Chibbaro, S., Pozorski, J., Minier, J.P.: Mean-field/PDF numerical approach for polydispersed turbulent two-phase flows. *Prog. Ene. Comb. Sci.*, **32**, 315–371 (2006)
- [31] Pope, S.B.: Turbulent flows. Cambridge University Press, Cambridge (2000)
- [32] Pope, S.B.: PDF methods for turbulent reactive flows. *Prog. Energy Combust. Sci.*, **11**, 119–92 (1985)
- [33] Pope, S.B.: Application of the velocity-dissipation probability density function model to inhomogeneous turbulent flows. *Phys. Fluids A*, **3**, 1947 (1991)
- [34] Pope, S.B.: Particle method for turbulent flows: integration of stochastic model equations. *J. Comput. Phys.*, 117:332–49 (1995)
- [35] Pope, S.B., Chen, Y.L.: The velocity-dissipation probability density function model for turbulent flows. *Phys. Fluids A*, **2**, 1437 (1990)
- [36] Pope, S.B.: On the relationship between stochastic Lagrangian models of turbulence and second moment closures. *Phys. Fluids* **6**, 973–985 (1994)
- [37] Pope, S.B.: Lagrangian PDF methods for turbulent flows. *Annu. Rev. Fluid Mech.*, 23–63 (1994)
- [38] Pope, S.B.: Mean Field Equations in PDF Particle Methods for Turbulent Reactive Flows, Technical Report FDA 97-06. Cornell University (1997)
- [39] Pozorski, J., Minier, J.P.: On the Lagrangian turbulent dispersion models based on the Langevin equation. *International Journal of Multiphase Flow*, **24**, 913–945 (1998)
- [40] Reeks, M.W.: On a kinetic equation for the transport of particles in turbulent flows. *Phys. Fluids A*, **3**, 446–456 (1991)
- [41] Simonin, O.: Prediction of the dispersed phase turbulence in particle-laden jets. In: Gas-Solid Flows 1991, ASME FED 121, 197–206 (1991)
- [42] Simonin, O., Deutsch, E., Minier, J.P.: Eulerian prediction of the fluid/particle correlated motion in turbulent two-phase flows. *Appl. Sci. Res.*, 51:275–83 (1993)
- [43] Simonin, O.: Combustion and turbulence in two-phase flows. Von Karman Institute for Fluid Dynamics, Lecture Series (1996)
- [44] Sommerfeld, M., Kohnen, G., Rüger, M.: Some open questions and inconsistencies of Lagrangian particle dispersion models. In: Proceedings of the Ninth Symposium on Turbulent Shear Flows, Kyoto, Paper 15.1, (1993)

- [45] Sommerfeld, M.: Modeling and calculation of turbulent gas-solid flows with the Euler/Lagrange approach. *KONA (Powder and Particles)*, **16**, 194–206 (1999)
- [46] Talay, D.: in Kree, P., Wedig, W, editors. *Simulation of stochastic differential equations, in probabilistic methods in applied physics*. Springer, Berlin (1995)
- [47] Xu, J., Pope, S.B.: Source of Bias in Particle-Mesh Methods for PDF Models for Turbulent Flows, Technical Report FDA 97-06. Cornell University (1997)
- [48] Xu, J., Pope, S.B.: Assessment of numerical accuracy of PDF/Monte-Carlo methods for turbulent reacting flows. *J. Comput. Phys.*, 152–192 (1999)

Chapter 2

A one-dimensional relaxation scheme for the hybrid modeling of gas-particle flows

Introduction

Dans ce chapitre on s'intéresse à la simulation numérique de la phase dispersée par une approche Eulerienne, qui décrit l'évolution des moments statistiques du premier ordre par un système d'équations aux dérivées partielles. Cette description est déduite des équations différentielles stochastiques (1.2.38) via le formalisme du calcul stochastique. Le choix du vecteur d'état Eulerien est d'une grande importance pour le couplage des descriptions. La seule donnée statistique associée à la phase dispersée qui est utilisée dans (1.2.38) étant la vitesse moyenne des particules, $\langle \mathbf{U}_p \rangle$, on considérera le modèle, ayant pour variable d'état la densité moyenne $\rho = \rho_p \langle \alpha_p \rangle(t, \mathbf{x})$ et la vitesse moyenne $\mathbf{U} = \langle \mathbf{U}_p \rangle(t, \mathbf{x}) \in \mathbb{R}^d$ des particules. Dans l'espace d -dimensionnel, ce modèle s'écrit

$$\begin{cases} \partial_t \rho + \partial_{x_j} (\rho U_j) = 0, & t > 0, \quad \mathbf{x} \in \mathbb{R}^d, \\ \partial_t (\rho U_i) + \partial_{x_j} (\rho U_i U_j) + \partial_{x_j} (\rho R_{ij}^L) = \rho g_i + \rho \langle U_{r,i}^L / \tau_p^U \rangle, \end{cases} \quad (2.0.1)$$

où l'exposant “ L ” désigne les variables calculées via la description Lagrangienne, qui représentent les *données extérieures bruitées*: $R_{ij}^L = \langle u'_i u'_j \rangle^L$, $i, j = 1, \dots, d$ est le tenseur cinétique particulaire avec $\mathbf{u}'(t, \mathbf{x}) \in \mathbb{R}^d$ la vitesse fluctuante des particules provenant de la décomposition de Reynolds de la vitesse instantanée; les termes sources dans la deuxième équation de (2.0.1) décrivent les forces de gravité et de traînée exercées sur les particules, où $\mathbf{U}_r^L(t, \mathbf{x})$ désigne la vitesse relative entre le fluide et la particule et τ_p^U le temps nécessaire à la particule pour s'adapter à la vitesse du fluide.

L'objectif principal consiste à développer une méthode numérique permettant d'obtenir les approx-

imations stables des solutions de (2.0.1), et qui serait adaptée aux taux de présence des particules très faibles (situations d'apparition du “vide”). Dans ce cadre d'études, une première approche numérique basée sur l'association des techniques de relaxation et de schémas de décentrement, appelée A1, a été proposée dans [10, 26, 27]. Elle consiste à rajouter une équation de transport du tenseur cinétique dans le système original (2.0.1) d'abord, pour permettre de prendre en compte toutes les ondes acoustiques présentes quand R^L est une variable interne, mais aussi pour pouvoir décentrer correctement le tenseur de Reynolds et les termes convectifs. Dans cette approche, l'équation de ρR est déduite naturellement à partir de l'équation d'évolution du tenseur cinétique dans le modèle R_{ij} en *une dimension d'espace* et en formulation Eulerienne. En effet, dans ce cas particulier on a $R_{ij} = \frac{1}{d} \operatorname{tr}(R) \delta_{ij}$, $d = 1$. Bien que le sursystème introduit contienne des *champs vraiment non-linéaires* (VNL) actifs dans les produits *non-conservatifs*, il permet d'obtenir des approximations stables du système (2.0.1). Néanmoins, les relations de saut approchées qui doivent être introduites pour les champs VNL sont susceptibles d'empêcher la convergence vers les bonnes solutions choc du système (2.0.1).

Ce constat a motivé une nouvelle approche de relaxation, A2, où le sursystème est hyperbolique mais ne contient pas de champs VNL. Pour ce système, les relations de saut sont définies de façon unique. En plus de ces propriétés, pour préserver la ressemblance avec la méthode A1 dite “naturelle”, on introduit le sursystème suivant:

$$\begin{cases} \partial_t \rho + \partial_x(\rho U) = 0, & t > 0, \quad x \in \mathbb{R}, \\ \partial_t(\rho U) + \partial_x(\rho U^2) + \partial_x(\rho R) = \rho g_i + \rho \langle U_{r,i}^L / \tau_p^U \rangle, \\ \partial_t(\rho R) + U \partial_x(\rho R) + \Psi \partial_x U = \rho(R^L - R) / \tau_p^R, \end{cases} \quad (2.0.2)$$

où τ_p^R est le petit paramètre de relaxation qui garantit la consistance avec le système original (2.0.1) dans la limite $\tau_p \rightarrow 0$, et où la fonction $\Psi = a_0^2 \vartheta$ avec une constante $a_0 = \sqrt{3R_0 \rho_0^2}$ permet d'obtenir les propriétés recherchées.

Concernant l'approximation numérique du système (2.0.2), on se base sur une technique de splitting d'opérateur, découpant les effets convectifs des différents termes sources (termes de relaxation, gravité et traînée). La partie convective est approchée par une méthode de Volumes Finis basée sur le schéma de Godunov. A la fin de chaque pas de temps, une fois les approximations $(\rho, \rho U)^{n+1}$ calculées, les vraies valeurs de R^L fournies par le modèle Lagrangien sont restaurées via le terme de relaxation instantanée ($\tau_p \rightarrow 0$). Sous la condition CFL et une condition de stabilité de type Whitham, cet algorithme garantit la positivité de la densité discrète.

On présente ensuite plusieurs cas tests de validation de cette méthode et de comparaison avec l'approche précédente (A1) [27]. Pour cela, on se place dans le cadre particulier qui correspond aux équations d'Euler barotropes de la dynamique des gaz où les solutions analytiques sont connues lorsque l'on choisit: $\rho R^L = \pi(\rho)$. On étudie notamment leur comportement dans quelques situations critiques: les doubles chocs très forts avec de grandes vitesses $|U| \simeq 10^4$, qui permettent d'évaluer la stabilité de la méthode; les ondes de détente supersoniques avec apparition du vide, ainsi que les ondes de détente supersoniques avec un rapport de pression allant jusqu'à $P_L/P_R \simeq 10^{21}$. De telles situations extrêmes ne sont pas faciles à traiter, mais peuvent survenir

dans les écoulements réels de type gaz-particules (par exemple, dans les configurations où un interface sépare les domaines aux taux de présence faible et élevé). Dans tous les cas tests, les deux approches A1 et A2 ont été comparées en termes de convergence, stabilité et précision et validées par les solutions analytiques. Les mesures de l'erreur de discréétisation en norme L^1 montrent que les taux de convergence sont corrects: on retrouve une convergence à la vitesse h^1 pour le système (2.0.1) comportant deux champs vraiment non-linéaires et aucun champ linéairement dégénéré (h est le pas de discréétisation d'espace). Dans l'ensemble, on peut noter que les deux schémas assurent la bonne convergence des approximations, même dans le cas des ondes de chocs, et peuvent traiter l'apparition du “vide” caractéristique pour les écoulements très dilués en particules. On remarque également que le schéma A2 est en mesure de traiter des ondes de choc plus fortes, pour lesquelles A1 peut développer des instabilités. Quelques cas-tests présentés dans les annexes confirment la capacité des deux schémas de traiter le tenseur R^L bruité dans l'opérateur de divergence de façon stable. Par ailleurs, l'annexe C traite des inégalités d'énergie pour les deux systèmes A1 et A2 et pour tout R^L .

A relaxation scheme for hybrid modeling of gas-particle flows ¹

K. Dorogan, M. Guingo, J.M. Hérard, J.P. Minier

Abstract

This paper aims at proposing a relaxation scheme that allows to obtain stable approximations for a system of partial differential equations which governs the evolution of the void fraction and the mean velocity in the particle phase of two-phase flows. This system involves the divergence of a particle kinetic tensor, which is provided by a Lagrangian code and whose components are not smooth. The simulation algorithm is based on the combined use of upwinding and relaxation techniques. The main properties of the method are given, together with the Finite Volume Godunov scheme and this approach is compared to an analogous one that was developed earlier. Some measured rates of convergence in L^1 -norm are provided, for a particular choice of the kinetic tensor. To complete the picture, we present some numerical results obtained when non-smooth external data are provided to the system.

2.1 Introduction

In the present paper, we are interested in the numerical solution of a system of partial differential equations arising from a hybrid modeling of polydispersed turbulent two-phase flows [10, 25, 26]. The general framework of the hybrid modeling is recalled in Appendix C, which explains in particular a coupling of Eulerian and Lagrangian descriptions introduced for the modeling of the dispersed phase of gas-particle two-phase flows. The main difficulty of such a coupling consists in *the treatment of non-smooth data provided by the Lagrangian part of the model in the divergence operator* in the partial differential equations.

In d space dimensions, we denote by \mathbf{x} the space variable, t the time, $\rho(t, \mathbf{x})$ the mean particle density, $\mathbf{u}(t, \mathbf{x}), \mathbf{U}(t, \mathbf{x}) \in \mathbb{R}^d$ the instantaneous and the mean particle velocities, $\mathbf{R}^L(t, \mathbf{x}) \in \mathbb{R}^{d \times d}$ the particle kinetic tensor, which can also be written as $R_{ij}^L = \langle u'_i u'_j \rangle^L$ with $i, j = 1, \dots, d$ and $\mathbf{u}'(t, \mathbf{x}) = \mathbf{u}(t, \mathbf{x}) - \mathbf{U}(t, \mathbf{x})$ the fluctuation of the particle velocity. The following system, which is deduced from the Lagrangian stochastic model (Appendix C), describes the time evolution of the first-order mean particle quantities:

$$\begin{cases} \partial_t \rho + \partial_{x_j} (\rho U_j) = 0, & t > 0, \quad \mathbf{x} \in \mathbb{R}^d, \\ \partial_t (\rho U_i) + \partial_{x_j} (\rho U_i U_j) + \partial_{x_j} (\rho R_{ij}^L) = \rho g_i + \rho \langle U_{r,i}^L / \tau_p^U, \rangle, \end{cases} \quad (2.1.1)$$

where the superscript “ L ” refers to variables computed using a Lagrangian description which, therefore, represent *external non-smooth data*. The right-hand side terms in the second equation in (2.1.1) describe the gravity and the drag forces, where \mathbf{U}_r^L stands for the local relative velocity of the fluid and the dispersed phases, and τ_p^U is the particle velocity relaxation time scale (the time necessary for a particle to adjust to the fluid velocity).

¹Accepted for publication in Computers and Fluids.

Obviously, due to ensemble averaging, these equations are *not closed* since the correlations of the fluctuating particle velocities $R_{ij}^L(t, \mathbf{x})$ appear explicitly. From analogous situations arising with Reynolds averaging in single phase flow, these stresses have an important influence on the nature of the convective subset. This fact suggests that they should be handled with great care. It is also important to emphasize that $R_{ij}^L(t, \mathbf{x})$ is *not smooth* since it contains the statistical error that may be a cause of instabilities. Furthermore, we know that treating this convective term as a source term is not allowed (see [6] for a similar situation). The need to overcome these difficulties has led us to search for a **method which would be stable during unsteady simulations with non-smooth external data**.

In order to compute *stable* approximations of solutions of (2.1.1), a first approach has been proposed in [10, 26, 27]. This approach, which will be referred to as **A1**, relies on the combined use of *relaxation-type techniques* [1, 4, 5, 9, 12, 13, 28, 35, 36, 38] and *upwinding schemes* [14, 19, 22, 23, 29, 30] and was first introduced in [25] in order to predict single-phase turbulent flows [32]. In the latter approach, an extended *hyperbolic* system was introduced in a natural way, following what is done for previous associated Eulerian models (see [2, 3, 6, 21]). Though they contain *non-conservative* contributions, which are active in *genuinely non linear fields*, these “relaxation” models enable to obtain stable results. However, they involve *a priori* approximate jump conditions that may inhibit the convergence to the correct shock solutions of original system (2.1.1). This has motivated a new approach relying on a hyperbolic **relaxation** model, where all fields are *linearly degenerate* and, therefore, jump conditions are uniquely defined. This second approach introduced in this work will be referred to as **A2**. Both approaches A1 and A2 will be presented and compared in terms of convergence, stability and accuracy.

Before beginning to discuss our new approach of simulation, it is worth noting that we compute approximate solutions of (2.1.1) using a splitting strategy, where we treat first the corresponding homogeneous system:

$$\begin{cases} \partial_t \rho + \partial_{x_j}(\rho U_j) = 0, & t > 0, \quad \mathbf{x} \in \mathbb{R}^d, \\ \partial_t(\rho U_i) + \partial_{x_j}(\rho U_i U_j) + \partial_{x_j}(\rho R_{ij}^L) = 0, \end{cases} \quad (2.1.2)$$

and then account for source terms through the second step:

$$\begin{cases} \partial_t \rho = 0, \\ \partial_t(\rho U_i) = \rho g_i + \rho \langle U_{r,i}^L / \tau_p^U \rangle. \end{cases} \quad (2.1.3)$$

The paper is organized as follows. We give first the main guidelines of the relaxation procedure in the one-dimensional space. This will be detailed in section 2. The numerical scheme will be given in section 3. Section 4 will be devoted to the assessment of the numerical approach and to the comparison with the previous approach (A1) [10, 26, 27], while focusing on analytical solutions **in the particular case** $\rho R^L = \pi(\rho)$ that refers to the barotropic Euler equations for gas dynamics. A quantitative analysis of the L^1 error norm will also be given. Some results given in appendices will complete the whole approach. Appendix B will focus on the energy control through both approaches (A1) and (A2) whatever R is. The last appendix will provide some two-dimensional

numerical results of coupling in realistic situations, where the kinetic tensor R_{ij}^L is provided at each time step by an external computation using a Lagrangian description.

2.2 Relaxation approach

2.2.1 Guidelines

We are looking for a method that would ensure stable unsteady approximations of the solution to system (2.1.2) in one space dimension:

$$\begin{cases} \partial_t \rho + \partial_x(\rho U) = 0, & t > 0, \quad x \in \mathbb{R}, \\ \partial_t(\rho U) + \partial_x(\rho U^2 + \rho R^L) = 0. \end{cases} \quad (2.2.1)$$

It is necessary to recall first that, since the kinetic tensor **$\mathbf{R}^L(t, x)$ is non-smooth external data which, in practical coupled computations with the Lagrangian code, is not a function of variables** $(\rho, \rho U)$, we are formally interested in finding “discontinuous” solutions of the problem. This may happen even if $R^L(t, x) = cst > 0$. These properties have led us to focus on Riemann solvers, these being particularly well suited for the simulation of problems with discontinuous solutions.

In this approach, we suggest that an Eulerian transport equation for the stresses be solved along with the above-mentioned mean particle quantities. The only purpose of the particle stress equation is to lead to a system of equations with a complete and meaningful description of the physical wave properties. The stress field will in fact be provided by the Lagrangian part of the overall model at each time step, but by keeping a (redundant) transport equation for the stresses, we will mimic the correct wave propagation within the Eulerian part, and thus will help to stabilize numerical approximations of the density and of the particle velocity.

To approximate the solutions of Eqs. (2.1.1) in the one-dimensional space, we introduce an augmented state vector $W(t, x) = (\rho, \rho U, \rho R)^t$ and a generalized relaxation system:

$$\begin{cases} \partial_t \rho + \partial_x(\rho U) = 0, \\ \partial_t(\rho U) + \partial_x(\rho U^2 + \rho R) = 0, & t > 0, \quad x \in \mathbb{R}, \\ \partial_t(\rho R) + \mathcal{A}(W, \partial_x W) = \rho(R^L - R)/\tau_p^R. \end{cases} \quad (2.2.2)$$

In order to guarantee the consistency of the new system with the original one at the discrete level, a relaxation time scale τ_p^R is introduced, and when this parameter is set formally to zero, the new system is consistent with the initial one.

Furthermore, we want to find an appropriate form of the operator $\mathcal{A}(W, \partial_x W)$, which describes the evolution of the fluctuating particle velocities, so that some important physical properties were respected. More precisely, we enforce the following features:

- (C1) we wish to define a ***hyperbolic system*** of equations. Hyperbolicity is one clue that the

physical reality is correctly modeled and moreover it guarantees some inner stability of the solutions. For this reason, it seems crucial *to preserve* the property of hyperbolicity, which characterizes the original system.

- (C2) we intend to have a system characterized by *linearly degenerated (LD) fields*. This feature avoids imposing approximate jump conditions. Actually, we note that in the conservative system (2.1.2), jump relations are defined in a unique way. This essentially differs from the strategy introduced in [25, 26, 27], where the relaxation system is chosen to be close to the physics and hence contains non-conservative terms active in genuinely non-linear (GNL) fields.
- (C3) the system should preserve *the positivity of the density distribution*:

$$\rho(x, t) \geq 0.$$

This property is expected in order to yield a physically meaningful solution.

- (C4) The relaxation system should be close enough to (A1) (introduced in [26, 27] and recalled below in sec. 2.2) that represents a relevant physical choice.

In the general case, the realizability of the kinetic tensor might also be required, which means that the associated quadratic form remains positive:

$$n_i R_{ij} n_j \geq 0 \quad \forall n_i, n_j (i, j = 1, \dots, d). \quad (2.2.3)$$

In the one-dimensional case it amounts to ensure $R(t, x) > 0$ for all $t > 0$, $x \in \mathbb{R}$. Actually, the relaxation approach will guarantee this property at the discrete level, at each time step, in all cells.

2.2.2 System construction

A preliminary study has revealed that conservative forms of the third equation in relaxation system (2.2.2) are not acceptable because they generally result in *degenerate* hyperbolic systems (eigen-vectors no longer span the whole space). Thus, as the most appropriate and the simplest candidate for the larger system in one space dimension, we suggest the following:

$$\begin{cases} \partial_t \rho + \partial_x(\rho U) = 0, \\ \partial_t(\rho U) + \partial_x(\rho U^2) + \partial_x(\rho R) = 0, \quad t > 0, x \in \mathbb{R} \\ \partial_t(\rho R) + U \partial_x(\rho R) + \Psi \partial_x U = \rho(R^L - R)/\tau_p^R, \end{cases} \quad (2.2.4)$$

where τ_p^R denotes some small relaxation time scale. Here, the choice of the evolution operator is reduced to the choice of the function:

$$\Psi(\rho, R) > 0, \quad (2.2.5)$$

which influences considerably the characteristics of the whole system. In the remainder of this section, we are interested mainly by the properties of the homogeneous system corresponding to

(2.2.4):

$$\begin{cases} \partial_t \rho + \partial_x(\rho U) = 0, \\ \partial_t(\rho U) + \partial_x(\rho U^2) + \partial_x(\rho R) = 0, \quad t > 0, \quad x \in \mathbb{R} \\ \partial_t(\rho R) + U \partial_x(\rho R) + \Psi \partial_x U = 0. \end{cases} \quad (2.2.6)$$

Since the convective part of the model is not in conservative form, we define a non-conservative variable $Z = (\rho, U, \rho R)^t$. Then, for smooth solutions, system (2.2.6) can be rewritten in the following condensed form:

$$\partial_t Z + A(Z) \partial_x Z = 0, \quad t > 0, \quad x \in \mathbb{R}, \quad (2.2.7)$$

with the system matrix

$$A(Z) = \begin{pmatrix} U & \rho & 0 \\ 0 & U & \vartheta \\ 0 & \Psi & U \end{pmatrix},$$

where $\vartheta(x, t) = 1/\rho(x, t)$ is the specific volume.

Property 1. For all Z in the phase space $\Omega = \{(\rho, U, \rho R)^t \in \mathbb{R}^3 \text{ such that } \rho > 0\}$, system (2.2.7) admits three real distinct eigenvalues:

$$\begin{aligned} \lambda_1 &= U - c \\ \lambda_2 &= U \\ \lambda_3 &= U + c \end{aligned} \quad (2.2.8)$$

with $\rho c^2 = \Psi > 0$. The corresponding right eigenvectors are given by:

$$\vec{r}_1 = \begin{pmatrix} \rho \\ -c \\ \rho c^2 \end{pmatrix} \quad \vec{r}_2 = \begin{pmatrix} 1 \\ 0 \\ 0 \end{pmatrix} \quad \vec{r}_3 = \begin{pmatrix} \rho \\ c \\ \rho c^2 \end{pmatrix} \quad (2.2.9)$$

and $\text{span } \mathbb{R}^3$. Thus, the system (2.2.7) is hyperbolic on Ω (unless vacuum occurs in the solution).

A natural choice for Ψ arising from R_{ij} model in one-dimensional space was given in [27]: $\Psi = 3\rho R$. This is referred to as **approach (A1)**.

Property 2.

(A1): If we assume that $\Psi = 3\rho R$, then system (2.2.6) admits two GNL fields and one LD field;

(A2): If we assume that $\Psi = a_0^2 \vartheta$ with constant $a_0 \in \mathbb{R}_+^*$, then system (2.2.6) admits three LD fields.

In fact, for calculated eigenvalues λ_k and eigenvectors \vec{r}_k ($k = 1, 2, 3$) of $A(Z)$ and for any function

$\Psi(\rho, R) > 0$ we have:

$$\begin{aligned}\frac{\partial \lambda_1}{\partial Z} \cdot \vec{r}_1 &= \frac{\partial(U - c)}{\partial Z} \cdot \vec{r}_1 = -\rho \frac{\partial c}{\partial \rho} - c - \rho c^2 \frac{\partial c}{\partial(\rho R)} = -\frac{\partial \lambda_3}{\partial Z} \cdot \vec{r}_3, \\ \frac{\partial \lambda_2}{\partial Z} \cdot \vec{r}_2 &= \frac{\partial U}{\partial Z} \cdot \vec{r}_2 = 0, \quad \Rightarrow \quad 2 - \text{field is LD.}\end{aligned}\tag{2.2.10}$$

- If we take $\Psi = 3\rho R$ then $c^2 = \Psi/\rho = 3R$ and the 1 and the 3 fields are GNL, because

$$\frac{\partial \lambda_1}{\partial Z} \cdot \vec{r}_1 = -\frac{\partial \lambda_3}{\partial Z} \cdot \vec{r}_3 = -2c \neq 0.$$

- It is also easily seen that for all function $\Psi = \Psi(\rho) = a_0^2 \vartheta$ with constant a_0 the following equality is verified for $c = \sqrt{\Psi/\rho} = a_0 \vartheta$:

$$\frac{\partial \lambda_1}{\partial Z} \cdot \vec{r}_1 = -\frac{\partial \lambda_3}{\partial Z} \cdot \vec{r}_3 = 0.$$

This means that all the fields in this case are LD.

In order to ensure the link with the expression in (A1), in (A2) we fix $a_0 = \sqrt{3R_0\rho_0^2}$ (see Appendix A (part II)).

Remark 1. *The form of the function Ψ of the approach (A1) is “natural”, but it requires introducing approximate jump conditions (see [26], [27]). The choice of Ψ associated with (A2) ensures the uniqueness of the jump conditions and results in the relaxation system that corresponds exactly to the system introduced for the simulation of barotropic Euler equations, when $\rho R^L = \pi(\rho)$. When restricting to (A2) and though equation (2.2.6.3) is slightly different from the formulations presented for instance in [4] and [9] for barotropic Euler equations (see Appendix A too), relaxation systems are equivalent for smooth solutions and the underlying idea is the same.*

Remark 2. *System (2.2.4) ensures the positivity of the density function. It follows from the mass continuity equation that when $\forall x, \rho(t = 0, x) = \rho_0 > 0$, the density values may never become negative in $[0, T]$ as soon as $U, \partial_x U \in L^\infty(\mathbb{R}_x \times [0, T])$.*

Remark 3. *Some energy estimates for relaxation systems corresponding to (A1) and (A2) are given in **Appendix B**, in a one-dimensional framework (and in [18, 16] in a 2D framework). These should not be confused with entropy estimates for barotropic Euler equations for instance, such as those provided in [4], [35] and [9] among others.*

In the remainder of this paper we will focus on the presentation of the approach (A2). A comparison of results obtained with both (A1) and (A2) will be provided and discussed in section 4.

2.2.3 Analytical solution of the Riemann problem

Before going further on, we recall that the one dimensional Riemann problem corresponds to the initial value problem associated with the hyperbolic system (2.2.6) and discontinuous initial

conditions:

$$\begin{bmatrix} \rho \\ U \\ \rho R \end{bmatrix} = \begin{bmatrix} \rho_l \\ U_l \\ (\rho R)_l \end{bmatrix} \text{ for } x \leq 0 \quad \text{and} \quad \begin{bmatrix} \rho \\ U \\ \rho R \end{bmatrix} = \begin{bmatrix} \rho_r \\ U_r \\ (\rho R)_r \end{bmatrix} \text{ for } x > 0. \quad (2.2.11)$$

In the remainder of the paper, we will use the following shortened notations:

$$\bar{U}_{lr} = \frac{U_l + U_r}{2}, \quad [U]_l^r = (U_r - U_l), \quad [\rho R]_l^r = (\rho R)_r - (\rho R)_l, \quad (2.2.12)$$

$$r_1 = \begin{cases} \max \left(\frac{-[U]_l^r \pm \sqrt{([U]_l^r)^2 + 8\vartheta_l[\rho R]_l^r}}{4\vartheta_l} \right), & \text{if } ([U]_l^r)^2 + 8\vartheta_l[\rho R]_l^r \geq 0 \\ 0, & \text{otherwise} \end{cases} \quad (2.2.13)$$

$$r_2 = \begin{cases} \max \left(\frac{-[U]_l^r \pm \sqrt{([U]_l^r)^2 - 8\vartheta_r[\rho R]_l^r}}{4\vartheta_r} \right), & \text{if } ([U]_l^r)^2 - 8\vartheta_r[\rho R]_l^r \geq 0 \\ 0, & \text{otherwise} \end{cases} \quad (2.2.14)$$

Property 3 (Existence and Uniqueness of the solution of the Riemann problem for (A2)). Assume that initial conditions are physically relevant ($\rho_{l,r} > 0$ and $R_{l,r} > 0$). Assume moreover that $a_0 > a_0^{\min} = \max(r_1, r_2, 0) \geq 0$ with constant a_0 and r_1, r_2 given by (2.2.13), (2.2.14). Then the Riemann problem associated with the homogeneous part of (2.2.4) that is (2.2.6), initial conditions (2.2.11) and $\Psi = a_0^2\vartheta$, admits a unique solution $(t, x) \mapsto Z^{\text{exact}}(x/t; Z_l, Z_r)$, composed of four constant states Z_l, Z_1, Z_2, Z_r separated by three LD waves. Z_1 and Z_2 are given by the following analytical expressions:

$$\begin{aligned} \vartheta_1 &= \vartheta_l + \frac{U_r - U_l}{2a_0} - \frac{(\rho R)_r - (\rho R)_l}{2a_0^2} \\ \vartheta_2 &= \vartheta_r + \frac{U_r - U_l}{2a_0} + \frac{(\rho R)_r - (\rho R)_l}{2a_0^2} \end{aligned} \quad (2.2.15)$$

$$U_1 = U_2 = \frac{U_l + U_r}{2} - \frac{(\rho R)_r - (\rho R)_l}{2a_0} \quad (2.2.16)$$

$$(\rho R)_1 = (\rho R)_2 = \frac{(\rho R)_l + (\rho R)_r}{2} - \frac{a_0(U_r - U_l)}{2}. \quad (2.2.17)$$

A straightforward consequence is that $\vartheta_1, \vartheta_2 > 0$ and the waves are ordered ($\lambda_1 < \lambda_2 < \lambda_3$).

A proof of this result can be found in [9] for instance, with a slightly different form of the relaxation system. The proof is obtained by construction and we recall it below. Let us consider only the solutions of the class of self-similar functions $(x, t) \mapsto Z(x/t)$, composed of constant states separated by three contact discontinuities (fig. 2.1):

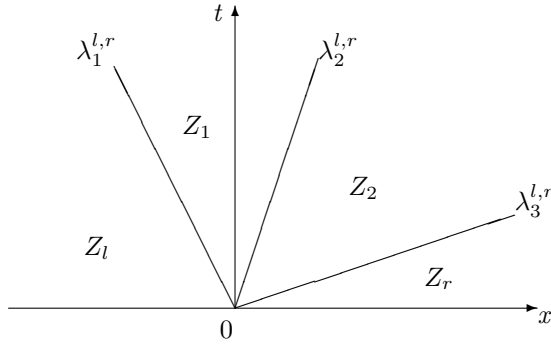


Figure 2.1: Sketch of the solution of the one-dimensional Riemann problem when $\lambda_2^{l,r} > 0$.

Here, $\lambda_1^{l,r} = U_l - a_0 \vartheta_l$, $\lambda_2^{l,r} = U_1 = U_2 = \bar{U}_{lr} - [\rho R]_l^r / 2a_0$, $\lambda_3^{l,r} = U_r + a_0 \vartheta_r$.

Associated with each k -wave we have two k -Riemann Invariants, I_R^k ($k = 1, 2, 3$), which satisfy:

$$\frac{\partial I_R^k}{\partial Z} \cdot \vec{r}_k = 0.$$

These k -Riemann Invariants remain constant through the k -contact discontinuity. For the present 1-D problem, Riemann Invariants are given by the following expressions:

$$\begin{aligned} I_R^1 &= \{U - c, \rho R + a_0^2 \vartheta\} \\ I_R^2 &= \{U, \rho R\} \\ I_R^3 &= \{U + c, \rho R + a_0^2 \vartheta\} \end{aligned} \tag{2.2.18}$$

Then, the structure of the solution of the Riemann problem can be written as:

1-wave

$$\begin{cases} U_l - c_l = U_1 - c_1 \\ (\rho R)_l + a_0^2 \vartheta_l = (\rho R)_1 + a_0^2 \vartheta_1 \end{cases} \tag{2.2.19}$$

2-wave

$$\begin{cases} U_1 = U_2 \\ (\rho R)_1 = (\rho R)_2 \end{cases} \tag{2.2.20}$$

3-wave

$$\begin{cases} U_2 + c_2 = U_r + c_r \\ (\rho R)_2 + a_0^2 \vartheta_2 = (\rho R)_r + a_0^2 \vartheta_r \end{cases} \tag{2.2.21}$$

We check at once that formulae (2.2.15), (2.2.16), (2.2.17) are the unique solutions of (2.2.19), (2.2.20), (2.2.21). Eventually, the constructed analytical solution to the Riemann problem associated with (2.2.6) and initial conditions (2.2.11) can be sketched as:

$$(x, t) \mapsto Z^{exact}(x/t; Z_l, Z_r). \tag{2.2.22}$$

For a_0 large enough, the positivity of ϑ_1, ϑ_2 is ensured for all initial conditions $(\rho, U, \rho R)_{l,r}$. At the same time, we would like to avoid a_0 being too large in order to preserve the accuracy of the

scheme. Hence, we aim at determining an appropriate value of a_0 . Using notations (2.2.12), we can rewrite the wave ordering condition $\lambda_1 < \lambda_2 < \lambda_3$ as follows:

$$U_l - a_0 \vartheta_l < \bar{U}_{lr} - \frac{1}{2a_0} [\rho R]_l^r < U_r + a_0 \vartheta_r. \quad (2.2.23)$$

After some simple transformations, this leads us to the next system of square inequalities :

$$\begin{cases} 2\vartheta_l a_0^2 + [U]_l^r a_0 - [\rho R]_l^r > 0, \\ 2\vartheta_r a_0^2 + [U]_l^r a_0 + [\rho R]_l^r > 0, \end{cases} \quad (2.2.24)$$

and we can see that imposing $\vartheta_1, \vartheta_2 > 0$ in (2.2.15) leads to the same constraints. The solution of (2.2.24) provides us with "natural" conditions to choose a physically relevant lower bound for a_0 .

Remark 4. When $\rho R^L = \pi(\rho)$ with π given, a further evaluation of a lower bound of the parameter a_0 needed in (A2) will be recalled in **Appendix A**, relying on Whitham's condition. This condition guarantees some dissipation in the entropy balance equation (see [9]). In the general case, where $\rho R^L = \rho R^L(t, x)$, this condition cannot be directly applied (see Appendix A).

Remark 5. The positivity of the kinetic tensor in the intermediate states is not preserved for any initial condition $(\rho, U, \rho R)_{l,r}$. However, it is crucial to emphasize that at each time step the local values of $R = R^L$ are restored, thus the realizability is ensured owing to the instantaneous relaxation step.

Remark 6. In the approach (A1) developed in [27], the positivity of the kinetic tensor is required to ensure the hyperbolicity property for the corresponding relaxation system and, at the same time, is preserved by the very construction of this system.

2.3 Numerical approximation

Following the relaxation technique described in section 2, we approximate the solutions of an initial value problem associated with original system (2.2.1) by those of extended system (2.2.4) with $\Psi = a_0^2 \vartheta$. For simplicity of the notations, both problems can be rewritten in a condensed form:

$$\begin{cases} \partial_t W_\phi + \partial_x F_\phi(W_\phi, R^L) = 0, & t > 0, x \in \mathbb{R}, \\ W_\phi(0, x) = W_{\phi,0}(x) \text{ and } R^L(0, x) = R_0^L(x). \end{cases} \quad (2.3.1)$$

for (2.2.1) with $W_\phi = (\rho, \rho U)^t$, $F_\phi(W_\phi, R^L) = (\rho U, \rho U^2 + \rho R^L)^t$, and

$$\begin{cases} \partial_t W + \partial_x F(W) + G(W) \partial_x W = S(W, R^L), & t > 0, x \in \mathbb{R}, \\ W(0, x) = W_0(x). \end{cases} \quad (2.3.2)$$

for (2.2.4), where $W = (\rho, \rho U, \rho R)^t$, $W \in \Omega$ is the unknown vector with the corresponding physical “fluxes” and the source term $S(W, R^L)$:

$$F(W) = \begin{pmatrix} \rho U \\ \rho U^2 + \rho R \\ \rho U R \end{pmatrix}, \quad G(W) \partial_x W = \begin{pmatrix} 0 \\ 0 \\ (a_0^2 \vartheta - \rho R) \partial_x U \end{pmatrix}, \quad S(W, R^L) = \begin{pmatrix} 0 \\ 0 \\ \rho(R^L - R)/\tau_p^R \end{pmatrix}. \quad (2.3.3)$$

We consider a uniform grid given by cell centers $x_i = ih$, $i \in \mathbb{Z}$. Each cell is an interval $\mathcal{C}_i = [x_{i-1/2}, x_{i+1/2}]$ of length h , where the points $x_{i+1/2} = x_i + h/2$ are called cell interfaces. The time is discretized with the time step $(\Delta t)^n$ such that $t^{n+1} = t^n + (\Delta t)^n$, $n \in \mathbb{N}$ are intermediate times. We assume the values of the approximate solution at time t^n , $x \in \mathbb{R} \mapsto W_\Delta(x, t^n) \in \Omega$, to be constant in each cell \mathcal{C}_i , $i \in \mathbb{Z}$, and denote them by W_i^n :

$$W_\Delta(x, t^n) = W_i^n, \quad \forall x \in \mathcal{C}_i, \quad i \in \mathbb{Z}, \quad n \in \mathbb{N}. \quad (2.3.4)$$

Besides, using the initial condition $W_0(x)$ at $t = 0$, we define the sequence $(W_i^0)_{i \in \mathbb{Z}}$ as the average of function $W_0(x)$ over the cell i ($i \in \mathbb{Z}$):

$$W_i^0 = \frac{1}{h} \int_{x_{i-1/2}}^{x_{i+1/2}} W_0(x) dx, \quad \forall i \in \mathbb{Z}. \quad (2.3.5)$$

At $t = 0$, $W_\Delta(x, t^0)$ is set at equilibrium which means that $(\rho R)_i^0 = (\rho R^L)_i^0$, $i \in \mathbb{Z}$.

At each time step, the *global algorithm* which provides the approximations $W_\Delta(., t^{n+1})$ from $W_\Delta(., t^n)$ can be written as follows:

- **Initialization** (at t^n): As initial condition we take $W_i^n = (\rho_i^n, \rho_i^n U_i^n, \rho_i^n R_i^{L,n})^t$;
- **Evolution step** ($t^n \rightarrow t^{n+1,-}$): approximation of the solution of the homogeneous system corresponding to (2.3.2) at $t^{n+1,-} = t^n + \Delta t^n$ with a Finite Volume scheme described in sec.2.3.1. This step computes the values $W_i^{n+1,-}$ from W_i^n ($i \in \mathbb{Z}$);
- **Relaxation step** ($t^{n+1,-} \rightarrow t^{n+1}$): accounts for the source term $S(W, R^L)$ by solving the differential equation $\partial_t W = S(W, R^L)$ at $t^{n+1} = t^n + \Delta t^n$ with the initial condition $W_i^{n+1,-}$ obtained at the previous stage. It traduces the return of the system to equilibrium assuming an instantaneous relaxation ($\tau_p^R \rightarrow 0$) and gives the values W_i^{n+1} , $i \in \mathbb{Z}$:

$$\begin{cases} \rho_i^{n+1} = \rho_i^{n+1,-} \\ (\rho U)_i^{n+1} = (\rho U)_i^{n+1,-} \\ (\rho R)_i^{n+1} = \rho_i^{n+1} (R^L)_i^{n+1} \Leftrightarrow R_i^{n+1} = (R^L)_i^{n+1}. \end{cases} \quad (2.3.6)$$

Finally, we retrieve $W_{\phi,i}^{n+1} = (\rho_i^{n+1}, (\rho U)_i^{n+1})^t$, $i \in \mathbb{Z}$, $n \geq 0$ that is an approximation of the solution to (2.3.1).

2.3.1 Evolution step: Godunov scheme and interface Riemann solver

The computations inside this step are made in terms of the conservative state vector $W = (\rho, \rho U, \rho R)^t$. Therefore, we approximate solutions of the following Cauchy problem

$$\begin{cases} \partial_t W + \partial_x F(W) + G(W) \partial_x W = 0, & t \in [0, (\Delta t)^n], x \in \mathbb{R} \\ W(x, 0) = W_\Delta(x, t^n). \end{cases} \quad (2.3.7)$$

Following properties 1, 2, this system is hyperbolic and admits three LD fields. Thus, the solution of the associated Riemann problem is uniquely defined. Since $x \mapsto W_\Delta(x, t^n)$ is piecewise constant, the solution to system (2.3.7) is obtained by solving the Riemann problem at each cell interface $x_{i+1/2}$, $i \in \mathbb{Z}$. To be consistent, the time step $(\Delta t)^n$, $n \in \mathbb{N}$ should be limited in such a way that the waves emanating from an interface do not interact with waves created at the adjacent interfaces during the time step. This leads to the CFL condition:

$$\frac{(\Delta t)^n}{h} \max_W (|\lambda_k(W)|, k = 1, 2, 3) \leq CFL < \frac{1}{2}, \quad n \in \mathbb{N}. \quad (2.3.8)$$

More precisely, for $(x, t) \in [x_i, x_{i+1}] \times [0, \Delta t]$ we have

$$W_\Delta(x, t) = W^{exact} \left(\frac{x - x_{i+1/2}}{t}; W_i^n, W_{i+1}^n \right), \quad i \in \mathbb{Z}. \quad (2.3.9)$$

where $(x, t) \mapsto W^{exact}(x/t; W_l, W_r)$ is the self-similar solution of the Riemann problem

$$\begin{cases} \partial_t W + \partial_x F(W) + G(W) \partial_x W = 0, \\ W(x, 0) = \begin{cases} W_l & \text{if } x < 0, \\ W_r & \text{if } x > 0. \end{cases} \end{cases} \quad (2.3.10)$$

given by property 3. Then, we can write

$$W^{exact} \left(x/t; W_i^n, W_{i+1}^n \right) = \begin{cases} W_i^n, & \text{if } \frac{x}{t} \leq \lambda_{1,i+1/2}, \\ W_{1,i+1/2}^n, & \text{if } \lambda_{1,i+1/2} < \frac{x}{t} < \lambda_{2,i+1/2}, \\ W_{2,i+1/2}^n, & \text{if } \lambda_{2,i+1/2} < \frac{x}{t} < \lambda_{3,i+1/2}, \\ W_{i+1}^n, & \text{if } \frac{x}{t} \geq \lambda_{3,i+1/2}, \end{cases} \quad (2.3.11)$$

where W_i^n , W_{i+1}^n are averaged cell values and $W_{1,i+1/2}^n$, $W_{2,i+1/2}^n$ are intermediate states in the solution of the Riemann problem at the interface $i + 1/2$ (Fig. 2).

In the following, we use this exact solution $W_\Delta(x, t)$ to construct the approximation $W_i^{n+1,-}$, $i \in \mathbb{Z}$ with a Godunov finite volume scheme:

$$h \left(W_i^{n+1,-} - W_i^n \right) + \Delta t^n \left(\mathcal{F}_{i+\frac{1}{2}}^{n,God} - \mathcal{F}_{i-\frac{1}{2}}^{n,God} \right) + \Delta t^n \mathcal{H}_i^n = 0, \quad i \in \mathbb{Z}, \quad n \geq 0, \quad (2.3.12)$$

where $\mathcal{F}_{i+\frac{1}{2}}^{n,God} = \mathcal{F}(W_i^n, W_{i+1}^n)$ is the exact Godunov flux through the interface $i + 1/2$:

$$\mathcal{F}_{i+\frac{1}{2}}^{n,God} = F \left(W^{exact} \left(0; W_i^n, W_{i+1}^n \right) \right), \quad (2.3.13)$$

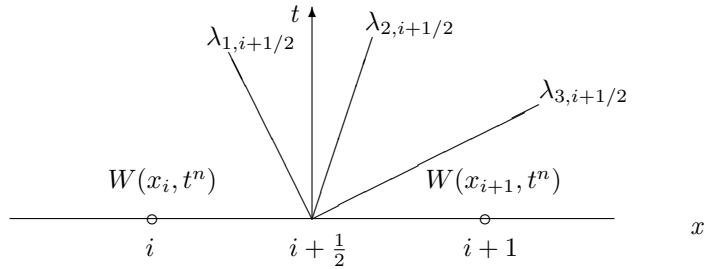


Figure 2.2: Sketch of a part of the grid

and \mathcal{H}_i^n is an approximation of the non-conservative contribution. If we denote for the sake of simplicity $W_{i+1/2}^* = W^{exact}(0; W_i^n, W_{i+1}^n)$, $i \in \mathbb{Z}$, the term \mathcal{H}_i^n is given by:

$$\mathcal{H}_i^n = \begin{pmatrix} 0 \\ 0 \\ \frac{1}{2} \left((a_0^2 \vartheta)_{i-\frac{1}{2}}^* + (a_0^2 \vartheta)_{i+\frac{1}{2}}^* - (\rho R)_{i-\frac{1}{2}}^* - (\rho R)_{i+\frac{1}{2}}^* \right) \left(U_{i+\frac{1}{2}}^* - U_{i-\frac{1}{2}}^* \right) \end{pmatrix}, \quad (2.3.14)$$

where the locally constant values $(a_0^2 \vartheta)_{i+1/2}^*$ are computed at each t^n , $n \in \mathbb{N}$ at each cell interface $i + 1/2$, $i \in \mathbb{Z}$ according to the wave ordering condition and, when possible, Whitham's condition (see Appendix A for further details).

The present algorithm gives us the piecewise constant values $Z_\Delta(x, t^{n+1, -})$ that are approximations averaged on each cell \mathcal{C}_i , $i \in \mathbb{Z}$.

Remark 7 (Positivity of cell values of the density). Assume that $|\lambda_{max}| \Delta t / h < 1/2$ and that the parameter a_0 guarantees the positivity of the density in the intermediate states defined by (2.2.15): $\vartheta_{1,i+1/2}, \vartheta_{2,i+1/2} > 0$, $i \in \mathbb{Z}$. Then the evolution step (2.3.12) preserves the positivity of the cell values of the density and the whole algorithm computes $\rho_i^{n+1} \geq 0$ (since the relaxation step (2.3.6) preserves cell densities).

The proof being classical is not recalled here.

2.4 Numerical results

In order to verify the approach (A2) we consider in the first subsections below some test cases where :

$$\rho R^L = \pi(\rho), \quad (2.4.1)$$

and thus, analytical solutions are known. Some theoretical results for (A2) (seen as a “true” relaxation technique for the barotropic Euler equations) can be found in this case in [4, 9] for instance and references called therein. Such a closure $\rho R^L = \pi(\rho)$ allows to measure the error of approximation and to verify the convergence towards the correct solution in practice. By the way, we will compare results obtained with both (A2) and (A1). The numerical scheme for approach (A1) has been proposed in [27] and is not recalled here. It relies on a different “relaxation” system

(see section 2.2) and on the use of the VFRoe-ncv scheme [8]. In order to emphasize the main differences between (A1) and (A2) we present numerical tests on shock tubes for the most difficult configurations, such as vacuum occurrence, strong shocks and rarefaction waves including sonic points.

In the second part, some results obtained with specific analytic kinetic tensor R^L will be presented.

2.4.1 Algorithm verification

In this part of the paper, we will assume the following “closure” relation:

$$\rho R^L = \pi(\rho) = S_0 \rho^\gamma \quad (2.4.2)$$

with constant entropy $S_0 = 10^5$ and $\gamma = 3$. This value of γ corresponds to the underlying isentropic case arising in [27], [6]. Thus

$$R_i^{L,n} = S_0 (\rho_i^n)^{\gamma-1}$$

within each cell i , and we can compute the exact solution of the one-dimensional Riemann problem associated with the homogeneous analogue of (2.1.1) in all cases.

Initial conditions refer to different 1D Riemann problems. The computational domain consists of a one-dimensional tube placed in $[-0.5, 0.5]$ with a membrane in the middle, which separates two different fluid states at the beginning of the computation ($t = 0$). All meshes used to solve these Riemann problems are regular. The time step is in agreement with the CFL condition and the CFL number is equal to $1/2$. For a qualitative study, we present profiles for the density, the velocity, the pressure and the flow rate. From a quantitative point of view, numerical convergence curves, at a given time, are represented by plotting the logarithm of the L1-norm of the error as a function of the logarithm of the mesh size. We recall that the expected rate of convergence for the isentropic one-dimensional Euler equations is equal to 1, due to the fact that the system only involves two GNL fields. The grids that have been used contain between $N = 10^2$ and $N = 10^5$ cells.

In order to stabilize the numerical approximations at each t^n , $n \in \mathbb{N}$ and at each cell interface $i + 1/2$, $i \in \mathbb{Z}$, we impose the (locally constant) values $(a_0)_{i+1/2}^n$ to satisfy the condition:

$$(a_0)_{i+1/2}^n \geq \max((a_0)_{i+1/2}^{\lambda,n}, (a_0)_{i+1/2}^{W,n}),$$

where a_0^λ and a_0^W are defined in **Appendix A** for all $n \in \mathbb{N}$, $i \in \mathbb{Z}$.

2.4.1.1 Supersonic shock tube

We study first a supersonic case, using the following initial conditions:

$$\rho_l = 1, \quad \rho_r = 0.35, \quad (2.4.3)$$

$$U_l = 100, \quad U_r = 290. \quad (2.4.4)$$

The exact solution is composed of a supersonic 1 - rarefaction wave and a right going 2 - shock wave, Fig. 2.4. From the Fig. 2.5 we may conclude that approximations obtained with the two schemes converge towards the correct solution with the same rate of convergence (which is about 0.85 and compares well with rates given in [7, 11]). Moreover, both methods provide almost the same accuracy for a given mesh size. In this case, the 1-rarefaction wave contains a sonic point. The VFRoe-ncv scheme used in approach (A1) requires an entropy correction at sonic points [24]; otherwise a wrong shock wave develops. On the other hand, the relaxation scheme (A2) exhibits the correct behavior in the rarefaction wave without any entropy correction.

2.4.1.2 Symmetrical double shock wave

This case is interesting in order to compare the stability of both schemes around a wall boundary, when the normal component of the velocity of the fluid close to the boundary is positive. We consider the initial conditions:

$$\rho_l = \rho_r = 1, \quad (2.4.5)$$

$$U_l = -U_r = 10^3. \quad (2.4.6)$$

The exact solution is composed of a 1 - shock wave and a 2 - shock wave. The numerical rate of convergence for both the density and the velocity is approximately 1 for both methods, which is in agreement with results obtained in [7] (see Fig. 2.6, 2.7). Moreover, the accuracy for the two schemes is almost the same for a given mesh size. Eventually, we emphasize that the relaxation approach (A2) exhibits a better stability since (A1) induces tiny - stable - oscillations near the shocks (that do not inhibit the convergence). Actually, this characterizes problems with a very high initial kinetic energy, even when the CFL number is such that waves do not interact. It has been shown that approximations obtained with a CFL number equal to 0.9 are also convergent in that case for (A2). In fact, the limit of stability of approach (A2) in the present configuration is reached for $U_l = -U_r = 10^4$, where stable approximations are still available, but tiny oscillations appear (Fig. 2.8). On the other hand, approach (A1) is no longer suitable to tackle such a problem.

Remark 8. This test case is essential since it provides some numerical evidence that both approximate solutions provided by methods (A1) and (A2) converge to the correct shock solutions of original system (2.2.1). This result was not obvious for the relaxation system corresponding to approach (A2), but it was even less expected for (A1), where approximate jump conditions have been introduced in the “relaxation” system.

2.4.1.3 Symmetrical double rarefaction wave

We now examine a symmetrical double rarefaction wave. This one is the counterpart of the previous test, when the inlet normal component of the velocity is negative. Initial conditions are the following:

$$\rho_l = \rho_r = 1, \quad (2.4.7)$$

$$U_l = -U_r = -100. \quad (2.4.8)$$

Two symmetric rarefaction waves develop when U_r is positive. We have plotted the approximations of the solution in Fig. 2.10. The error obviously vanishes as the mesh size tends towards zero and the numerical rates of convergence are still close to 0.85 (Fig. 2.11).

2.4.1.4 Symmetrical double rarefaction wave with vacuum occurrence

Here, we study a more complex case where the speeds of rarefaction waves are so large that it leads to a vacuum occurrence in the solution. Before going further on, we recall that for isentropic Euler equations with a perfect gas equation of state, a vacuum may occur only when

$$U_r - U_l > \frac{2}{\gamma - 1} (c_{\phi,r} + c_{\phi,l}), \quad (2.4.9)$$

where c_ϕ is the celerity associated with system (2.2.1) when $\rho R^L = \pi(\rho) = S_0 \rho^\gamma$. Assuming the initial conditions:

$$\rho_l = \rho_r = 1, \quad (2.4.10)$$

$$U_l = -U_r < 0, \quad (2.4.11)$$

$$c_{\phi,l} = c_{\phi,r} = \sqrt{S_0 \gamma \rho_r^{\gamma-1}},$$

we conclude that the vacuum may occur when

$$\frac{U_r}{c_{\phi,r}} > \frac{2}{\gamma - 1}. \quad (2.4.12)$$

If we take $U_l = -U_r = -1000$, relation (2.4.12) is satisfied. The exact solution is composed of two symmetric rarefaction waves. *The intermediate state exhibits a vacuum zone where the velocity is not defined but the flow rate and the density are zero. When focusing on (ρ, Q) , both approximations obtained with (A1), (A2) converge towards the correct solution with vanishing h .* A glance at profiles in Fig. 2.12 enables to check that both schemes give *almost the same accuracy*. Numerical rates of convergence in Fig. 2.13 are close to 0.7 (see also [7], [11], [20]).

2.4.1.5 Supersonic rarefaction wave

This case is somewhat equivalent to a dam break with shallow-water equations. One initial condition (on the right) is such that the density is very small:

$$\rho_l = 1, \quad \rho_r = 10^{-7}, \quad (2.4.13)$$

$$U_l = 0, \quad U_r = U_l + \frac{2c_{\phi,l}}{\gamma - 1} \left(1 - \frac{c_{\phi,r}}{c_{\phi,l}} \right). \quad (2.4.14)$$

Here, a supersonic 1 - rarefaction wave is followed by a “ghost” 2 - shock wave. Once more, we check that approximations converge towards the correct solution when the mesh is refined (Fig. 2.14). The rate of convergence is slightly higher than in the previous test case (about 0.82, Fig.

[2.15](#)). This suggests that the true vacuum zone actually pollutes the approximations. We note a small loss of monotonicity at the end of the rarefaction wave. Actually, this drawback vanishes with a mesh refinement, and therefore, the positivity of cell values of the density is preserved. As mentioned before, an important issue here is that *the relaxation scheme (A2) does not need any entropy correction*.

2.4.2 Numerical results for (A2) with a noisy kinetic tensor

We focus now on some numerical test cases when a noisy kinetic tensor is plugged in the system of equations [\(2.2.1\)](#). For that purpose, we apply a noise to the values of R^L , which refer to the isentropic case studied in section 4.1, at each time step in the cells that belong to the region $x \in [-0.25, 0.25]$ as follows:

$$R_i^{L,n} = S_0(\rho_i^n)^{\gamma-1}(1 + rms(0.5 - rand(0, 1))), \quad i \in \mathbb{Z}, \quad n \in \mathbb{N},$$

where rms stands for the noise intensity and $rand$ (random numbers generator) allows to manage the noise amplitude.

We choose the initial conditions of a subsonic shock tube problem:

$$\rho_l = 1, \quad \rho_r = 0.24, \quad (2.4.15)$$

$$U_l = -10, \quad U_r = -282. \quad (2.4.16)$$

We fix the final time T , such that the boundary of the domain is not yet attained by the traveling waves. In order to estimate the stability of numerical approximations in such a case, we analyze their evolution when the mesh is refined: $N = 10^2, 10^3, 10^4, 5 \times 10^4, 10^5$ cells. The comparison displayed in Fig. [2.3](#) shows that the noise is not diminishing when the mesh is refined, and that approximations do not converge towards some smooth solution. Moreover, we note that the L^1 norm of the difference between the approximations with $rms = 0.1$ and $rms = 0$ tends to be constant when h tends to zero [\[17\]](#).

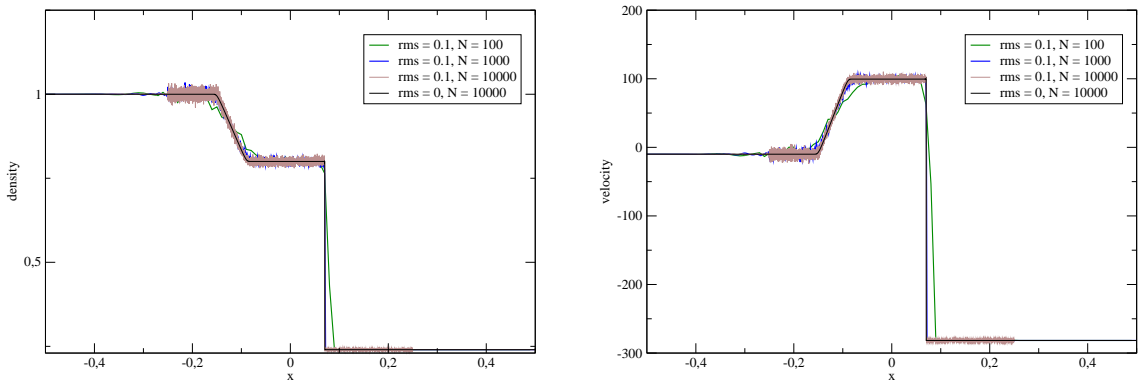


Figure 2.3: Subsonic shock tube: density and velocity approximations

Conclusion

We have introduced in this paper a new approach (A2) in order to tackle approximations of solutions to (2.1.1) in the one-dimensional case. This method is quite similar to (A1) introduced in [10, 26, 27] but it no longer requires the definition of approximate jump conditions since the relaxation system admits only linearly degenerated fields. The approach (A2) has been validated by computing exact solutions in a specific case, where $R^L = R^L(\rho)$, and associated errors. Numerical results have also been compared with those provided by approach (A1). On the whole, we would like to note that:

- both methods (A1) and (A2) guarantee a correct convergence of approximations, even when shocks arise in the solution. This was foreseen to happen, due to the conservative form of the schemes associated with (A1) and (A2) for the basic two conservative equations in (2.1.1);
- both methods can handle vacuum occurrence. This is crucial for practical hybrid computations.

We also emphasize that approach (A1), which relies on the approximate Godunov solver VF Roe-ncv, requires an entropy correction at sonic points in rarefaction waves, whereas approach (A2) does not. Moreover, (A2) may handle stronger shock waves.

The reference [17] shows several numerical experiments which have been achieved while plugging noisy kinetic tensor in the governing set of partial differential equations (2.2.1). A sample result can be found in sec. 4.2. One may conclude from [17] that approaches (A1), (A2) enable stable computations, which means that a mesh refinement is always possible, whatever the noise level. Moreover, for a given noise, the difference between approximations obtained with or without noise varies linearly with respect to the noise intensity and disturbances due to the noisy region are smoothed by the numerical scheme and tend to disappear out of this region (see [17]).

Eventually, we note that the present relaxation approach has been extended to a two-dimensional framework. This work is presented roughly in [18] and in detail in [15, 16]. A two-dimensional coupled simulation in a realistic configuration is presented in Appendix C.

Acknowledgments:

The first author receives a financial support through an EDF-CIFRE contract 203/2009. Computational facilities were provided by EDF. We would like to thank Thierry Gallouet who accepted to read the initial manuscript.

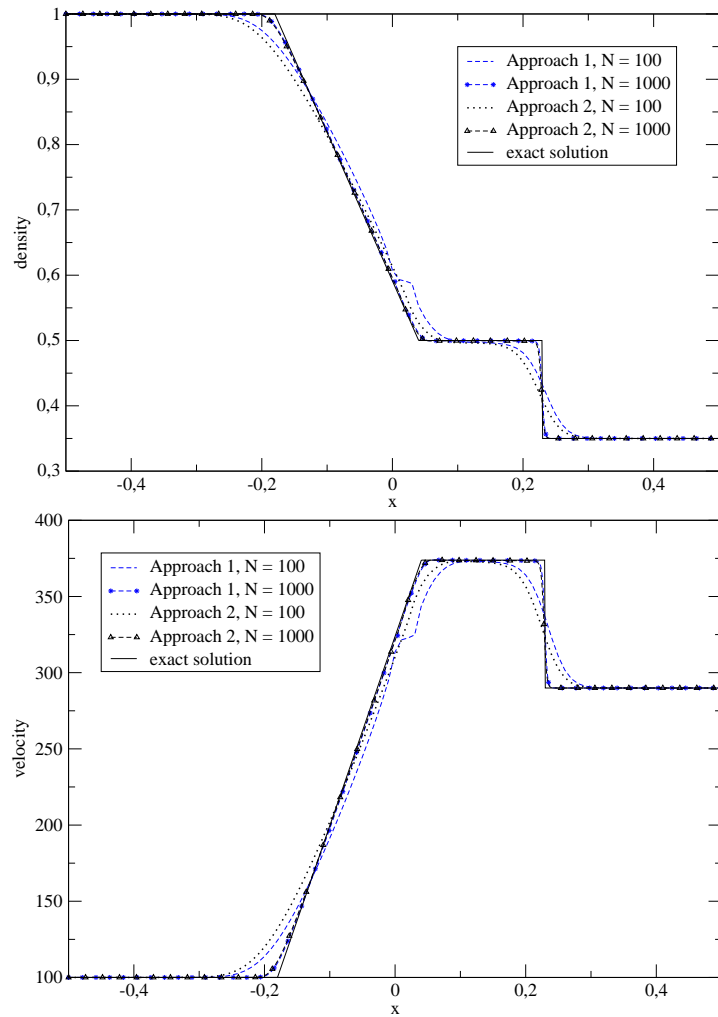


Figure 2.4: Supersonic shock tube: comparison of density and velocity solutions

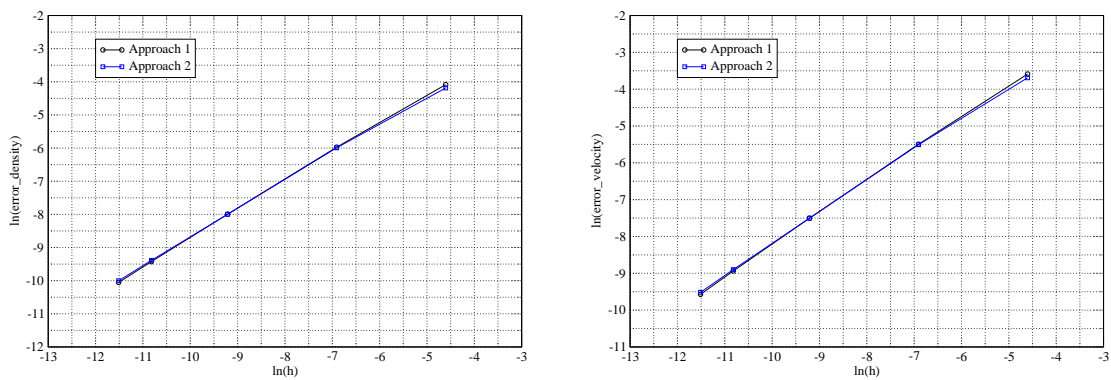


Figure 2.5: L1 convergence curves for supersonic shock tube: density (left), velocity (right). Coarser mesh: 100 cells; finer mesh: 10^5 cells

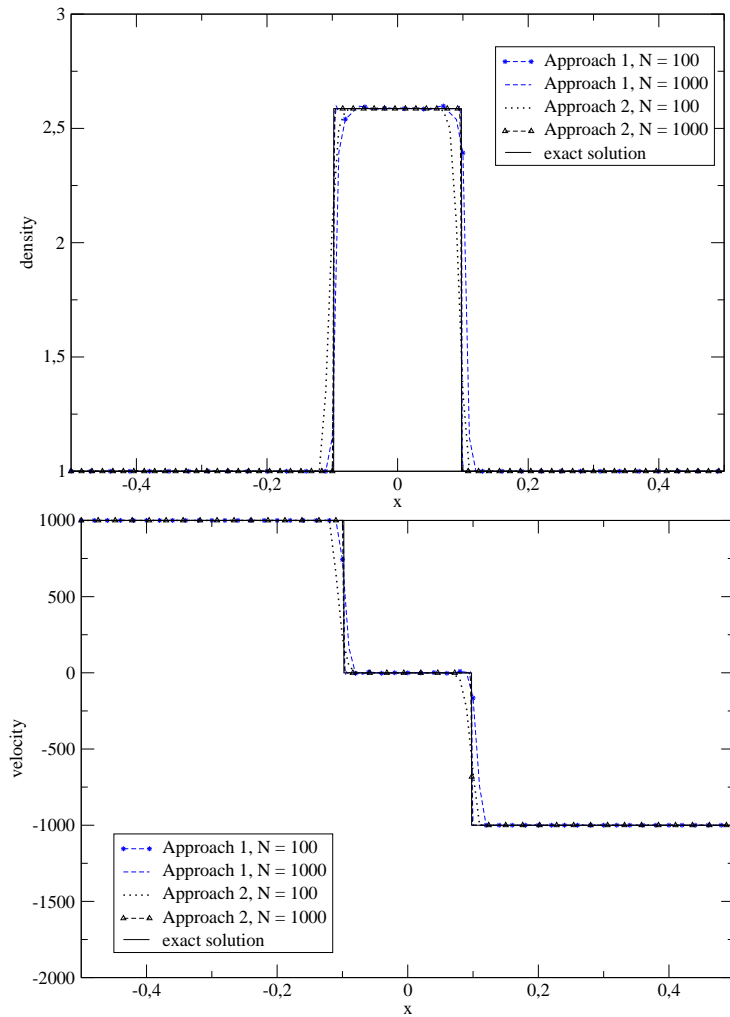
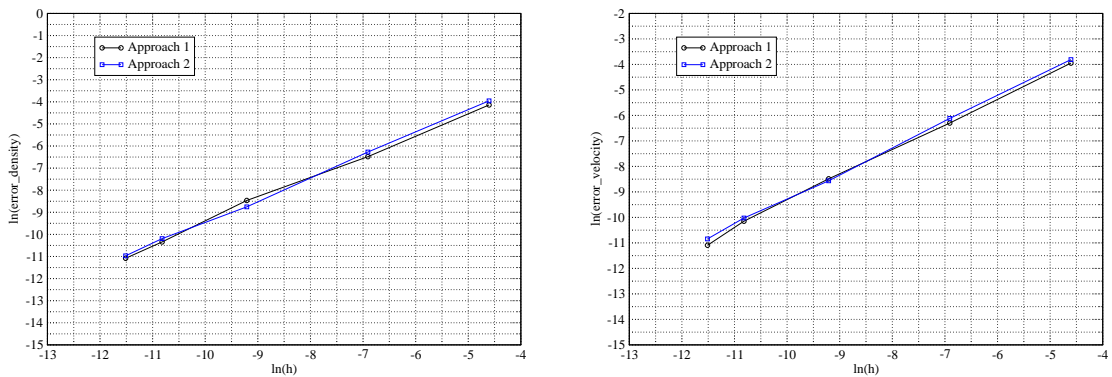


Figure 2.6: Symmetric double shock: comparison of density and velocity solutions

Figure 2.7: L1 convergence curves for symmetric double shock: density (left), velocity (right). Coarser mesh: 100 cells; finer mesh: 10^5 cells

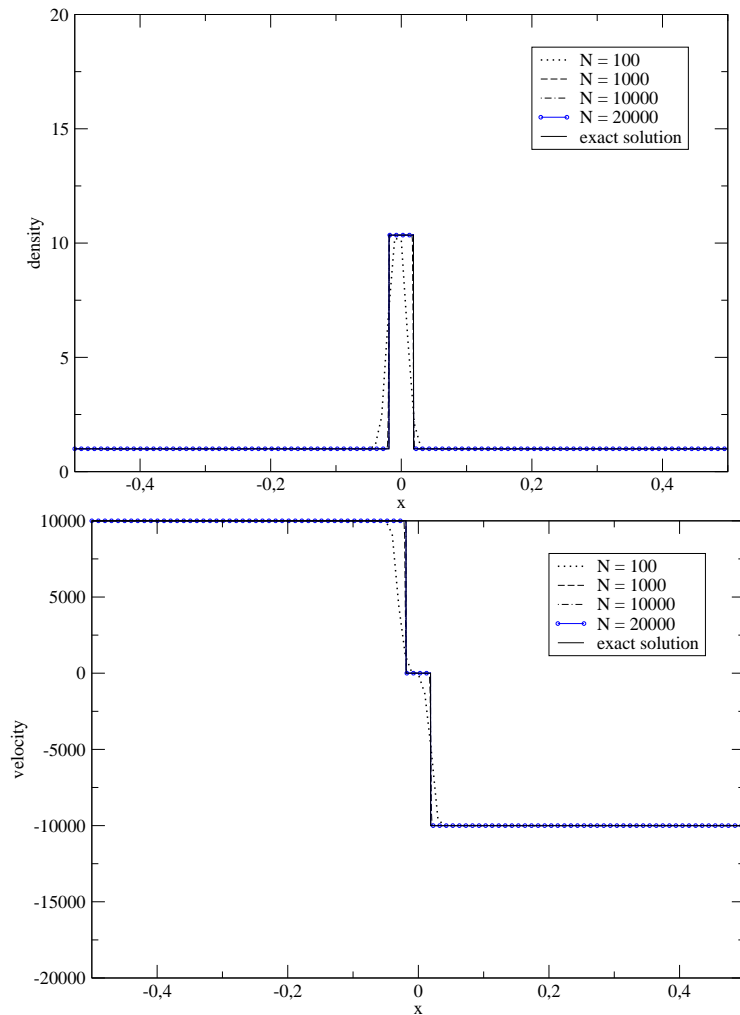


Figure 2.8: Symmetric double shock: density and velocity solutions with approach A2

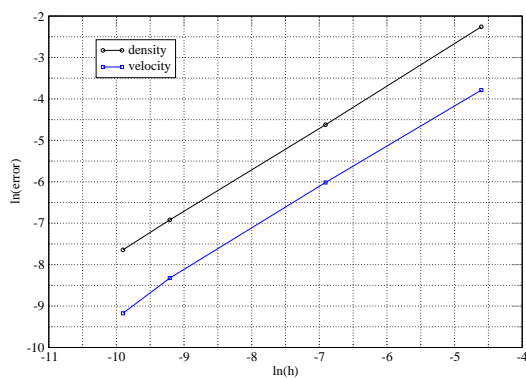


Figure 2.9: L1 convergence curves for symmetric double shock using approach A2. Coarser mesh: 100 cells; finer mesh: 10^5 cells

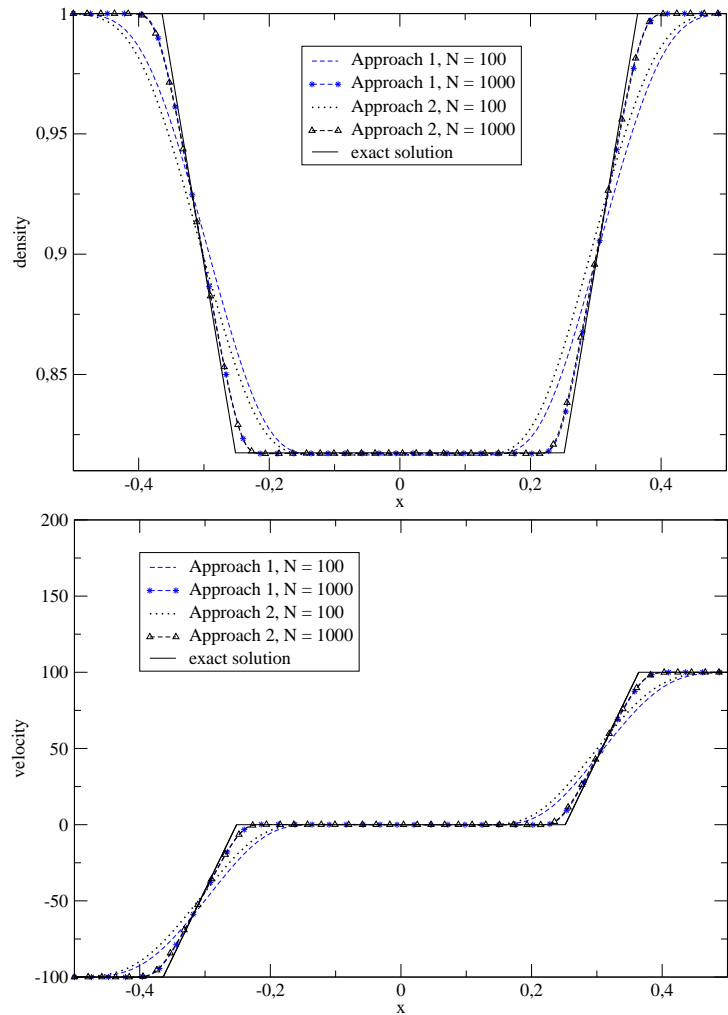


Figure 2.10: Symmetric double rarefaction: comparison of density and velocity solutions

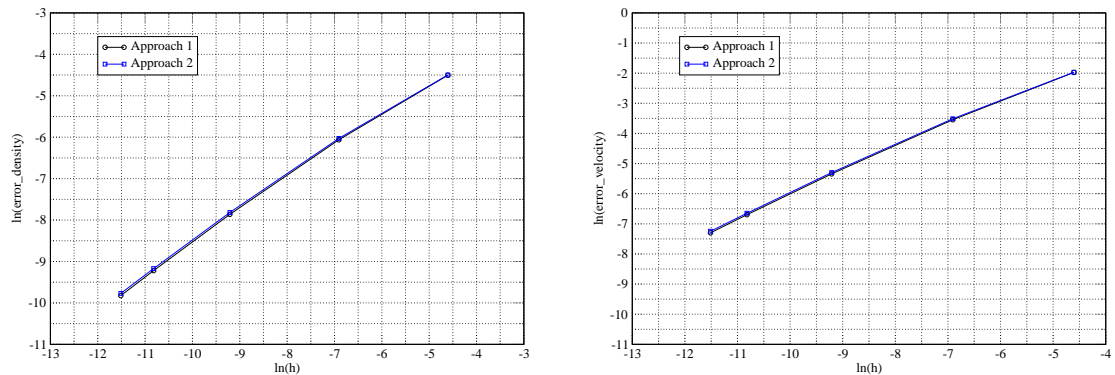


Figure 2.11: L1 convergence curves for symmetric double rarefaction: density (left), velocity (right). Coarser mesh: 100 cells; finer mesh: 10^5 cells

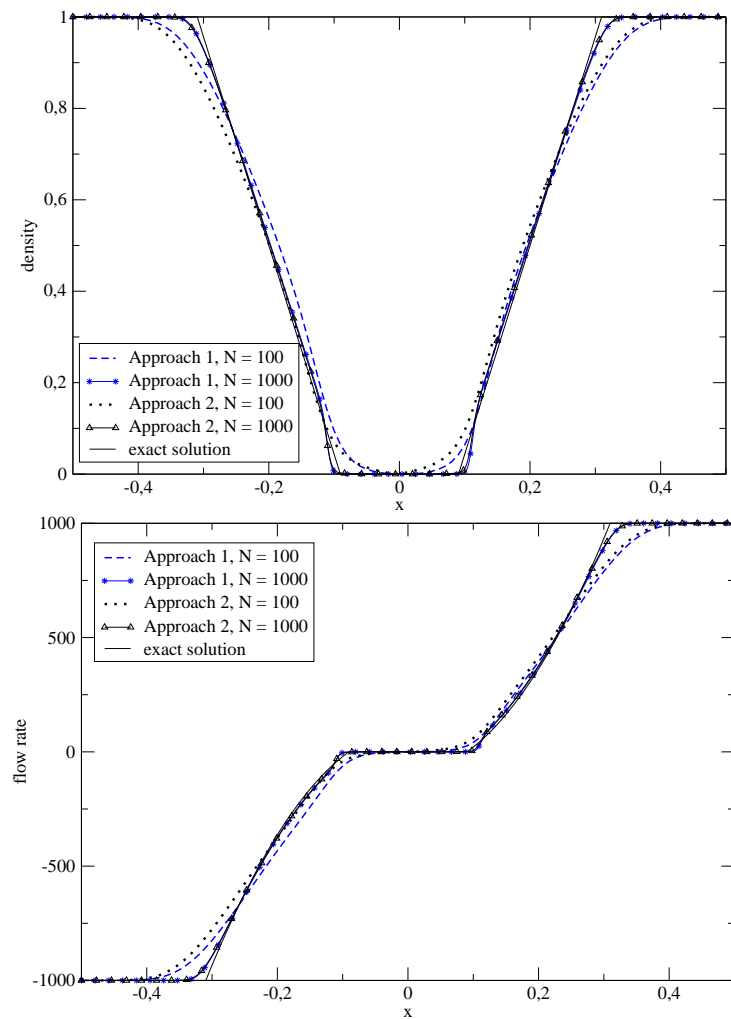


Figure 2.12: Symmetric double rarefaction with vacuum occurence: comparison of density and flow rate solutions

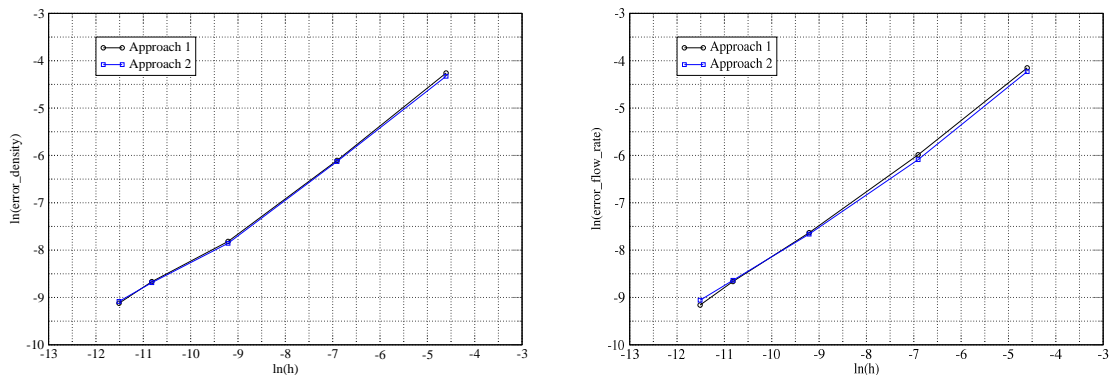


Figure 2.13: L1 convergence curves for symmetric double rarefaction with vacuum: density (left), flow rate (right). Coarser mesh: 100 cells; finer mesh: 10^5 cells

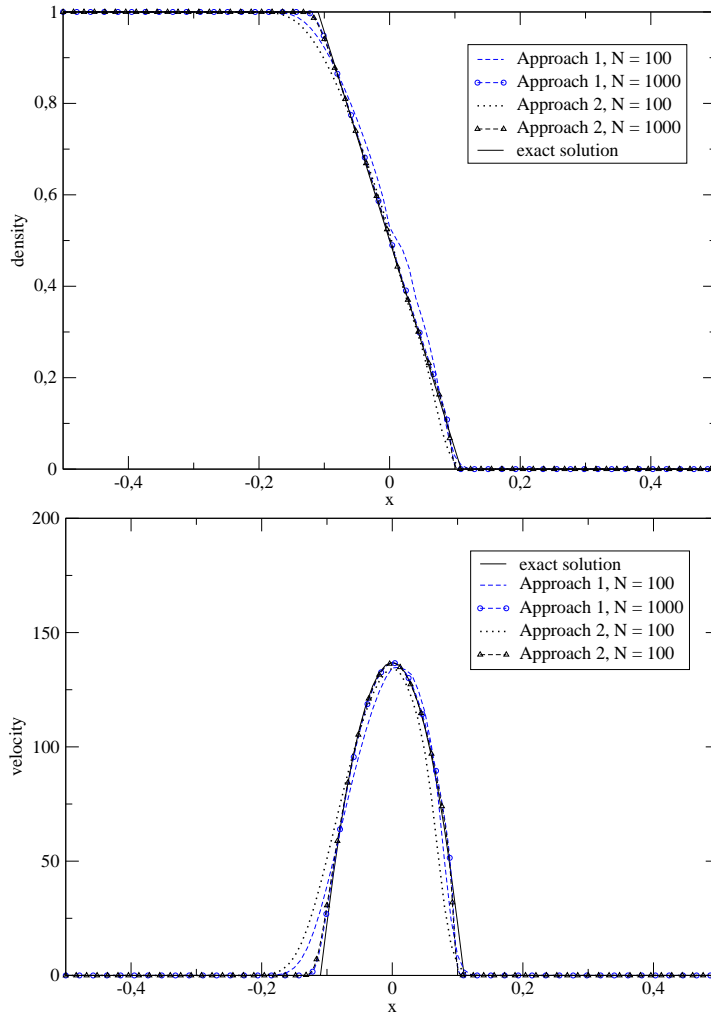


Figure 2.14: 1-supersonic rarefaction wave: comparison of density and velocity solutions

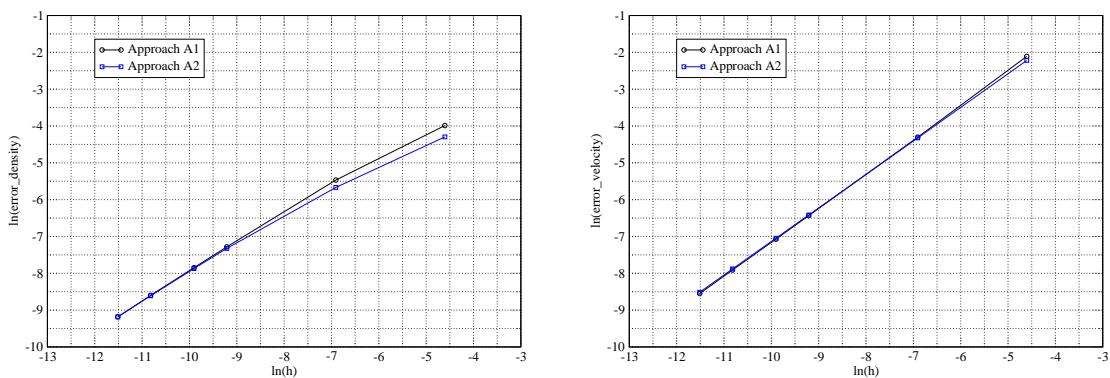


Figure 2.15: L1 convergence curve for 1-supersonic rarefaction wave: density (left), velocity (right). Coarser mesh: 100 cells; finer mesh: 10^5 cells

Appendix A. a_0 parameter evaluation

We consider two constant states Z_l, Z_r that refer to the Riemann problem (2.2.6), (2.2.11) with $\Psi = a_0^2 \vartheta$ and such that: $R_{l,r} > 0$ and $\rho_{l,r} > 0$. To find a suitable value of a_0 associated with this problem (that is the value that allows to find a compromise between the stability and the accuracy of numerical approximations) the following two conditions are imposed:

- **Wave ordering condition**

As it has been shown in sec. 2.2.3, the wave ordering condition

$$\lambda_1(Z) < \lambda_2(Z) < \lambda_3(Z) \quad (2.4.17)$$

ensures the positivity of ϑ_1, ϑ_2 and is used to get a lower bound for a_0 . With shortened notations

$$\bar{x}_{lr} = \frac{x_l + x_r}{2}, \quad [x]_l^r = (x_r - x_l), \quad (2.4.18)$$

condition (2.4.17) leads us to the next system of inequalities:

$$\begin{cases} 2\vartheta_l a_0^2 + [U]_l^r a_0 - [\rho R]_l^r > 0 \\ 2\vartheta_r a_0^2 + [U]_l^r a_0 + [\rho R]_l^r > 0 \end{cases} \quad (2.4.19)$$

with discriminants expressed by

$$\begin{aligned} \Delta_1 &= ([U]_l^r)^2 + 8\vartheta_l [\rho R]_l^r \\ \Delta_2 &= ([U]_l^r)^2 - 8\vartheta_r [\rho R]_l^r. \end{aligned} \quad (2.4.20)$$

Then, if $\Delta_1 \geq 0$ we have

$$(a_0)_{1,2} = \frac{-[U]_l^r \pm \sqrt{\Delta_1}}{4\vartheta_l}.$$

When $\Delta_2 \geq 0$, we find

$$(a_0)_{3,4} = \frac{-[U]_l^r \pm \sqrt{\Delta_2}}{4\vartheta_r}.$$

Finally, the whole algorithm for computing a_0 under the wave ordering condition can be summarized as follows.

Algorithm:

We take an initial value for the parameter ε :

$$\varepsilon = (3R_0)^{1/2} \rho_0 \quad \text{with} \quad R_0 = \bar{R}_{lr}, \quad \rho_0 = \bar{\rho}_{lr}$$

If $\Delta_1 \geq 0$ and $\Delta_2 \geq 0$ then $a_0 = \max \{\varepsilon, (a_0)_i\}$, $i = 1, 2, 3, 4$.

If $\Delta_1 \geq 0$ and $\Delta_2 < 0$ then $a_0 = \max \{\varepsilon, (a_0)_i\}$, $i = 1, 2$.

If $\Delta_1 < 0$ and $\Delta_2 \geq 0$ then $a_0 = \max \{\varepsilon, (a_0)_i\}$, $i = 3, 4$.

If $\Delta_1 < 0$ and $\Delta_2 < 0$ then $a_0 = \varepsilon$.

Let us denote the lower bound obtained for a_0 at this stage by a_0^λ .

• Whitham's condition

- Following for instance [9], in order to obtain stable approximations of the barotropic Euler equations

$$\begin{cases} \partial_t \rho + \partial_x(\rho U) = 0, & t > 0, \quad x \in \mathbb{R}, \\ \partial_t(\rho U) + \partial_x(\rho U^2) + \partial_x p(\tau) = 0, \end{cases} \quad (2.4.21)$$

where ρ is the density, U is the velocity, $\tau(t, x) = 1/\rho(t, x)$ is the specific volume, and p is the pressure law, one may introduce a relaxation system of the form ($\lambda > 0$):

$$\begin{cases} \partial_t \rho + \partial_x(\rho U) = 0, & t > 0, \quad x \in \mathbb{R}, \\ \partial_t(\rho U) + \partial_x(\rho U^2) + \partial_x \pi = 0, \\ \partial_t(\rho \mathcal{T}) + \partial_x(\rho \mathcal{T} U) = \lambda \rho(\tau - \mathcal{T}), \end{cases} \quad (2.4.22)$$

with the so-called relaxed pressure:

$$\pi(\mathcal{T}, \tau) = p(\mathcal{T}) + a_0^2(\mathcal{T} - \tau),$$

which is expected to tend to $p(\tau)$ when $\mathcal{T} \rightarrow \tau$. Setting $\varepsilon(\tau)$: $\varepsilon(\tau) = -p'(\tau)$ and restricting to smooth solutions, the governing equation of the relaxation entropy

$$\rho \Sigma = \frac{\rho U^2}{2} + \rho \varepsilon(\mathcal{T}) + \rho \frac{\pi^2 - p^2(\mathcal{T})}{2a_0^2},$$

is given by (see [9]):

$$\partial_t(\rho \Sigma) + \partial_x(\rho \Sigma U + \pi U) = -\lambda \rho(a_0^2 + p'(\mathcal{T}))(\mathcal{T} - \tau)^2. \quad (2.4.23)$$

Thus, the relaxation entropy is dissipated by the relaxation procedure if

$$a_0^2 > -p'(\mathcal{T}), \text{ for all realizable } (\tau, U, \mathcal{T}). \quad (2.4.24)$$

At the discrete level, the explicit numerical algorithm corresponding to formulation (2.4.22) only requires at each time $t = t^n$ the knowledge of

$$\begin{cases} \mathcal{T}^n = \tau^n = 1/\rho^n, \\ \pi^n = p(\mathcal{T}^n) = p(\tau^n) = p^n. \end{cases} \quad (2.4.25)$$

Hence, the explicit form of the function $p(\mathcal{T})$ is not compulsory, only the cell values p^n are needed. However, condition (2.4.24) requires an estimation of $p'(\mathcal{T})$, which is unknown if $p(\mathcal{T})$ is unknown. Thus, if $p(\mathcal{T})$ is unknown, this entropy dissipation principle cannot be used in practice to compute a lower bound for a_0^2 .

- In our framework, the correspondence can be made between the present system (2.4.21) and equations (2.2.1) setting $p(\tau, R^L) = R^L/\tau$, but a lower bound of a_0^2 cannot be obtained on the basis of (2.4.23), (2.4.24), which no longer make sense.

Thus, in order to ensure the numerical stability of the method at a discrete level, we introduce a local estimate:

$$\frac{\Delta p}{\Delta \tau} = \frac{\Delta_{l,r}(R^L/\tau)}{\Delta_{l,r}(\tau)},$$

where “ l “ and “ r “ refers to the left and right discrete states respectively, by assuming that locally $p = \rho R^L$ behaves as $K_{l,r}\tau^{-3}$ with

$$K_{l,r} = \frac{1}{2} (\tau_l^2 R_l^L + \tau_r^2 R_r^L).$$

Then, the local **counterpart of Whitham's condition** is given by the inequality:

$$a_0^2 > K_{l,r} (\tau_l^{-2} + (\tau_l \tau_r)^{-1} + \tau_r^{-2}) (\tau_l \tau_r)^{-1},$$

and the associated lower bound for a_0 is denoted by: $(a_0^W)^2 = K_{l,r} (\tau_l^{-2} + (\tau_l \tau_r)^{-1} + \tau_r^{-2}) (\tau_l \tau_r)^{-1}$.

- If we assume a **particular expression** in Eqs.(2.2.1): $\rho R^L = \pi(\rho)$ with $\pi \in C^\infty([0, +\infty[)$, such that $\pi'(\rho) > 0$ for all $\rho > 0$, in order to prevent the relaxation system (2.2.4) (with $\Psi = a_0^2 \vartheta$) from instabilities, we need to comply with Whitham's condition (see for instance [4, 5]):

$$a_0 \vartheta > c_\phi. \quad (2.4.26)$$

where c_ϕ is the celerity corresponding to original system (2.2.1). In this particular case, we can calculate the speed of acoustic waves:

$$c_\phi^2 = \pi'(\rho).$$

For the isentropic Euler equations with $\gamma = 3$ (which besides corresponds to the approach A1), we have an explicit formula:

$$\rho R = S_0 \rho^3 \quad \text{with} \quad S_0 = \frac{R_0}{\rho_0^2}. \quad (2.4.27)$$

Then,

$$c_\phi = \sqrt{3R_0} \left(\frac{\rho}{\rho_0} \right) \quad (2.4.28)$$

and, taking $\rho = \max(\rho_l, \rho_r)$, Whitham's condition can be formulated as follows:

$$a_0 > \sqrt{3R_0} \left(\frac{\rho^2}{\rho_0} \right), \quad (2.4.29)$$

with a lower bound $a_0^W = \sqrt{3R_0} \rho^2 / \rho_0$.

Finally, we take $a_0 = \max(a_0^\lambda, a_0^W)$.

Appendix B. Energy control in the relaxation systems (A1/A2)

In order to give an estimate of the mean kinetic energy, which is characterizing the initial system of equations (2.2.1), we study the evolution of the “total” energy in the relaxation system. We focus on smooth solutions in this appendix.

Let us denote by

$$E(x, t) = \frac{1}{2} (\rho U^2)(x, t) \geq 0 \quad \text{and} \quad \mathbb{E}(t) = \int_{\Omega} E(x, t) dx \geq 0 \quad (2.4.30)$$

the kinetic energy of the drift (the mean motion), by

$$K(x, t) = \frac{1}{2} (\rho R)(x, t) \geq 0 \quad \text{and} \quad \mathbb{K}(t) = \int_{\Omega} K(x, t) dx \geq 0 \quad (2.4.31)$$

the energy of fluctuating particle motion, and by

$$\mathcal{E}(x, t) = E(x, t) + K(x, t) = \frac{1}{2} (\rho U^2)(x, t) + \frac{1}{2} (\rho R)(x, t) \geq 0, \quad (2.4.32)$$

$$\Sigma(t) = \int_{\Omega} \mathcal{E}(x, t) dx = \mathbb{E}(t) + \mathbb{K}(t) \geq 0 \quad (2.4.33)$$

the “total” particle energy.

Approach (A1). We study the homogeneous relaxation system corresponding to the approach (A1):

$$\begin{cases} \frac{\partial \rho}{\partial t} + \frac{\partial}{\partial x}(\rho U) = 0 \\ \frac{\partial}{\partial t}(\rho U) + \frac{\partial}{\partial x}(\rho U^2) + \frac{\partial}{\partial x}(\rho R) = 0 \\ \frac{\partial}{\partial t}(\rho R) + \frac{\partial}{\partial x}(\rho U R) + 2\rho R \frac{\partial U}{\partial x} = 0 \end{cases} \quad (2.4.34)$$

on the closed domain $\Omega \times [0, T]$ with realizable initial conditions and homogeneous Dirichlet boundary conditions on U : $U(x, t)|_{\partial\Omega} = 0$.

From (3.2.12.1), (3.2.12.2) we obtain an equation for the mean energy evolution:

$$\frac{\partial}{\partial t} \left(\frac{1}{2} \rho U^2 \right) + \frac{\partial}{\partial x} \left(U \cdot \frac{1}{2} \rho U^2 \right) + U \frac{\partial}{\partial x} (\rho R) = 0 \quad (2.4.35)$$

or

$$\frac{\partial E}{\partial t} + \frac{\partial}{\partial x} (UE) + \frac{\partial}{\partial x} (2KU) - 2K \frac{\partial U}{\partial x} = 0 \quad (2.4.36)$$

In the same manner, from (3.2.12.3) we develop an equation for the evolution of $K(x, t)$:

$$\frac{\partial K}{\partial t} + \frac{\partial}{\partial x} (UK) + 2K \frac{\partial U}{\partial x} = 0 \quad (2.4.37)$$

Finally, we get an equation for the “total” energy variation:

$$\frac{\partial \mathcal{E}}{\partial t} + \frac{\partial}{\partial x} (U\mathcal{E}) + \frac{\partial}{\partial x} (2UK) = 0. \quad (2.4.38)$$

From this equation, owing to the homogeneous Dirichlet boundary conditions on U it follows that

$$\frac{\partial}{\partial t} \int_{\Omega} \mathcal{E} dx = 0. \quad (2.4.39)$$

Thus, during the evolution step the total energy is conserved:

$$\Sigma(t^{n+1,-}) = \Sigma(t^n) \quad (2.4.40)$$

that can be rewritten in the form:

$$\mathbb{E}(t^{n+1,-}) + \mathbb{K}(t^{n+1,-}) = \mathbb{E}(t^n) + \mathbb{K}(t^n). \quad (2.4.41)$$

If we assume that:

- $K(x, t^n) \geq 0$ is ensured by initial conditions,
- $\forall t \in [t^n, t^{n+1}], K(x_{\Gamma^-}, t^n) \geq 0$ on $\Gamma^- = \{x \in \partial\Omega \mid U(x, t).n < 0\}$, where n denotes the outward normal,
- $\forall t \in [t^n, t^{n+1}], U(x, t)$ and $\frac{\partial U}{\partial x}(x, t) \in L^\infty(\Omega \times [t^n, t^{n+1}])$,

then on $\Omega \times [t^n, t^{n+1,-}]$ $K(x, t)$ solution of (2.4.37) remains positive. Thus:

$$\mathbb{K}(t^{n+1,-}) = \int_{\Omega} K(x, t^{n+1,-}) dx \geq 0, \quad (2.4.42)$$

where $K(x, t^{n+1,-})$ is solution of (2.4.37).

We have also:

$$\mathbb{E}(t^{n+1}) = \mathbb{E}(t^{n+1,-}) \quad (2.4.43)$$

since $E = E(\rho, U)$, and $\rho^{n+1} = \rho^{n+1,-}$, $U^{n+1} = U^{n+1,-}$.

Finally, since $(\mathbb{E}(t^n) + \mathbb{K}(t^n))$ is bounded we obtain from (2.4.41) the following estimate of the energy $\mathbb{E}(t^{n+1})$:

$$0 \leq \mathbb{E}(t^{n+1}) = \mathbb{E}(t^n) + \mathbb{K}(t^n) - \mathbb{K}(t^{n+1,-}) \leq \mathbb{E}(t^n) + \mathbb{K}(t^n). \quad (2.4.44)$$

Thus $\mathbb{E}(t^{n+1}) = \mathbb{E}(\rho^{n+1}, U^{n+1})$ is bounded.

Approach (A2). Now, we apply the same reasoning to obtain the estimate for the mean kinetic energy for the relaxation system corresponding to approach (A2):

$$\begin{cases} \frac{\partial \rho}{\partial t} + \frac{\partial}{\partial x}(\rho U) = 0 \\ \frac{\partial}{\partial t}(\rho U) + \frac{\partial}{\partial x}(\rho U^2 + \rho R) = 0 \\ \frac{\partial}{\partial t}(\rho R) + \frac{\partial}{\partial x}(\rho U R) + (a_0^2 \vartheta - \rho R) \frac{\partial U}{\partial x} = 0 \end{cases} \quad (2.4.45)$$

Keeping the notations (2.4.30) - (2.4.33), we have the same equation for the mean kinetic energy evolution:

$$\frac{\partial E}{\partial t} + \frac{\partial}{\partial x} (UE) + \frac{\partial}{\partial x} (2KU) - 2K \frac{\partial U}{\partial x} = 0 \quad (2.4.46)$$

The counterpart of (2.4.37) for the evolution of the fluctuating motion energy $K(x, t)$ is:

$$\frac{\partial K}{\partial t} + \frac{\partial}{\partial x} (UK) + 2K \frac{\partial U}{\partial x} + \frac{1}{2} (a_0^2 \vartheta - 3\rho R) \frac{\partial U}{\partial x} = 0. \quad (2.4.47)$$

But here, we can not obtain a conservative equation for the “total” energy evolution. Actually, the sum of the last two equations results in a non-conservative equation:

$$\frac{\partial \mathcal{E}}{\partial t} + \frac{\partial}{\partial x} (U\mathcal{E}) + \frac{\partial}{\partial x} (2UK) + \frac{1}{2} (a_0^2 \vartheta - 3\rho R) \frac{\partial U}{\partial x} = 0. \quad (2.4.48)$$

For this reason, we introduce a slightly modified definition of the total energy, which is now called \mathcal{E}' :

$$\mathcal{E}' = \mathcal{E} + \rho g(\omega) = E + K + \rho g(\omega), \quad (2.4.49)$$

where

$$\omega(\rho, R) = a_0^2 \vartheta - 3\rho R. \quad (2.4.50)$$

We note that ω may be viewed as a “small parameter” that measures the drift between (A1) and (A2).

For any solution (ρ, R) of the system (3.2.13), the function $g(\omega)$ complies with:

$$\frac{\partial(\rho g)}{\partial t} + \frac{\partial}{\partial x} (\rho U g) - 4a_0^2 g'(\omega) \frac{\partial U}{\partial x} = 0. \quad (2.4.51)$$

Moreover, we have:

$$\frac{\partial \mathcal{E}}{\partial t} + \frac{\partial}{\partial x} (U\mathcal{E}) + \frac{\partial}{\partial x} (2UK) + \frac{\omega}{2} \frac{\partial U}{\partial x} = 0, \quad (2.4.52)$$

The sum of these two gives us the equation for the “total” energy \mathcal{E}' evolution:

$$\frac{\partial}{\partial t} (\mathcal{E} + \rho g) + \frac{\partial}{\partial x} (U(\mathcal{E} + \rho g)) + \frac{\partial}{\partial x} (2UK) + \left(\frac{\omega}{2} - 4a_0^2 g'(\omega) \right) \frac{\partial U}{\partial x} = 0. \quad (2.4.53)$$

If we choose

$$g(\omega) = \frac{\omega^2}{16a_0^2} \geq 0, \quad (2.4.54)$$

we can rewrite equations for E, K and (ρg) as follows:

$$\begin{cases} \frac{\partial E}{\partial t} + \frac{\partial}{\partial x} (UE) + \frac{\partial}{\partial x} (2KU) - 2K \frac{\partial U}{\partial x} = 0 \\ \frac{\partial K}{\partial t} + \frac{\partial}{\partial x} (UK) + 2K \frac{\partial U}{\partial x} + \frac{\omega}{2} \frac{\partial U}{\partial x} = 0 \\ \frac{\partial(\rho g)}{\partial t} + \frac{\partial}{\partial x} (U\rho g) - \frac{\omega}{2} \frac{\partial U}{\partial x} = 0 \end{cases} \quad (2.4.55)$$

Hence, equation (2.4.53) for the energy \mathcal{E}' evolution is conservative:

$$\frac{\partial \mathcal{E}'}{\partial t} + \frac{\partial}{\partial x} (U\mathcal{E}') + \frac{\partial}{\partial x} (2UK) = 0. \quad (2.4.56)$$

Thus, the total energy \mathcal{E}' is conserved during the evolution step:

$$\Sigma'(t) = \int_{\Omega} \mathcal{E}'(x, t) dx, \quad \Sigma'(t^{n+1,-}) = \Sigma'(t^n), \quad (2.4.57)$$

still using homogeneous Dirichlet boundary conditions for $U(x, t)$. This is equivalent to:

$$\mathbb{E}(t^{n+1,-}) + \mathbb{K}(t^{n+1,-}) + \int_{\Omega} (\rho g)(x, t^{n+1,-}) dx = \mathbb{E}(t^n) + \mathbb{K}(t^n) + \int_{\Omega} (\rho g)(x, t^n) dx, \quad (2.4.58)$$

or:

$$0 \leq \mathbb{E}(t^{n+1}) = \mathbb{E}(t^{n+1,-}) = \mathbb{E}(t^n) + \mathbb{K}(t^n) + \int_{\Omega} (\rho g)(x, t^n) dx - \mathbb{K}(t^{n+1,-}) - \int_{\Omega} (\rho g)(x, t^{n+1,-}) dx. \quad (2.4.59)$$

Hence:

$$0 \leq \mathbb{E}(t^{n+1}) \leq \mathbb{E}(t^n) + \mathbb{K}(t^n) + \int_{\Omega} (\rho g)(x, t^n) dx - \mathbb{K}(t^{n+1,-}) \quad (2.4.60)$$

since $(\rho g)(x, t) \geq 0$.

Appendix C. On hybrid modeling of dispersed turbulent two-phase flows

Polydispersed two-phase flows consisting of a turbulent carrier phase (a liquid or a gas) and dispersed particles (solid particles, droplets or bubbles) are complex processes which are very important in many industrial situations. Therefore, an accurate prediction of these flows is required for engineering purposes. Furthermore, for the modeling and numerical simulation of a polydispersed two-phase flow, the two phases (fluid and particles phase) have to be treated in a coupled way.

However, the two most popular approaches (Eulerian and Lagrangian) for two-phase flow modeling have disadvantages which limit their capacities. Hybrid methods try to gather the advantages of the Eulerian approach (expected values free from statistical error and low calculation costs) with those of the Lagrangian approach (polydispersity and non-linear local source terms are treated without approximations) [31, 32]. At the moment, most hybrid methods use only one description (Eulerian or Lagrangian) for each phase. The idea of the hybrid method introduced in [10] is to use a mixed Eulerian/Lagrangian formulation for the dispersed phase while the properties of fluid remain calculated with the Eulerian approach. By treating some statistical quantities (such as the mean particle velocity and the local particle concentration) in an Eulerian manner (i.e. as mean fields defined on a fixed grid), the overall system is less sensitive to errors introduced by statistical noise. This, in turn, will eventually allow for computations using a smaller number of computational particles, thus leading to faster calculations. Therefore, in this new hybrid method the two approaches are coupled in a fully consistent manner while keeping the high level of physical information provided by the Lagrangian description. The incompressible fluid phase is described by Reynolds Averaged Navier-Stokes (RANS) equations which are solved by an Eulerian Finite Volume solver (that is not detailed here). Then, the fluid-related mean fields (i.e. mean pressure

$\langle P \rangle$ (or its gradient), mean fluid velocity $\langle \mathbf{U}_f \rangle$, Reynolds stress tensor $\mathbf{R} = \{R_{ij}\}_{i,j=1}^d$, with d – space dimensions and the dissipation rate of the turbulent kinetic energy $\langle \epsilon \rangle$) are provided to the particle-phase model. The flows we are dealing with are considered to be dilute enough in particles not to consider the turbulence modulation. The dispersed (particle) phase is modeled by a coupled Eulerian/Lagrangian description. The Lagrangian part of the model is given by stochastic differential equations (SDEs), which are solved by resorting to particle/mesh Monte-Carlo methods [34]. The Eulerian part of the particle model is given by a system of partial differential equations for mean quantities which present an important convective part. These equations describe the time evolution of the first order moments of the particle volume fraction and the instantaneous particle velocity and are deduced from Lagrangian stochastic description ([31], chap.6.7). Thus, both systems are consistent by construction.

In order to guarantee the coupling of methods for the particle description we have to choose the averaging and interpolation procedures, that is how information is exchanged from the mesh to the stochastic particles (interpolation of Eulerian mean fields at particle positions) and from the stochastic particles to the mesh (how mean fields are extracted). Moreover, such a coupling introduces noisy quantities (computed by the stochastic equations) in the Eulerian part of the model.

An example of the particle phase simulation using hybrid method

In this appendix we present a two-dimensional case of turbulent two-phase wall jet, where solid particles are involved in the turbulent air flow, which is characterized by the non-homogeneous anisotropic stationary turbulence. Only the particle hybrid (Eulerian/Lagrangian) model is solved, whereas the fluid mean fields are provided by a preliminary single-phase computation and are taken as frozen fields. We consider heavy enough particles in a such a way that the gravity and the drag forces are predominant in a two-dimensional framework, and we intend to compare the first order particle moments computed using the present hybrid model (these will be referred to as Eulerian coupled approximations) with those provided by a stand alone Lagrangian computation (“pure” Lagrangian) for the particle phase in the same flow configurations.

Mean-field/PDF hybrid model and experimental setup

We consider a rectangular domain of dimensions $Lx \times Ly$. A sketch of the geometry is given in Fig.2.16, where AE is a wall boundary. Air at ambient temperature and atmospheric pressure is injected both in AB and BC regions. Solid particles are injected in AB region of diameter d and after some time leave the domain by outlets CD and DE. A stationary turbulent two-phase flow is eventually obtained.

- The Lagrangian stochastic description of the dispersed phase is given by the Simple Langevin Model (SLM) [31]:

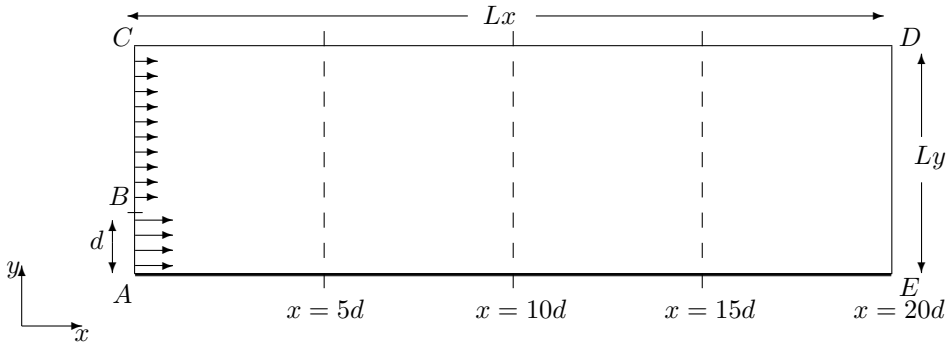


Figure 2.16: Computational domain, definition of the geometry of a wall jet of diameter d .

$$\begin{cases} dx_{p,i} = U_{p,i} dt, \\ dU_{p,i} = \frac{U_{s,i} - U_{p,i}}{\tau_p} dt, \quad i = 1, 2, \quad t > 0, \\ dU_{s,i} = -\frac{1}{\rho_f} \frac{\partial \langle P \rangle}{\partial x_i} dt - \frac{U_{s,i} - \langle U_{f,i} \rangle}{T_L} dt + \sqrt{C_0 \langle \varepsilon \rangle} dW_{t,i}, \end{cases} \quad (2.4.61)$$

where $\mathbf{x}_p(t)$ the particle position, $\mathbf{U}_p(t)$ the particle velocity, $\mathbf{U}_s(t)$ the fluid velocity seen at the particle position and $\mathbf{W}(t)$ the vector of independent Wiener processes, all variables (random processes) being defined on the same probability space [33]. The particle relaxation time scale τ_p is a function of the particle inertia and represents the time necessary for a particle to adjust to fluid velocities, T_L stands for the fluid integral timescale. The fluid mean fields $k, \langle \varepsilon \rangle, \langle \mathbf{U}_f \rangle, \langle P \rangle$ are external data computed in advance with $k - \varepsilon$ model and then used as a frozen field. Following Monte-Carlo algorithm, particle related statistics can be obtained from equations (2.4.61) for a given averaging operator. In practice, at each cell $j \in \mathbb{Z}$ of the mesh (with the cell center \mathbf{x}_j) containing $N_p^{[j]}$ particles at the time t , the following approximation is used to compute the particle volumetric fraction α_p :

$$\alpha_p(t, \mathbf{x}_j) = \frac{\sum_{n=1}^{N_p^{[j]}} v^{(n)}}{\mathcal{V}_j}, \quad (2.4.62)$$

where $v^{(n)}$ is the volume occupied by a particle and \mathcal{V}_j - the volume of the cell j , $j \in \mathbb{Z}$. For other mean particle quantities, we obtain the numerical approximations as mean averages:

$$\langle H_p \rangle(t, \mathbf{x}_j) \simeq \langle H_p \rangle_{N_p}(t, \mathbf{x}_j) = \frac{\sum_{n=1}^{N_p^{[j]}} H_p^{(n)}(t)}{N_p^{[j]}}. \quad (2.4.63)$$

- The Eulerian part of the hybrid model describes the time evolution of the first order statistical moments: the mean particle density, $\rho_p = \alpha_p \rho_p^0$ with constant ρ_0 , and the instantaneous mean particle velocity, $\langle \mathbf{U}_p \rangle$, whose governing equations are

$$\begin{cases} \partial_t \rho_p + \partial_{x_j} (\rho_p \langle U_{p,j} \rangle) = 0, \quad t > 0, \quad \mathbf{x} \in \mathbb{R}^2, \\ \partial_t (\rho_p \langle U_{p,i} \rangle) + \partial_{x_j} (\rho_p \langle U_{p,i} \rangle \langle U_{p,j} \rangle) + \partial_{x_j} (\rho_p R_{p,ij}^L) = \rho_p g_i + \rho_p \langle U_{r,i}^L / \tau_p^U \rangle, \end{cases} \quad (2.4.64)$$

where $\tau_p^U = \tau_p^L$ is the particle velocity relaxation time scale and $\mathbf{U}_r^L = (\mathbf{U}_s - \mathbf{U}_p)^L$ is the local relative velocity. The subscript “ p ” is used to emphasize the particle related variables, whereas the superscript “ L ” now refers to variables computed using Lagrangian description (2.4.61). For instance, the particle related kinetic tensor $R_{p,ij} = \langle u'_i u'_j \rangle$ ($i, j = 1, 2$) is computed using (2.4.63) and provided to the Eulerian particle model (2.4.64). In both Eulerian and Lagrangian descriptions, Reynolds decomposition takes place, thus $\mathbf{u}'_p(t, \mathbf{x}) = \mathbf{U}_p(t, \mathbf{x}) - \langle \mathbf{U}_p(t, \mathbf{x}) \rangle$. Right-hand side terms in the second equation of (2.4.64) describe the gravity and the drag forces. It is important to note that equations (2.4.64) have been actually deduced from system (2.4.61) ([31], chap.6.7). Thus, both Eulerian and Lagrangian descriptions are consistent by construction.

A two-dimensional relaxation scheme

As it was emphasized above, the coupling of descriptions (2.4.61), (2.4.64) introduces non-smooth quantities in the Eulerian part of the model (2.4.64), that can result in instabilities during numerical simulations. The present section aims at introducing a two-dimensional relaxation scheme for simulation of system (2.4.64) that could enable stable approximations in a number of limit situations. From now on, we omit the subscripts “ p ” and denote by ρ the mean particle density and by $U_i = \langle U_{p,i} \rangle$, $i = 1, 2$ the mean particle velocity. Hence, for given non-smooth values of the Lagrangian kinetic tensor $R_{ij}^L = \langle u'_{p,i} u'_{p,j} \rangle^L$, $\forall i, j \in \mathbb{Z}$, we want to compute stable approximations of solutions of:

$$\begin{cases} \partial_t \rho + \partial_{x_j}(\rho U_j) = 0, & t > 0, \quad \mathbf{x} \in \mathbb{R}^2, \\ \partial_t(\rho U_i) + \partial_{x_j}(\rho U_i U_j) + \partial_{x_j}(\rho R_{ij}^L) = \rho g_i + \rho \langle U_{r,i}/\tau_p \rangle^L. \end{cases} \quad (2.4.65)$$

By construction, R_{ij}^L , $i, j = 1, 2$ complies with the *realizability condition*:

$$x_i R_{ij}^L x_j \geq 0 \quad \forall x_i, x_j \quad (i, j = 1, 2). \quad (2.4.66)$$

On the basis of [3, 27], getting rid of physical source terms $(\rho g_i + \rho \langle U_{r,i}/\tau_p \rangle^L)$, $i = 1, 2$, the following relaxation system naturally arises:

$$\begin{cases} \partial_t \rho + \partial_{x_j}(\rho U_j) = 0, & t > 0, \quad \mathbf{x} \in \mathbb{R}^2, \\ \partial_t(\rho U_i) + \partial_{x_j}(\rho U_i U_j) + \partial_{x_j}(\rho R_{ij}) = 0, \\ \partial_t(\rho R_{ij}) + \partial_{x_k}(\rho U_k R_{ij}) + \rho(R_{ik}\partial_{x_k} U_j + R_{jk}\partial_{x_k} U_i) = \rho(R_{ij}^L - R_{ij})/\tau_p^R. \end{cases} \quad (2.4.67)$$

This system is invariant under frame rotation. If we consider the reference frame (\mathbf{n}, τ) , where $\mathbf{n} = (n_x, n_y)$, $\tau = (-n_y, n_x)$, such that $n_x^2 + n_y^2 = 1$, we may introduce: $U_n = \mathbf{U} \cdot \mathbf{n}$, $U_\tau = \mathbf{U} \cdot \tau$, $R_{nn} = \mathbf{n}^t \cdot \mathbf{R} \cdot \mathbf{n}$, $R_{n\tau} = \mathbf{n}^t \cdot \mathbf{R} \cdot \tau = \tau^t \mathbf{R} \cdot \mathbf{n} = R_{\tau n}$, $R_{\tau\tau} = \tau^t \cdot \mathbf{R} \cdot \tau$. While neglecting transverse variations, the homogeneous system corresponding to (3.2.2) written in terms of the new variable $Z_{2D} = (\rho, U_n, U_\tau, \rho R_{nn}, \rho R_{n\tau}, S)^t$ with $S = ((\rho R_{nn})(\rho R_{\tau\tau}) - (\rho R_{n\tau})^2)/\rho^4$ takes the following form for smooth solutions:

$$\partial_t Z_{2D} + A_n(Z_{2D}) \partial_n Z_{2D} = 0, \quad (2.4.68)$$

with system matrix

$$A_n(Z_{2D}) = \begin{pmatrix} U_n & \rho & 0 & 0 & 0 & 0 \\ 0 & U_n & 0 & \vartheta & 0 & 0 \\ 0 & 0 & U_n & 0 & \vartheta & 0 \\ 0 & \Psi_{nn} & 0 & U_n & 0 & 0 \\ 0 & 2\rho R_{n\tau} & \Phi_{n\tau} & 0 & U_n & 0 \\ 0 & 0 & 0 & 0 & 0 & U_n \end{pmatrix},$$

$$\text{where: } \Psi_{nn} = 3\rho R_{nn}, \quad \Phi_{n\tau} = \rho R_{nn}, \quad (2.4.69)$$

and $Z_{2D} = Z_{2D}(t, x_n)$. This method associated with the choice (2.4.69) is approach **(A1)** introduced in [27] and defined in the one-dimensional framework in sec. 2.2.2 of the present paper.

Then, by denoting $\vartheta(x, t) = 1/\rho(x, t)$ and choosing constant $(R_{nn})_0 \in \mathbb{R}_+^*$, we may introduce in a two-dimensional framework approach **(A2)** as corresponding to the choice:

$$\Psi_{nn} = 3\rho_0^2(R_{nn})_0\vartheta, \quad \Phi_{n\tau} = \rho_0^2(R_{nn})_0\vartheta. \quad (2.4.70)$$

We note that the relaxation system corresponding to *system (3.2.10) together with choice (2.4.70) is hyperbolic and only admits LD fields*. A more detailed presentation can be found in [15, 16] and [18].

Numerical simulation

In present computations we use the following dimensions: $Lx = 1.0 \text{ m}$, $Ly = 0.2 \text{ m}$, $d = 0.05 \text{ m}$. The fluid is characterized by the density $\rho_f = 2.1 \text{ kg/m}^3$, the dynamical viscosity $\mu_f = 1.85 \times 10^{-5} \text{ Pa.s}$ and $C_0 = 2.1$. The normal components of the inlet gas velocity are: 1.5 m/s in region AB and 1.0 m/s in BC. The dispersed phase is described by the particle density $\rho_p = 2000 \text{ kg/m}^3$ and the diameter $d_p = 10^{-5} \text{ m}$. The computations are performed on a uniform mesh with $Nx \times Ny = 200 \times 40$ cells and $\Delta t = 10^{-3} \text{ s}$. At the beginning of each time step, particles are injected in the domain with the fluid velocity. For a particle (n) injected in the cell $[i]$ of the domain, we assume the following initial conditions:

$$\mathbf{U}_p^{(n)} = \langle \mathbf{U}_f \rangle^{[i]}, \quad \mathbf{U}_s^{(n)} = \langle \mathbf{U}_f \rangle^{[i]} + \sqrt{\frac{2}{3}} k^{[i]} \zeta, \quad (2.4.71)$$

where $\zeta = (\zeta_x, \zeta_y)$ is a vector of independent $\mathcal{N}(0, 1)$ random variables. For such a configuration, τ_p is equal approximately $6 \times 10^{-4} \text{ s}$. When the stationary state is reached, the total number of particles present in the domain at each time t varies around $N_p = 8 \times 10^4$ (or approximately 10 particles per cell).

Finally, we are interested by the first order particle statistics only, more precisely, by the particle volume fraction α_p and the mean particle flow rate $(\alpha_p \rho_0 \langle \mathbf{U}_p \rangle)$. We compare the results computed by the Eulerian part (2.4.64) of the hybrid model, where the kinetic tensor is provided by system (2.4.61), with those obtained with a “stand-alone” Lagrangian computation using “pure” PDF description (2.4.61). The profiles of the solution corresponding to the cross-stream sections $x = 0d, 5d, 10d, 15d$ are shown in Fig. 2.17 - 2.19.

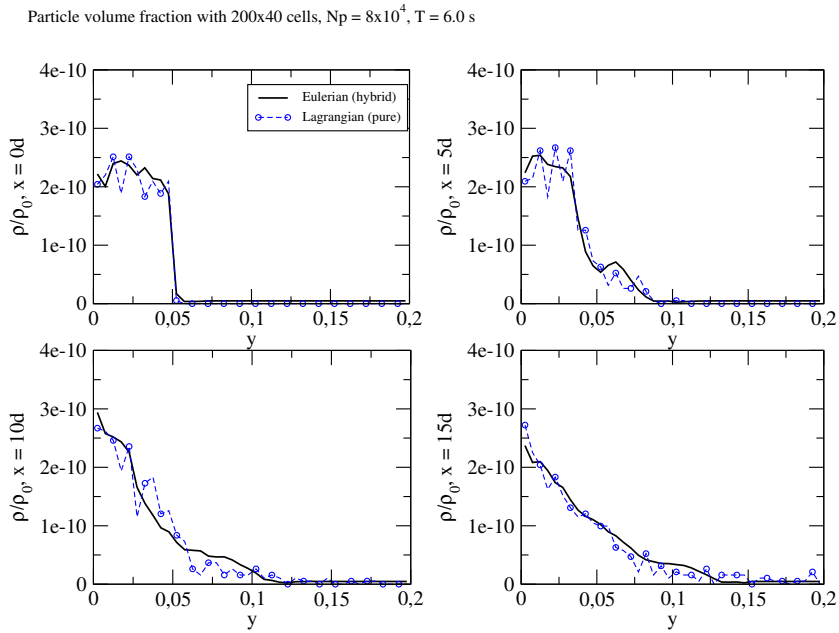


Figure 2.17: Particle volume fraction. Numerical simulation of hybrid model (2.4.61), (2.4.64) with 10 particles per cell on the mesh of 200×40 cells with $\Delta t = 10^{-3}s$. Comparison with the results of the stand-alone Lagrangian computation.

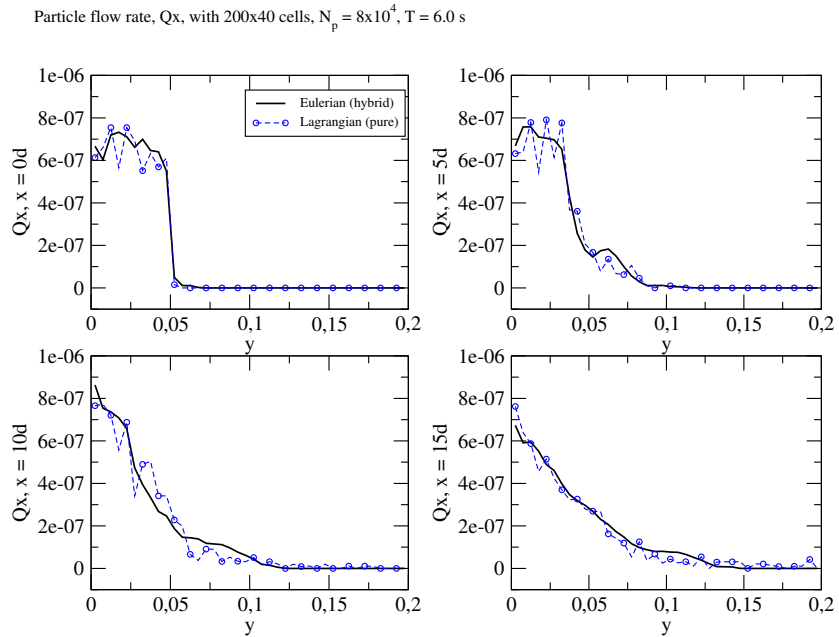


Figure 2.18: Mean particle flow rate in the longitudinal direction. Numerical simulation of hybrid model (2.4.61), (2.4.64) with 10 particles per cell on the mesh of 200×40 cells with $\Delta t = 10^{-3}s$. Comparison with the results of the stand-alone Lagrangian computation.

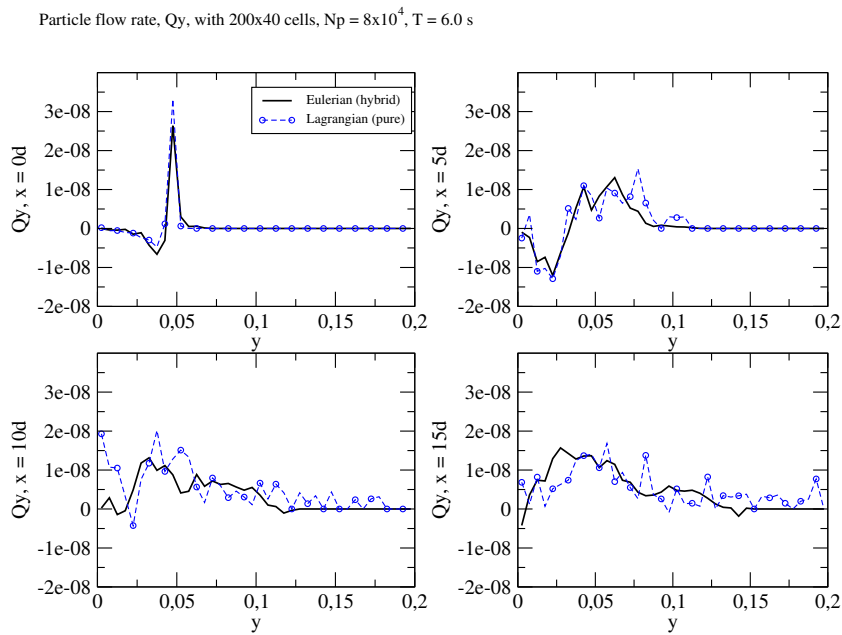


Figure 2.19: Mean particle flow rate in the transversal direction. Numerical simulation of hybrid model (2.4.61), (2.4.64) with 10 particles per cell on the mesh of 200×40 cells with $\Delta t = 10^{-3}s$. Comparison with the results of the stand-alone Lagrangian computation.

Bibliography

- [1] A. AMBROSO, C. CHALONS, F. COQUEL AND T. GALIÉ, "Relaxation and numerical approximation of a two-fluid two-pressure diphasic model", *ESAIM: M2AN*, vol. 43 (6), pp. 1063-1097, 2009.
- [2] B. AUDEBERT, "Contribution à l'analyse de l'interaction onde de choc - couche limite", *Université Pierre et Marie Curie*, PhD thesis, 2006.
- [3] C. BERTHON, F. COQUEL, J.M. HÉRARD AND M. UHLMANN, "An approximate solution of the Riemann problem for a realisable second-moment turbulent closure", *Shock Waves Journal*, vol. 11 (4), pp. 245-269, 2002.
- [4] F. BOUCHUT, "Nonlinear stability of finite volume methods for hyperbolic conservation laws and well-balanced schemes for source", *Frontiers in Mathematics Series*, Birkhauser, 2004.
- [5] F. BOUCHUT, "A reduced stability condition for nonlinear relaxation to conservation laws", *J. Hyp. Diff. Eq.*, vol 1(1), pp. 149-170, 2004.
- [6] G. BRUN, J.M. HÉRARD, D. JEANDEL AND M. UHLMANN, "An approximate Riemann solver for a class of realizable second order closures", *Int. J. of Comp. Fluid Dynamics*, vol. 13, n 3, pp. 223-249, 1999.
- [7] T. BUFFARD, T. GALLOUET AND J.M. HÉRARD, "Un schéma simple pour les équations de Saint-Venant", *C. R. Acad. Sci. Paris*, t. 326, Serie I, pp. 385-390, 1998.
- [8] T. BUFFARD, T. GALLOUET AND J.M. HÉRARD, "A sequel to a rough Godunov scheme: application to real gases", *Computers and Fluids*, t. 29, pp. 813-847, 2000.
- [9] C. CHALONS, J.F. COULOMBEL, "Relaxation approximation of the Euler equations", *J. Math. Anal. Appl.*, vol. 348, pp. 872-893, 2008.
- [10] S. CHIBBARO, J.M. HÉRARD AND J.P. MINIER, "A novel Hybrid Moments/Moments-PDF method for turbulent two-phase flows", *Final Technical Report Activity Marie Curie Project. TOK project LANGE Contract MTKD-CT-2004 509849*, 2006.
- [11] L. COMBE, "Simulation numérique d'écoulements gaz-particules sur maillage non structuré", *Institut National Polytechnique de Toulouse*, PhD thesis, 1997.

- [12] F. COQUEL, E. GODLEWSKI, A. IN, B. PERTHAME AND P. RASCLE, "Some new Godunov and relaxation methods for two phase flows", *Proceedings of the International Conference on Godunov methods : theory and applications*, Kluwer Academic, Plenum Publisher, 2001.
- [13] F. COQUEL, E. GODLEWSKI, SEGUIN, N., "Relaxation of fluid systems", *Mathematical Models and Methods in Applied Sciences*, 2011.
- [14] R. COURANT, K. FRIEDRICHS AND H. LEWY, "On the partial difference equations of mathematical physics", *IBM Journal*, vol. 11, pp. 215-234, 1967.
- [15] K. DOROGAN, "Numerical schemes for the hybrid modelling of turbulent gas-particle flows", *Université Aix-Marseille 1*, PhD thesis to appear in 2012.
- [16] K. DOROGAN, J.M. HÉRARD, "A two-dimensional relaxation scheme for hybrid modelling of gas-particle two-phase flows", *EDF report H-i81-2012-00646-EN*, 2012, unpublished.
- [17] K. DOROGAN, J.M. HÉRARD, J.P. MINIER, "Development of a new scheme for hybrid modelling of gas-particle two-phase flows", *EDF report H-I81-2010-2352-EN*, pp. 1-50, 2010, unpublished.
- [18] K. DOROGAN, J.M. HÉRARD, J.P. MINIER, "A two-dimensional relaxation scheme for the hybrid modelling of two-phase flows", International Conference Finite Volumes for Complex Applications 6, Prague, 6-10 juin 2011. Published in proceedings "*Finite Volumes for Complex Applications. Problems and Perspectives*", pp. 351-359, Springer-Verlag (2011), available on <http://www.springerlink.com/>.
- [19] R. EYMARD, T. GALLOUET AND R. HERBIN, "Finite Volume Methods", *Handbook of Numerical Analysis*, vol. VII, pp. 713-1020, 2000.
- [20] T. GALLOUET, J.M. HÉRARD AND N. SEGUIN, "On the use of symmetrizing variables for vacuum", *Calcolo*, vol. 40 (3), pp. 163-194, 2003.
- [21] S. GAVRILYUK, H. GOUPIL, "Geometric evolution of the Reynolds stress tensor in three-dimensional turbulence", *European J. Mechanics B/Fluids*, <http://hal.archives-ouvertes.fr/hal-00371444/en/>, submitted, 2010.
- [22] E. GODLEWSKI AND P.A. RAVIART, "Numerical approximation of hyperbolic systems of conservation laws", *AMS*, vol. 118, Springer, 1996.
- [23] S.K. GODUNOV, "A difference method for numerical calculation of discontinuous equations of hydrodynamics", *Sbornik*, pp. 271-300, 1959.
- [24] P. HELLUY, J.M. HÉRARD, H. MATHIS AND S. MULLER, "A simple parameter-free entropy correction for approximate Riemann solvers", *CR Mécanique*, vol. 338, pp. 493-498, 2010.
- [25] J.M. HÉRARD, "A relaxation tool to compute hybrid Euler-Lagrange compressible models", *AIAA paper 2006-2872, 36th AIAA FD Conference*, <http://www.aiaa.org>, 2006.
- [26] J.M. HÉRARD, J.P. MINIER AND S. CHIBBARO, "A Finite Volume scheme for hybrid turbulent two-phase flow models", *AIAA paper 2007-4587, 18th AIAA CFD Conference*, <http://www.aiaa.org>, 2007.

- [27] J.M. HÉRARD, M. UHLMANN AND D.E. VAN DER VELDEN, "Numerical techniques for solving hybrid Eulerian-Lagrangian models for particulate flows", *EDF report H-I81-2009-3961-EN*, pp. 1-50, 2009, unpublished.
- [28] S. JIN AND Z. XIN, "The relaxation schemes for systems of conservation laws in arbitrary space dimensions", *Comm. Pure Appl. Math.*, vol 48, pp. 235-276, 1995.
- [29] P.D. LAX, "Hyperbolic systems of conservation laws", *II*, *Comm. Pure Appl. Math.*, vol. 10, pp. 537-566, 1957.
- [30] R. LEVEQUE, "Numerical methods for conservation laws", *Lectures in Mathematics, ETH*, Birkhauser, 1990.
- [31] J.P. MINIER, E. PEIRANO, "The pdf approach to polydispersed turbulent two-phase flows", *Physics reports*, vol. 352 (1-3), pp. 1-214, 2001.
- [32] M. MURADOGLU, P. JENNY, S.B. POPE AND D.A. CAUGHEY, "A consistent hybrid finite-volume/particle method for the pdf equations of turbulent reactive flows", *Journal of Computational Physics*, vol. 154, pp. 342-371, 1999.
- [33] B. ØKSENDAL, "Stochastic differential equations. An introduction with applications", *Springer, Berlin*, 1995.
- [34] E. PEIRANO, S. CHIBBARO, J. POZORSKI AND J.P. MINIER, "Mean-field/PDF numerical approach for polydispersed turbulent two-phase flows", *Progress in Energy and Combustion Science*, <http://www.sciencedirect.com>, vol. 32, pp. 315-371, 2006.
- [35] K. SALEH, F. COQUEL, N. SEGUIN, "Relaxation and numerical approximation for fluid flows in a nozzle", *submitted to publication*, also in *EDF report H-I81-2011-01469-EN*, 2011.
- [36] I. SULICIU, "On the thermodynamics of fluids with relaxation and phase transitions. Fluids with relaxation", *Internat. J. Engrg. Sci.*, vol. 36, pp. 921-947, 1998.
- [37] J. WHITHAM, "Linear and nonlinear waves", *Wiley*, 1974.
- [38] W.-A. YONG, "Singular perturbations of first-order hyperbolic systems with stiff source terms", *J. Differential Equations*, vol. 155(1), pp. 89-132, 1999.

Chapter 3

A two-dimensional relaxation scheme for the hybrid modelling of two-phase flows

Introduction

On aborde dans ce chapitre le problème de la simulation hybride en dimension deux d'espace, en s'appuyant sur les travaux précédents du chapitre 2, et sur les travaux antérieurs réalisés dans [16]. La difficulté ici est double, puisqu'il s'agit non seulement de contrôler le bruit associé au signal Lagrangien, sans introduire de phénomène de diffusion excessif, mais aussi de prendre en compte les effets totalement anisotropes associés au tenseur de Reynolds intervenant dans la divergence spatiale pour l'équation de quantité de mouvement moyenne.

L'idée consiste ici encore à s'appuyer sur la stabilisation par technique de relaxation, sachant que celle-ci ne concerne plus un tenseur isotrope associé aux classiques effets de pression, mais le tenseur anisotrope de Reynolds, celui-ci étant en outre indépendant de la variable d'état densité moyenne/vitesse moyenne. Le formalisme introduit dans [16] permet de gérer ce problème, mais on a vu qu'il nécessitait d'introduire, pour le problème de relaxation, des relations de saut approchées, qui paramétreraient donc la solution du problème de Riemann associé au système de relaxation. On considère donc ici encore une modification de la contribution identifiée dans le registre des turbulenciers comme étant le "tenseur de production", qui n'est en fait qu'une partie de la convection tensorielle, et est en outre totalement déterministe. La méthode, notée **R2**, sera l'analogue de l'approche **A2** examinée au chapitre précédent.

On présente parallèlement l'approche antérieure **R1** et la nouvelle approche **R2**, afin de mieux comprendre les mécanismes mis en oeuvre. On donne ensuite les principales propriétés des deux

systèmes de relaxation, incluant l'hyperbolicité, la structure des champs, la paramétrisation des ondes, et on termine en donnant dans chaque cas le critère d'existence et d'unicité de la solution du problème de Riemann unidimensionnel associé au système de relaxation dans le repère associé à l'interface séparant deux cellules adjacentes, ceci étant fait en négligeant classiquement les contributions des dérivées transverses locales. Un paragraphe est consacré à la stabilité continue, qui permet de vérifier que l'on contrôle ainsi l'énergie cinétique associée au mouvement moyen, même en l'absence de tout effet diffusif ou dissipatif, modulo bien entendu un choix de conditions aux limites *ad hoc*. Une présentation succincte du schéma Volumes Finis d'intégration de maille est ensuite effectuée. Ce choix est totalement pertinent puisque le système relaxé physique est totalement conservatif. Le critère CFL qui doit être respecté est ici encore peu contraignant puisque les ondes ont approximativement toutes la même amplitude. On termine ce chapitre en montrant quelques cas de simulation bidimensionnelle lorsque le tenseur de Reynolds synthétique est très bruité.

On pourra alors utiliser le solveur développé pour le couplage des modules Lagrangien et Eulérien nécessaires à la mise en place de la méthode hybride ; ceci constituera le corps du dernier chapitre consacré aux simulations numériques hybrides.

A Two-Dimensional Relaxation Scheme for the Hybrid Modelling of Two-Phase Flows ¹

K. Dorogan, J.M. Hérard

Abstract

This paper presents a two-dimensional relaxation scheme for the hybrid modelling of two-phase gas-particle flows. The method is grounded on a previous relaxation scheme that has been proposed to cope with one-dimensional flows. One of the main difficulties here is due to the fact that the Reynolds tensor occurring in the Lagrangian framework is highly anisotropic. The interface relaxation scheme mimics a previously proposed "relaxation scheme" that involves GNL fields. The method is described and its main properties are given, including a very short stability analysis. Numerical results are also provided.

3.1 Introduction

This paper deals with the modelling and the numerical simulation of polydispersed turbulent two-phase flows, where one phase is a turbulent fluid (considered to be a continuum) and the other appears as separate inclusions carried by the fluid (solid particles, droplets or bubbles). Such a kind of flows can be encountered in many industrial situations (combustion, water sprays, smokes) and in some environmental problems. Despite the need of their accurate prediction, the physical complexity of these processes is so broad that existing methods are either too expensive (in calculation cost) or not sufficiently accurate.

A hybrid approach was proposed in [9] in order to cope with one-dimensional flows, which consists in enlarging the size of the Eulerian set of equations, in order to retrieve a natural upwinding of so-called source terms corresponding to the divergence of the Reynolds stress tensor. In a one dimensional framework, this approach may be confused with classical relaxation schemes used for the numerical approximation of solutions of barotropic Euler equations (see [3, 6, 8, 17, 24]). The main point is that in the 1D case, the -unique- Reynolds stress component may be viewed as a pressure field, whereas in the multi-dimensional case the -possibly high- anisotropy of the Reynolds stress tensor inhibits such an analogy. Therefore, one needs to introduce another -more complex- relaxation system for such a purpose.

As emphasized in [9], a first proposal was made which consists in mimicing the natural evolution equations of the Reynolds stress tensor, which may be easily derived (see [16], and also [15] which give some very first ideas in that direction). Such a procedure enables to recover a correct upwinding of complex multi-D waves that may pollute -and even blow out- numerical approximations obtained with more naive Riemann type solvers, for instance those relying of Euler type solvers

¹An initial version of this paper has appeared as EDF report H-i81-2012-00646-EN, 2012.

(see for instance [20] and also [4] that exhibits a very simple instability pattern arising with Euler-type solvers). A drawback of this approach is that it requires enforcing *a priori* approximate jump conditions which can hardly be assessed. This motivates investigating true relaxation techniques involving only linearly degenerate fields, which is precisely what will be done within this paper.

The system of governing equations for the mean particle concentration α_p^E , the mean flow rate $\alpha_p^E \langle U_{p,i}^E \rangle$, which represents an Eulerian description of the particle phase, may be written as follows:

$$\begin{aligned}\partial_t \alpha_p^E + \partial_{x_i} (\alpha_p^E \langle U_{p,i}^E \rangle) &= 0 \\ \partial_t (\alpha_p^E \langle U_{p,i}^E \rangle) + \partial_{x_j} (\alpha_p^E (\langle U_{p,i}^E \rangle \langle U_{p,j}^E \rangle + \langle u_{p,i} u_{p,j} \rangle^L)) &= \alpha_p^E g_i + \alpha_p^E \langle U_{r,i} / \tau_p \rangle^L\end{aligned}\tag{3.1.1}$$

These are deduced from a Lagrangian formulation (see [7]), where the right-hand side terms represent the gravity and drag forces respectively. Obviously, the Reynolds stress term $\langle u_{p,i} u_{p,j} \rangle^L$ in system (3.1.1) must be provided by some external Lagrangian code, as occurs in the 1D case. We recall that the hybrid approach consists in solving simultaneously Eulerian system (3.1.1) and its Lagrangian counterpart, which in turn provides everywhere and at any time all components of the Reynolds stress tensor. Besides, the Eulerian model provides the values of $\langle U_{p,i}^E \rangle$ expected free from any statistical error, that should enable computations with a smaller number of particles in the Lagrangian code.

In the sequel, we omit the superscripts “ E ” and subscripts “ p ”, and introduce the -constant-density of particles ρ_p . We denote by $\rho = \alpha_p^E \rho_p$ the mean density distribution of the particles in the domain, by $U_i = \langle U_{p,i}^E \rangle, i = 1, 2$ the mean particle velocity. Hence, for given non-smooth values of the Lagrangian Reynolds stress tensor $\underline{\underline{R}}_{ij}^L = \langle u_{p,i} u_{p,j} \rangle^L$, we want to compute stable approximations of solutions of:

$$\begin{aligned}\partial_t \rho + \partial_{x_j} (\rho U_j) &= 0 \\ \partial_t (\rho U_i) + \partial_{x_j} (\rho U_i U_j) + \partial_{x_j} (\rho R_{ij}^L) &= \rho g_i + \rho \langle U_{r,i} / \tau_p \rangle^L\end{aligned}\tag{3.1.2}$$

We emphasize that, by construction, the Reynolds stress tensor $\underline{\underline{R}}_{ij}^L$ complies with the so-called *realisability condition* (see [19, 23]):

$$\underline{x}^t \underline{\underline{R}}^L \underline{x} \geq 0\tag{3.1.3}$$

for all $\underline{x} \in \mathcal{R}^2$.

Before going further on, we also mention that a time-splitting strategy is applied to system (3.1.2), which means that approximations of unsteady solutions of system (3.1.2) are obtained by solving successively an homogeneous evolution system:

$$\begin{aligned}\partial_t \rho + \partial_{x_j} (\rho U_j) &= 0 \\ \partial_t (\rho U_i) + \partial_{x_j} (\rho U_i U_j) + \partial_{x_j} (\rho R_{ij}^L) &= 0\end{aligned}\tag{3.1.4}$$

and then taking source terms into account, with frozen densities:

$$\begin{aligned}\partial_t \rho &= 0 \\ \partial_t (\rho U_i) &= \rho g_i + \rho \langle U_{r,i} / \tau_p \rangle^L\end{aligned}\tag{3.1.5}$$

The present paper is organised as follows. In section 1, we propose two forms of the relaxation system associated with (3.1.4) that are quite similar. Then we discuss properties of both approaches in section 2, including some stability results. The last section is devoted to some two-dimensional numerical results.

3.2 Two distinct relaxation systems

In order to obtain approximate solutions of system (3.1.4) with non-smooth external data $\underline{\underline{R}}_{ij}^L$, we first introduce new variables $\underline{\underline{R}}_{ij}$ that are expected to relax towards $\underline{\underline{R}}_{ij}^L$ when some given relaxation time scale τ_p^R tends to 0. Since the tensor $\underline{\underline{R}}_{ij}^L$ is symmetric by construction, its counterpart $\underline{\underline{R}}_{ij}$ is also assumed to be symmetric. Hence, we need to introduce new partial differential equations that will govern the evolution of the Reynolds stresses $\underline{\underline{R}}_{ij}$.

This should be achieved in such a way that the new relaxation system were hyperbolic and would preserve the realizability of solutions, which means that $\underline{\underline{R}}_{ij}$ should comply with (3.1.3).

On the basis of [2, 15, 16], while introducing invariants II and I^L as defined below:

$$I^L = R_{ii}^L \quad \text{and:} \quad II = R_{ik}R_{ki} \quad (3.2.1)$$

the following relaxation system (3.2.2) naturally arises:

$$\begin{aligned} \partial_t \rho + \partial_{x_j} (\rho U_j) &= 0 \\ \partial_t (\rho U_i) + \partial_{x_j} (\rho U_i U_j) + \partial_{x_j} (\rho R_{ij}) &= 0 \\ \partial_t (\rho R_{ij}) + \partial_{x_k} (\rho U_k R_{ij}) + \rho (R_{ik} \partial_{x_k} U_j + R_{jk} \partial_{x_k} U_i) &= \rho \phi_{ij} / (\tau_p^R) \end{aligned} \quad (3.2.2)$$

noting :

$$\phi_{ij} = R_{ik} (R_{kl}^L - R_{kl}) R_{lj} / I^L / (II)^{1/2}$$

with a classical Einstein summation notation for k, l . In the present work, the time scale τ_p^R is expected to be infinitely small. The differential part on the left hand side of (3.2.2) arises from the classical construction of motion of second-moment closures (see [1, 2, 12, 19, 22, 21, 23] among others). The non conservative terms $\rho (R_{ik} \partial_{x_k} U_j + R_{jk} \partial_{x_k} U_i)$ are usefully and abusively called the production terms in the turbulent literature. These are actually convective contributions, and should be handled as such (see [1, 2, 4, 12]).

A first important point that is worth being mentioned is that the structure of the third equation in (3.2.2) guarantees the realizability of smooth solutions R_{ij} . The proof is rather simple. Introducing the determinant δ_R of the Reynolds stress tensor $\underline{\underline{R}}_{ij}$, which is precisely the product of the eigenvalues of $\underline{\underline{R}}_{ij}$, noting :

$$H_{ik} = R_{il} (R_{lk}^L - R_{lk}) / (2I^L) / (II)^{1/2} / (\tau_p^R) - \partial_{x_k} U_i \quad (3.2.3)$$

and taking into account the mass balance equation (that is the first equation in (3.2.2)), we can rewrite the third equation of (3.2.2) as follows:

$$\partial_t(R_{ij}) + U_k \partial_{x_k}(R_{ij}) = H_{ik}R_{kj} + H_{jk}R_{ki} \quad (3.2.4)$$

Hence, we get the governing equation for δ_R (see [13, 14] for instance):

$$\partial_t(\delta_R) + U_k \partial_{x_k}(\delta_R) = 2H_{ll}\delta_R \quad (3.2.5)$$

which implies that, for positive initial conditions and inlet boundary conditions for δ_R , and assuming bounded values of the velocity U_k , its divergence $\partial_{x_k}(U_k)$ and the trace H_{ll} , smooth solutions $\delta_R(\mathbf{x}, t)$ of equation (3.2.5) remain positive for $t \in [0, T]$, using a classical positivity lemma.

We focus now on the homogeneous part of system (3.2.2), thus concentrating on the evolution part of the relaxation system.

$$\begin{aligned} \partial_t\rho + \partial_{x_j}(\rho U_j) &= 0 \\ \partial_t(\rho U_i) + \partial_{x_j}(\rho U_i U_j) + \partial_{x_j}(\rho R_{ij}) &= 0 \\ \partial_t(\rho R_{ij}) + \partial_{x_k}(\rho U_k R_{ij}) + \rho(R_{ik}\partial_{x_k}U_j + R_{jk}\partial_{x_k}U_i) &= 0 \end{aligned} \quad (3.2.6)$$

3.2.1 A nonlinear interface relaxation system

System (3.2.6) is invariant under frame rotation, and it also contains only one non-objective term corresponding to the non-conservative terms (see [23]). In order to define our interface solvers, we consider the reference frame $(\underline{n}, \underline{\tau})$: $\underline{n} = (n_x, n_y)$, $\underline{\tau} = (-n_y, n_x)$, such that $n_x^2 + n_y^2 = 1$, for a given interface whose normal is \underline{n} . In practice, this interface will correspond to the interface separating two adjacent cells in the computational domain. We also introduce normal and tangential velocities U_n , U_τ , and components of the Reynolds stress tensor in the new reference frame $\underline{n}, \underline{\tau}$:

$$\begin{aligned} U_n &= \underline{U} \cdot \underline{n}, \\ U_\tau &= \underline{U} \cdot \underline{\tau}, \\ R_{nn} &= \underline{n}^t \cdot \underline{\underline{R}} \cdot \underline{n}, \\ R_{n\tau} &= \underline{n}^t \cdot \underline{\underline{R}} \cdot \underline{\tau} = \underline{\tau}^t \underline{\underline{R}} \cdot \underline{n} = R_{\tau n}, \\ R_{\tau\tau} &= \underline{\tau}^t \cdot \underline{\underline{R}} \cdot \underline{\tau}. \end{aligned} \quad (3.2.7)$$

Eventually, we define a normalized determinant called S :

$$S = ((R_{nn})(R_{\tau\tau}) - (R_{n\tau})^2) / \rho^2 \quad (3.2.8)$$

together with a "non-conservative" variable:

$$Z^t = (\rho, U_n, U_\tau, \rho R_{nn}, \rho R_{n\tau}, S) \quad (3.2.9)$$

When neglecting transverse variations, thus assuming that $\forall \phi$, we have:

$$\partial\phi/\partial\tau = 0$$

and the relaxation system corresponding to system (3.2.6) written in terms of the new variable Z takes the following form for smooth solutions of (3.2.6):

$$\partial_t Z + A_n(Z) \partial_n Z = 0, \quad (3.2.10)$$

The exact expression of the matrix $A_n(Z)$ is given by:

$$A_n(Z) = \begin{pmatrix} U_n & \rho & 0 & 0 & 0 & 0 \\ 0 & U_n & 0 & \vartheta & 0 & 0 \\ 0 & 0 & U_n & 0 & \vartheta & 0 \\ 0 & \Psi_{nn} & 0 & U_n & 0 & 0 \\ 0 & 2\rho R_{n\tau} & \Phi_{n\tau} & 0 & U_n & 0 \\ 0 & 0 & 0 & 0 & 0 & U_n \end{pmatrix} \quad (3.2.11)$$

noting as usual the covolume $\vartheta(x, t) = 1/\rho(x, t)$, and setting:

$$\Psi_{nn} = 3\rho R_{nn}, \quad \Phi_{n\tau} = \rho R_{nn}. \quad (3.2.12)$$

This approach (**R1**) corresponds to the approach introduced in [16]. Properties of system (3.2.10), (3.2.11), (3.2.12) will be detailed in section 2.

3.2.2 A true interface relaxation system

Rather than solving the one-dimensional Riemann problem in the n direction, on the basis of the previous system (3.2.10, 3.2.11), together with (3.2.12), the following approximation (3.2.13) is considered instead of (3.2.12):

$$\Psi_{nn} = 3A_0\vartheta, \quad \Phi_{n\tau} = A_0\vartheta. \quad (3.2.13)$$

where : $A_0 = \rho_0^2(R_{nn})_0$, where $(R_{nn})_0 > 0$. This approach (**R2**) is actually a straightforward extension of the approach introduced in [9] and detailed in the previous chapter.

3.3 Main properties of relaxation systems **R1**, **R2**

We examine now the two systems connected with approaches **R1** and **R2**; more precisely, we wish to detail the structure of the solution of the one-dimensional Riemann problem in each case. This is of course mandatory in order to construct exact or approximate interface Riemann solvers. We also wonder whether this solution -if any- complies with the realizability constraint -or not-.

3.3.1 Non-linear relaxation system **R1**

Before going further on, we need to define two celerities c_1, c_2 as follows:

$$c_1^2 = 3R_{nn} \quad \text{and:} \quad c_2^2 = R_{nn} \quad (3.3.1)$$

We thus get:

Property 1:

System (3.2.10, 3.2.11) with closure (3.2.12) admits six real eigenvalues that read:

$$\lambda_{1,6} = U_n \pm c_1, \quad \lambda_{2,5} = U_n \pm c_2, \quad \lambda_3 = \lambda_4 = U_n, \quad (3.3.2)$$

Fields associated with eigenvalues $\lambda_{1,6}$ are genuinely non linear. Other fields are linearly degenerate.

Proof: The reader is referred to [16] for proof. As it occurs in the incompressible framework (see [13, 14]), eigenvalues are real if and only if the realizability constraint is fulfilled.

Due to the occurrence of non-conservative products that are active in GNL fields, we must introduce *approximate* jump conditions in order to examine solutions of the associated one-dimensional Riemann problem (see [18]). For that purpose, we fix the following relations through discontinuities travelling at speed σ and separating two states Z_l, Z_r :

$$\begin{aligned} -\sigma [\rho] + [\rho U_n] &= 0 \\ -\sigma [\rho U_n] + [\rho U_n^2 + \rho R_{nn}] &= 0 \\ -\sigma [\rho U_\tau] + [\rho U_n U_\tau + \rho R_{n\tau}] &= 0 \\ -\sigma [\rho R_{nn}] + [\rho U_n R_{nn}] + 2 (\overline{\rho R_{nn}}) [U_n] &= 0 \\ -\sigma [\rho R_{n\tau}] + [\rho U_n R_{n\tau}] + (\overline{\rho R_{nn}}) [U_\tau] + (\overline{\rho R_{n\tau}}) [U_n] &= 0 \\ -\sigma [\rho R_{\tau\tau}] + [\rho U_n R_{\tau\tau}] + 2 (\overline{\rho R_{n\tau}}) [U_\tau] &= 0 \end{aligned} \quad (3.3.3)$$

where we note as usual $[\phi] = \phi_r - \phi_l$, and also $\bar{\phi} = (\phi_r + \phi_l)/2$, whatever ϕ is.

Moreover, we get the form of Riemann invariants after some calculations:

Property 2 (Riemann invariants in system associated with **R1**):

Denoting I_R^k the list of Riemann invariants associated with field k , we get:

$$\begin{aligned} I_R^1 &= \left\{ S, \frac{R_{nn}}{\rho^2}, \frac{R_{n\tau}}{\rho^2}, U_n + c_1, U_\tau + R_{n\tau} \frac{\sqrt{3}}{c_2} \right\} \\ I_R^2 &= \left\{ \rho, U_n, \rho R_{nn}, S, U_\tau + \frac{R_{n\tau}}{c_2} \right\} \\ I_R^{3,4} &= \{U_n, U_\tau, \rho R_{nn}, \rho R_{n\tau}\} \\ I_R^5 &= \left\{ \rho, U_n, \rho R_{nn}, S, U_\tau - \frac{R_{n\tau}}{c_2} \right\} \\ I_R^6 &= \left\{ S, \frac{R_{nn}}{\rho^2}, \frac{R_{n\tau}}{\rho^2}, U_n - c_1, U_\tau - R_{n\tau} \frac{\sqrt{3}}{c_2} \right\} \end{aligned} \quad (3.3.4)$$

Proof: The reader is refered to [16] for proof.

Therefore, we obtain the following result:

Property 3 (Existence and Uniqueness of the solution of the Riemann problem for **R1**):

The Riemann problem associated with (3.2.10, 3.2.11, 3.2.12), approximate jump relations (3.3.3), and realizable initial conditions for left and right states Z_l, Z_r , admits a unique solution with no vacuum occurence if:

$$(U_n)_r - (U_n)_l < \sqrt{3} \left(\sqrt{(R_{nn})_l} + \sqrt{(R_{nn})_r} \right). \quad (3.3.5)$$

The solution is composed of six constant states $Z_l, Z_1, Z_2, Z_3, Z_4, Z_r$ separated by 2 GNL waves associated with $\lambda_{1,6}$ and 4 LD waves associated with $\lambda_{2,3,4,5}$. All intermediate states arising in the solution of the one-dimensional Riemann problem comply with the realizability condition (3.1.3).

Proof: The reader is refered to [16] for proof.

Actually, we emphasize that the 2 and 5 fields are ghost waves for the three components ρ, U_n, R_{nn} . This explains why the condition of existence and uniqueness of the approximate solution is exactly the same as in the pure one-dimensional framework. We also note that S is a Riemann invariant in the 1, 2, 5, 6 waves; besides, the approximate jump conditions (3.3.3) are such that $[S] = 0$, thus S satisfies some maximum principle : $\min(S_l, S_r) \leq S(x_n/t) \leq \max(S_l, S_r)$.

However, as occurs in the one-dimensional case, the validity of *a priori* jump conditions (3.3.3) is questionable. Hence it seems natural to introduce a slightly modified version of the approach (**R1**), which consists in replacing closure (3.2.12) by (3.2.13). This one is analyzed in detail below.

3.3.2 Relaxation system **R2**

We turn now to **R2** and we introduce:

$$(\tilde{c}_1)^2 = 3A_0\vartheta^2 \quad \text{and:} \quad (\tilde{c}_2)^2 = A_0\vartheta^2 \quad (3.3.6)$$

and get:

Property 4:

Assume that $0 \leq \rho$; then system (3.2.10, 3.2.11) with closure (3.2.13) admits six real eigenvalues that read:

$$\tilde{\lambda}_{1,6} = U_n \pm \tilde{c}_1, \quad \tilde{\lambda}_{2,5} = U_n \pm \tilde{c}_2, \quad \tilde{\lambda}_3 = \lambda_4 = U_n, \quad (3.3.7)$$

All fields are linearly degenerate.

The proof is straightforward and is left to the reader. The determinant of $A_n(Z) - \tilde{\lambda}\mathcal{I}$ is:

$$\det(A_n(Z) - \tilde{\lambda}\mathcal{I}) = (W_n)^2((W_n)^2 - \vartheta\Phi_{n\tau})((W_n)^2 - \vartheta\Psi_{nn})$$

where $W_n = U_n - \tilde{\lambda}$. This provides in a straightforward way the expression of eigenvalues. Thus, it only remains to check that :

$$\nabla_Z \tilde{\lambda}_k(Z) \cdot \tilde{r}_k(Z) = 0$$

where $\tilde{r}_k(Z)$ stands for the right eigenvector associated with the eigenvalue $\tilde{\lambda}_k$, whatever k is. Starting from (3.2.11), the complete list of right eigenvectors $\tilde{r}_k(Z)$ of $A_n(Z)$ may be written in the general case:

$$\begin{aligned} \tilde{r}_1 &= (\rho, -c_1, \frac{-2\rho c_1 R_{n\tau}}{\rho c_1^2 - \Phi_{n\tau}}, \rho c_1^2, \frac{\rho c_1^2}{\rho c_1^2 - \Phi_{n\tau}}, 0) \\ \tilde{r}_2 &= (0, 0, 1, 0, -\rho c_2, 0) \\ \tilde{r}_3 &= (1, 0, 0, 0, 0, 0) \\ \tilde{r}_4 &= (0, 0, 0, 0, 0, 1) \\ \tilde{r}_5 &= (0, 0, 1, 0, \rho c_2, 0) \\ \tilde{r}_6 &= (\rho, c_1, \frac{2\rho c_1 R_{n\tau}}{\rho c_1^2 - \Phi_{n\tau}}, \rho c_1^2, \frac{\rho c_1^2}{\rho c_1^2 - \Phi_{n\tau}}, 0), \end{aligned} \quad (3.3.8)$$

where $\Phi_{n\tau} = A_0\vartheta$ when focusing on **R2**.

Unlike in the previous case (**R1**) where approximate jump conditions were prescribed, the connection between two states separated by a contact discontinuity is uniquely defined, and it only requires giving Riemann invariants through all fields. When looking for $f_k(Z)$ such that:

$$\nabla_Z f_k(Z) \cdot \tilde{r}_k(Z) = 0$$

we obtain the counterpart of property 2 which is now:

Property 5 (Riemann invariants in system associated with **R2**):
Riemann invariants associated with (3.2.10, 3.2.11, 3.2.13) are the following:

$$\begin{aligned} \tilde{I}_R^1 &= \left\{ S, \rho R_{nn} + 3A_0\vartheta, \frac{R_{n\tau}}{\rho^2}, U_n - a_0\vartheta, U_\tau + \frac{\rho R_{n\tau}}{a_0} \right\} \\ \tilde{I}_R^2 &= \left\{ \rho, U_n - \sqrt{A_0}\vartheta, \rho R_{nn}, S, U_\tau + \frac{R_{n\tau}}{c_2} \right\} \\ \tilde{I}_R^{3,4} &= \{U_n, U_\tau, \rho R_{nn}, \rho R_{n\tau}\} \\ \tilde{I}_R^5 &= \left\{ \rho, U_n + \sqrt{A_0}\vartheta, \rho R_{nn}, S, U_\tau - \frac{R_{n\tau}}{\bar{c}_2} \right\} \\ \tilde{I}_R^6 &= \left\{ S, \rho R_{nn} + 3A_0\vartheta, \frac{R_{n\tau}}{\rho^2}, U_n + a_0\vartheta, U_\tau - \frac{\rho R_{n\tau}}{a_0} \right\} \end{aligned} \quad (3.3.9)$$

setting $a_0 = \sqrt{3A_0}$.

We may then construct the whole solution of the one-dimensional Riemann problem, which is rather easy since the connection through waves is uniquely defined by the Riemann invariant parametrization. We may give the following result:

Property 6 (Existence and Uniqueness of the solution of the Riemann problem for **R2**). *Assume that $\rho_0^2(R_{nn})_0 \geq 0$ is such that it satisfies the Wave Ordering Condition (WOC):*

$$\tilde{\lambda}_1 < \tilde{\lambda}_2 < \tilde{\lambda}_3 = \tilde{\lambda}_4 < \tilde{\lambda}_5 < \tilde{\lambda}_6. \quad (3.3.10)$$

Then the Riemann problem associated with (3.2.10), (3.2.13) and initial conditions Z_l, Z_r satisfying (3.1.3), admits a unique solution composed of six constant states $Z_l, \tilde{Z}_1, \tilde{Z}_2, \tilde{Z}_3, \tilde{Z}_4, Z_r$ separated by six LD waves. These are such that:

$$\tilde{\rho}_1 = \tilde{\rho}_2 > 0 \quad \tilde{\rho}_3 = \tilde{\rho}_4 > 0$$

and also:

$$\tilde{S}_1 = \tilde{S}_2 > 0 \quad \tilde{S}_3 = \tilde{S}_4 > 0.$$

The proof is obtained by construction. The normal component of the velocity is unique:

$$(\tilde{U}_n)_1 = (\tilde{U}_n)_2 = (\tilde{U}_n)_3 = (\tilde{U}_n)_4 = \tilde{U}_n, \quad (3.3.11)$$

where:

$$\tilde{U}_n = ((U_n)_l + (U_n)_r)/2 - ((\rho R_{nn})_r - (\rho R_{nn})_l)/(2a_0)$$

We also note that the component ρR_{nn} is unique since:

$$(\tilde{\rho} \tilde{R}_{nn})_1 = (\tilde{\rho} \tilde{R}_{nn})_2 = (\tilde{\rho} \tilde{R}_{nn})_3 = (\tilde{\rho} \tilde{R}_{nn})_4 = \Pi \quad (3.3.12)$$

where:

$$\Pi = ((\rho R_{nn})_r + (\rho R_{nn})_l)/2 - a_0((U_n)_r - (U_n)_l)/2$$

Obviously, Π is positive provided that initial conditions are such that:

$$(U_n)_r - (U_n)_l < ((\rho R_{nn})_l + (\rho R_{nn})_r)/a_0 \quad (3.3.13)$$

which should be compared with the condition of existence and uniqueness of the solution with no vacuum occurrence to the Riemann problem associated with **R1** in (3.3.5). The condition (3.3.13) may be violated in strong rarefaction waves. Intermediate values of the density are given by:

$$\begin{aligned} \tilde{\vartheta}_1 &= \vartheta_l + ((U_n)_r - (U_n)_l - ((\rho R_{nn})_r - (\rho R_{nn})_l)/a_0)/(2a_0) \\ \tilde{\vartheta}_3 &= \vartheta_r + ((U_n)_r - (U_n)_l + ((\rho R_{nn})_r - (\rho R_{nn})_l)/a_0)/(2a_0) \end{aligned} \quad (3.3.14)$$

The WOC condition implies that :

$$\tilde{\lambda}_1 < \tilde{\lambda}_3 = \tilde{\lambda}_4 < \tilde{\lambda}_6$$

which guarantees positive values of densities $\tilde{\rho}_1$ and $\tilde{\rho}_3$ (see [9]). It only remains to check that: $\tilde{\lambda}_1 < \tilde{\lambda}_2 < \tilde{\lambda}_3$, which is quite obvious since:

$$\tilde{\lambda}_1 = (\tilde{U}_n)_1 - \tilde{c}_1 = U_n - a_0 \tilde{\vartheta}_1 < U_n - \sqrt{A_0} \tilde{\vartheta}_1 = \tilde{\lambda}_2 < U_n = \tilde{\lambda}_3 = \tilde{\lambda}_4$$

A similar result holds on the right hand side of the central wave associated with U_n .

We also emphasize that components U_τ and $\rho R_{n\tau}$ do not vary through the central wave associated with the eigenvalue $\lambda_3 = \lambda_4 = U_n$; concerning U_τ , this basically differs from what happens in a compressible laminar framework.

Components $R_{\tau\tau}$ are calculated using the identity:

$$R_{\tau\tau} = (\rho^2 S + (R_{n\tau})^2)/R_{nn}$$

Hence $R_{\tau\tau}$ is positive if and only if R_{nn} is positive. The normalized determinant S is positive since:

$$\tilde{S}_1 = \tilde{S}_2 = S_l > 0 \quad \text{and} \quad \tilde{S}_3 = \tilde{S}_4 = S_r > 0$$

Details on intermediate states $U_\tau, R_{n\tau}$ are given in appendix A.

Property 6 was more or less expected, for readers who are familiar with turbulent compressible models.

Eventually, we wish to emphasize that the WOC is the same as in the pure one-dimensional framework (see [6, 9]), and we only briefly recall it in appendix A.

3.3.3 Stability properties

We focus on the evolution step in the relaxation procedure, and thus on the homogeneous system corresponding to the left hand side of (3.2.2), in a two-dimensional framework, restricting to smooth solutions $\rho(\underline{x}, t)$, $U_i(\underline{x}, t)$, $R_{ij}(\underline{x}, t) \in \mathcal{C}^1$. We denote by

$$\mathcal{E}_1(t) = \frac{1}{2} \int_{\Omega} \rho U_i^2(\underline{x}, t) d\Omega \quad \text{and} \quad \mathcal{E}_2(t) = \frac{1}{2} \int_{\Omega} \rho \operatorname{tr}(\underline{\underline{R}})(\underline{x}, t) d\Omega, \quad i = 1, 2. \quad (3.3.15)$$

the kinetic energy of the mean motion and the energy of the fluctuating particle motion respectively. The total particle energy is given by

$$\mathcal{E}(t) = \mathcal{E}_1(t) + \mathcal{E}_2(t).$$

We also assume wall-boundary conditions on the boundary of the domain, that is: $\forall \underline{x} \in \partial\Omega \quad \underline{U} \cdot \underline{n} = 0$ and $\underline{\underline{R}} \underline{n} = \underline{\underline{0}}$.

Property 7.

We assume that $S(\underline{x} \in \partial\Omega, t > t_0) > 0$ on the boundary, and also that the initial condition is such that $S(\underline{x} \in \Omega, t_0) > 0$. Then smooth solutions of the homogeneous relaxation system corresponding to the left-hand side of system (3.2.2) satisfy the following estimate:

$$0 \leq \mathcal{E}_1(t) = \mathcal{E}(t_0) - \mathcal{E}_2(t) \leq \mathcal{E}(t_0), \quad (3.3.16)$$

since $\mathcal{E}_2(t) \geq 0$

Proof: Starting from (3.2.2)), and using the mass balance equation, we easily obtain that smooth solutions comply with:

$$\partial_t(\rho U_l U_l / 2) + \partial_{x_j} (\rho U_l U_l U_j / 2) + U_l \partial_{x_j} (\rho R_{lj}) = 0$$

but also:

$$\partial_t(\rho R_{ll}) + \partial_{x_k} (\rho U_k R_{ll}) + 2\rho R_{lk} \partial_{x_k} U_l = 0$$

and thus:

$$\partial_t \left(\frac{\rho(U_l U_l + R_{ll})}{2} \right) + \partial_{x_k} \left(U_k \frac{\rho(U_l U_l + R_{ll})}{2} + \rho U_l R_{lk} \right) = 0$$

Adding the latter two equations, integrating over the whole domain Ω , using definitions (3.3.15), and taking wall boundary conditions into account on $\partial\Omega$, we get at once:

$$\partial_t(\mathcal{E}(t)) + \int_{\partial\Omega} \left(\frac{\rho(U_l U_l + R_{ll})}{2} U_k n_k + \rho U_l R_{lk} n_k \right) d\sigma = 0$$

and eventually:

$$\partial_t(\mathcal{E}(t)) = 0$$

which means that : $\mathcal{E}(t) = \mathcal{E}(0)$ at any time $t > 0$. Furthermore, as it has been emphasized in section 1, the governing equation of S is:

$$\partial_t S + (\underline{U} \cdot \nabla S) = 0. \quad (3.3.17)$$

Integrating along smooth characteristic lines, and owing to relevant initial and boundary conditions on S , we may conclude that the eigenvalues remain positive, which in turn provides: $R_{ll}(\underline{x}, t) > 0$, since R_{ll} corresponds with the sum of eigenvalues of \underline{R} . Thus : $\mathcal{E}_2(t) > 0$. On the whole, we may conclude that for $t > 0$:

$$0 \leq \mathcal{E}_1(t) \leq \mathcal{E}(t_0)$$

We emphasize here that this result cannot be obtained directly, using the sole mass balance and mean momentum equations. Moreover, there is no need to use a gradient-type closure law for Reynolds stresses in order to obtain this result, as it is sometimes argued. Of course, viscous -or other dissipative- effects might be added in the mean momentum equation ; these would result in a strict dissipation of the whole kinetic energy of the mean motion. Inlet/Outlet boundary conditions may also be investigated.

3.4 Numerical algorithm

In order to compute the approximations of solutions of system (3.1.2) at each time step, the Finite Volume method relies on a classical fractional step method, which proceeds in three distinct steps:

- An evolution step;

- An instantaneous relaxation step;
- A physical step to take sources into account.

3.4.1 Algorithm

The whole algorithm is thus the following:

- **Step 1 (Evolution):**

Starting from the conservative variable W^n :

$$W^n = (\rho^n, (\rho U_i)^n, (\rho R_{ij})^n),$$

compute approximate solutions $\rho^{n+1,-}, (\rho U_i)^{n+1,-}, (\rho R_{ij})^{n+1,-}$ of the homogeneous system corresponding to the left hand side of (3.2.2) at time t^{n+1} , using an approximate Godunov solver for (R1) (see [16]) or a relaxation interface solver for (R2).

- **Step 2 (Relaxation):**

Restore local values of the Reynolds stresses $R_{ij} = R_{ij}^L$:

$$\rho^{n+1} = \rho^{n+1,-}, \quad (\rho U_i)^{n+1} = (\rho U_i)^{n+1,-}, \quad (\rho R_{ij})^{n+1} = \rho^{n+1}(R_{ij}^L)^{n+1}.$$

- **Step 3 (Sources):**

Account for physical source terms (right hand side of (3.1.2)).

We describe now the Finite Volume algorithm [11] that is used in order to obtain numerical approximations of solutions of the evolution step.

3.4.2 Evolution step

We introduce a partition of the computational domain in non-overlapping cells Ω_i , the measure of which is $vol(\Omega_i)$. The surface separating two adjacent cells i and j is S_{ij} , the outward normal vector n_{ij} pointing from cell i to cell j . We denote $V(i)$ the set of neighbouring cells of Ω_i . A time step Δt^n is obtained using a classical CFL-like condition. At each time step, the scheme computes approximate values W_i^n of $\int_{\Omega_i} W(\underline{x}, t^n) d\omega / vol(\Omega_i)$, using the rule:

$$\begin{aligned} vol(\Omega_i)(\rho_i^{n+1} - \rho_i^n) + \Delta t^n \sum_{j \in V(i)} ((\rho^* \underline{U}^* \cdot \underline{n})_{ij} S_{ij}) &= 0 \\ vol(\Omega_i)((\rho \underline{U}_i)^{n+1} - (\rho \underline{U}_i)^n) + \Delta t^n \sum_{j \in V(i)} ((\rho^* \underline{U}^* (\underline{U}^* \cdot \underline{n}))_{ij} S_{ij}) \\ + \Delta t^n \sum_{j \in V(i)} ((\rho^* \underline{\underline{R}}^* \underline{n}))_{ij} S_{ij} &= 0 \end{aligned} \quad (3.4.1)$$

We use here the convention that:

$$(\phi^*)_{ij} = \phi^{Riemann}(W_L = W_i^n, W_R = W_j^n, \underline{n}_{ij}; \frac{x_n - (x_n)_{ij}}{t} = 0)$$

where the solution of the one-dimensional Riemann problem corresponds to approach **R2** (or **R1**) in the x_n direction.

3.5 Numerical results

An extensive validation of both methods (**R1**, **R2**) has been achieved in [10] in the one-dimensional framework, by computing the L^1 norm of the error for analytical solutions of Riemann problems associated with the homogeneous part of (3.1.2), assuming specific forms for $R_{ij}^L = r_{ij}(\rho, U)$. One important conclusion in the latter reference was that rather small discrepancies between (**R1**) and (**R2**) were observed in all computations investigated ; another essential point was that both of them could handle shock computations, which was expected due to the conservative form of the relaxed system (3.1.4). Thus we only show here a few two-dimensional noisy computations and we put emphasis on the main conclusions.

3.5.1 A two-dimensional shock tube with noise

We start with a two-dimensional test case where the form of Lagrangian stress tensor \underline{R}^L is synthetic. The exact values are given by:

$$R_{ij}^L(\underline{x}, t) = R_0 \rho^{\gamma-1} (1 + RMS(0.5 - random(0, 1))) \delta_{ij}$$

with $\gamma = 3$, $R_0 = 10^5$, $RMS = 0.5$. The value of RMS enables to fix the noise amplitude. Obviously solutions may no longer be spherical, even when the initial condition is invariant under rotation. The regular mesh contains 10^4 squares, and the CFL number is set to 0.5. The initial conditions for the mean values ρ and U are the following.

If $x + y < 0$, we set:

$$\rho(\underline{x}, t = 0) = 1 \quad U_x(\underline{x}, t = 0) = U_y(\underline{x}, t = 0) = 0$$

Otherwise, for $x + y > 0$, we set:

$$\rho(\underline{x}, t = 0) = 0.35 \quad U_x(\underline{x}, t = 0) = U_y(\underline{x}, t = 0) = 0$$

All boundary conditions are left free, using a discrete homogeneous Neumann approach for states on both sides of boundary interfaces.

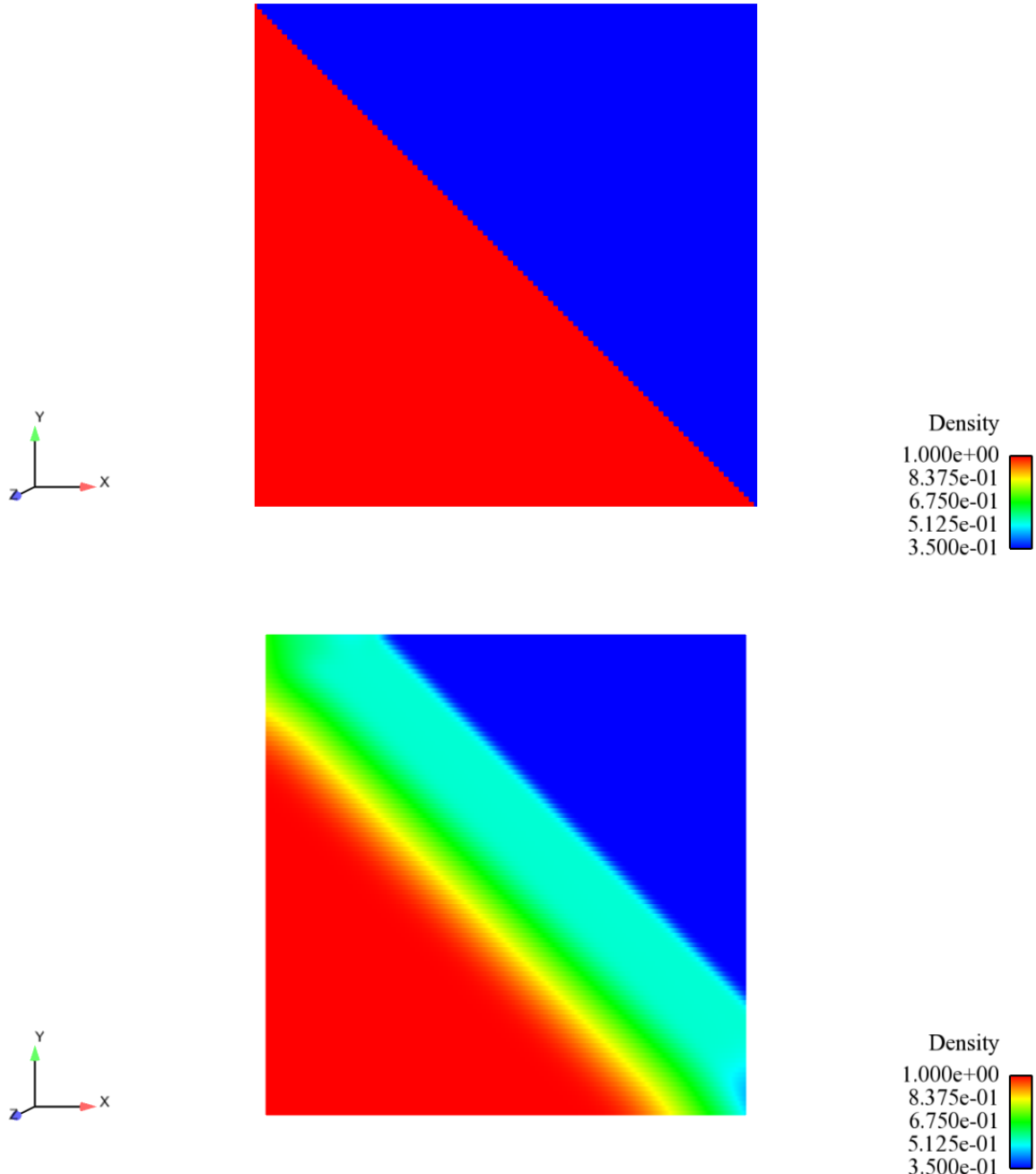


Figure 3.1: Shock tube with noise: density contours at times $t = 0$ (top) and $t = 4 \times 10^{-4}$ (bottom). The CFL is $1/2$.

Hence oblique rarefaction waves and shock waves propagate parallel to the direction $y = x$, and, when restricting to the density contours (see figure 3.1), we retrieve an important smoothing effect

of noise, though the value of RMS is rather high here, especially close to the shock structure. We may conjecture that both the non-linear pattern of the set of PDE, and the stabilization due to the upwinding scheme contribute to this pattern. Of course, the mesh is rather coarse here, which emphasizes the smoothing effect.

Details on the effect of RMS values on solutions are available in [10], together with classical studies of mesh refinement.

3.5.2 A two-dimensional collapse over a moving fluid

The second case we consider corresponds to the collapse of a fluid structure plunged in a uniform moving frame. We use again a synthetic signal:

$$R_{ij}^L(\underline{x}, t) = R_0 \rho^{\gamma-1} (1 + RMS(0.5 - \text{random}(0, 1))) \delta_{ij}$$

with the same values of parameters as defined above. The initial condition for ρ, U is as follows:

- If $(x - x_0)^2 + (y - y_0)^2 < r_0^2$, we set:

$$\rho(\underline{x}, t=0) = 1 \quad \rho U_x(\underline{x}, t=0) = 100 \quad \rho U_y(\underline{x}, t=0) = 0$$

- Otherwise, for: $(x - x_0)^2 + (y - y_0)^2 > r_0^2$, we set:

$$\rho(\underline{x}, t=0) = 0.35 \quad \rho U_x(\underline{x}, t=0) = 290 \quad \rho U_y(\underline{x}, t=0) = 0$$

with $(x_0, y_0) = (0, 0)$, $r_0 = 0.1$ and $\Omega = [-0.5, 0.5]^2$. Hence there is a slip in the initial condition at the bottom of the circular region $(x - x_0)^2 + (y - y_0)^2 < r_0^2$. Values of RMS are uniform and equal to $RMS = 0.5$ in the region $0 < (x - x_0)^2 + (y - y_0)^2 < r_1^2$ with $r_1 = \sqrt{2}/2$.

The first mesh contains 1000×100 rectangular uniform cells. Figures 3.2 give the contours of the density at times $t = 0$ and $t = 4 \times 10^{-4}$. We may observe the "wall" effects around the surface travelling at a smaller speed, which result in a local increase of the density. This relative speed effect is superimposed to the collapsing effect. Profiles of the density are also available in figure 3.4, at two different times $t = T_1 = 5 \times 10^{-5}$ and $t = T_2 = 4 \times 10^{-4}$, together with ρU and the R_{xx} component; one can observe strong oscillations connected with the noise contribution, especially in almost uniform regions. A strong rarefaction wave develops behind the collapse, which was expected, and its perturbation by the synthetic Reynolds tensor tends to vanish as the mean density tends to zero, and then increases again when ρ increases.

Figures 3.3 show the norm of the particle velocity field. Though the structures seem to be symmetric with respect to the line $y = 0$, we emphasize that it is not, owing to the random contributions.

However, this can be hardly observed on figure 3.5 due to the post-processing.

Figures 3.5 provide the same density contours when the computational mesh is refined (the second mesh contains 4000×400 regular rectangles). In addition, we provide the counterpart for density and x-velocity profiles along the vertical line $y = 0$ (see figure 3.7). The analysis of computational results becomes easier when looking at time evolutions in movies.

We again refer to [10] that examines in detail the influence of the mesh size on noisy calculations in a one-dimensional framework.

3.5.3 A highly anisotropic case

The third test case is quite similar except for the fact that the synthetic Reynolds stress tensor is highly anisotropic, since:

$$R_{ij}^L(\underline{x}, t) = R_0 \rho^{\gamma-1} (1 + RMS(0.5 - random(0, 1))) M_{ij}$$

with $\gamma = 3$, $R_0 = 10^5$, $RMS = 0.5$, and:

$$M_{xx} = 5/4, \quad M_{xy} = M_{yx} = 1/4, \quad M_{yy} = 3/4.$$

R_{ij}^L is symmetric positive definite unless a vacuum occurs in the solution. The initial condition for ρ, U is given below.

- If $(x - x_0)^2 + (y - y_0)^2 < 0.01$, we set:

$$\rho(\underline{x}, t = 0) = 1$$

- Otherwise, we set:

$$\rho(\underline{x}, t = 0) = 0.35$$

still using: $(x_0, y_0) = (0, 0)$. The fluid is at rest at the beginning of the computation:

$$U_x(\underline{x}, t = 0) = U_y(\underline{x}, t = 0) = 0.$$

The computational domain is again: $\Omega = [-0.5, 0.5]^2$, and we use here a fine mesh including 1000×1000 regular cells.

The structure of the solution is rather complex. Nonetheless we may retrieve the principal axes that are aligned with :

$$r_+ = (1, (1 + \sqrt{2})^{-1}) \quad , \quad r_- = (1, (1 - \sqrt{2})^{-1})$$

Moreover, the ratio of diameters of principal axes D/d of the ellipse is approximately equal to the following ratio c_+/c_- (see figure 3.8):

$$\frac{c_+}{c_-} = \left(\frac{\lambda_+}{\lambda_-}\right)^{1/2} (\rho_+/\rho_-)^{(\gamma-1)/2}$$

where ρ_+ (respectively ρ_-) stands for the value of the mean density just before the shock propagating in the r_+ (respectively r_-) direction, and also noting λ_{\pm} the eigenvalue associated with the right eigenvector r_{\pm} :

$$\lambda_{\pm} = 1 \pm (2\sqrt{2})^{-1}$$

The low values of the mean density at the origin $(0,0)$ are due to the interaction and reflection of initial -anisotropic- rarefaction waves generated by the initial discontinuity of the mean density at $r = 0.1$.

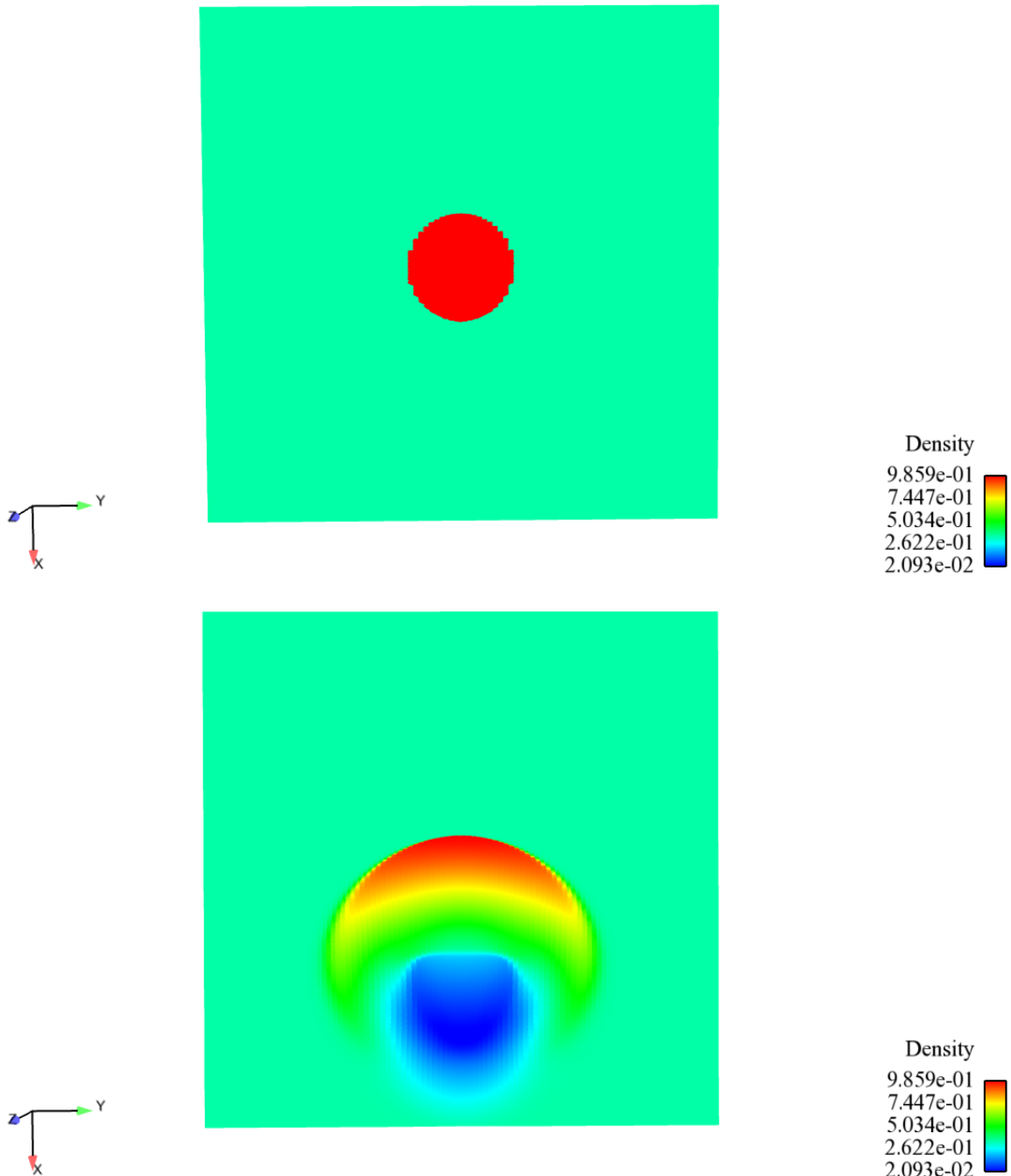


Figure 3.2: Collapse with noise: density contours at times $t = 0$ (top) and $t = 4 \times 10^{-4}$ (bottom). The CFL is $1/2$.

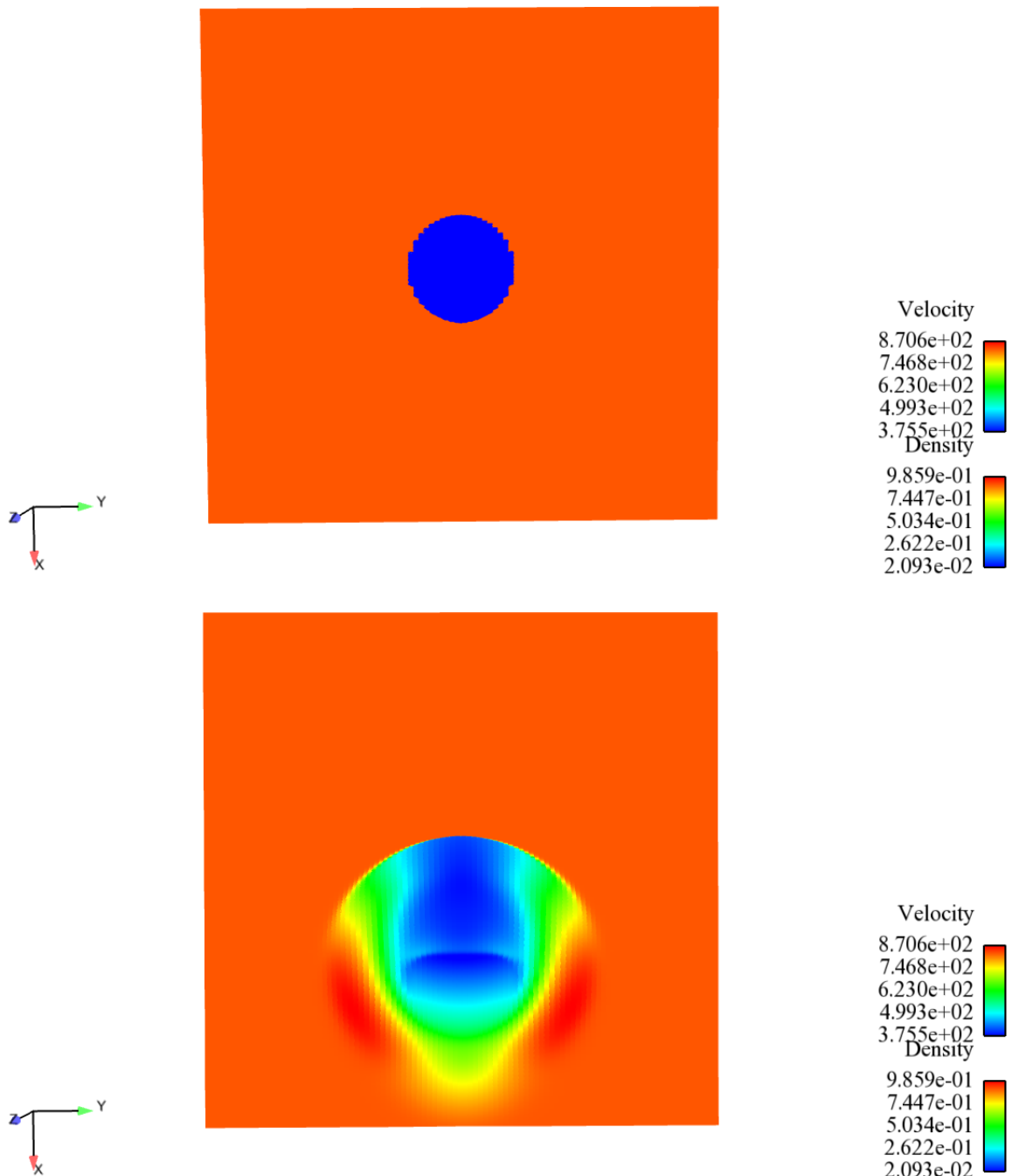


Figure 3.3: Collapse with noise: velocity contours at times $t = 0$ (top) and $t = 4 \times 10^{-4}$ (bottom). Coarse mesh including 1000×100 regular cells. The CFL is $1/2$.

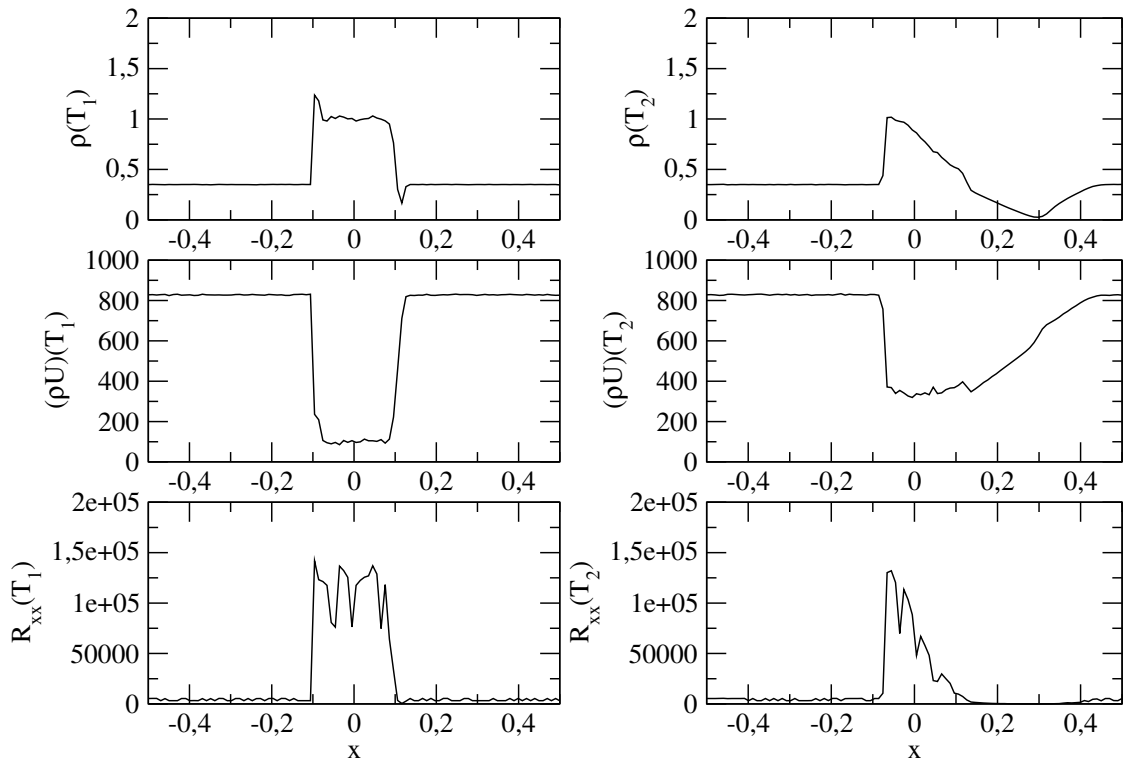


Figure 3.4: Collapse with noise: density (top) and x-momentum profiles at times $t = T_1 = 5 \times 10^{-5}$ (left) and $t = T_2 = 4 \times 10^{-4}$ (right) along the line $y = 0$, together with R_{xx} component (bottom). Coarse mesh including 1000×100 regular cells. The CFL is $1/2$.

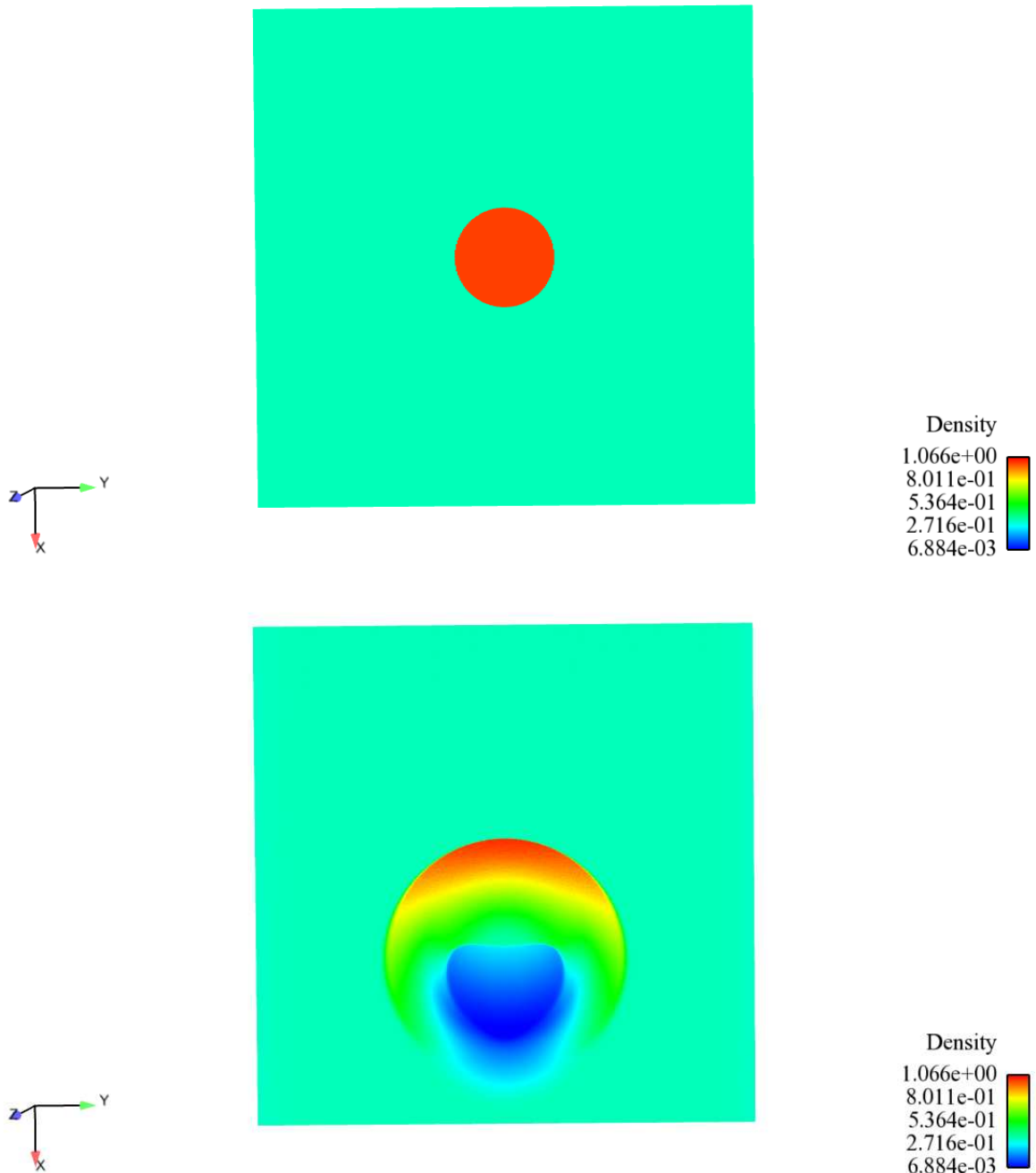


Figure 3.5: Collapse with noise: density contours at times $t = 0$ (top) and $t = 4 \times 10^{-4}$ (bottom). This fine mesh includes 4000×400 regular cells. The CFL is $1/2$.

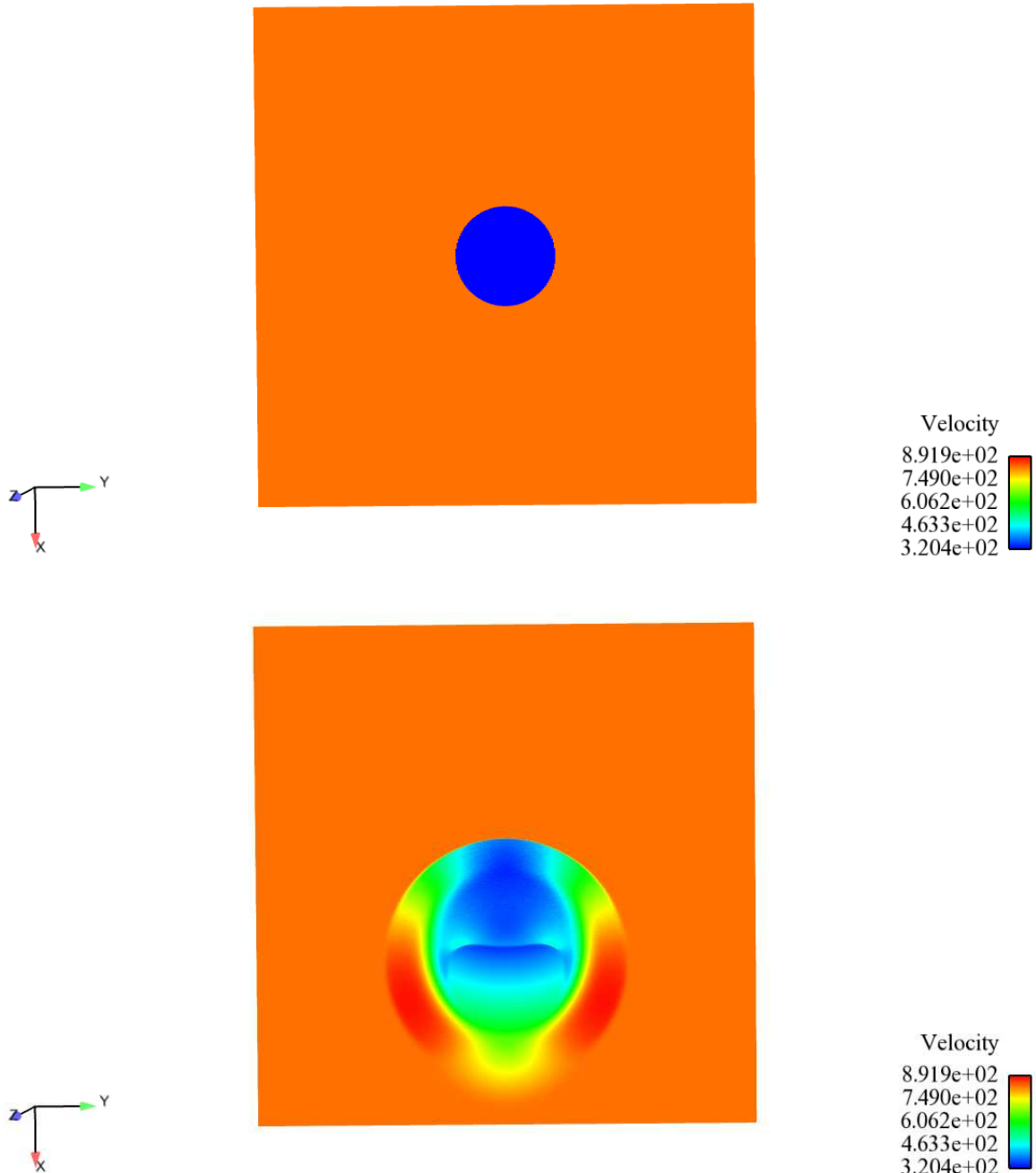


Figure 3.6: Collapse with noise: velocity contours at times $t = 0$ (top) and $t = 4 \times 10^{-4}$ (bottom). This fine mesh includes 4000×400 regular cells. The CFL is $1/2$.

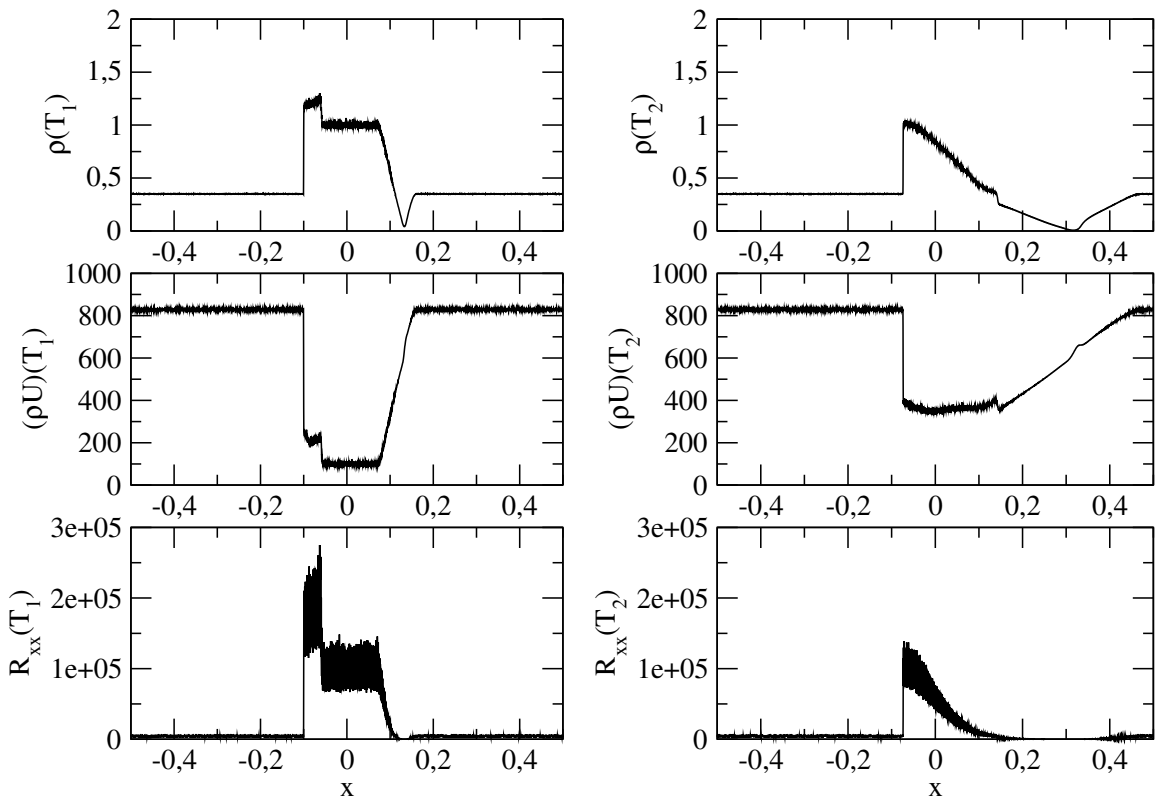


Figure 3.7: Collapse with noise: density (top) and x-momentum profiles at times $t = T_1 = 5 \times 10^{-5}$ (left) and $t = T_2 = 4 \times 10^{-4}$ (right) along the line $y = 0$, together with R_{xx} component (bottom). This fine mesh includes 4000x400 regular cells. The CFL is 1/2.

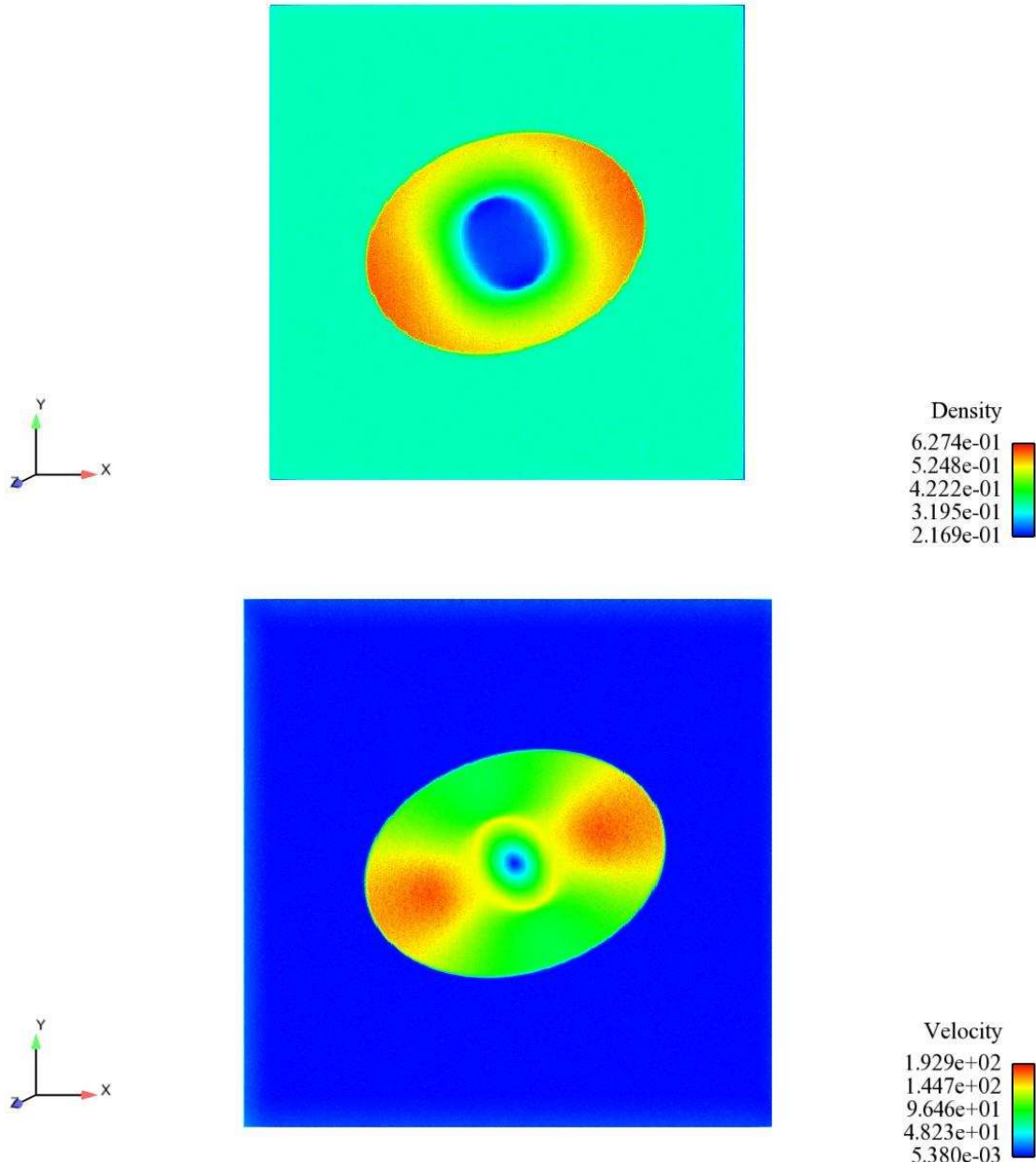


Figure 3.8: Anisotropic collapse with noise: density (top) and velocity contours (bottom) at time $t = 4 \times 10^{-4}$. Fine mesh including 1000×1000 regular cells, with $CFL = 1/2$.

Conclusion

We have presented in this paper a new relaxation technique **R2**, and the main properties of the former approach **R1** and of the new one **R2** have been detailed. It has been shown that the stability of the relaxation system is such that the kinetic energy of the mean momentum remains bounded in the Eulerian approach. Some two-dimensional results have been discussed, and we refer to the reference paper [10] where the mesh refinement effects have been investigated in detail.

Actually, when computing approximations of solutions of system 3.1.2, the relaxation technique **R2** provides a useful tool in order to compute approximate values of fluxes at each interface of the Finite Volume mesh. It does not require introducing approximate jump conditions in the Riemann problem for the relaxation system, unlike in the former relaxation approach **R1** (see [16]). The anisotropy of the Reynolds stress tensor R_{ij}^L may be taken into account, which is known to be mandatory for real computations involving fully-developped turbulence (see for instance appendix in [4] where some nice example of numerical instability is exhibited). The relaxation approach **R2** provides a rather nice stability of the whole algorithm. We conjecture that the convergence to the correct solution of the relaxed system (3.1.4) is due to the conservative form of the scheme (3.4.1).

Eventually, we emphasize that this algorithm has been extensively used for the unsteady coupling of a Lagrangian code with its Eulerian counterpart, while focusing on the particle jet in a coaxial air flow along a wall boundary, as detailed in chapter 4.

The extension to the three-dimensional framework is almost straightforward, but rather technical and tedious.

Appendix A

- Wave ordering condition (WOC)

Intermediate states of density are positive if:

$$\begin{cases} 2\vartheta_l a_0^2 + [U_n]_l^r a_0 - [\rho R_{nn}]_l^r > 0 \\ 2\vartheta_r a_0^2 + [U_n]_l^r a_0 + [\rho R_{nn}]_l^r > 0 \end{cases} \quad (3.5.1)$$

We introduce :

$$\Delta_1 = ([U_n]_l^r)^2 + 8\vartheta_l [\rho R_{nn}]_l^r \quad \Delta_2 = ([U_n]_l^r)^2 - 8\vartheta_r [\rho R_{nn}]_l^r. \quad (3.5.2)$$

If $\Delta_1 \geq 0$ we set:

$$(a_0)_{1,2} = \frac{-[U_n]_l^r \pm \sqrt{\Delta_1}}{4\vartheta_l}.$$

If $\Delta_2 \geq 0$, we set:

$$(a_0)_{3,4} = \frac{-[U_n]_l^r \pm \sqrt{\Delta_2}}{4\vartheta_r}.$$

Starting with a minimal value $a_{min} > 0$, a_0 must be chosen such that :

If $\Delta_1 \geq 0$ and $\Delta_2 \geq 0$ then a_0 should be greater than $\max \{a_{min}, (a_0)_{i \in (1,2,3,4)}\}$

If $\Delta_1 \geq 0$ and $\Delta_2 < 0$ then a_0 should be greater than $\max \{a_{min}, (a_0)_{i \in (1,2)}\}$

If $\Delta_1 < 0$ and $\Delta_2 \geq 0$ then a_0 should be greater than $\max \{a_{min}, (a_0)_{i \in (3,4)}\}$.

If $\Delta_1 < 0$ and $\Delta_2 < 0$ then $a_0 > a_{min}$.

In practice, a_{min} is chosen such that:

$$a_{min} = \max(\rho_l(|U_n| + c_1)_l, \rho_r(|U_n| + c_1)_r)$$

- Intermediate states 1, 2, 3, 4 for $R_{n\tau}$ and U_τ :

$$(\tilde{\rho} \tilde{R}_{n\tau})_1 = (\rho R_{n\tau})_L (\vartheta_L / \vartheta_1)^3,$$

$$\begin{aligned} (\tilde{\rho} \tilde{R}_{n\tau})_2 = (\tilde{\rho} \tilde{R}_{n\tau})_3 = & a_0 / (2\sqrt{3}) \{ (U_\tau)_L - (U_\tau)_R + (\rho R_{n\tau}/a_0)_L + (\rho R_{n\tau}/a_0)_R \} + \\ & (\sqrt{3} - 1) \left[(\tilde{\rho} \tilde{R}_{n\tau}/a_0)_1 + (\tilde{\rho} \tilde{R}_{n\tau}/a_0)_4 \right] a_0 / (2\sqrt{3}), \end{aligned} \quad (3.5.3)$$

$$(\tilde{\rho} \tilde{R}_{n\tau})_4 = (\rho R_{n\tau})_R (\vartheta_R / \vartheta_4)^3,$$

$$(\tilde{U}_\tau)_1 = (U_\tau)_L + (\rho R_{n\tau})_L/a_0 - (\tilde{\rho} \tilde{R}_{n\tau})_1/a_0,$$

$$(\tilde{U}_\tau)_2 = (\tilde{U}_\tau)_3 = ((U_\tau)_L + (U_\tau)_R)/2 + ((\rho R_{n\tau})_L - (\rho R_{n\tau})_R)/2a_0 + \left((\sqrt{3} - 1)(\tilde{\rho} \tilde{R}_{n\tau})_1 + (1 - \sqrt{3})(\tilde{\rho} \tilde{R}_{n\tau})_4 \right) / 2a_0, \quad (3.5.4)$$

$$(\tilde{U}_\tau)_4 = (U_\tau)_R - (\rho R_{n\tau})_R/a_0 + (\tilde{\rho} \tilde{R}_{n\tau})_4/a_0.$$

Bibliography

- [1] B. AUDEBERT, "Contribution à l'analyse de l'interaction onde de choc - couche limite", *Université Pierre et Marie Curie*, PhD thesis, 2006.
- [2] C. BERTHON, F. COQUEL, J.M. HÉRARD AND M. UHLMANN, "An approximate solution of the Riemann problem for a realisable second-moment turbulent closure", *Shock Waves Journal*, vol. 11 (4), pp. 245-269, 2002.
- [3] F. BOUCHUT, "Nonlinear stability of finite volume methods for hyperbolic conservation laws and well-balanced schemes for source", *Frontiers in Mathematics Series*, Birkhauser, 2004.
- [4] G. BRUN, J.M. HÉRARD, D. JEANDEL AND M. UHLMANN, "An approximate Riemann solver for a class of realizable second order closures", *Int. J. of Comp. Fluid Dynamics*, vol. 13, n 3, pp. 223-249, 1999.
- [5] C. CHALONS, F. COQUEL AND C. MARMIGNON, "Well-balanced time implicit formulation of relaxation schemes for the Euler equations", *SIAM J. Sci. Comput*, vol 30, issue 1, pp 394-415, 2007.
- [6] C. CHALONS, J.F. COULOMBEL, "Relaxation approximation of the Euler equations", *J. Math. Anal. Appl.*, vol. 348, pp. 872-893, 2008.
- [7] S. CHIBBARO, J.M. HÉRARD AND J.P. MINIER, "A novel Hybrid Moments/Moments-PDF method for turbulent two-phase flows", *Final Technical Report Activity Marie Curie Project. TOK project LANGE Contract MTKD-CT-2004 509849*, 2006.
- [8] F. COQUEL, E. GODLEWSKI, SEGUIN, N., "Relaxation of fluid systems", *Mathematical Models and Methods in Applied Sciences*, DOI No: 10.1142/S0218202512500145, 2012.
- [9] K. DOROGAN, M. GUINGO, J.M. HÉRARD, J.P. MINIER, "A relaxation scheme for hybrid modelling of gas-particle flows", *Accepted for publication in Computers and Fluids (2012)*.
- [10] K. DOROGAN, J.M. HÉRARD, J.P. MINIER, "Development of a new scheme for hybrid modelling of gas-particle two-phase flows", *EDF report H-I81-2010-2352-EN*, 2010.
- [11] R. EYMARD, T. GALLOUET AND R. HERBIN, "Finite Volume Methods", *Handbook of Numerical Analysis*, vol. VII, pp. 713-1020, 2000.

- [12] S. GAVRILYUK, H. GOUIN, "Geometric evolution of the Reynolds stress tensor in three-dimensional turbulence", *European J. Mechanics B/Fluids*, <http://hal.archives-ouvertes.fr/hal-00371444/en/>, submitted, 2010.
- [13] J.M. HÉRARD, "Basic analysis of some second-moment closures. Part II: incompressible turbulent flows including buoyant effects", *EDF report HE-41/93/37A*, 1993.
- [14] J.M. HÉRARD, "Realizable non-degenerate second-moment closures for incompressible turbulent flows", *CRAS Paris Ib*, vol. 322, pp. 371-377, 1996.
- [15] J.M. HÉRARD, "A relaxation tool to compute hybrid Euler-Lagrange compressible models", *AIAA paper 2006-2872, 36th AIAA FD Conference*, <http://www.aiaa.org>, 2006.
- [16] J.M. HÉRARD, M. UHLMANN AND D.E. VAN DER VELDEN, "Numerical techniques for solving hybrid Eulerian-Lagrangian models for particulate flows", *EDF report H-I81-2009-3961-EN*, pp. 1-50, 2009 (unpublished).
- [17] S. JIN AND Z. XIN, "The relaxation schemes for systems of conservation laws in arbitrary space dimensions", *Comm. Pure Appl. Math.*, vol 48, pp. 235-276, 1995.
- [18] P.G. LE FLOC'H, "Entropy weak solutions to non-linear hyperbolic systems in non-conservative form", *Comm. in Part. Diff. Eq.*, vol 13(6), pp. 669-727, 1988.
- [19] J.L. LUMLEY, "Computational modelling of turbulent flows", *Advances in Applied Mechanics*, vol. 18, pp. 123-176, 1978.
- [20] M. MURADOGLU, P. JENNY, S.B. POPE AND D.A. CAUGHEY, "A consistent hybrid finite-volume/particle method for the pdf equations of turbulent reactive flows", *Journal of Computational Physics*, vol. 154, pp. 342-371, 1999.
- [21] S.B. POPE, "PDF methods for turbulent reactive flows", *Prog. Energy Comb. Sci.*, vol. 11, pp. 119-192, 1985.
- [22] S.B. POPE, "On the relationship between stochastic Lagrangian models of turbulence and second-moment closures", *Physics of Fluids*, vol. 6(2), pp. 973-985, 1984.
- [23] U. SCHUMANN, "Realizability of Reynolds stress turbulent models", *Physics of Fluids*, vol. 20 (5), pp. 721, 1977.
- [24] I. SULICIU, "On the thermodynamics of fluids with relaxation and phase transitions. Fluids with relaxation", *Internat. J. Engrg. Sci.*, vol. 36, pp. 921-947, 1998.

Chapter 4

A hybrid Moments/Moments-PDF approach to simulation of turbulent two-phase flows

4.1 Introduction

The classical Moments/PDF method described in Chapter 1 has been shown to be suitable for the numerical simulation of turbulent two-phase flows, especially in non-equilibrium situations. In order to overcome some of its limitations due, for example, to the relatively slow convergence rate of the statistical error and, possibly, to the occurrence of a bias, an alternative hybrid approach has been proposed in [4]. The latter is based on the classical Moments/PDF method but introduces a mixed Moments/PDF description within the particle phase itself, the fluid phase being still simulated using RANS-type moments equations. In the particle phase description, the Lagrangian stochastic equations are supplemented with partial differential equations for a chosen number of the particle statistical moments, which are derived from them. Therefore, the idea consists in computing some of particle statistics by a Moments method and providing it to the coefficients of the stochastic model so that resulting particle statistics are not biased by construction. Eventually, since such a coupling should reduce the bias and the statistical error of the Lagrangian approximations, it could also reduce the number of particles needed for a given precision. Following the notations given in Chapter 1, the particle phase description within the hybrid model for turbulent two-phase flow is given by a coupled Moments/PDF representation:

- **Lagrangian (PDF) description of the particle phase.** Stochastic differential equations SDE_p^{Lag} :

$$\begin{aligned} dx_{p,i} &= U_{p,i} dt \\ d\mathbf{U}_{p,i} &= \frac{1}{\tau_p} (U_{s,i} - U_{p,i}) dt + g_i dt \\ dU_{s,i} &= -\frac{1}{\rho_g} \frac{\partial \langle P_g \rangle}{\partial x_i} dt + (\langle \mathbf{U}_{p,j}^E \rangle - \langle U_{g,j} \rangle) \frac{\partial \langle U_{g,i} \rangle}{\partial x_j} dt - \frac{(U_{s,i} - \langle U_{g,i} \rangle)}{\mathbf{T}_{L,i}^{E*}} dt + \\ &\quad \sqrt{\langle \varepsilon \rangle \left(C_0 b_i \tilde{k}/k + \frac{2}{3} (b_i \tilde{k}/k - 1) \right)} dW_{t,i}, \quad i, j \in \mathbb{Z} \end{aligned} \quad (4.1.1)$$

where the gas-related statistics, denoted with subscript “ g ”, are computed by the fluid Finite Volume Solver PDE_g^{Eul} , whereas the terms provided by the Eulerian particle solver are indicated by superscript “ E ”.

- **Eulerian description of the particle phase.** Conservation laws deduced from (4.1.1) for particle statistical quantities, PDE_p^{Eul} :

$$\begin{aligned} \frac{\partial \alpha_p^E \rho_p}{\partial t} + \frac{\partial}{\partial x_i} (\alpha_p^E \rho_p \langle U_{p,i}^E \rangle) &= 0, \quad i \in \mathbb{Z} \\ \frac{\partial \alpha_p^E \rho_p \langle \mathbf{U}_{p,i}^E \rangle}{\partial t} + \frac{\partial}{\partial x_j} (\alpha_p^E \rho_p (\langle U_{p,i}^E \rangle \langle U_{p,j}^E \rangle + \langle \mathbf{u}_{p,i} \mathbf{u}_{p,j} \rangle^L)) &= \alpha_p^E \rho_p g_i + \left\langle \frac{\alpha_p^E \rho_p \mathbf{U}_{r,i}^L}{\tau_p^L} \right\rangle, \end{aligned} \quad (4.1.2)$$

where the variables computed by the Lagrangian solver are denoted with the script “ L ” and ρ_p is the constant particle density. The right-hand-side terms account for the gravity and the drag forces.

Thus, the particle mean velocity computed by the Eulerian moments equations (4.1.2), $\langle \mathbf{U}_p^E \rangle$ is used as a not-biased averaged quantity in the Lagrangian set of equations (4.1.1) (it is involved in the terms marked in blue). These, in turn, will provide the Eulerian part (PDE_p^{Eul}) of the particle model with the particle kinetic tensor $\mathbf{R}_p^L = \langle \mathbf{u}_p \mathbf{u}_p \rangle^L$ and with local nonlinear source terms (marked in red), enabling in this way physically meaningful closures in the Eulerian equations. It is worth noting that the particle position \mathbf{x}_p is also implicitly involved in the coupling since it is used for the calculation of the Lagrangian particle statistics. The difference with the classical Moments/PDF description of two-phase flow is illustrated in Fig. 4.1.

In practice, in order to implement this coupling method and before stating its efficiency, many numerical features have to be worked out. In this work, two issues among others will be evaluated:

- The ability of the Finite Volume particle solver developed in chapters 2 and 3 to provide *stable instationary approximations* to (4.1.2) even when noisy data are introduced in the system of equations. Moreover, the *correct convergence* of these approximations must be ensured.
- The Monte-Carlo convergence of the Lagrangian approximations to (4.1.1) in hybrid computations and the influence of the new coupling strategy on *the statistical and the bias errors*.

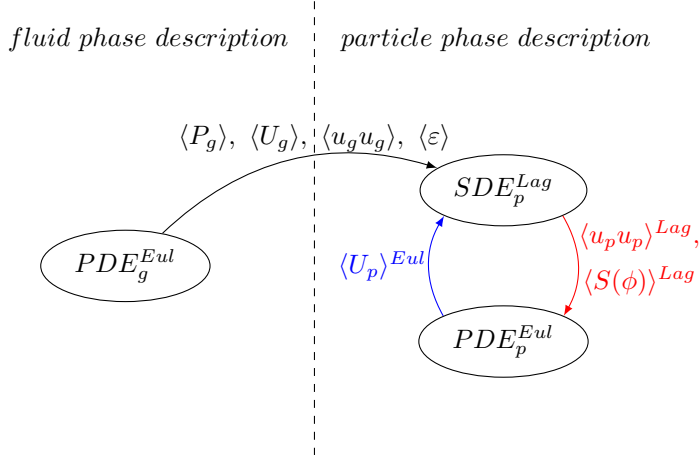


Figure 4.1: An extension of the classical representation - a hybrid Moments/Moments-PDF description corresponding to algorithm A defined below.

Therefore, this chapter is organized as follows. A hybrid Finite Volume (FV)/FV-DSMC (Direct Simulation Monte-Carlo) numerical algorithm of hybrid Moments/Moments-PDF simulations is given in section 3 as an extension of the "classical" FV/DSMC approach described in chapter 1. Numerical results are presented and discussed in section 4, which details also several numerical issues as well as the treatment of boundary conditions in hybrid configuration. Analysis of the numerical errors arising in the hybrid method is presented together with a comprehensive study of convergence for both Eulerian and Lagrangian particle modules. The numerical results demonstrate the stability of hybrid FV/FV-DSMC computations and the global convergence of the method. Conclusions are drawn in section 5 which presents a broad discussion on the perspectives of such hybrid descriptions.

4.2 A hybrid FV/FV-DSMC algorithm

We recall that in the present hybrid computations, as well as in "classical" Moments/PDF methods, we are interested by the particle volumetric fraction $\alpha_p(t, \mathbf{x})$, by the mean particle velocity $\langle \mathbf{U}_p \rangle(t, \mathbf{x})$ and by the particle related kinetic tensor $\mathbf{R}_p(t, \mathbf{x})$ computed with the Lagrangian part (4.1.1) of the particle model. Here, in each cell i (with the cell center \mathbf{x}_i) containing $N_{pc}^{[i]}$ particles at time t , the following approximations are used:

$$\alpha_p(t, \mathbf{x}_i) = \frac{\sum_{n=1}^{N_{pc}^{[i]}} v^{(n)}}{\mathcal{V}_i}, \quad (4.2.1)$$

where $v^{(n)}$ is the volume occupied by a particle and \mathcal{V}_i - the volume of the cell i . For other mean particle quantities we obtain the numerical approximations as ensemble averages:

$$\langle \mathcal{H}_p \rangle(t, \mathbf{x}_i) \simeq \langle \mathcal{H}_p \rangle_{N_{pc}}(t, \mathbf{x}_i) = \frac{\sum_{n=1}^{N_{pc}^{[i]}} \mathcal{H}_p^{(n)}(t)}{N_{pc}^{[i]}}. \quad (4.2.2)$$

On the other hand, the system of partial differential equations (4.1.2) provides the Eulerian (duplicate) fields, $\alpha_p^E(t, \mathbf{x})$ and $\langle \mathbf{U}_p^E \rangle(t, \mathbf{x})$, computed on a mesh by a Finite Volume (FV) Solver. Thus, in the numerical simulations, the two notions of particles and mesh are involved. Though, in principle, different grids may be used for each description, it requires the introduction of several averaging and projection operators:

- between the particle locations and the grid where the Lagrangian particle statistics are computed using (4.2.1), (4.2.2). These operators have been described in chapter 1 (sec. 1.3.2.4) following [32] and play an important role in the propagation of the statistical and deterministic errors;
- between the particle locations, the particle grid and the particle Finite Volume mesh used to approximate the solutions of PDE_p^{Eul} (4.1.2).

Moreover, we have to quantify the contribution of these averaging/projection operations to the global numerical error. In the present work both spatial and temporal discretizations related to Lagrangian and Eulerian parts of the particle description are assumed to *coincide*. The time and space discretization used in the gas-phase Finite-Volume Solver do not vary between different computations. Otherwise, the differences in approximations could be misinterpreted. Thus, the only numerical parameters to be introduced are the mesh "size" \mathbf{h} , the time step Δt and the number of statistical particles per cell, N_{pc} . However, this *choice* has many important outcomes. For instance, the mesh refinement in the Eulerian part of the particle method requires increasing the total number of particles in the domain in order to preserve the accuracy of Lagrangian computations related to N_{pc} .

The time step of the global algorithm is specified through the CFL condition, which ensures the stability of the particle Finite Volume Solver: $\Delta t^n = \min(\Delta t^{L,n}, \Delta t^{E,n})$, where $\Delta t^{E,n}$ satisfies

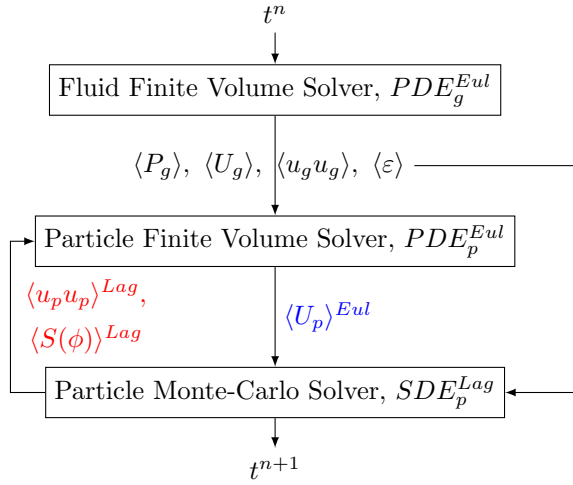
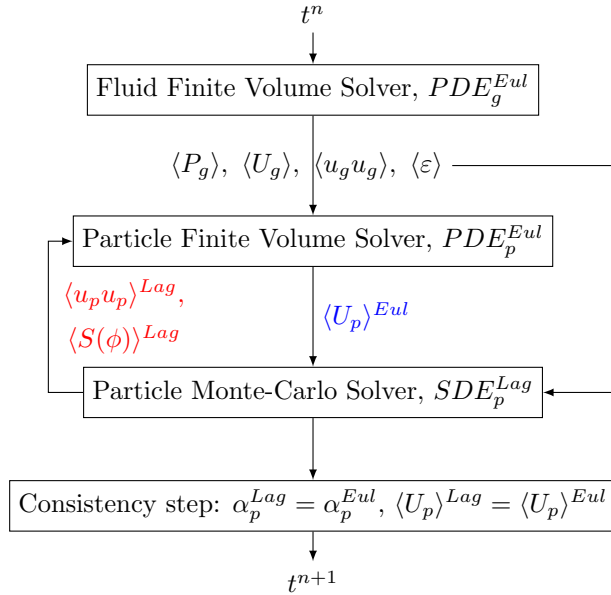
$$\Delta t^{E,n} \max_{\mathbf{W}, k} (|\lambda_k(\mathbf{W})|)/d \leq CFL, \quad n, k \in \mathbb{N}, \quad (4.2.3)$$

\mathbf{W} is the Eulerian particle state vector, $\lambda_k, k \in \mathbb{N}$ are characteristic wave speeds corresponding to system (4.1.2) for all the \mathbf{W} under consideration. We recall that $\Delta t^{L,n}$ may be chosen arbitrarily (in terms of stability), since the numerical scheme used to compute the approximations to (4.1.1) is unconditionally stable (see sec. 1.3.2.5).

4.2.1 Algorithm

It is worth pointing out that the present algorithm of hybrid computations is an extension of the "classical" FV/DSMC approach. In fact, it is based on the Lagrangian module for the system SDE_p^{Lag} , which has been developed in Chapter 1 to approximate the solutions of the pdf equation (sec. 1.3.2.2), and is now supplemented by an Eulerian module simulating PDE_p^{Eul} . Two different solutions may be proposed (Fig. 4.2 and 4.3), where the **algorithm B** is an extension of the **algorithm A** in order to explicitly ensure the unsteady consistency of duplicate fields whatever the choice of $\mathbf{h}, \Delta t, N_{pc}$:

$$\alpha_p^{Lag} = \alpha_p^{Eul}, \quad \langle \mathbf{U}_p \rangle^{Lag} = \langle \mathbf{U}_p \rangle^{Eul}, \quad (4.2.4)$$

Figure 4.2: Numerical **algorithm A** of hybrid Moments/Moments-PDF simulations.Figure 4.3: Numerical **algorithm B** of hybrid Moments/Moments-PDF simulations.

where the Eulerian and the Lagrangian fields are computed by different parts, PDE_p^Eul and SDE_p^Lag respectively, of the particle hybrid description (4.1.1) - (4.1.2).

In the present work we focus on the numerical implementation of the **algorithm A** in order to verify the *correct convergence* of the Eulerian and Lagrangian particle "hybrid" approximations to the solution obtained using the "classical" Lagrangian description alone (1.3.5) when $\mathbf{h}, \Delta t \rightarrow 0$ and $N_{pc} \rightarrow \infty$. In fact, the implementation of the consistency step (4.2.4), which is introduced in algorithm B and implies the unsteady corrections of the particle positions and velocities, is not at

all straightforward and requires further developments, and justifications for a given "mesh" size. Otherwise the counterpart of problems such as those described in [15] (where it is shown that enforcing a continuous condition on each mesh size may lead to a convergence towards a wrong solution) might appear.

Let $\{\mathbf{Y}^{[\mathbf{x}]}\}$ denote the set of the fluid mean fields at the mesh points and let $\{\mathbf{Y}^{(N)}\}$ be the fluid mean fields interpolated at particle locations. Let $\{\mathbf{Z}^{(N)}\}$ denote the set of variables attached to the stochastic particles and $\{\mathbf{Z}^{[\mathbf{x}]}\}$ the set of statistics, defined at cell centers, extracted from $\{\mathbf{Z}^{(N)}\}$. We assume also that $\{\mathbf{W}^{[\mathbf{x}]}\}$ states for the Eulerian mean particle properties, which are evaluated on a mesh and $\{\mathbf{W}^{(N)}\}$ for their interpolation at the particle locations. The time is discretized with the time step $\Delta t^n = t^{n+1} - t^n$ and the space with some non-uniform mesh. The **general unsteady particle-mesh algorithm** within a time step $t^n \rightarrow t^{n+1}$ is sketched in Fig. 4.2 and can be detailed as the following sequence of operators:

Step 1: Solution of the partial differential equations describing the fluid (PDE_g^{Eul}).

$$\{\mathbf{Y}^{[\mathbf{x}]}\}(t^n) \xrightarrow{F} \{\mathbf{Y}^{[\mathbf{x}]}\}(t^{n+1}). \quad (4.2.5)$$

The F operator corresponds to a finite volume solver for system (1.3.1)-(1.3.4), which provides the instantaneous values of the fluid-related statistical moments: the mean pressure $\langle P_g \rangle$ (or its gradient), the mean velocity $\langle \mathbf{U}_g \rangle$, the Reynolds stress tensor $\langle \mathbf{u}_g \mathbf{u}_g \rangle$, the mean dissipation rate $\langle \varepsilon \rangle$ and additional fields depending on applications.

Step 2: The Particle Finite Volume Solver approximating the solutions of PDE_p^{Eul} (4.1.2) with three-step splitting technique detailed in Chapters 2 and 3:

2.a At the *Evolution step* (operator E), the Godunov numerical scheme computes the evolution of an extended state vector $\tilde{\mathbf{W}} = (\alpha_p^E \rho_p, \alpha_p^E \rho_p \langle \mathbf{U}_p^E \rangle, \alpha_p^E \rho_p \mathbf{R}_p^E)$, where $\mathbf{R}_p^E = \langle \mathbf{u}_p \mathbf{u}_p \rangle^E$ is an Eulerian counterpart of the particle kinetic tensor:

$$\{\tilde{\mathbf{W}}^{[\mathbf{x}]}\}(t^n) \xrightarrow{E} \{\tilde{\mathbf{W}}^{[\mathbf{x}]}\}(t^{n+1,-}). \quad (4.2.6)$$

2.b Then, the equilibrium values are restored via the *Instantaneous Relaxation step* (operator R), from which the approximations for $\mathbf{W}(t^{n+1,-}) = (\alpha_p^E \rho_p, \alpha_p^E \rho_p \langle \mathbf{U}_p^E \rangle)(t^{n+1,-})$ are retrieved:

$$\{\tilde{\mathbf{W}}^{[\mathbf{x}]}\}(t^{n+1,-}) \xrightarrow{R} \{\mathbf{W}^{[\mathbf{x}]}\}(t^{n+1,-}). \quad (4.2.7)$$

2.c Finally, the right-hand-side terms describing the gravity and the drag forces are taken into account via operator S :

$$\{\mathbf{W}^{[\mathbf{x}]}\}(t^{n+1,-}) \xrightarrow{S} \{\mathbf{W}^{[\mathbf{x}]}\}(t^{n+1}). \quad (4.2.8)$$

Step 3: Using projection operator P , Eulerian mean-particle properties and mean-fluid properties are transferred to the particle locations:

$$\{\mathbf{W}^{[\mathbf{x}]}\}(t^n) \text{ and } \{\mathbf{Y}^{[\mathbf{x}]}\}(t^n) \xrightarrow{P} \{\mathbf{W}^{(N)}\}(t^n) \text{ and } \{\mathbf{Y}^{(N)}\}(t^n). \quad (4.2.9)$$

Step 4: The Particle Monte-Carlo Solver for SDE_p^{Lag} . The system of stochastic differential equations (4.1.1) is integrated in time (operator T) using Euler scheme (see Appendix A):

$$\{\mathbf{Z}^{(N)}\}(t^n) \text{ and } \{\mathbf{Y}^{(N)}\}(t^n) \xrightarrow{T} \{\mathbf{Z}^{(N)}\}(t^{n+1}). \quad (4.2.10)$$

This step computes the temporal evolution of the particle state vector $\mathbf{Z}(t) = (\mathbf{x}_p, \mathbf{U}_p, \mathbf{U}_s)$ for N independent realizations.

Step 5: Finally, from the new computed set of variables at particle locations, new statistical moments are evaluated at cell centers using the averaging operator A ,

$$\{\mathbf{Z}^{(N)}\}(t^{n+1}) \xrightarrow{A} \{\mathbf{Z}^{[\mathbf{x}]}\}(t^{n+1}). \quad (4.2.11)$$

This way, we obtain all local particle statistics: $\alpha_p^L(t^{n+1}, \mathbf{x})$, $\langle U_p \rangle^L(t^{n+1}, \mathbf{x})$, $\langle u_p u_p \rangle^L(t^{n+1}, \mathbf{x})$, etc. evaluated at the grid nodes.

4.2.2 Boundary conditions

Of course, in hybrid computations, the consistency of Eulerian and Lagrangian boundary conditions must be ensured. In particular, this section is devoted to the treatment of wall and inlet/outlet boundary conditions in the present implementation. For a more general presentation of techniques which could be used with such an approach, the reader is referred for instance to [12, 27].

Wall boundary conditions

- In the Lagrangian part of the particle phase description, SDE_p^{Lag} , we consider an elastic wall-particle collision, so that when a particle reaches the wall boundary during a time iteration the following correction is made at the end of the time step (see Fig. 4.4):

$$\begin{aligned} x_p^{n+1} &= \tilde{x}_p^{n+1}, & y_p^{n+1} &= -\tilde{y}_p^{n+1}, \\ U_{p,x}^{n+1} &= \tilde{U}_{p,x}^{n+1}, & U_{p,y}^{n+1} &= -\tilde{U}_{p,y}^{n+1}, \\ U_{s,x}^{n+1} &= \tilde{U}_{s,x}^{n+1}, & U_{s,y}^{n+1} &= -\tilde{U}_{s,y}^{n+1}, \end{aligned} \quad (4.2.12)$$

where the wall boundary is aligned with the x-axis.

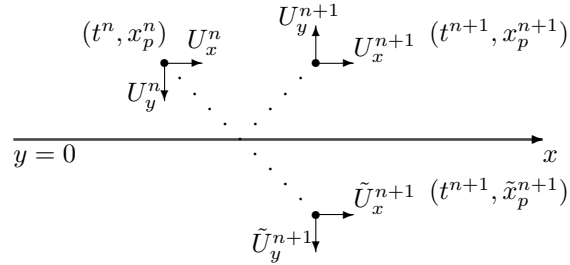


Figure 4.4: The treatment of the wall boundary conditions in the Lagrangian particle simulations.

- In the Eulerian part PDE_p^{Eul} of the particle model, we need to define a boundary condition which would ensure zero mass flux through the boundary. Given an approximation of the Eulerian state vector $\mathbf{W} = (\alpha_p \rho_p, \alpha_p \rho_p \langle \mathbf{U}_p \rangle, \alpha_p \rho_p \mathbf{R}_p)^t$ in the near wall cell i , $i \in \mathbb{Z}$ at time t^k , $k \in \mathbb{N}$ denoted by \mathbf{W}_i^k , we can compute the corresponding state outside the computational domain, \mathbf{W}_∞^k , using the "mirror state" technique [2], see Fig. 4.5. In the reference frame (\mathbf{n}, τ) , where $\mathbf{n} = (n_x, n_y)$ is a unit normal vector outward for cell i , $\tau = (-n_y, n_x)$, omitting the superscript k , we may introduce: $U_n = \langle \mathbf{U}_p \rangle \cdot \mathbf{n}$, $U_\tau = \langle \mathbf{U}_p \rangle \cdot \tau$, $R_{nn} = \mathbf{n}^t \cdot \mathbf{R}_p \cdot \mathbf{n}$, $R_{n\tau} = \mathbf{n}^t \cdot \mathbf{R}_p \cdot \tau = \tau^t \cdot \mathbf{R}_p \cdot \mathbf{n} = R_{\tau n}$, $R_{\tau\tau} = \tau^t \cdot \mathbf{R}_p \cdot \tau$. The "mirror state" technique associates with \mathbf{W}_∞ the following approximations:

$$\begin{aligned}\alpha_{p,\infty} &= \alpha_{p,i}, & \text{since } \rho_p = cst, \\ U_{n,\infty} &= -U_{n,i}, & U_{\tau,\infty} &= U_{\tau,i} \\ R_{nn,\infty} &= R_{nn,i}, & R_{n\tau,\infty} &= -R_{n\tau,i}, & R_{\tau\tau,\infty} &= R_{\tau\tau,i}\end{aligned}\tag{4.2.13}$$

Then, the boundary flux is a function of the solution of the corresponding interface Riemann problem with the initial conditions $\mathbf{W}_l = \mathbf{W}_i^k$ and $\mathbf{W}_r = \mathbf{W}_\infty^k$.

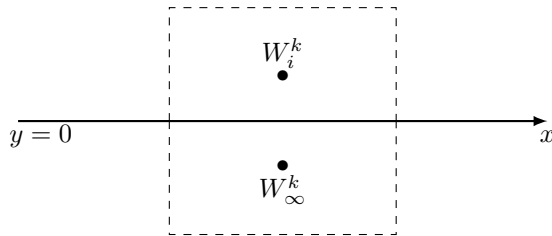


Figure 4.5: The treatment of the wall boundary conditions in the Eulerian particle simulations.

Inlet and outlet boundary conditions

- In the Lagrangian formulation, the particle injection is defined by the inlet flow rate. The particles which are injected during a time step, are in fact uniformly distributed in some volume of a computational domain as if they were crossing the boundary. Then, if during a time step a particle passes out of the domain, it is taken off from the computation.
- In the Eulerian formulation, the boundary conditions depend on the flow configuration; the technique used in the present implementation is detailed in [2].

4.3 Numerical experiments and results

4.3.1 Co-current gas-particle wall jet

In this section, we come back to the case of two-dimensional turbulent co-current wall jet, which has been retained in Chapter 1 for the numerical verification of the Lagrangian module approximating

the solutions of SDE_p^{Lag} (4.1.1). The experimental setup is detailed in sec. 1.4.3, and in the present simulations all the dimensions are conserved. We recall that the gas phase is characterized by the density $\rho_g = 2.1 \text{ kg/m}^3$, the dynamical viscosity $\mu_g = 1.85 \times 10^{-5} \text{ Pa.s}$ and $C_0 = 2.1$. It is injected in the normal to the inlet direction with the constant velocity 1.5 m/s in region AB and 1.0 m/s in BC (Fig. 2.16). Then, a *stationary* turbulent flow may be obtained after some transient period. The dispersed phase is described by the constant particle density $\rho_p = 2000 \text{ kg/m}^3$ and the diameter $d_p = 10^{-5} \text{ m}$. For such a configuration, τ_p is equal approximately $6 \times 10^{-4} \text{ s}$.

Since we deal with a stationary situation, the fluid mean fields are provided by a preliminary single-phase computation with *Code-Saturne* [1] on the mesh of 1600×320 cells, on which the convergence is almost reached. The particle statistics are computed using the hybrid Moments/PDF description (4.1.1), (4.1.2) (Fig. 4.2), which is an extension of the Lagrangian module implemented in Chapter 1. Below, we denote by hx, hy the dimensions of a uniform mesh, by Δt^n , $n \geq 0$ the time step used in both Eulerian and Lagrangian computations and by N_{pc} the number of statistical particles per cell. At the beginning of each time step, particles are injected in the inlet AB with the fluid velocity. For a particle (n) injected in the cell $[i]$ of the domain, we assume the following initial conditions:

$$\begin{aligned}\mathbf{U}_p^{(n)} &= \langle \mathbf{U}_g \rangle^{[i]}, \\ \mathbf{U}_s^{(n)} &= \langle \mathbf{U}_g \rangle^{[i]} + \sqrt{\frac{2}{3} k^{[i]}} \zeta,\end{aligned}\tag{4.3.1}$$

where $\zeta = (\zeta_x, \zeta_y)$ is a vector of independent $\mathcal{N}(0, 1)$ random variables. The number of statistical particles injected in the domain at each time step is determined from the inlet particle flow rate. In order to preserve the same mass of particles in different computations, a *statistical weight* of particles is introduced; it allows to define how many physical particles are represented by a statistical sample.

In the rest of the chapter, we compare the numerical approximations of the mean particle quantities which are obtained using the present hybrid Moments/Moments-PDF algorithm (these will be referred to as $CS_g - HLM2D_p/EM2D_p$) with those of the classical Moments/PDF method ($CS_g - LM2D_p$) in terms of statistical and deterministic errors as functions of $(\mathbf{h}, \Delta t, N_{pc})$. The sketches of the numerical solutions are given in Fig. 4.6 - Fig. 4.15 for the classical simulations ($CS_g - LM2D_p$) and in Fig. 4.16 - Fig. 4.23 for the hybrid ones ($CS_g - HLM2D_p/EM2D_p$), where the approximations obtained with the Eulerian module $EM2D_p$ are said to be Eulerian, and those obtained with the Lagrangian module $HLM2D_p$ are said to be Lagrangian.

Assuming that the fluid phase computations are free from numerical errors, we recall that the whole error of the Monte-Carlo Solver approximating the solutions of "stand-alone" SDE_p^{Lag} is composed by *the deterministic and the statistical errors*, coming from the spatial and temporal discretization and due to the number of particles per cell being finite. Then, an estimation of these errors is necessary to verify the correct convergence of the Lagrangian particle statistics obtained using the hybrid FV/FV-DSMC algorithm and to conclude whether the whole numerical error can be reduced when using the present hybrid approach with reference to "classical" Moments/PDF simulations.

4.3.2 Deterministic error

Following the definitions of the numerical errors given in chapter 1, the deterministic error is composed by the bias, the spatial and the temporal discretization errors. In order to eliminate the statistical error in the further analysis, we will study the time-averaged statistics which contain the same deterministic errors as the unsteady approximations but do not (almost) contain any statistical noise. Thus, for any function \mathcal{H} and for given N_{pc} , we compute an ensemble average for M independent simulations:

$$\langle \mathcal{H}_T \rangle_{N_{pc}} = \frac{1}{M} \sum_{i=1}^M \frac{1}{N_{pc}} \sum_{n=1}^{N_{pc}} \mathcal{H}^{(n)}(t_i), \quad (4.3.2)$$

where N_{pc} is finite, but $M \rightarrow \infty$.

Then, we try to measure the contribution of the bias and of the discretization errors to the deterministic error in the Monte-Carlo Solver for SDE_p^{Lag} which is used in the "classical" Moments/PDF approach (chapter 1).

4.3.2.1 Convergence of the "classical" Monte-Carlo Solver

The classical algorithm of the Monte-Carlo simulations of SDE_p^{Lag} has been described and implemented in chapter 1 in the framework of the Moments/PDF method. Here, we aim at identifying each numerical error related to these simulations in order to compare it to the error of the hybrid algorithm.

Bias. Bias is a deterministic error which is difficult to measure in practice since it appears only in non-linear models where analytical solutions are not known. Moreover, it is often one of the dominant errors in the particle methods that has been shown to scale as N_{pc}^{-1} [49, 50, 36]. In order to identify the bias in the "stand-alone" stochastic simulations of SDE_p^{Lag} and to measure its contribution to the deterministic error, we study the evolution of the time averaged statistics as functions of the number of particles per cell, N_{pc} , for given time and space discretizations. Let us fix $\mathbf{h} = \mathbf{h}_0$ or $(1/Nx_0, 1/Ny_0)$ and the corresponding Δt_0 , computed with the CFL condition, thus fixing the spatio-temporal discretization error. Two series of test cases will be presented:

Case A: On a uniform mesh of $Nx \times Ny = 100 \times 20$ cells with $\Delta t = 2.5 \times 10^{-3}s$ we take $N_{pc} = 10, 50, 100, 150$. As before, we denote by $CS_g - LM2D_p$ the numerical approximations obtained when using *Code-Saturne* for the gas phase (PDE_g^{Eul}) and the Lagrangian module realizing the Monte-Carlo simulations of SDE_p^{Lag} for the particle phase. We present the numerical solutions for $\alpha_p, \langle \mathbf{U}_p \rangle, \alpha_p \rho_p \langle \mathbf{U}_p \rangle$ and $\mathbf{R}_p = \langle \mathbf{u}_p \mathbf{u}_p \rangle$ at four cross-sections: $x = 5d, 10d, 15d, 20d$, where $d = 0.05$ is the diameter of the jet. The time-averaged approximations are given in Fig. 4.24 - Fig. 4.31 and show that there is in fact a dependence on N_{pc} . It can be seen that the maximum bias occurs in the second order statistics (for instance in $R_{p,xy}$) which is in line with [29]. Moreover, we note that *in the present case*, the convergence to some limit is almost reached for $N_{pc} = 100$.

Case B: Fixing another mesh: $Nx \times Ny = 200 \times 40$ and $N_{pc} = 10, 100, 150, 200$ (which correspond now to the total number of statistical samples four times higher than in case A), we obtain a similar conclusion (Fig. 4.32 - Fig. 4.39).

In the following computations, we consider that $\forall h, \Delta t > 0$, the bias of approximations may be neglected for $N_{pc} \geq 100$.

Spatial and temporal discretization error. Assuming now $N_{pc} = 100$, we are trying to measure the discretization error of these "unbiased" approximations. Let us take several meshes: $Nx \times Ny = 100 \times 20, 200 \times 40, 400 \times 80$ and the corresponding time steps $\Delta t \approx 2.5 \times 10^{-3}s, 1.25 \times 10^{-3}s, 6.3 \times 10^{-4}s$. One can see in Fig. 4.40 - Fig. 4.47 that the discretization error is substantially diminished on the meshes finer than $Nx \times Ny = 400 \times 80$ cells.

Remark 4.1. We note the bias appears to be the dominant deterministic error in the classical Lagrangian computations for system SDE_p^{Lag} .

Remark 4.2. Since the correct convergence of the Lagrangian solver has been verified in chapter 1, we assume that the convergent approximations are correct and we take the time-averaged approximations obtained using "classical" Moments/PDF approach with $M = 4000, N_{pc} = 100$ particles per cell on the mesh of $Nx \times Ny = 400 \times 80$ cells as the **reference solution**.

This choice is justified by the need in simultaneous refinement of the space-, time- discretizations and of the total number of samples in the domain in order to preserve the accuracy of Monte-Carlo computations, since it may rapidly result in high computational costs.

4.3.2.2 Convergence of the hybrid Monte-Carlo Solver

Now, the chosen reference solution will allow to conclude whether the hybrid Lagrangian approximations obtained with $CS_g - HLM2D_p/EM2D_p$ simulations converge to the correct solution and whether this hybrid method is efficient in terms of the precision/computational costs.

For a given mesh $Nx \times Ny = 400 \times 80, \Delta t \approx 6.3 \times 10^{-4}s$ and $N_{pc} = 10$, we compare the numerical results of the classical Lagrangian module $LM2D_p$ used in the Moments/PDF numerical approach with the approximations obtained using the hybrid Moments/Moments-PDF method, thus the hybrid module $HLM2D_p/EM2D_p$ for the particle phase (Fig. 4.48 - Fig. 4.55). These parameters are chosen in order to maximize the bias in the classical Lagrangian approximations and minimize the discretization error in both classical and hybrid simulations.

A more detailed analysis (for instance Fig. 4.56 - Fig. 4.58) has shown that both approximate Lagrangian solutions *converge* to the reference solution when $h, \Delta t \rightarrow 0$ and $N_{pc} \rightarrow \infty$. In particular, we note that the approximations obtained with $LM2D_p$ do not vary significantly with $h, \Delta t \rightarrow 0$, but converge very fast when N_{pc} is increased (that confirm the results given in the previous section and reveals from bias behavior). On the other hand, in the "hybrid" approximations obtained using $CS_g - HLM2D_p/EM2D_p$ the discretization error appears to be dominant and slows down the convergence.

4.3.2.3 Convergence of the Finite Volume Solver

In the Eulerian FV simulations, the discretization error has been shown to be a substantial error. In fact, unlike for the Lagrangian approximations, the time-averaged Eulerian approximations do not almost vary with N_{pc} but change with $h, \Delta t$. Thus, fixing $N_{pc} = 10$, we study the convergence of approximations when $h, \Delta t \rightarrow 0$.

The numerical results obtained on the uniform meshes of 100×20 , 200×40 , 400×80 cells and with Δt determined using the CFL condition: $\Delta t \approx 2.5 \times 10^{-3}s$, $1.25 \times 10^{-3}s$, $6.3 \times 10^{-4}s$ are presented in Fig. 4.59 - Fig. 4.63. They allow to conclude that the Finite Volume scheme developed in chapters 2 and 3 enables *stable* approximations to PDE_p^{Eul} and suggest that for given N_{pc} , these approximations *converge to the correct solution* with vanishing $h, \Delta t$. However, the meshes which are used in the present analysis are found to be too coarse. In order to obtain the approximations on finer meshes, a simultaneous refinement in $h, \Delta t$ and N (the total number of particles in the domain) would be necessary, that would make the computations very expensive.

4.3.3 Statistical error

On the contrary to the previous section, in this part we want to take into account the statistical error only. Following the definition given in sec. 1.3.2.3, the statistical error is due to the number of particles per cell N_{pc} being finite and scales as $N_{pc}^{-1/2}$. This relatively slow convergence rate is the main reason of potentially high computational costs of Monte-Carlo simulations.

Let us fix $Nx \times Ny = 200 \times 40$ and the corresponding time step, computed via CFL condition, $\Delta t \approx 1.25 \times 10^{-3}s$. The comparisons of unsteady profiles resulting from the hybrid Moments/Moments-PDF simulations (denoted by $CS_g - HLM2D_p/EM2D_p$) and from the classical Moments/PDF computations ($CS_g - LM2D_p$) are given in Fig. 4.64 - Fig. 4.71 for $N_{pc} = 10$ particles per cell and in Fig. 4.72 - Fig. 4.79 for $N_{pc} = 50$.

A quantitative analysis may be done by computing the normalized difference between unsteady approximations with given N_{pc} and the time-averaged solutions:

$$\|\langle \mathcal{H} \rangle_{N_{pc}} - \langle \mathcal{H}_T \rangle_{N_{pc}}\|_{L^2} / \|\langle \mathcal{H}_T \rangle_{N_{pc}}\|_{L^2}, \quad (4.3.3)$$

where $\langle \mathcal{H}_T \rangle$ denotes the time-averaged quantities. The measures are given in Tables 4.3.3, 4.3.3.

Module	α_p	$\alpha_p \langle U_{p,x} \rangle$	$\alpha_p \langle U_{p,y} \rangle$	$R_{p,xx}$	$R_{p,xy}$	$R_{p,yy}$
$LM2D_p$	0.093	0.09	0.34	0.27	0.5	0.2
$HLM2D_p$	0.091	0.088	0.33	0.18	0.42	0.16
$EM2D_p$	1.3×10^{-7}	1.6×10^{-7}	2×10^{-7}			

Table 4.1: The statistical error in norm L^2 for $Nx \times Ny = 200 \times 40$ and $N_{pc} = 10$.

On the whole, we note that the statistical error in the Lagrangian hybrid computations $HLM2D_p$ is *slightly reduced* (in particular for the second order moments) with reference to the classical

Module	α_p	$\alpha_p \langle U_{p,x} \rangle$	$\alpha_p \langle U_{p,y} \rangle$	$R_{p,xx}$	$R_{p,xy}$	$R_{p,yy}$
$LM2D_p$	0.042	0.04	0.16	0.19	0.3	0.11
$HLM2D_p$	0.04	0.039	0.16	0.08	0.19	0.07
$EM2D_p$	8.3×10^{-8}	1×10^{-7}	1.4×10^{-7}			

Table 4.2: The statistical error in norm L^2 for $Nx \times Ny = 200 \times 40$ and $N_{pc} = 50$.

simulations $LM2D_p$ and that the statistical error in the Eulerian approximations is tiny. Moreover, we see that the *correct Monte-Carlo convergence* of hybrid Lagrangian approximations $HLM2D_p$ in $N_{pc}^{-1/2}$ is verified.

4.4 Conclusion

In this part of the work, we have presented a hybrid Moments/Moments-PDF approach to the simulation of turbulent gas-particle flows. A hybrid numerical algorithm for the simulation of the *dispersed phase*, based on a coupling of Finite Volume and Monte-Carlo methods which have been developed in previous chapters, has been proposed and implemented.

First, it is important to note that the computational cost of the simulations with the hybrid algorithm is exactly the same as the cost of the classical Monte-Carlo computations (*FV/DSCM*):

$$\frac{CPU(FV/FV - DSMC)}{CPU(FV/DSCM)} \approx 1.05. \quad (4.4.1)$$

The numerical results allow to conclude that the *Finite Volume scheme* developed for the Eulerian particle phase simulations enables *stable unsteady approximations* which seems to *converge to the correct solution* when $h, \Delta t \rightarrow 0$. We have also seen that these approximations contain a very small statistical noise which tends to zero with $N_{pc} \rightarrow \infty$. The time-averaged approximations do not depend on N_{pc} .

On the other hand, the discretization error which is coming from the Eulerian Finite Volume solver appears to be dominant in both Eulerian and Lagrangian "hybrid" approximations and *slows down the speed of convergence* of the whole method. Thus, in spite of the reduction of the bias by the coupling strategy, the total deterministic error in the hybrid method is *increased*.

We recall that in the developed Finite Volume scheme the issue of the *numerical stability* has been privileged. The present numerical results could motivate the development of alternative numerical techniques which could reduce this discretization error.

Another possible solution consists in using *different time and space discretizations* for the Lagrangian and Eulerian particle modules. In fact, the accuracy of the present Eulerian approximations is poor, but finer discretizations require too long computations (several weeks) due to the very high number of particles. Thus, this improvement appears *necessary* for further developments in order to avoid the increase of the total number of particles when the mesh and time step are

refined. However, such a technique is not at all straightforward and demands to control some supplementary numerical errors.

Finally, we note that some *reduction of the statistical error* in the hybrid simulations is observed and that results verify its correct convergence with N_{pc} .

Eventually, the present hybrid method may be extended by applying the consistency relations on the duplicate fields (*algorithm B*) that would substantially reduce the statistical error, see for instance [4] and [7, 29]. However, their formulation and numerical implementation, especially in unsteady situations, require further analysis in terms of the correct convergence of approximations [15].

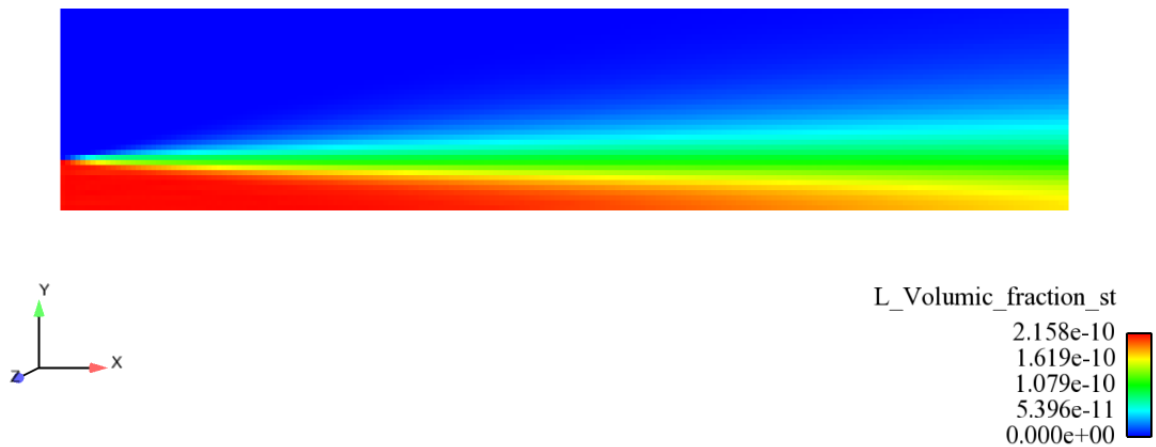


Figure 4.6: The time-averaged particle volumetric fraction: numerical simulation $CS_g - LM2D_p$ with $N_{pc} = 50$ particles per cell on the meshes $N_x \times N_y = 200 \times 40$.

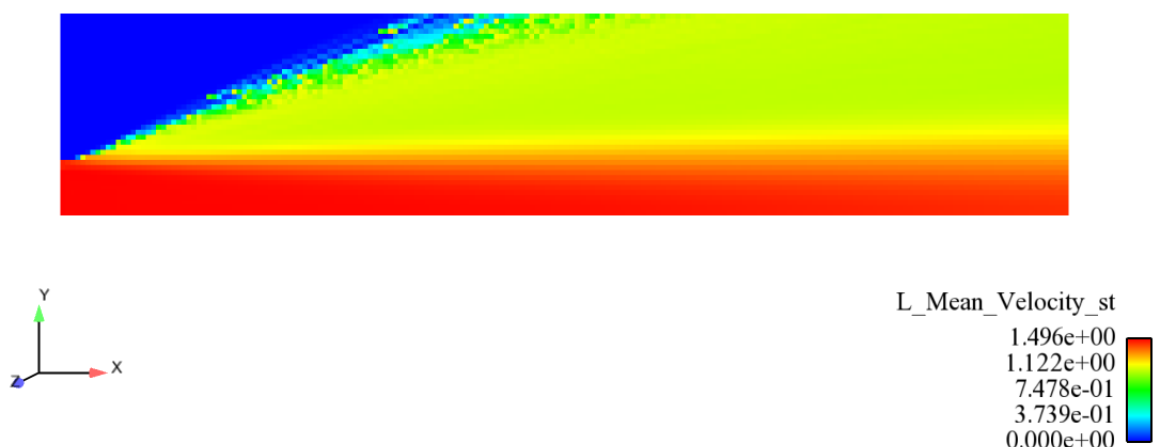


Figure 4.7: The time-averaged mean particle velocity: numerical simulation $CS_g - LM2D_p$ with $N_{pc} = 50$ particles per cell on the meshes $N_x \times N_y = 200 \times 40$.

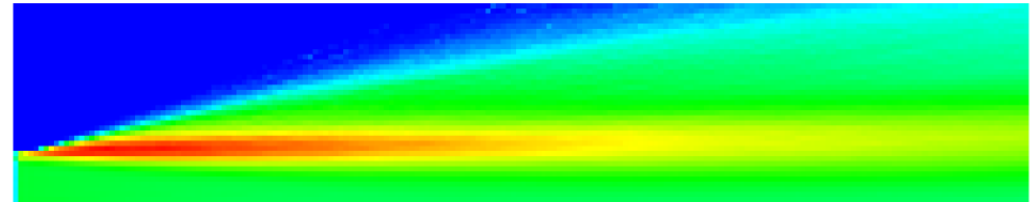


Figure 4.8: The time-averaged particle kinetic tensor, $R_{p,xx}$: numerical simulation $CS_g - LM2D_p$ with $N_{pc} = 50$ particles per cell on the meshes $Nx \times Ny = 200 \times 40$.

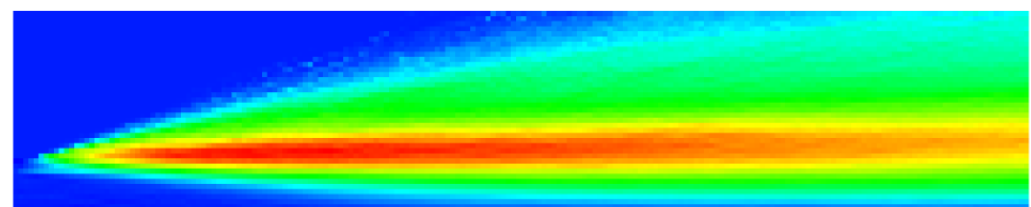


Figure 4.9: The time-averaged particle kinetic tensor, $R_{p,xy}$: numerical simulation $CS_g - LM2D_p$ with $N_{pc} = 50$ particles per cell on the meshes $Nx \times Ny = 200 \times 40$.

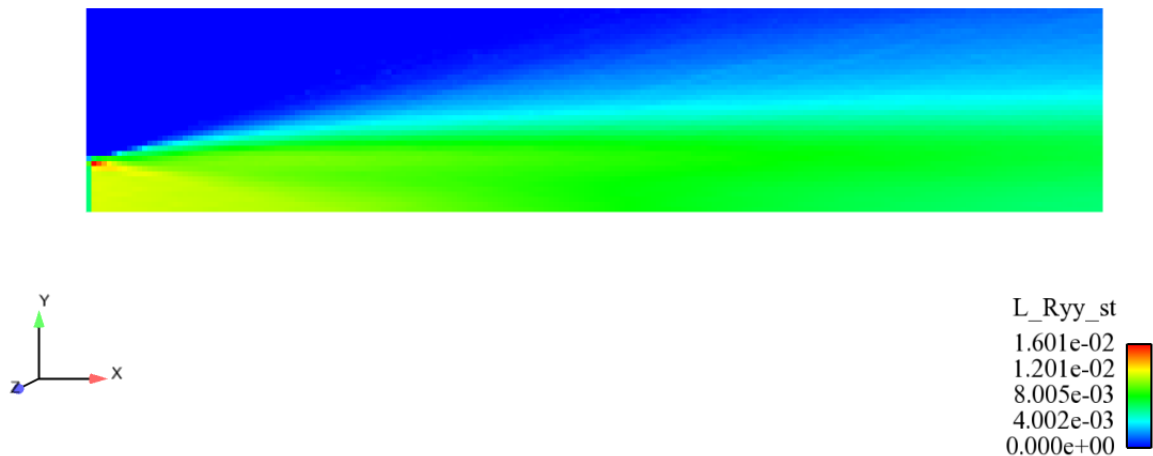


Figure 4.10: The time-averaged particle kinetic tensor, $R_{p,yy}$: numerical simulation $CS_g - LM2D_p$ with $N_{pc} = 50$ particles per cell on the meshes $N_x \times N_y = 200 \times 40$.

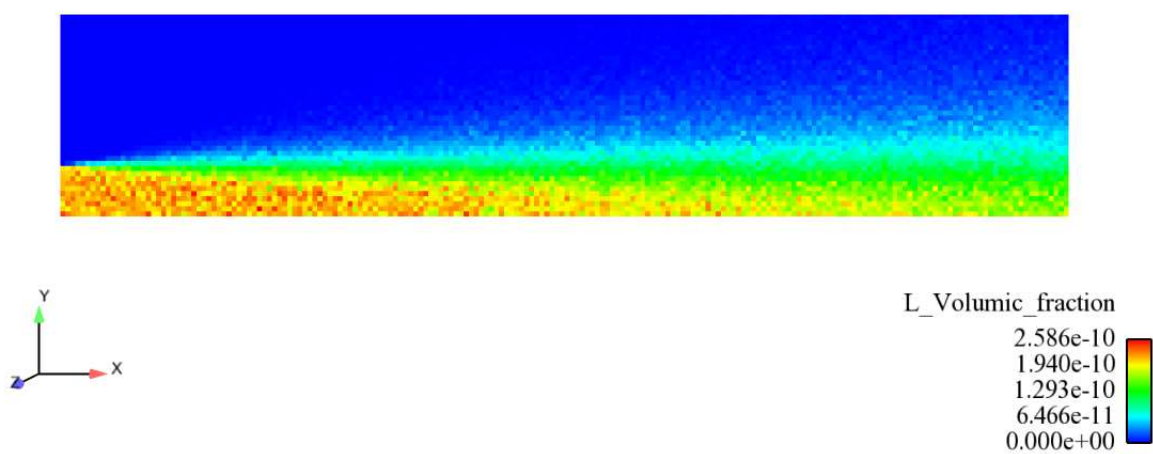


Figure 4.11: The time-averaged particle volumetric fraction: numerical simulation $CS_g - LM2D_p$ with $N_{pc} = 50$ particles per cell on the meshes $N_x \times N_y = 200 \times 40$.

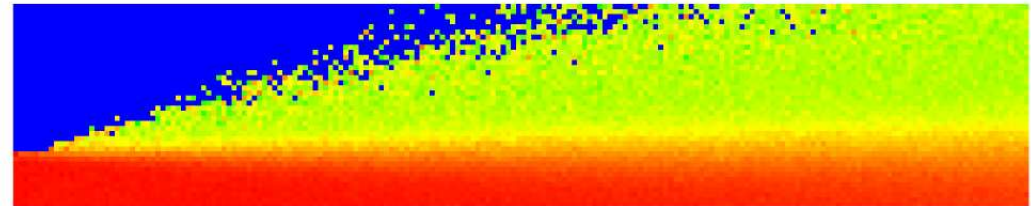


Figure 4.12: The time-averaged mean particle velocity: numerical simulation $CS_g - LM2D_p$ with $N_{pc} = 50$ particles per cell on the meshes $N_x \times N_y = 200 \times 40$.

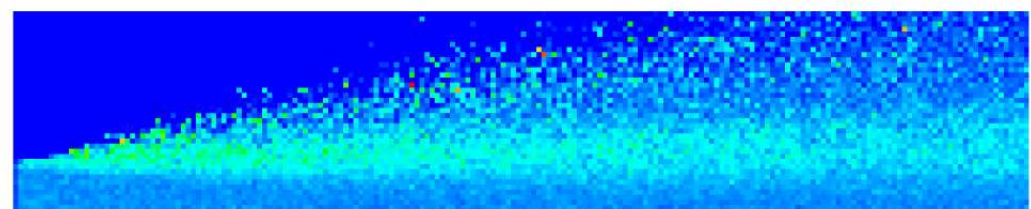


Figure 4.13: The particle kinetic tensor, $R_{p,xx}$: numerical simulation $CS_g - LM2D_p$ with $N_{pc} = 50$ particles per cell on the meshes $N_x \times N_y = 200 \times 40$.

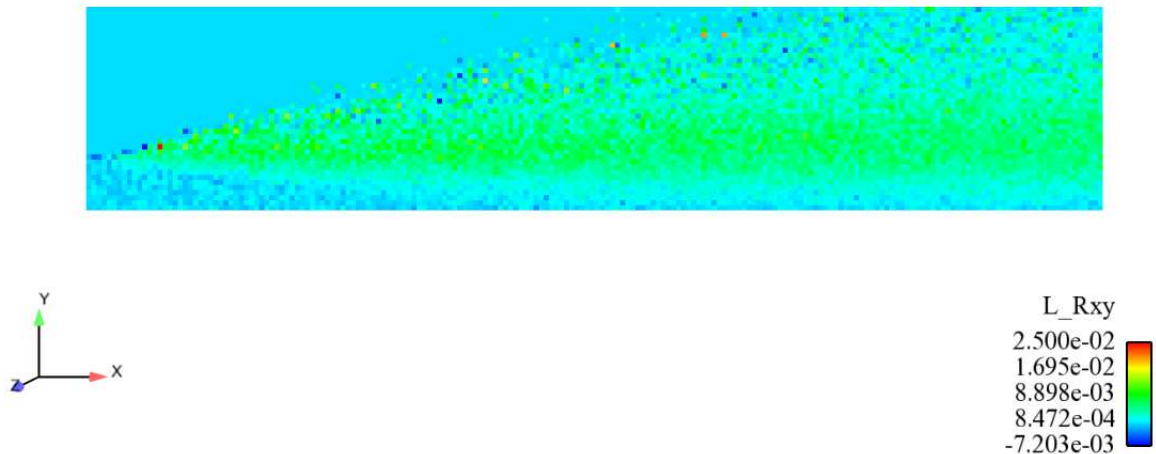


Figure 4.14: The particle kinetic tensor, $R_{p,xy}$: numerical simulation $CS_g - LM2D_p$ with $N_{pc} = 50$ particles per cell on the meshes $Nx \times Ny = 200 \times 40$.

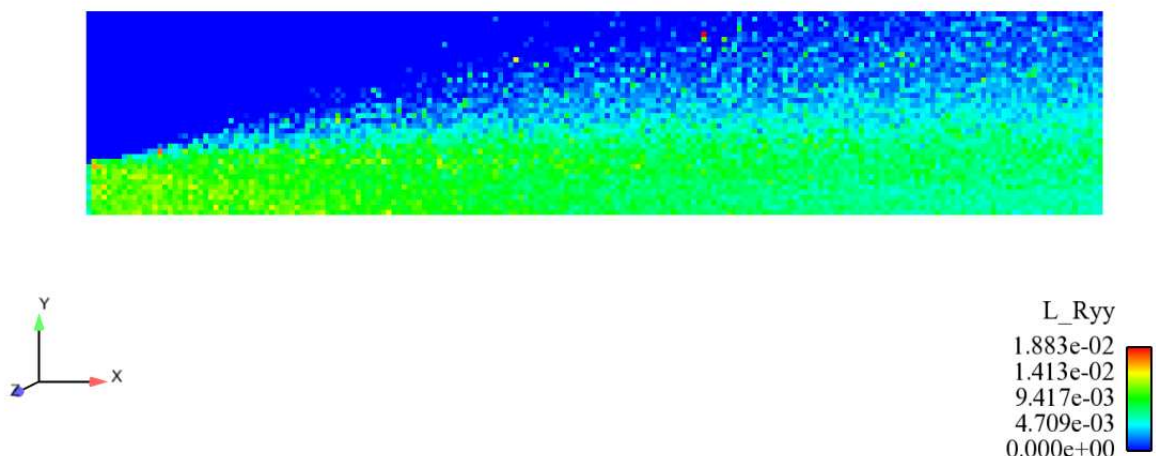


Figure 4.15: The particle kinetic tensor, $R_{p,yy}$: numerical simulation $CS_g - LM2D_p$ with $N_{pc} = 50$ particles per cell on the meshes $Nx \times Ny = 200 \times 40$.

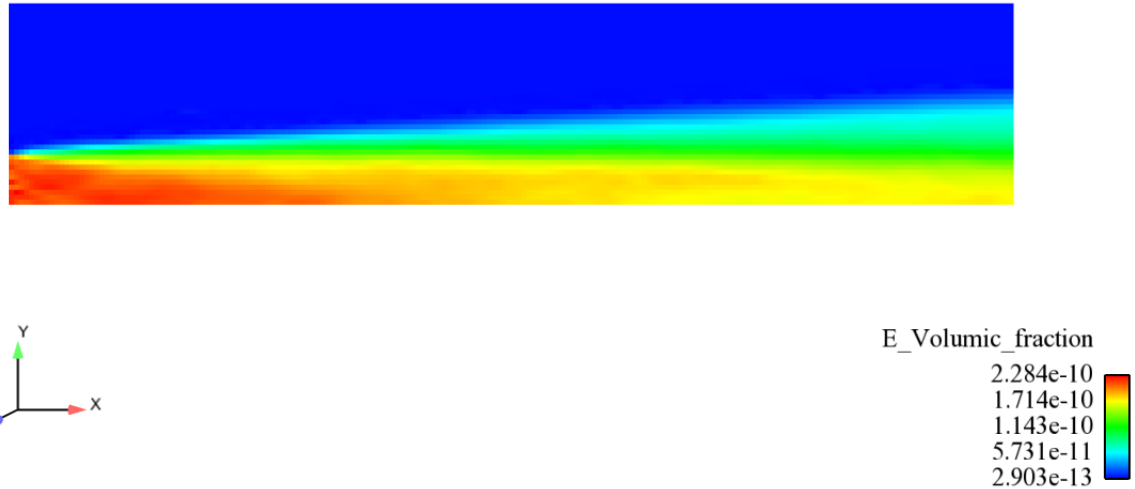


Figure 4.16: The Eulerian particle volumetric fraction: numerical simulation $CS_g - HLM2D_p/EM2D_s$ with $N_{pc} = 50$ particles per cell on the meshes $Nx \times Ny = 200 \times 40$.

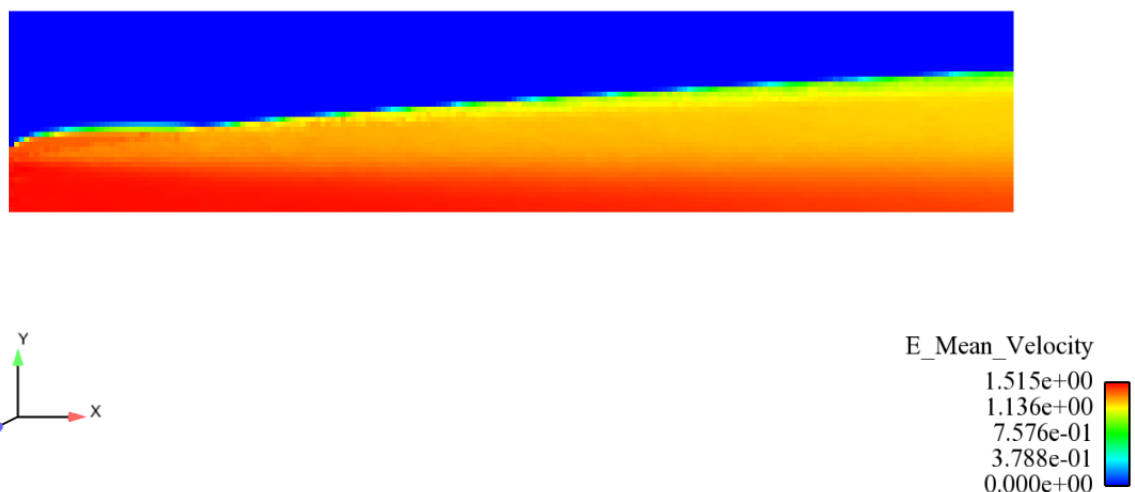


Figure 4.17: The Eulerian mean particle velocity: numerical simulation $CS_g - HLM2D_p/EM2D_s$ with $N_{pc} = 50$ particles per cell on the meshes $Nx \times Ny = 200 \times 40$.

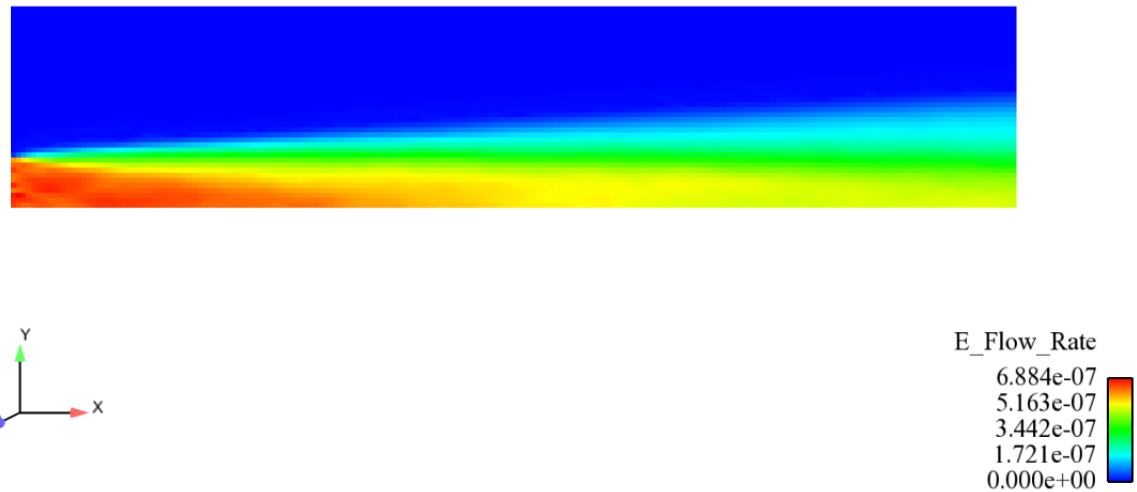


Figure 4.18: The Eulerian mean particle flow rate: numerical simulation $CS_g - HLM2D_p/EM2D_s$ with $N_{pc} = 50$ particles per cell on the meshes $N_x \times N_y = 200 \times 40$.

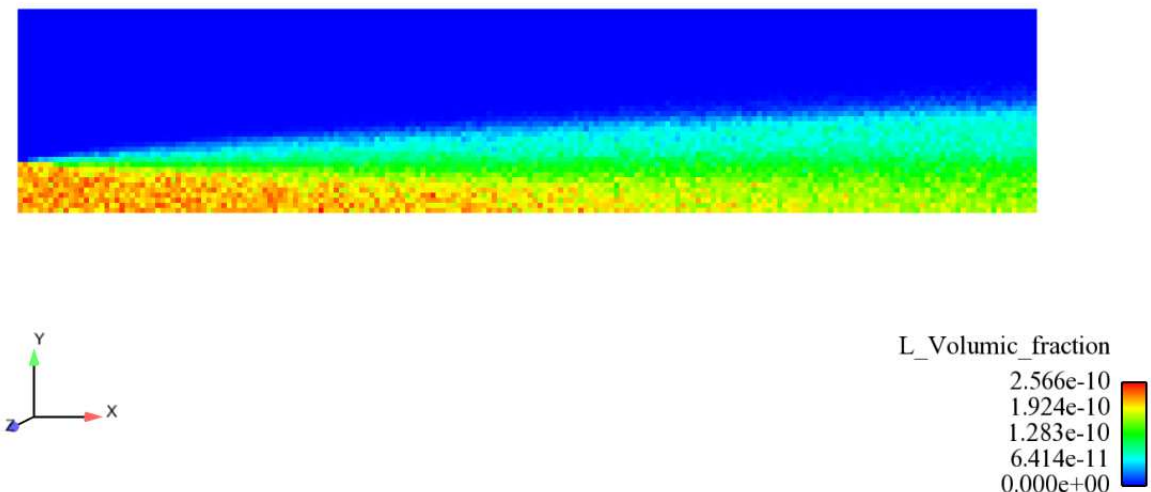


Figure 4.19: The Lagrangian particle volumetric fraction: numerical simulation $CS_g - HLM2D_p/EM2D_s$ with $N_{pc} = 50$ particles per cell on the meshes $N_x \times N_y = 200 \times 40$.

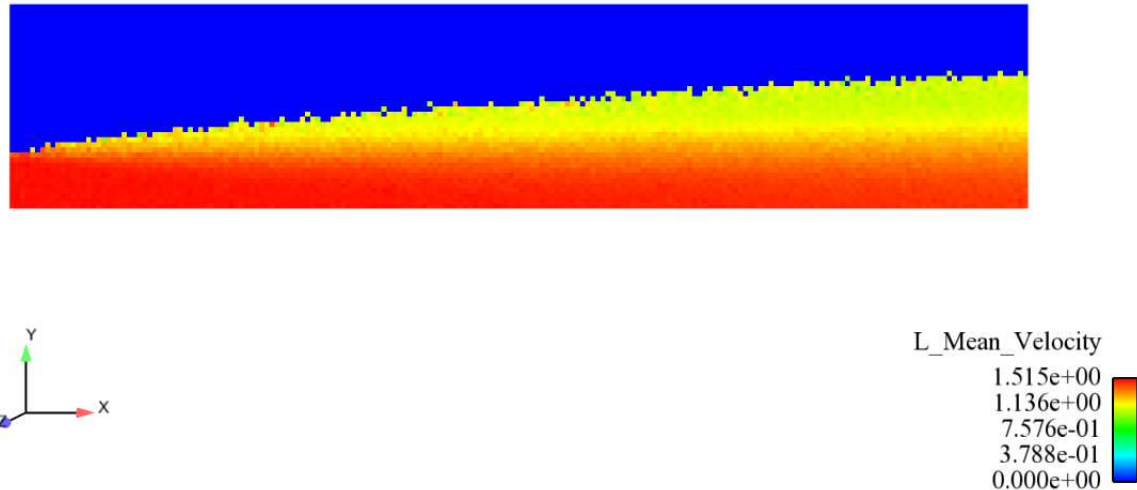


Figure 4.20: The Lagrangian mean particle velocity: numerical simulation $CS_g - HLM2D_p/EM2D_s$ with $N_{pc} = 50$ particles per cell on the meshes $N_x \times N_y = 200 \times 40$.

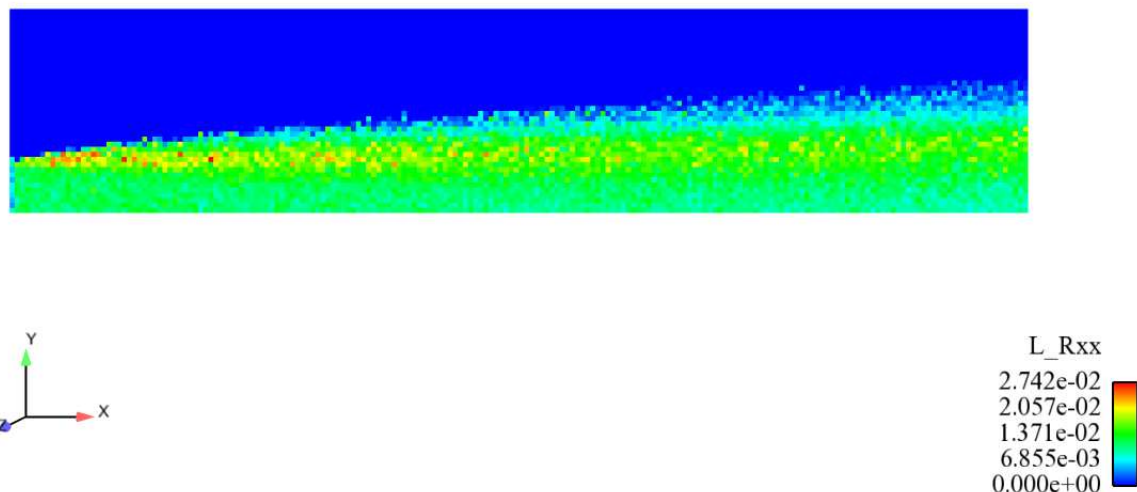


Figure 4.21: The Lagrangian particle kinetic tensor, $R_{p,xx}$: numerical simulation $CS_g - HLM2D_p/EM2D_s$ with $N_{pc} = 50$ particles per cell on the meshes $N_x \times N_y = 200 \times 40$.

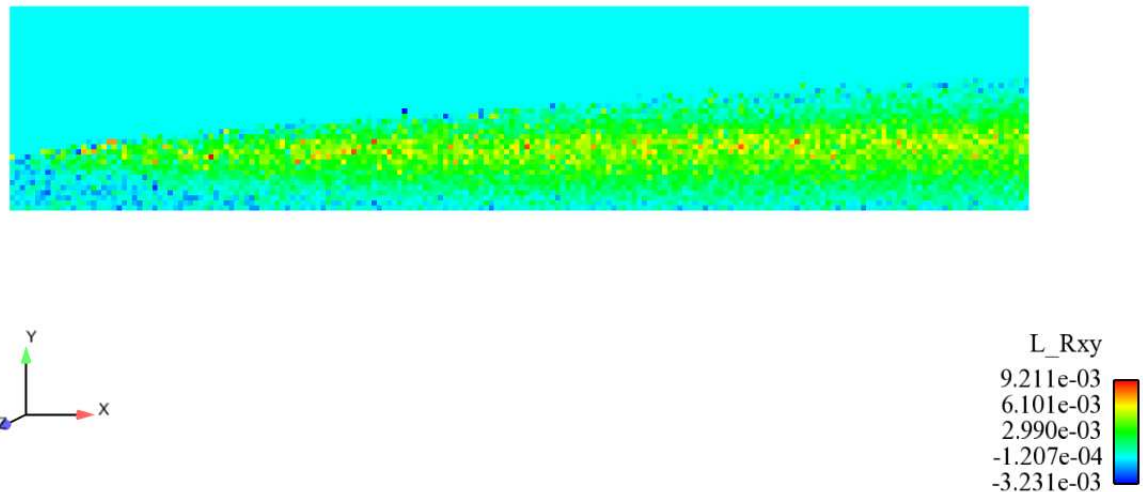


Figure 4.22: The Lagrangian particle kinetic tensor, $R_{p,xy}$: numerical simulation CS_g – $HLM2D_p/EM2D_s$ with $N_{pc} = 50$ particles per cell on the meshes $Nx \times Ny = 200 \times 40$.

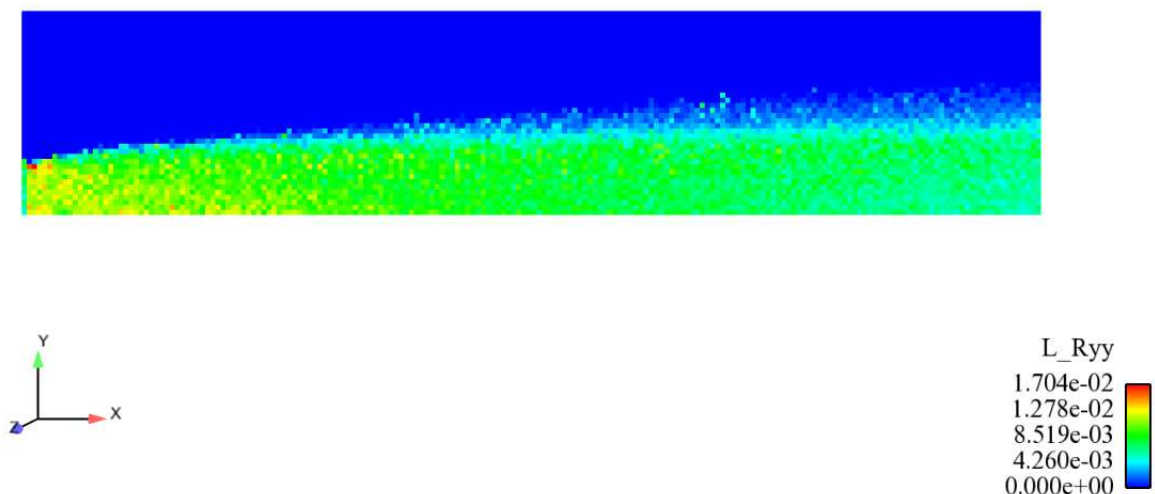


Figure 4.23: The Lagrangian particle kinetic tensor, $R_{p,yy}$: numerical simulation CS_g – $HLM2D_p/EM2D_s$ with $N_{pc} = 50$ particles per cell on the meshes $Nx \times Ny = 200 \times 40$.

Particle volumetric fraction: $N_x \cdot N_y = 100 \times 20$, $T = 5.0$ s.

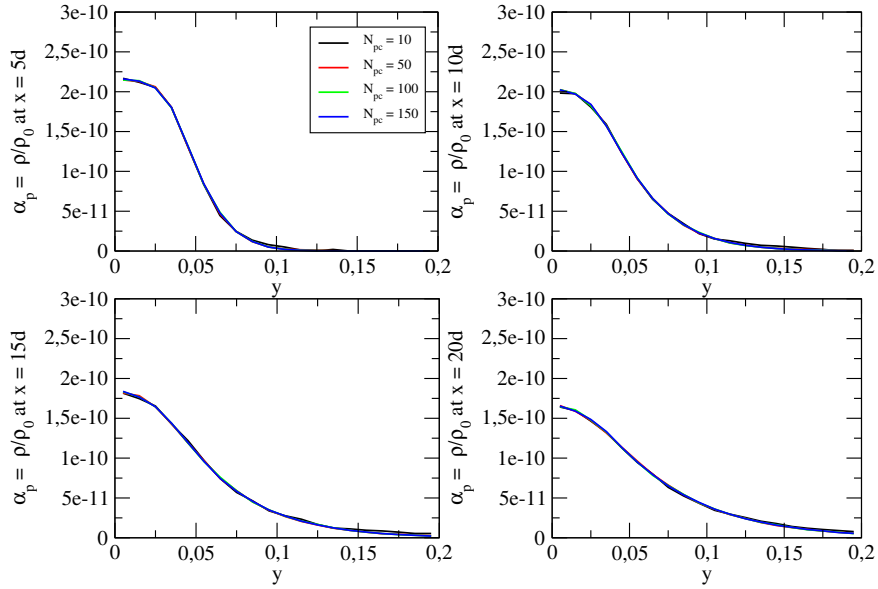


Figure 4.24: Bias estimation: cross-sections of the particle volumetric fraction. Numerical simulation $CS_g - LM2D_p$ for system (1.3.5) on the mesh of 100×20 cells with $\Delta t = 2.5 \times 10^{-3}$ s.

Mean particle velocity $\langle Up_x \rangle$: $N_x \cdot N_y = 100 \times 20$, $T = 5.0$ s

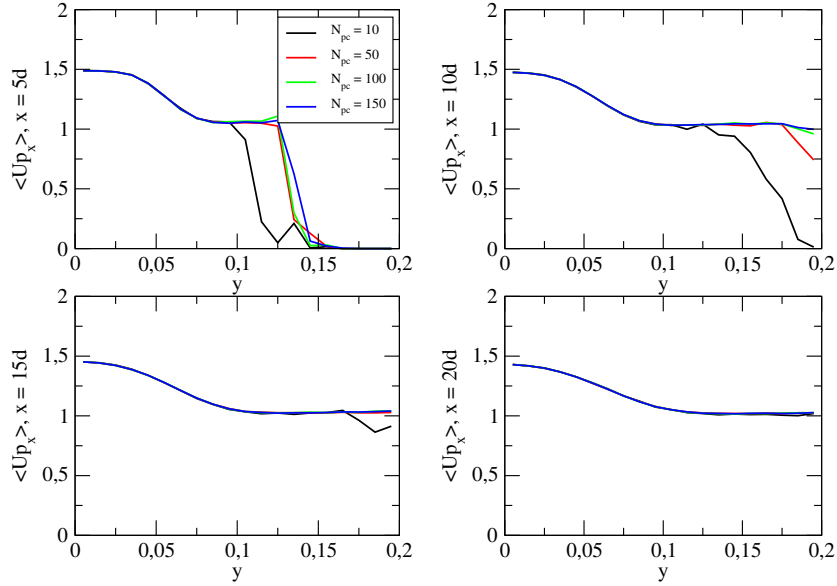


Figure 4.25: Bias estimation: cross-sections of the mean particle velocity in the longitudinal direction. Numerical simulation $CS_g - LM2D_p$ for system (1.3.5) on the mesh of 100×20 cells with $\Delta t = 2.5 \times 10^{-3}$ s.

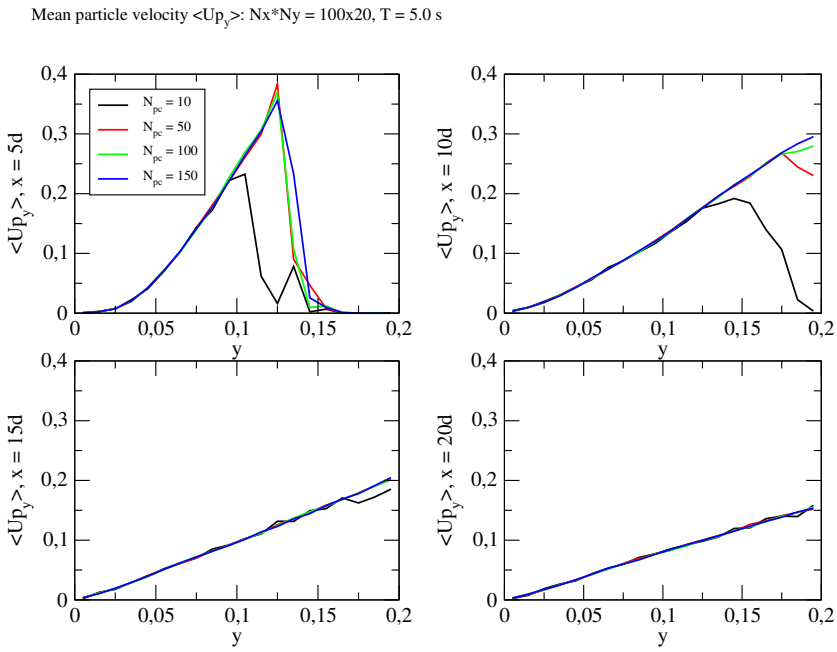


Figure 4.26: Bias estimation: cross-sections of the mean particle velocity in the transversal direction. Numerical simulation $CS_g - LM2D_p$ for system (1.3.5) on the mesh of 100×20 cells with $\Delta t = 2.5 \times 10^{-3}$ s.

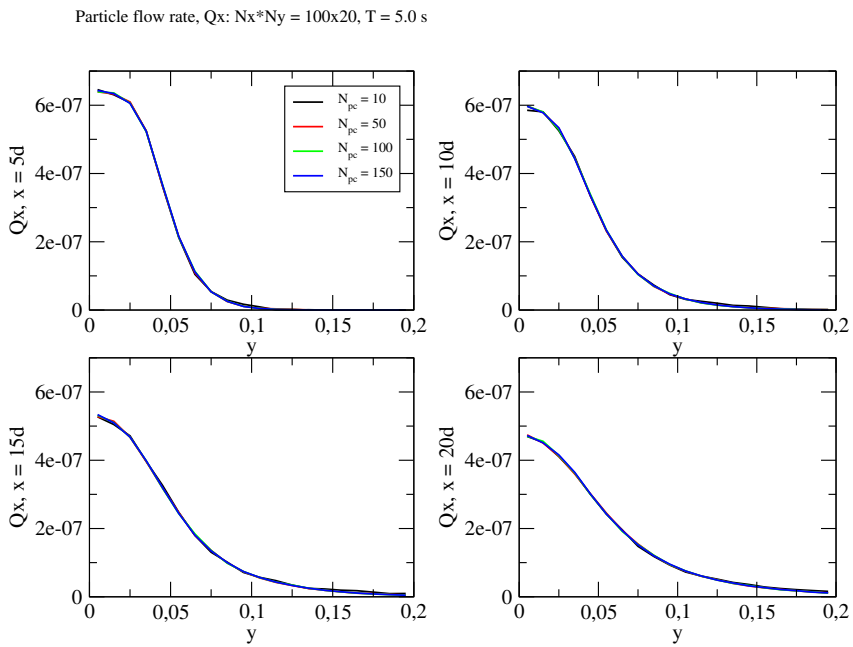


Figure 4.27: Bias estimation: cross-sections of the mean particle flow rate in the longitudinal direction. Numerical simulation $CS_g - LM2D_p$ for system (1.3.5) on the mesh of 100×20 cells with $\Delta t = 2.5 \times 10^{-3}$ s.

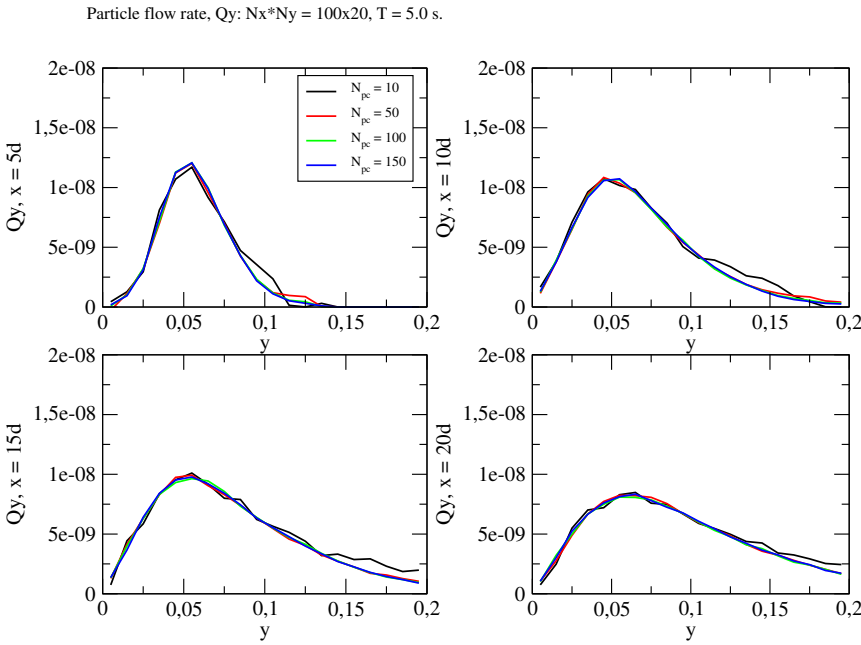


Figure 4.28: Bias estimation: cross-sections of the mean particle flow rate in the transversal direction. Numerical simulation $CS_g - LM2D_p$ for system (1.3.5) on the mesh of 100×20 cells with $\Delta t = 2.5 \times 10^{-3}$ s.

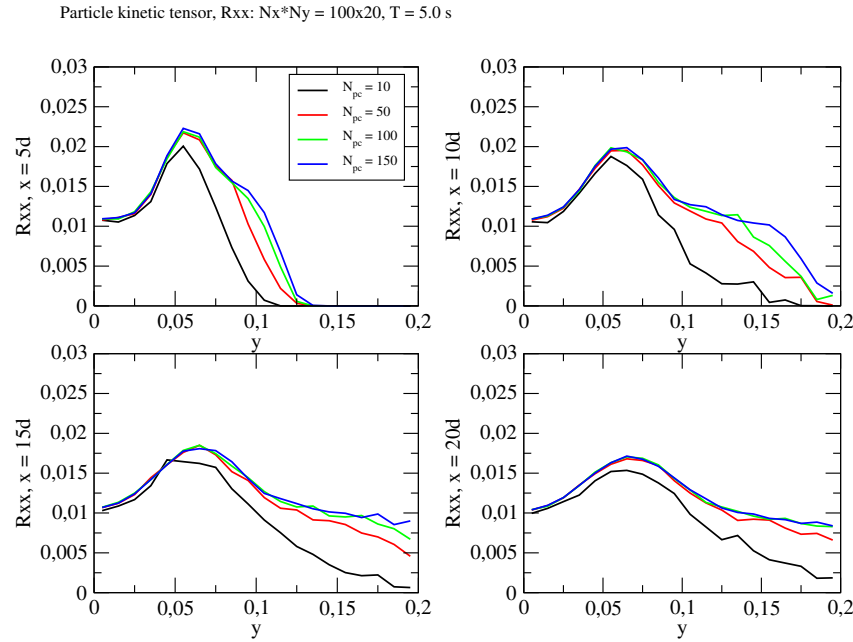


Figure 4.29: Bias estimation: cross-sections of the particle kinetic tensor. Numerical simulation $CS_g - LM2D_p$ for system (1.3.5) on the mesh of 100×20 cells with $\Delta t = 2.5 \times 10^{-3}$ s.

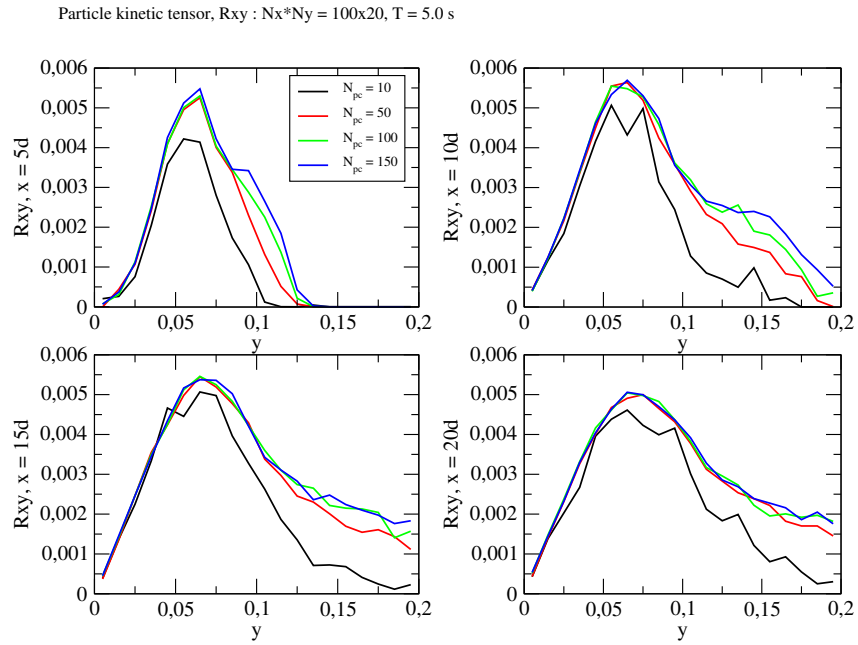


Figure 4.30: Bias estimation: cross-sections of the particle kinetic tensor. Numerical simulation $CS_g - LM2D_p$ for system (1.3.5) on the mesh of 100×20 cells with $\Delta t = 2.5 \times 10^{-3} \text{ s}$.

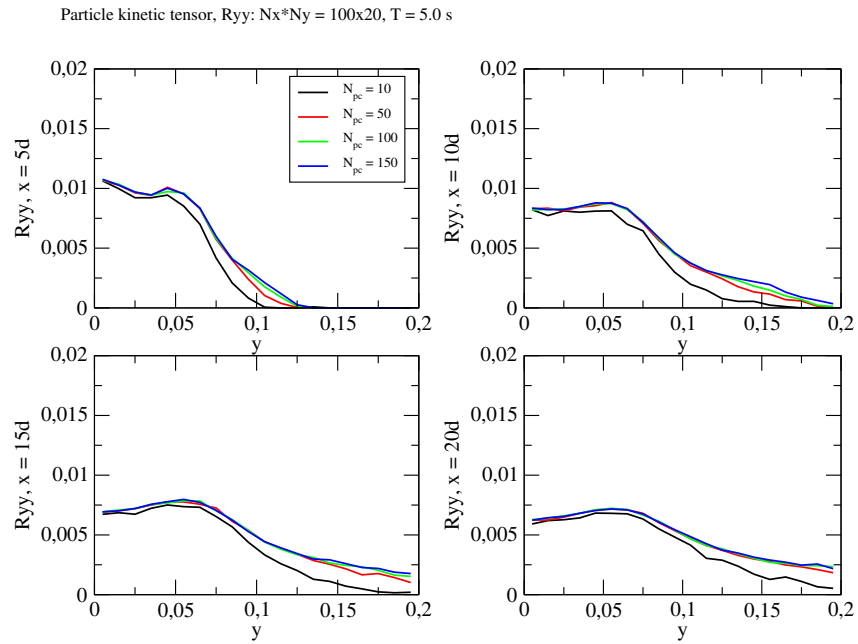


Figure 4.31: Bias estimation: cross-sections of the particle kinetic tensor. Numerical simulation $CS_g - LM2D_p$ for system (1.3.5) on the mesh of 100×20 cells with $\Delta t = 2.5 \times 10^{-3} \text{ s}$.

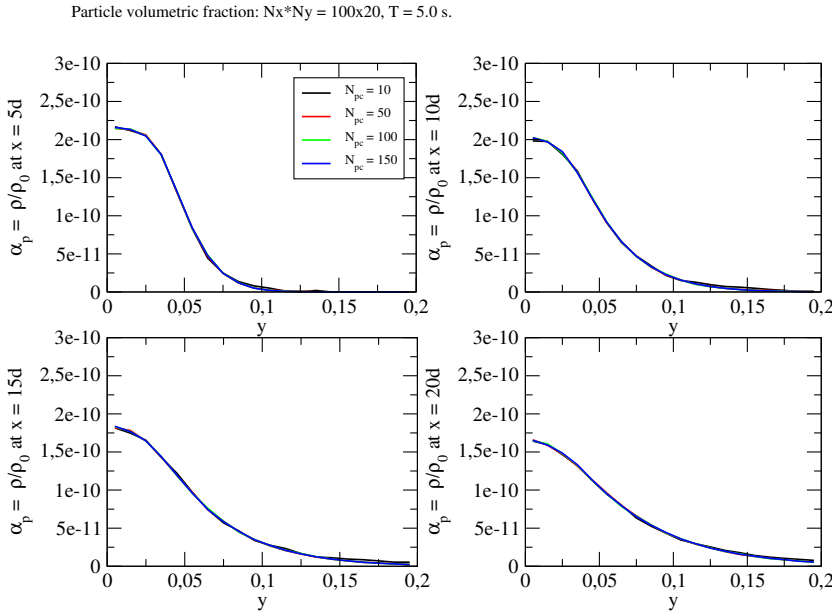


Figure 4.32: Bias estimation: cross-sections of the particle volumetric fraction. Numerical simulation $CS_g - LM2D_p$ for system (1.3.5) on the mesh of 200×40 cells with $\Delta t = 1.25 \times 10^{-3}$ s.

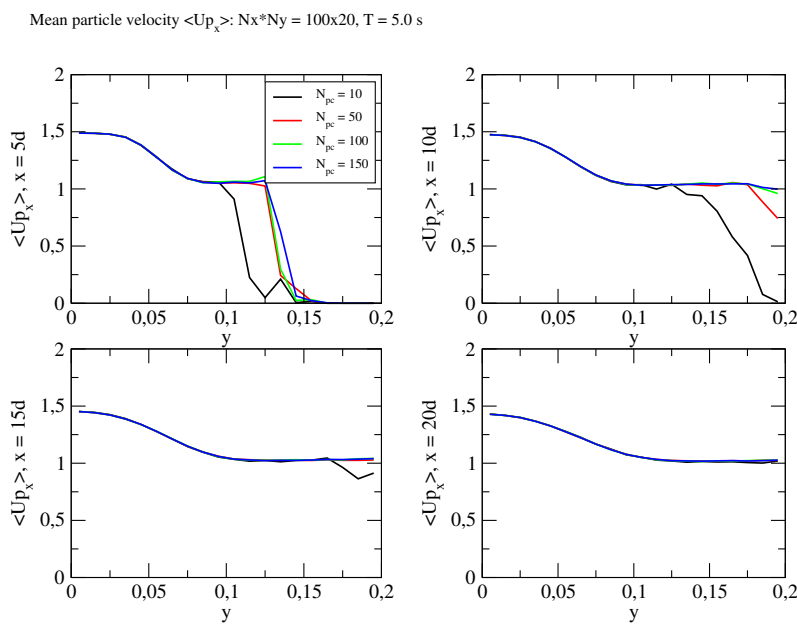


Figure 4.33: Bias estimation: cross-sections of the mean particle velocity in the longitudinal direction. Numerical simulation $CS_g - LM2D_p$ for system (1.3.5) on the mesh of 200×40 cells with $\Delta t = 1.25 \times 10^{-3}$ s.

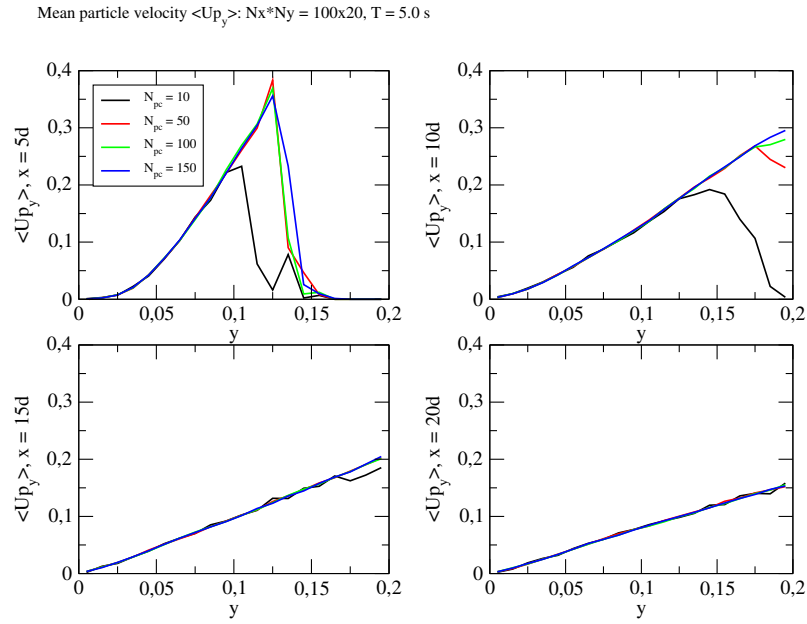


Figure 4.34: Bias estimation: cross-sections of the mean particle velocity in the transversal direction. Numerical simulation $CS_g - LM2D_p$ for system (1.3.5) on the mesh of 200×40 cells with $\Delta t = 1.25 \times 10^{-3}$ s.

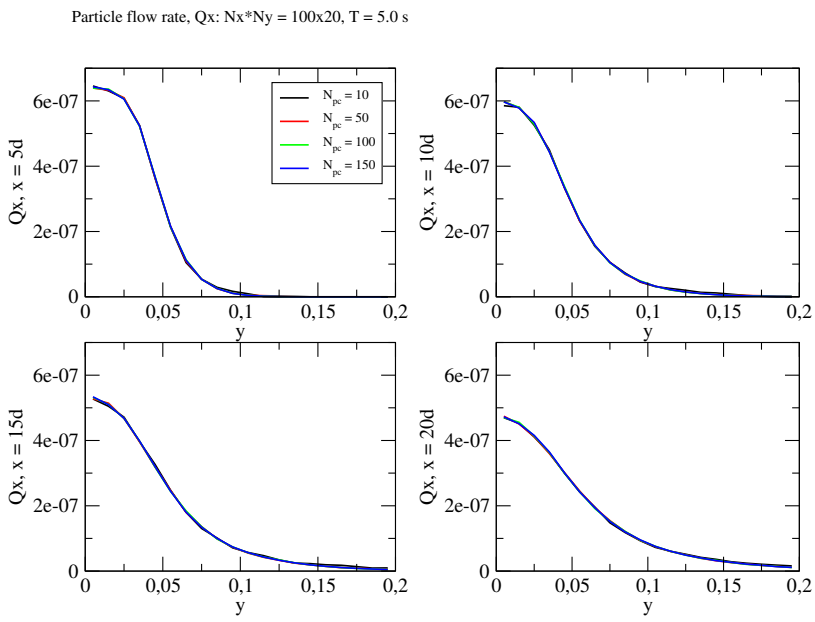


Figure 4.35: Bias estimation: cross-sections of the mean particle flow rate in the longitudinal direction. Numerical simulation $CS_g - LM2D_p$ for system (1.3.5) on the mesh of 200×40 cells with $\Delta t = 1.25 \times 10^{-3}$ s.

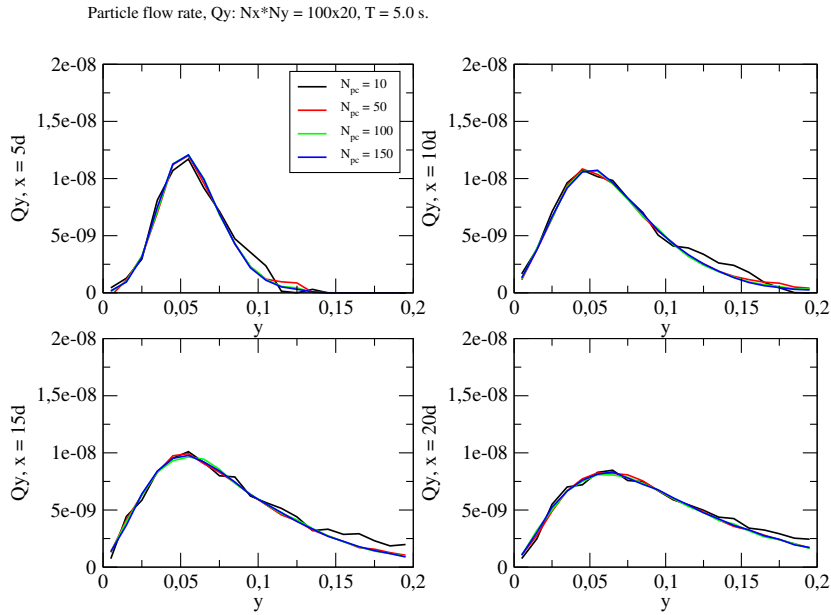


Figure 4.36: Bias estimation: cross-sections of the mean particle flow rate in the transversal direction. Numerical simulation $CS_g - LM2D_p$ for system (1.3.5) on the mesh of 200×40 cells with $\Delta t = 1.25 \times 10^{-3}$ s.

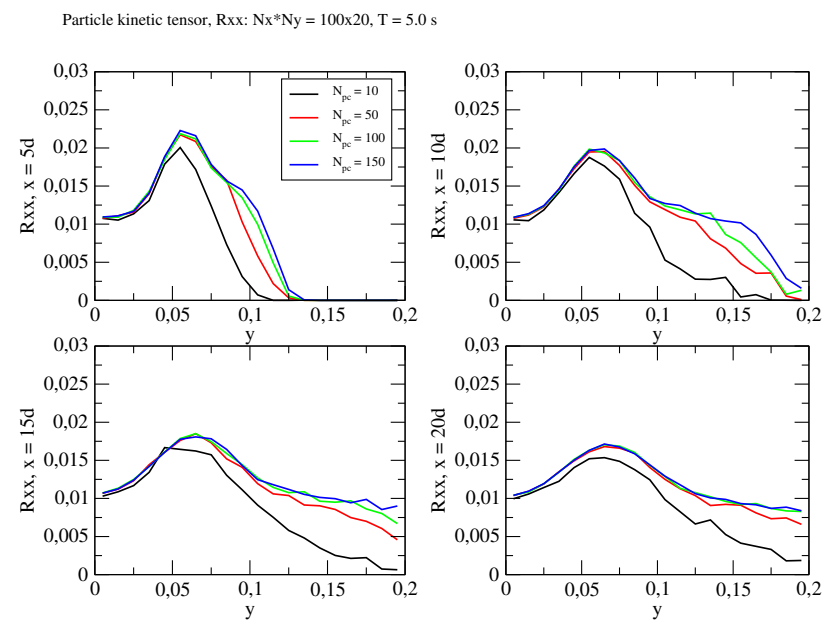


Figure 4.37: Bias estimation: cross-sections of the particle kinetic tensor. Numerical simulation $CS_g - LM2D_p$ for system (1.3.5) on the mesh of 200×40 cells with $\Delta t = 1.25 \times 10^{-3}$ s.

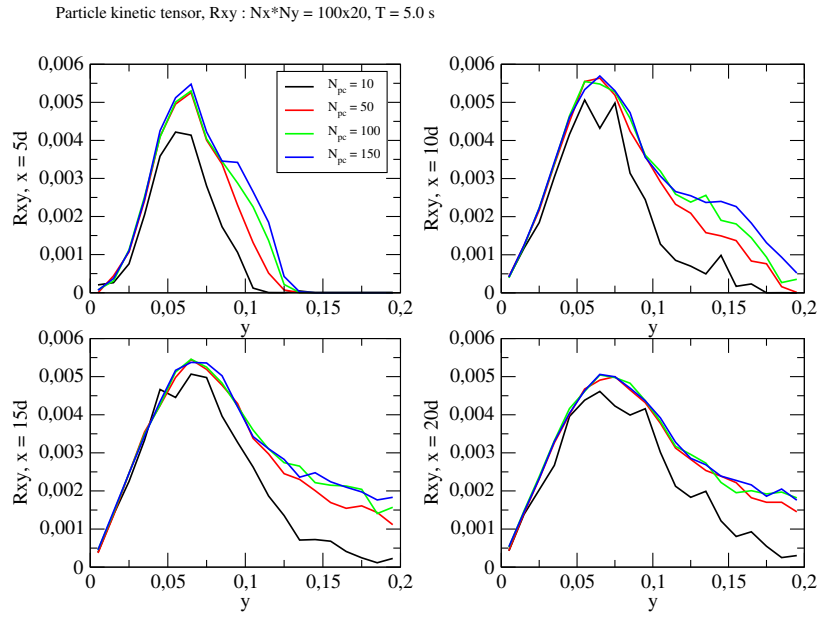


Figure 4.38: Bias estimation: cross-sections of the particle kinetic tensor. Numerical simulation $CS_g - LM2D_p$ for system (1.3.5) on the mesh of 200×40 cells with $\Delta t = 1.25 \times 10^{-3}$ s.

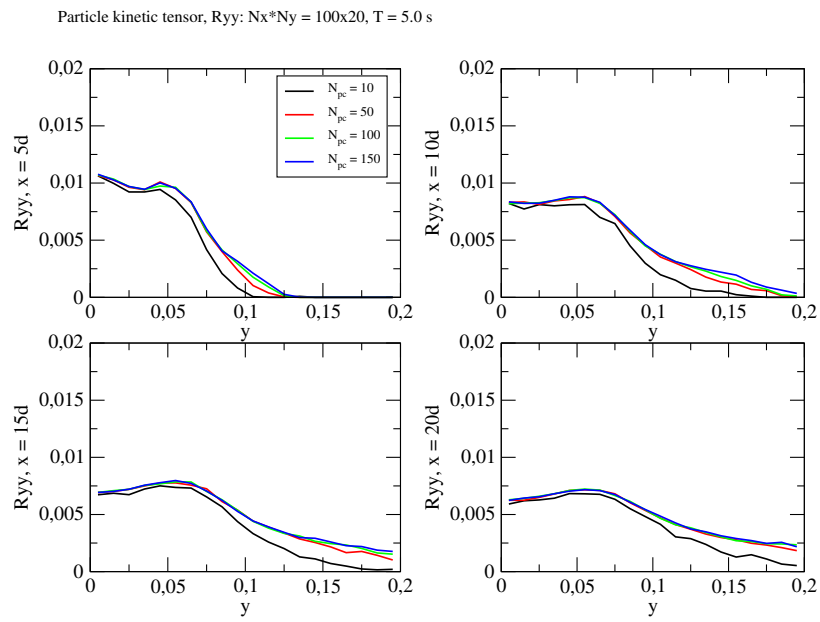


Figure 4.39: Bias estimation: cross-sections of the particle kinetic tensor. Numerical simulation $CS_g - LM2D_p$ for system (1.3.5) on the mesh of 200×40 cells with $\Delta t = 1.25 \times 10^{-3}$ s.

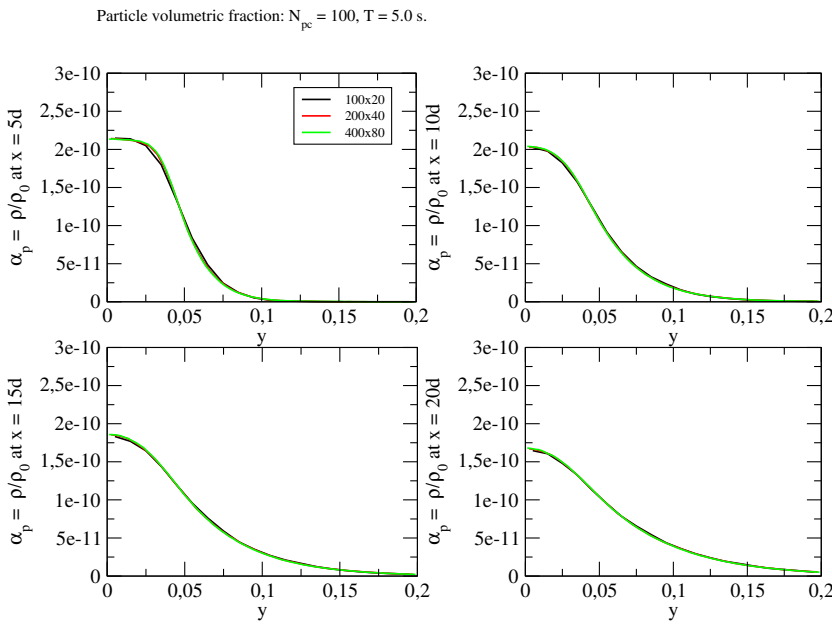


Figure 4.40: Discretization error: cross-sections of the particle volumetric fraction. Numerical simulation $CS_g - LM2D_p$ for system (1.3.5) with $N_{pc} = 100$ particles per cell on the meshes $Nx \times Ny = 100 \times 20, 200 \times 40, 400 \times 80$.

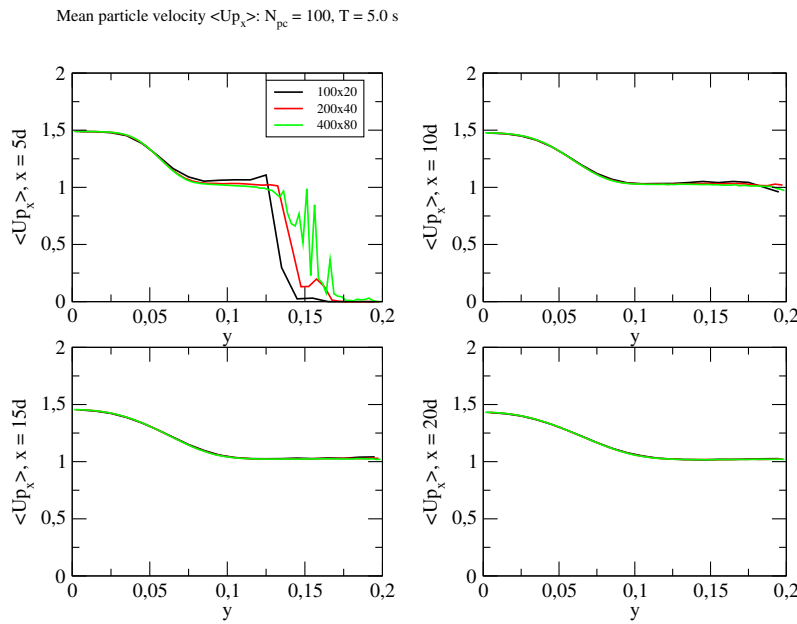


Figure 4.41: Discretization error: cross-sections of the mean particle velocity in the longitudinal direction. Numerical simulation $CS_g - LM2D_p$ for system (1.3.5) with $N_{pc} = 100$ particles per cell on the meshes $Nx \times Ny = 100 \times 20, 200 \times 40, 400 \times 80$.

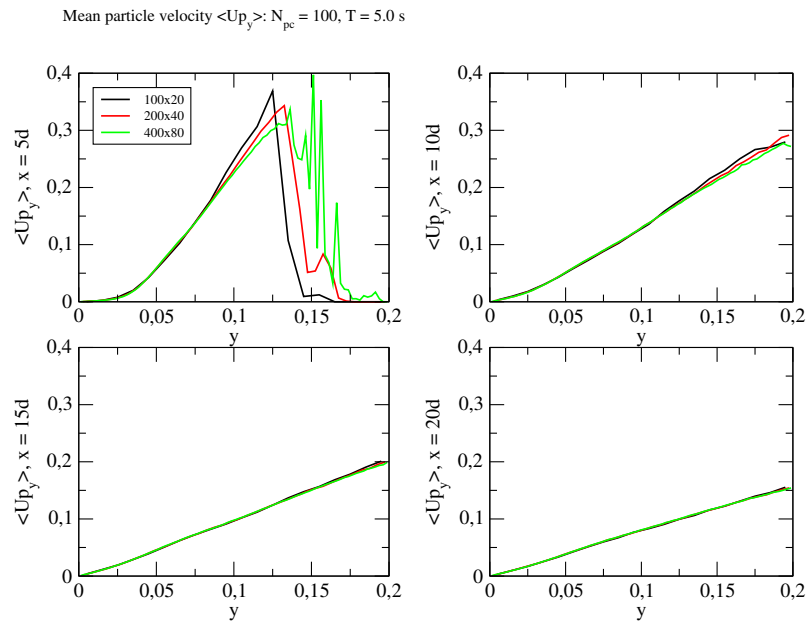


Figure 4.42: Discretization error: cross-sections of the mean particle velocity in the transversal direction. Numerical simulation $CS_g - LM2D_p$ for system (1.3.5) with $N_{pc} = 100$ particles per cell on the meshes $N_x \times N_y = 100 \times 20, 200 \times 40, 400 \times 80$.

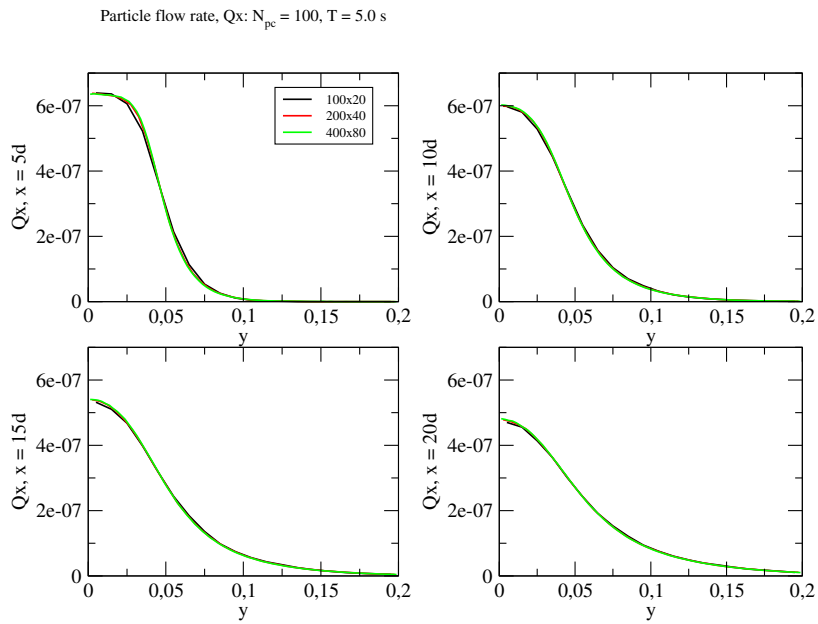


Figure 4.43: Discretization error: cross-sections of the mean particle flow rate in the longitudinal direction. Numerical simulation $CS_g - LM2D_p$ for system (1.3.5) with $N_{pc} = 100$ particles per cell on the meshes $N_x \times N_y = 100 \times 20, 200 \times 40, 400 \times 80$.

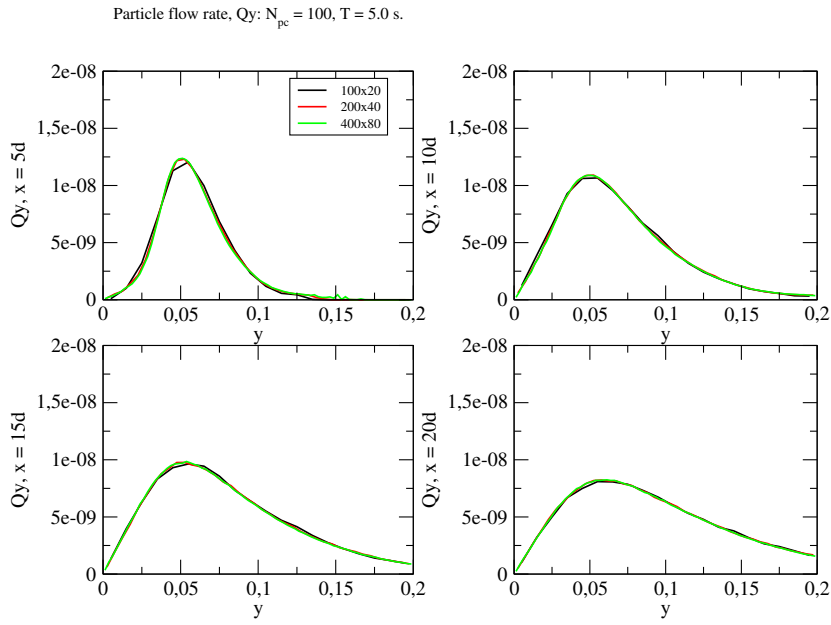


Figure 4.44: Discretization error: cross-sections of the mean particle flow rate in the transversal direction. Numerical simulation $CS_g - LM2D_p$ for system (1.3.5) with $N_{pc} = 100$ particles per cell on the meshes $N_x \times N_y = 100 \times 20, 200 \times 40, 400 \times 80$.

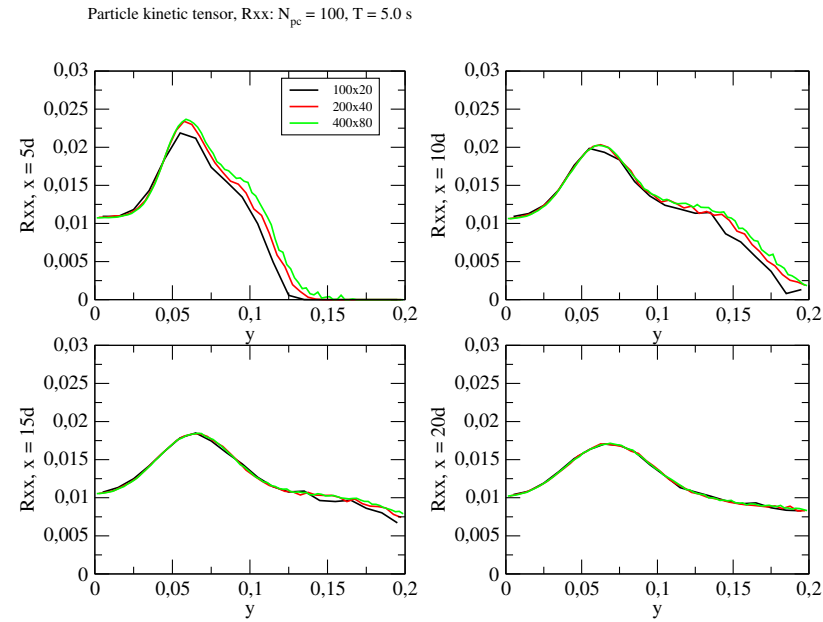


Figure 4.45: Discretization error: cross-sections of the particle kinetic tensor. Numerical simulation $CS_g - LM2D_p$ for system (1.3.5) with $N_{pc} = 100$ particles per cell on the meshes $N_x \times N_y = 100 \times 20, 200 \times 40, 400 \times 80$.

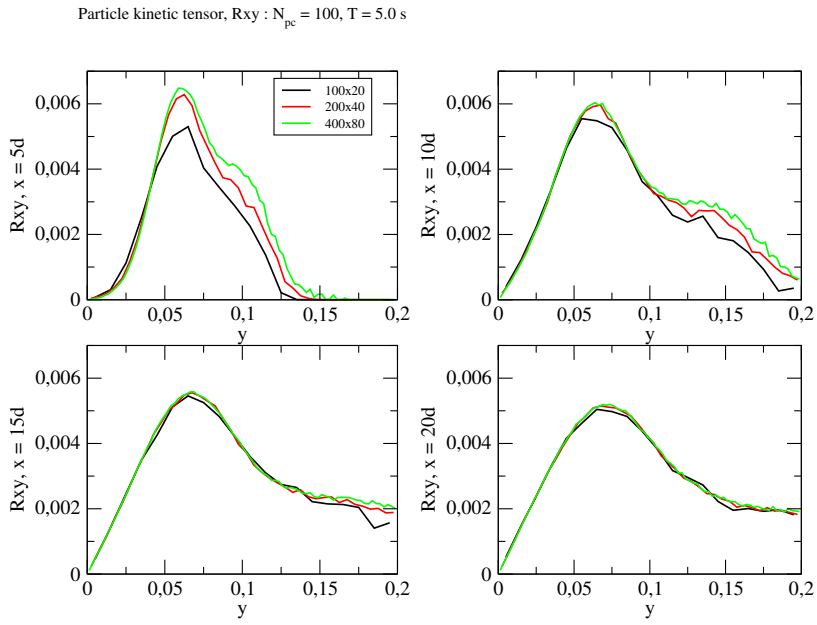


Figure 4.46: Discretization error: cross-sections of the particle kinetic tensor. Numerical simulation $CS_g - LM2D_p$ for system (1.3.5) with $N_{pc} = 100$ particles per cell on the meshes $N_x \times N_y = 100 \times 20, 200 \times 40, 400 \times 80$.

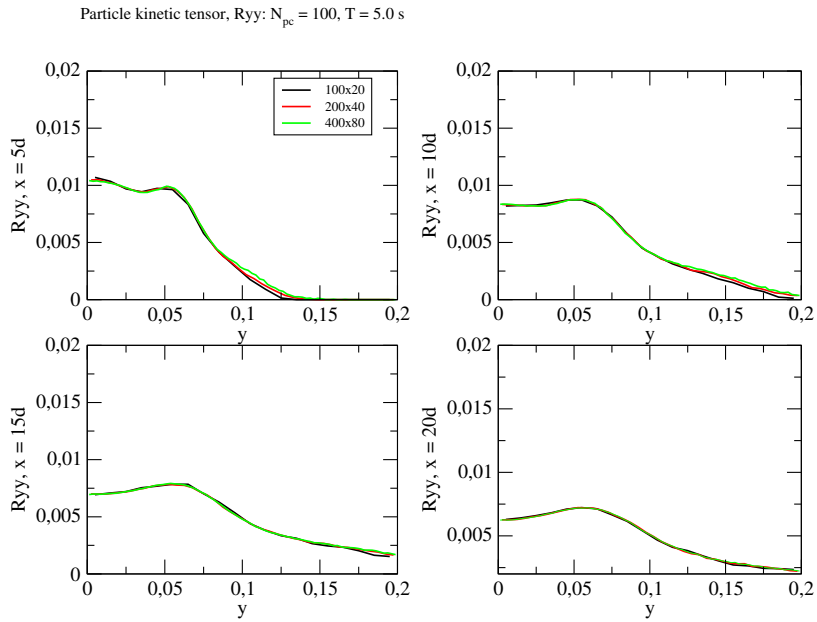


Figure 4.47: Discretization error: cross-sections of the particle kinetic tensor. Numerical simulation $CS_g - LM2D_p$ for system (1.3.5) with $N_{pc} = 100$ particles per cell on the meshes $N_x \times N_y = 100 \times 20, 200 \times 40, 400 \times 80$.

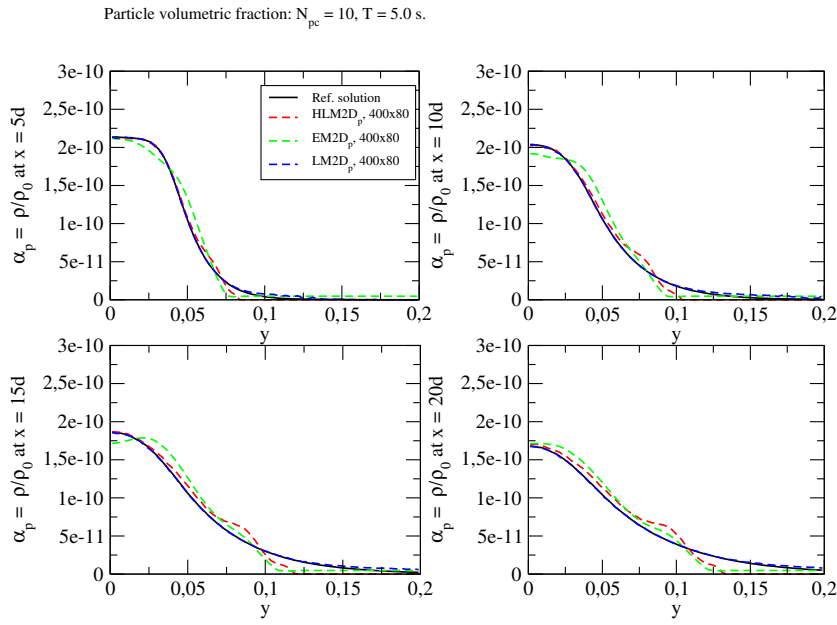


Figure 4.48: Cross-sections of the particle volumetric fraction. Comparison of the hybrid simulations $CS_g - HLM2D_p/EM2D_p$ for system (4.1.1)-(4.1.2) with the "classical" ones using $CS_g - LM2D_p$ for $N_{pc} = 10$ particles per cell on the mesh of 400×80 cells.

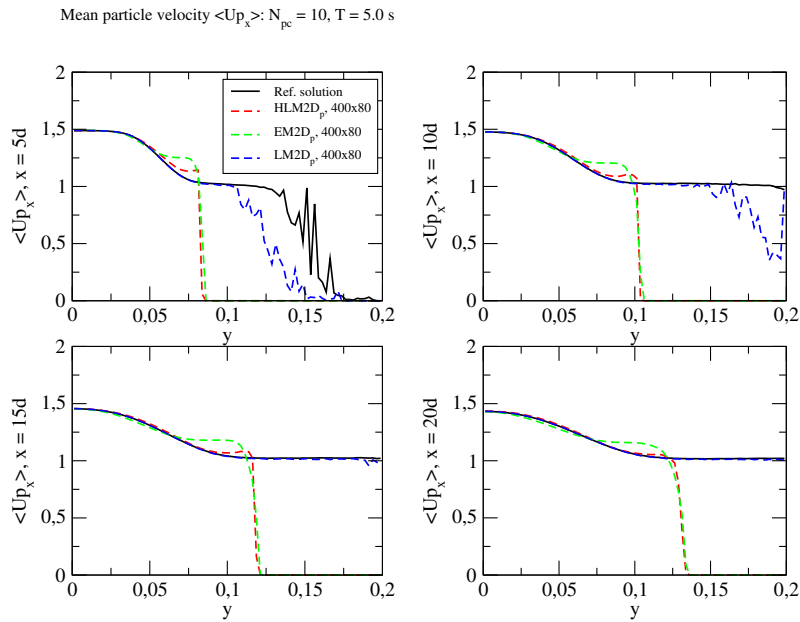


Figure 4.49: Cross-sections of the mean particle velocity in the longitudinal direction. Comparison of the hybrid simulations $CS_g - HLM2D_p/EM2D_p$ for system (4.1.1)-(4.1.2) with the "classical" ones using $CS_g - LM2D_p$ for $N_{pc} = 10$ particles per cell on the mesh of 400×80 cells.

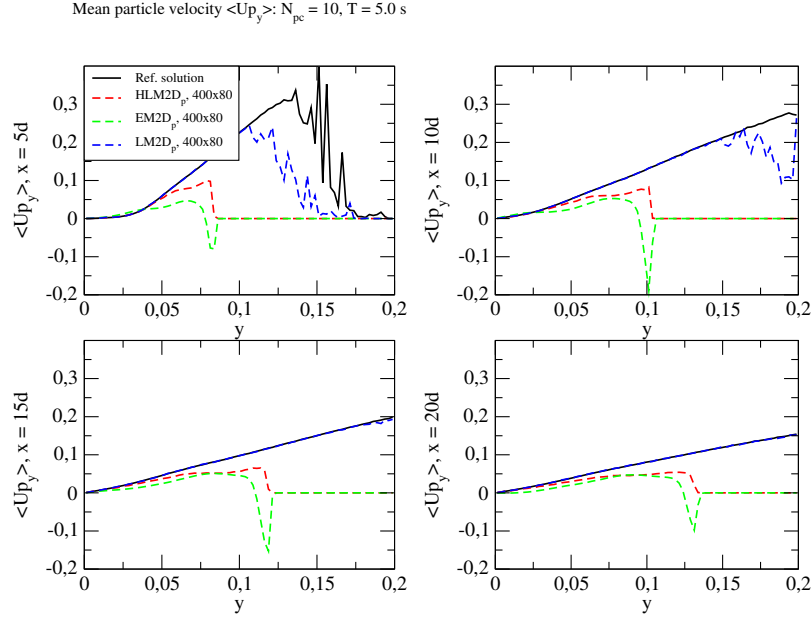


Figure 4.50: Cross-sections of the mean particle velocity in the transversal direction. Comparison of the hybrid simulations $CS_g - HLM2D_p/EM2D_p$ for system (4.1.1)-(4.1.2) with the "classical" ones using $CS_g - LM2D_p$ for $N_{pc} = 10$ particles per cell on the mesh of 400×80 cells.

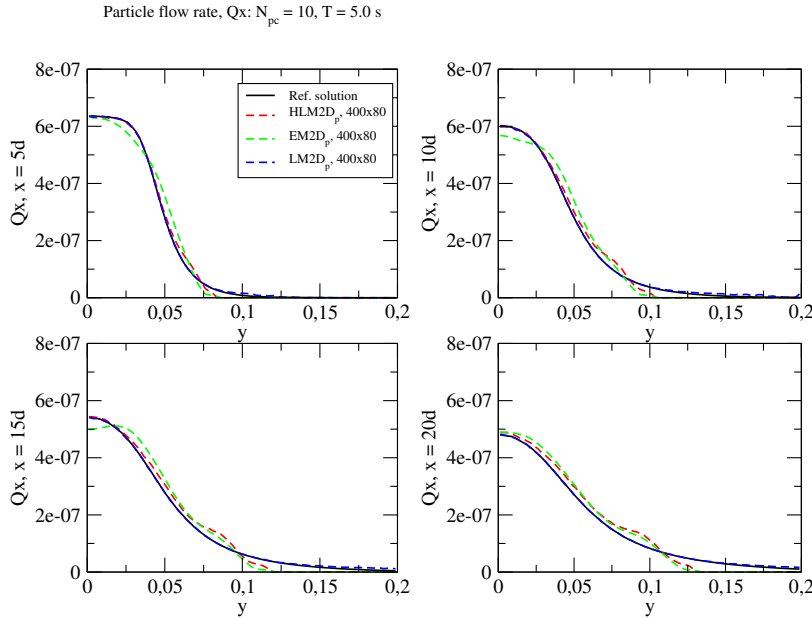


Figure 4.51: Cross-sections of the mean particle flow rate in the longitudinal direction. Comparison of the hybrid simulations $CS_g - HLM2D_p/EM2D_p$ for system (4.1.1)-(4.1.2) with the "classical" ones using $CS_g - LM2D_p$ for $N_{pc} = 10$ particles per cell on the mesh of 400×80 cells.

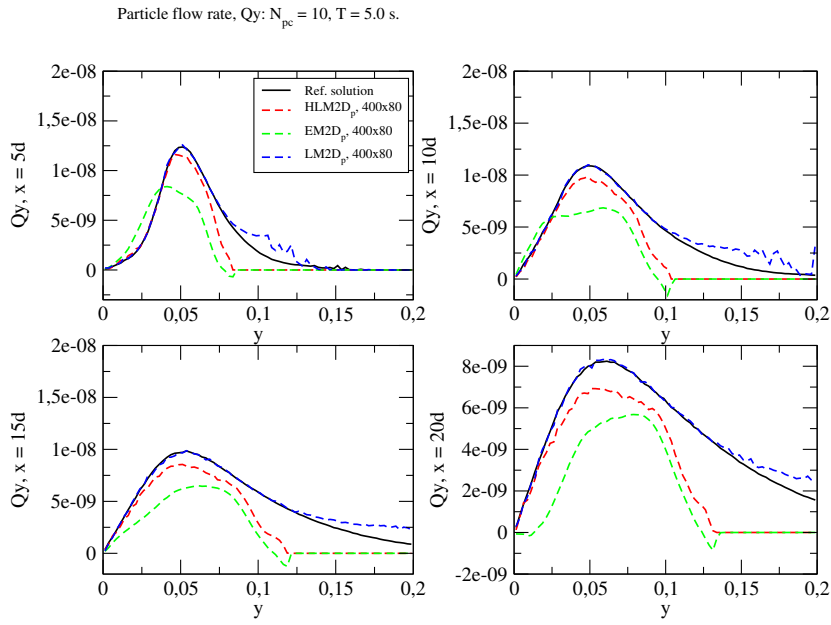


Figure 4.52: Cross-sections of the mean particle flow rate in the transversal direction. Comparison of the hybrid simulations $CS_g - HLM2D_p/EM2D_p$ for system (4.1.1)-(4.1.2) with the "classical" ones using $CS_g - LM2D_p$ for $N_{pc} = 10$ particles per cell on the mesh of 400×80 cells.

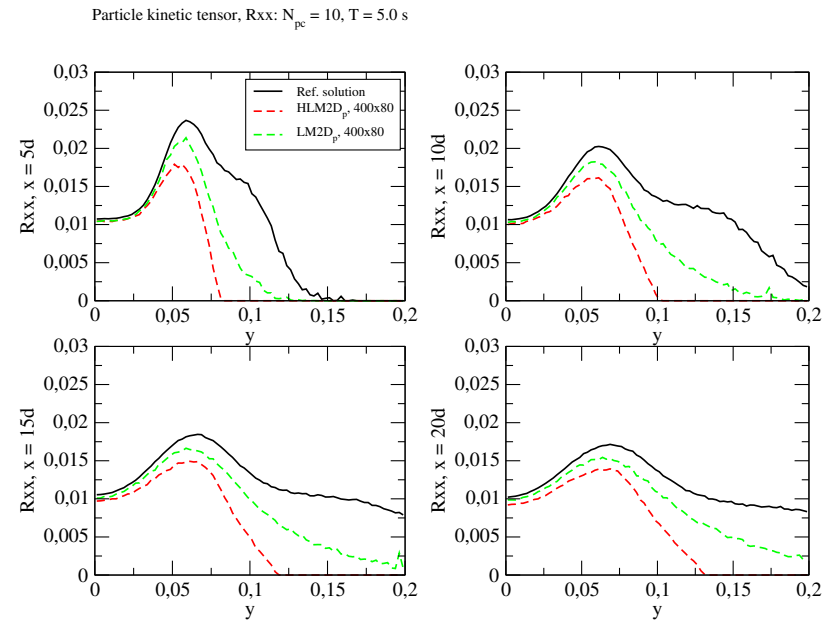


Figure 4.53: Cross-sections of the particle kinetic tensor. Comparison of the hybrid simulations $CS_g - HLM2D_p/EM2D_p$ for system (4.1.1)-(4.1.2) with the "classical" ones using $CS_g - LM2D_p$ for $N_{pc} = 10$ particles per cell on the mesh of 400×80 cells.

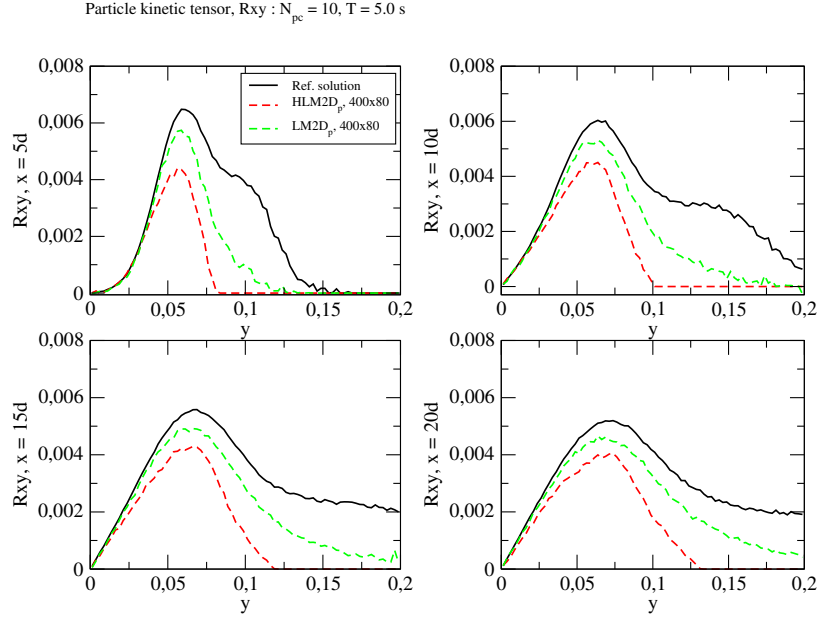


Figure 4.54: Cross-sections of the particle kinetic tensor. Comparison of the hybrid simulations $CS_g - HLM2D_p/EM2D_p$ for system (4.1.1)-(4.1.2) with the "classical" ones using $CS_g - LM2D_p$ for $N_{pc} = 10$ particles per cell on the mesh of 400×80 cells.

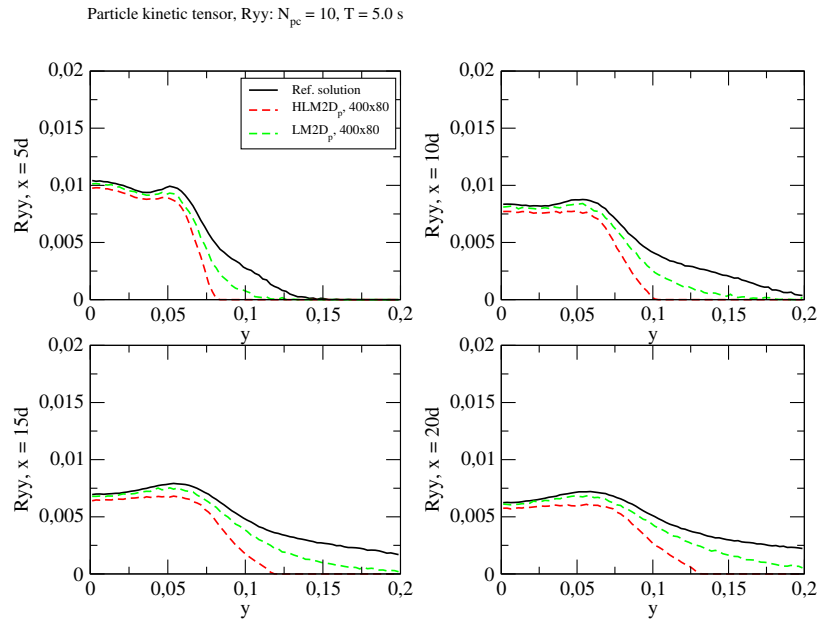


Figure 4.55: Cross-sections of the particle kinetic tensor. Comparison of the hybrid simulations $CS_g - HLM2D_p/EM2D_p$ for system (4.1.1)-(4.1.2) with the "classical" ones using $CS_g - LM2D_p$ for $N_{pc} = 10$ particles per cell on the mesh of 400×80 cells.

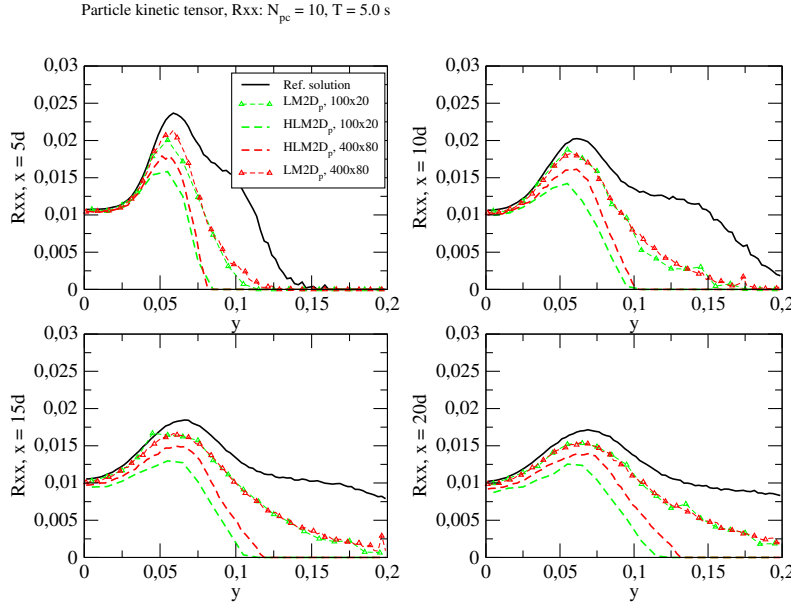


Figure 4.56: Cross-sections of the particle kinetic tensor. Comparaison of hybrid simulations $CS_g - HLM2D_p/EM2D_p$ for system (4.1.1)-(4.1.2) with $CS_g - LM2D_p$ for $N_{pc} = 10$ particles per cell on the meshes of 100×20 and 200×40 cells.

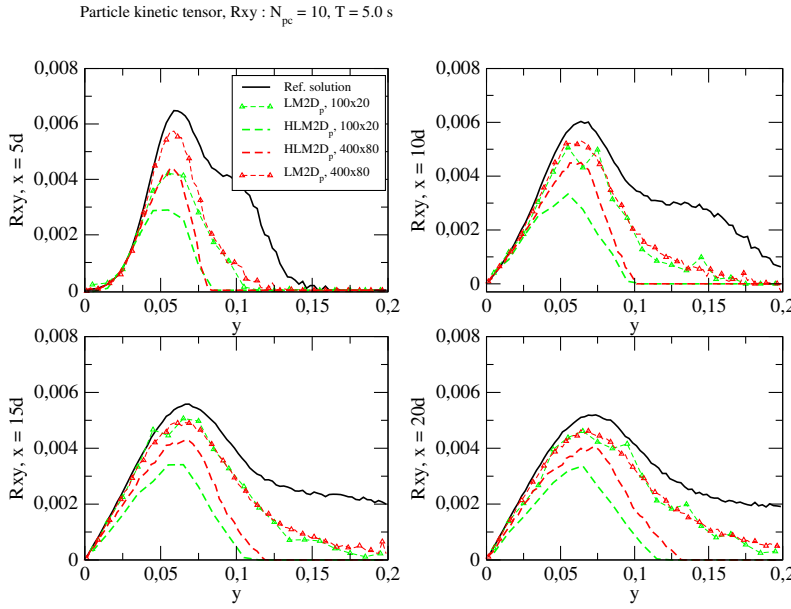


Figure 4.57: Cross-sections of the particle kinetic tensor. Comparaison of hybrid simulations $CS_g - HLM2D_p/EM2D_p$ for system (4.1.1)-(4.1.2) with $CS_g - LM2D_p$ for $N_{pc} = 10$ particles per cell on the meshes of 100×20 and 200×40 cells.

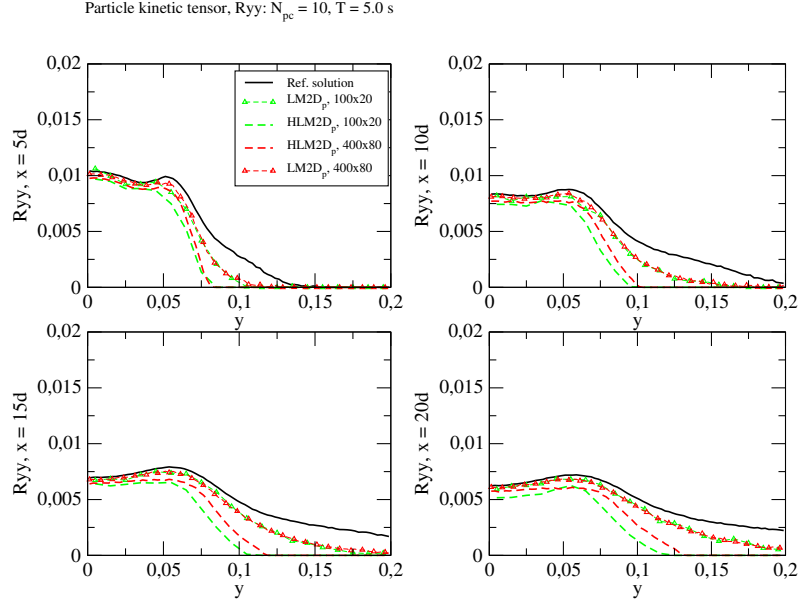


Figure 4.58: Cross-sections of the particle kinetic tensor. Comparaison of hybrid simulations $CS_g - HLM2D_p/EM2D_p$ for system (4.1.1)-(4.1.2) with $CS_g - LM2D_p$ for $N_{pc} = 10$ particles per cell on the meshes of 100×20 and 200×40 cells.

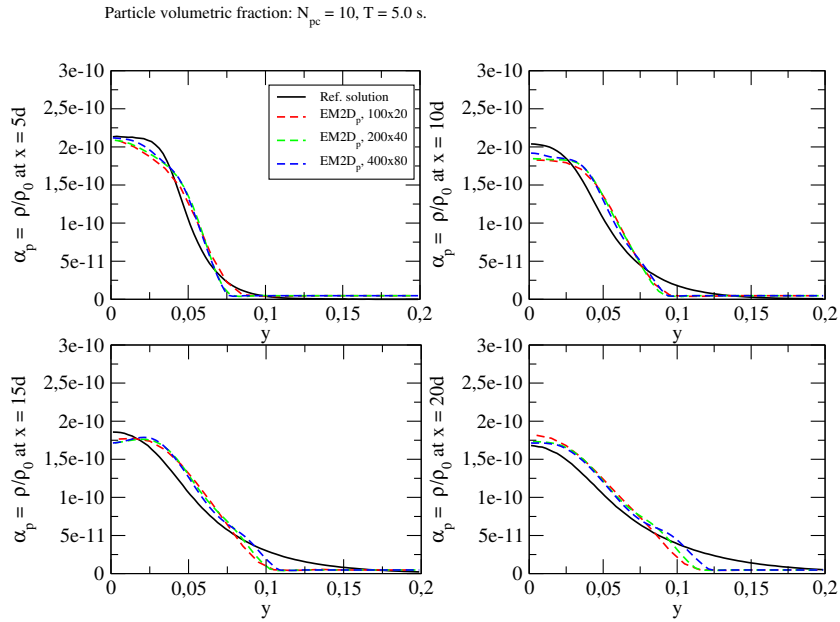


Figure 4.59: Convergence of the Finite Volume Particle Solver: cross-sections of the particle volumetric fraction. Hybrid numerical simulation $CS_g - HLM2D_p/EM2D_p$ for system (4.1.1)-(4.1.2) with $N_{pc} = 10$ particles per cell on the meshes $N_x \times N_y = 100 \times 20$, 200×40 , 400×80 .

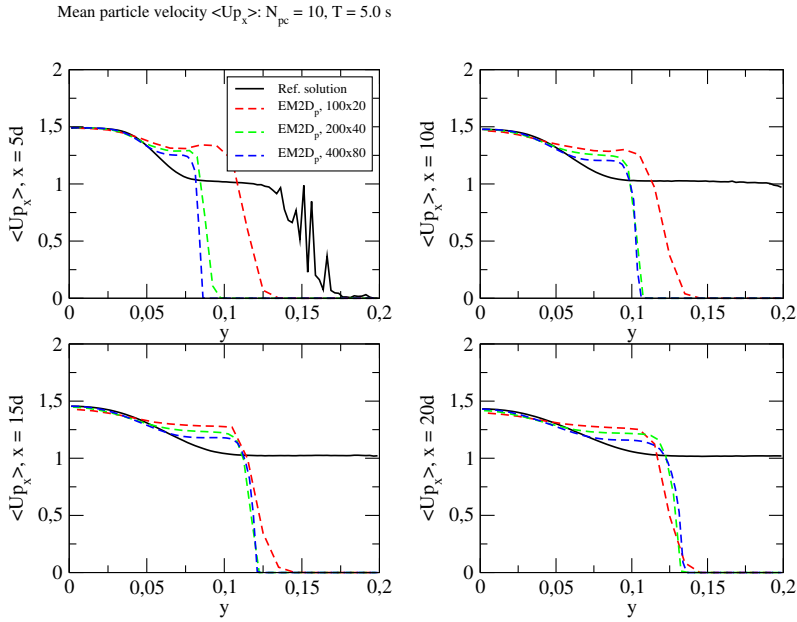


Figure 4.60: Convergence of the Finite Volume Particle Solver: cross-sections of the mean particle velocity in the longitudinal direction. Hybrid numerical simulation $CS_g - HLM2D_p/EM2D_p$ for system (4.1.1)-(4.1.2) with $N_{pc} = 10$ particles per cell on the meshes $N_x \times N_y = 100 \times 20$, 200×40 , 400×80 .

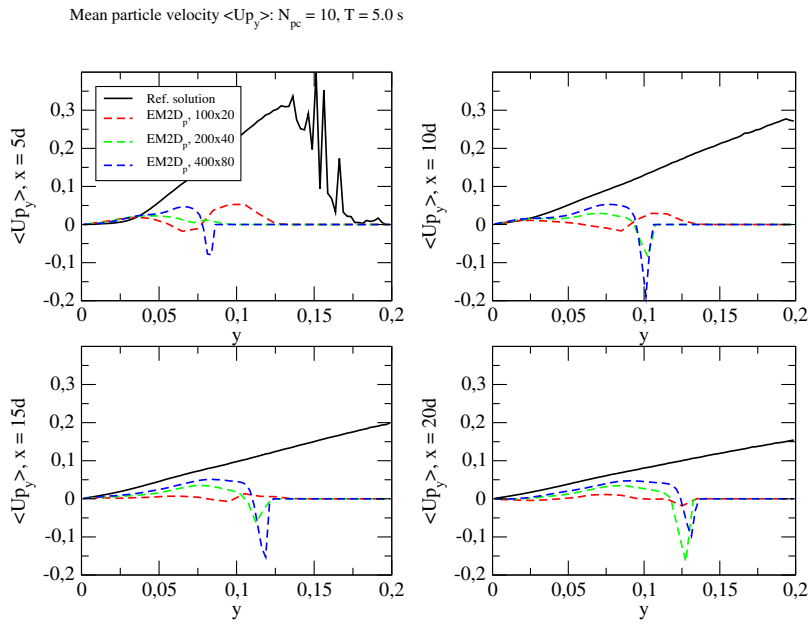


Figure 4.61: Convergence of the Finite Volume Particle Solver: cross-sections of the mean particle velocity in the transversal direction. Hybrid numerical simulation $CS_g - HLM2D_p/EM2D_p$ for system (4.1.1)-(4.1.2) with $N_{pc} = 10$ particles per cell on the meshes $N_x \times N_y = 100 \times 20$, 200×40 , 400×80 .

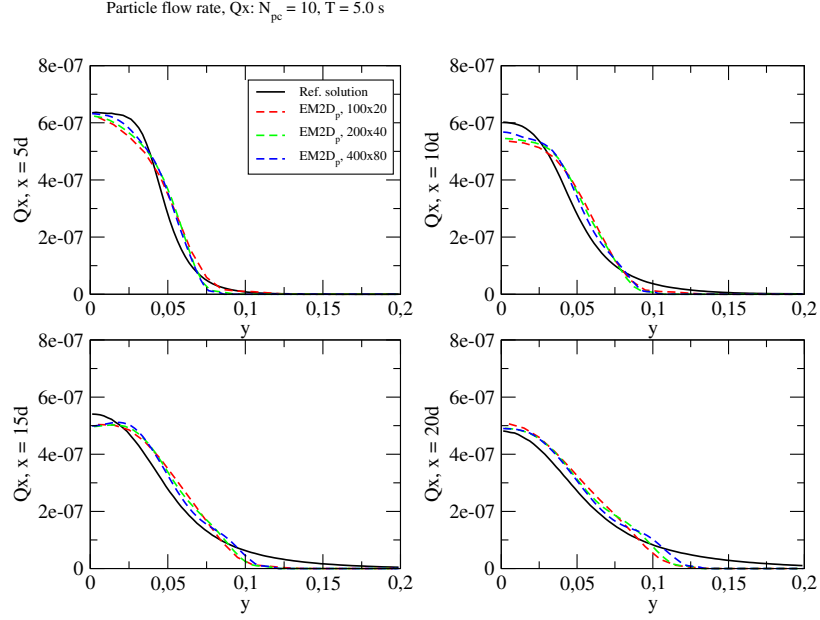


Figure 4.62: Convergence of the Finite Volume Particle Solver: cross-sections of the mean particle flow rate in the longitudinal direction. Hybrid numerical simulation $CS_g - HLM2D_p/EM2D_p$ for system (4.1.1)-(4.1.2) with $N_{pc} = 10$ particles per cell on the meshes $Nx \times Ny = 100 \times 20, 200 \times 40, 400 \times 80$.

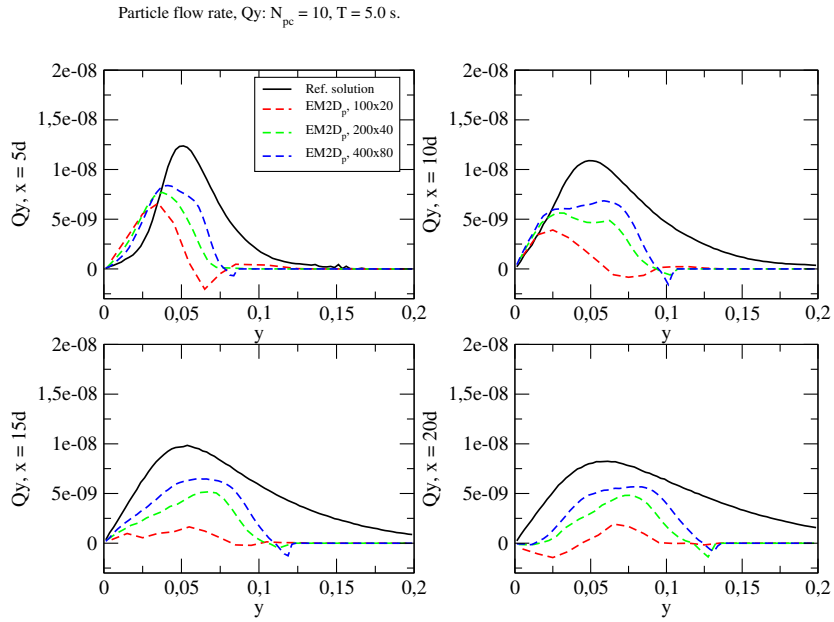


Figure 4.63: Convergence of the Finite Volume Particle Solver: cross-sections of the mean particle flow rate in the transversal direction. Hybrid numerical simulation $CS_g - HLM2D_p/EM2D_p$ for system (4.1.1)-(4.1.2) with $N_{pc} = 10$ particles per cell on the meshes $Nx \times Ny = 100 \times 20, 200 \times 40, 400 \times 80$.

Particle volumetric fraction: $N_x \times N_y = 200 \times 40$, $N_{pc} = 10$, $T = 5.0$ s.

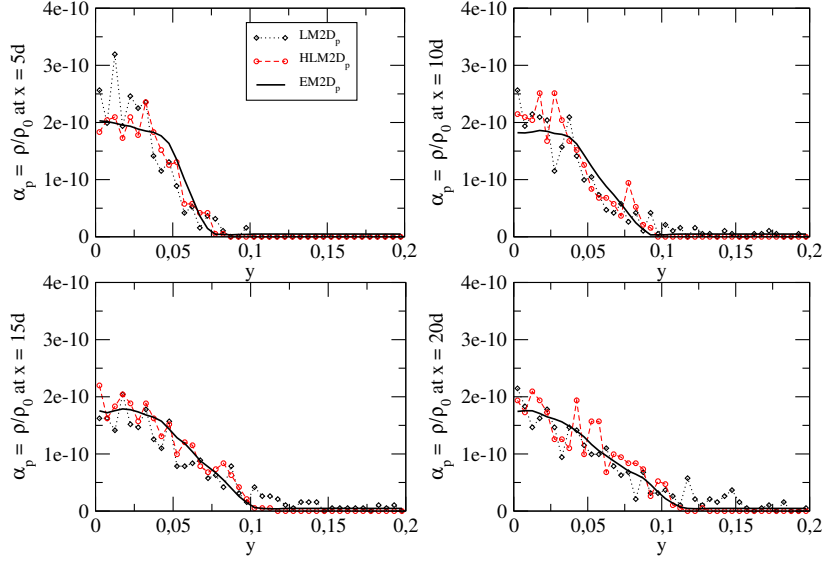


Figure 4.64: Cross-sections of the particle volumetric fraction. Comparaison of hybrid simulations $CS_g - HLM2D_p/EM2D_p$ for system (4.1.1)-(4.1.2) with $CS_g - LM2D_p$ for $N_{pc} = 10$ particles per cell on the mesh $N_x \times N_y = 200 \times 40$.

Mean particle velocity $\langle Up_x \rangle$: $N_x \times N_y = 200 \times 40$, $N_{pc} = 10$, $T = 5.0$ s

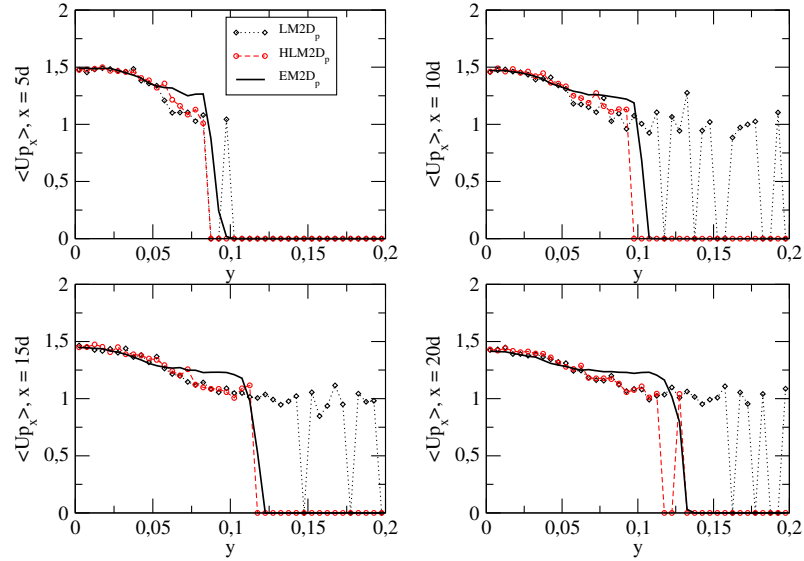


Figure 4.65: Cross-sections of the mean particle velocity in the longitudinal direction. Comparaison of hybrid simulations $CS_g - HLM2D_p/EM2D_p$ for system (4.1.1)-(4.1.2) with $CS_g - LM2D_p$ for $N_{pc} = 10$ particles per cell on the mesh $N_x \times N_y = 200 \times 40$.

Mean particle velocity $\langle U_{p_y} \rangle$; $N_x \times N_y = 200 \times 40$, $N_{pc} = 10$, $T = 5.0$ s

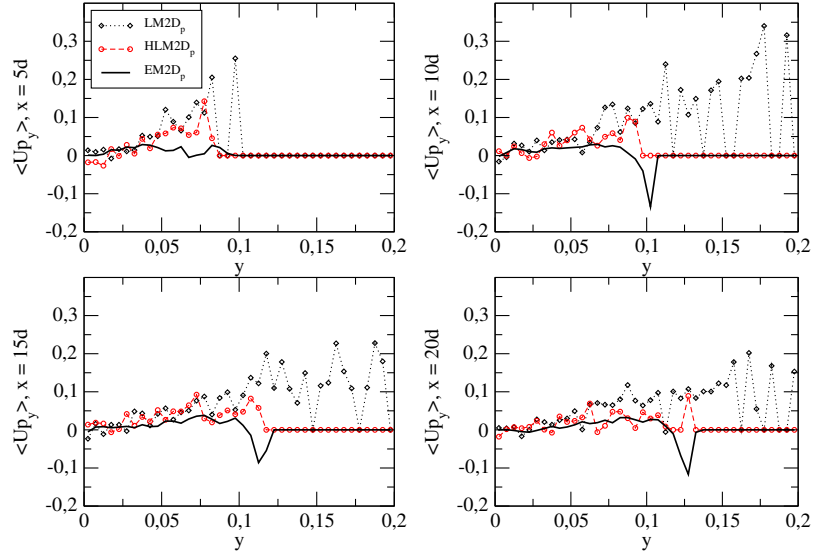


Figure 4.66: Cross-sections of the mean particle velocity in the transversal direction. Comparaison on hybrid approximations $CS_g - HLM2D_p/EM2D_p$ for system (4.1.1)-(4.1.2) with $CS_g - LM2D_p$ for $N_{pc} = 10$ particles per cell on the mesh $N_x \times N_y = 200 \times 40$.

Particle flow rate, Q_x ; $N_x \times N_y = 200 \times 40$, $N_{pc} = 10$, $T = 5.0$ s

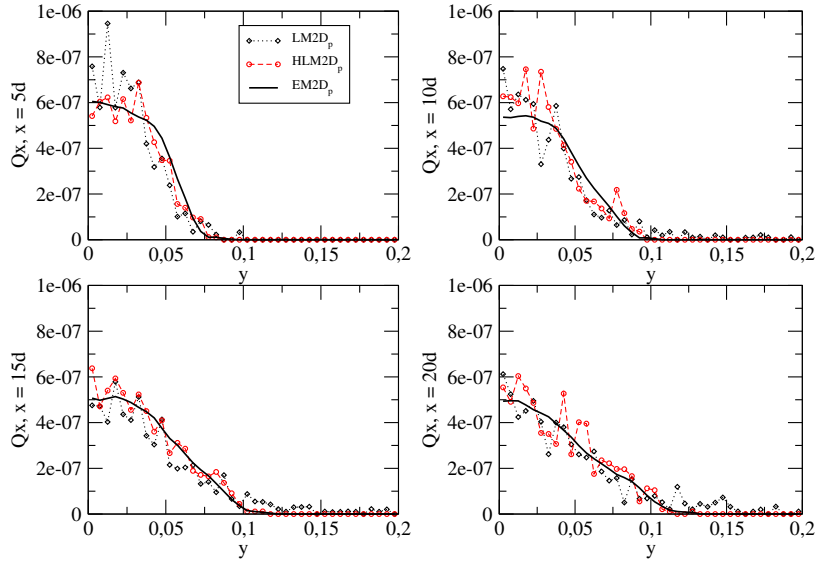


Figure 4.67: Cross-sections of the mean particle flow rate in the longitudinal direction. Comparaison of hybrid simulations $CS_g - HLM2D_p/EM2D_p$ for system (4.1.1)-(4.1.2) with $CS_g - LM2D_p$ for $N_{pc} = 10$ particles per cell on the mesh $N_x \times N_y = 200 \times 40$.

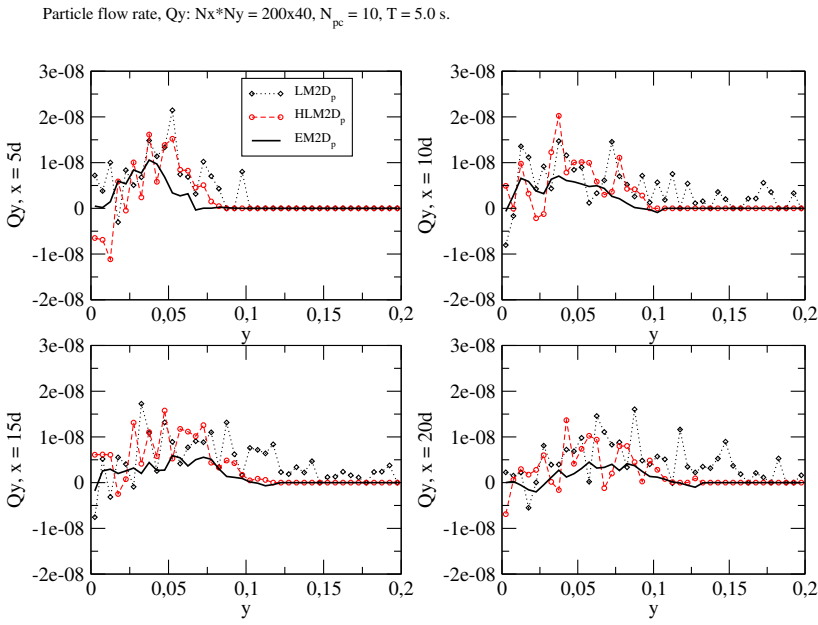


Figure 4.68: Cross-sections of the mean particle flow rate in the transversal direction. Comparaison of hybrid simulations $CS_g - HLM2D_p/EM2D_p$ for system (4.1.1)-(4.1.2) with $CS_g - LM2D_p$ for $N_{pc} = 10$ particles per cell on the mesh $N_x \times N_y = 200 \times 40$.

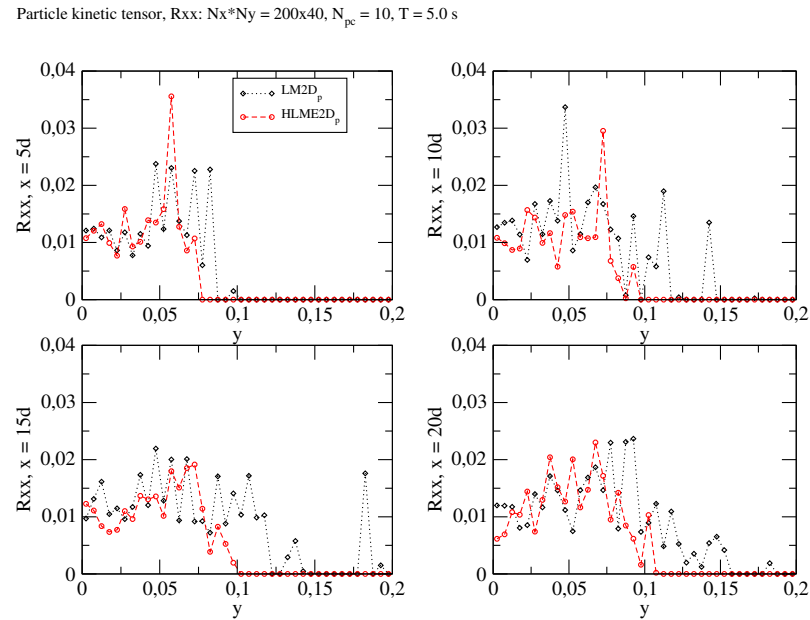


Figure 4.69: Cross-sections of the particle kinetic tensor. Comparaison of hybrid simulations $CS_g - HLM2D_p/EM2D_p$ for system (4.1.1)-(4.1.2) with $CS_g - LM2D_p$ for $N_{pc} = 10$ particles per cell on the mesh $N_x \times N_y = 200 \times 40$.

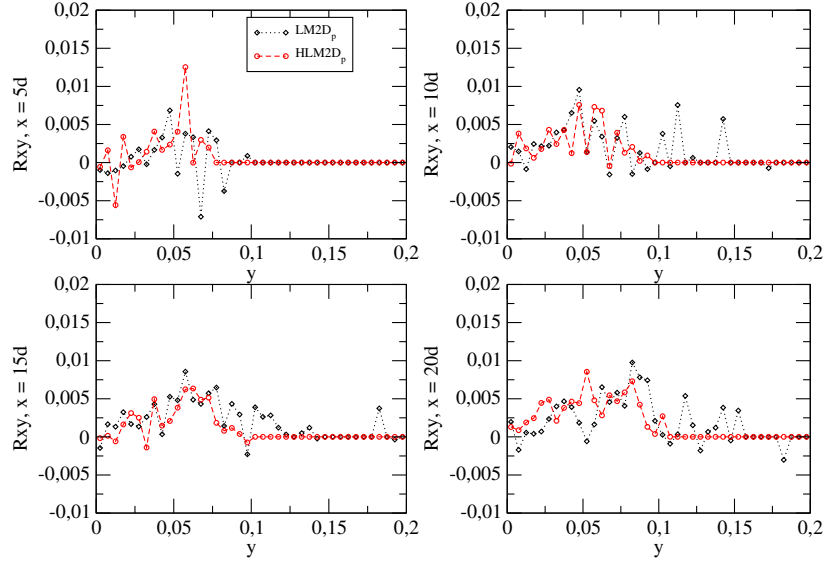
Particle kinetic tensor, R_{xy} : $N_x \times N_y = 200 \times 40$, $N_{pc} = 10$, $T = 5.0$ s

Figure 4.70: Cross-sections of the particle kinetic tensor. Comparaison of hybrid simulations $CS_g - HLM2D_p/EM2D_p$ for system (4.1.1)-(4.1.2) with $CS_g - LM2D_p$ for $N_{pc} = 10$ particles per cell on the mesh $N_x \times N_y = 200 \times 40$.

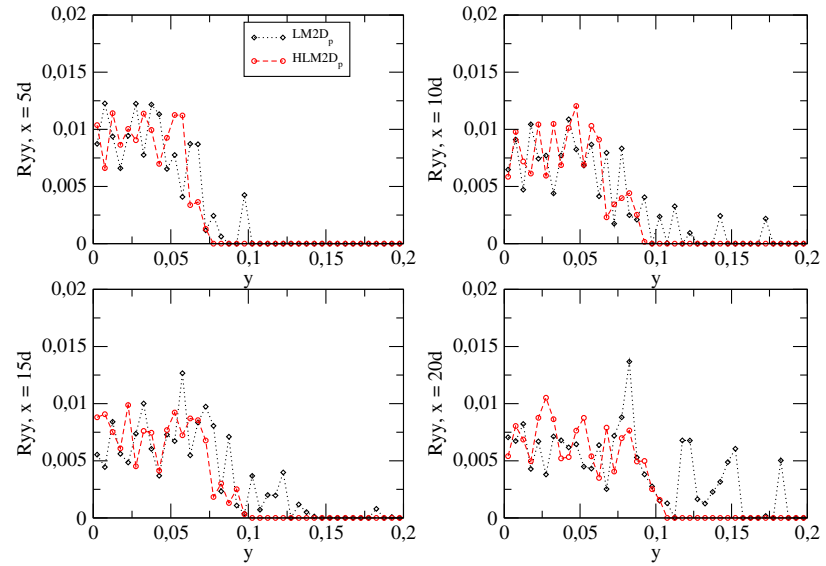
Particle kinetic tensor, R_{yy} : $N_x \times N_y = 200 \times 40$, $N_{pc} = 10$, $T = 5.0$ s

Figure 4.71: Cross-sections of the particle kinetic tensor. Comparaison of hybrid simulations $CS_g - HLM2D_p/EM2D_p$ for system (4.1.1)-(4.1.2) with $CS_g - LM2D_p$ for $N_{pc} = 10$ particles per cell on the mesh $N_x \times N_y = 200 \times 40$.

Particle volumetric fraction: $N_x \times N_y = 200 \times 40$, $N_{pc} = 50$, $T = 5.0$ s.

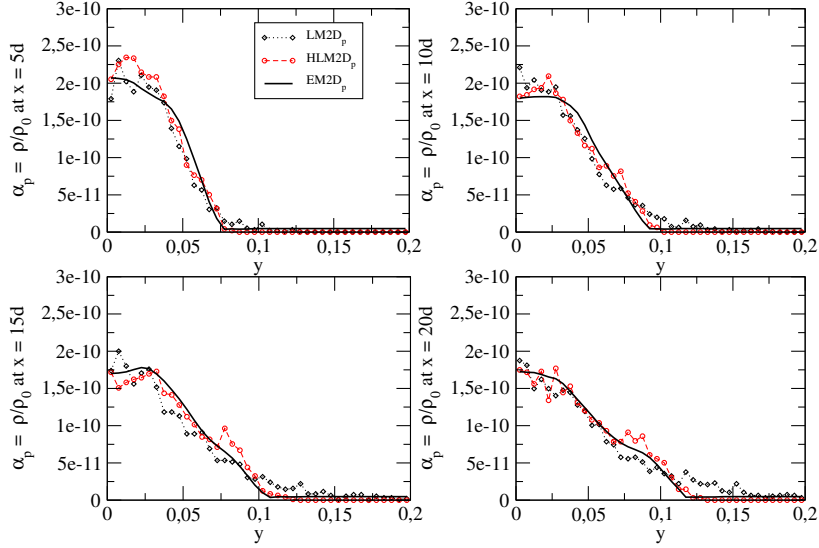


Figure 4.72: Cross-sections of the particle volumetric fraction. Comparaison of hybrid simulations $CS_g - HLM2D_p/EM2D_p$ for system (4.1.1)-(4.1.2) with $CS_g - LM2D_p$ for $N_{pc} = 50$ particles per cell on the mesh $N_x \times N_y = 200 \times 40$.

Mean particle velocity $\langle U_{p_x} \rangle$: $N_x \times N_y = 200 \times 40$, $N_{pc} = 50$, $T = 5.0$ s

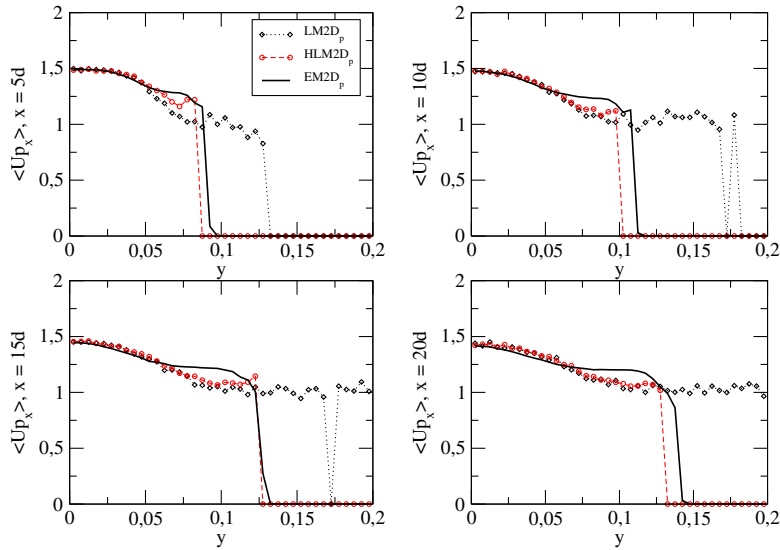


Figure 4.73: Cross-sections of the mean particle velocity in the longitudinal direction. Comparaison of hybrid simulations $CS_g - HLM2D_p/EM2D_p$ for system (4.1.1)-(4.1.2) with $CS_g - LM2D_p$ for $N_{pc} = 50$ particles per cell on the mesh $N_x \times N_y = 200 \times 40$.

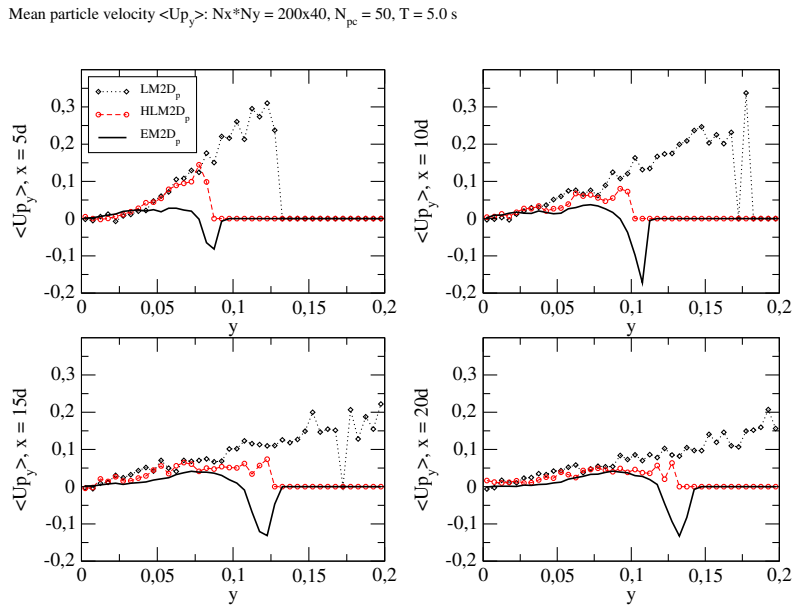


Figure 4.74: Cross-sections of the mean particle velocity in the transversal direction. Comparaison on hybrid approximations $CS_g - HLM2D_p/EM2D_p$ for system (4.1.1)-(4.1.2) with $CS_g - LM2D_p$ for $N_{pc} = 50$ particles per cell on the mesh $N_x \times N_y = 200 \times 40$.

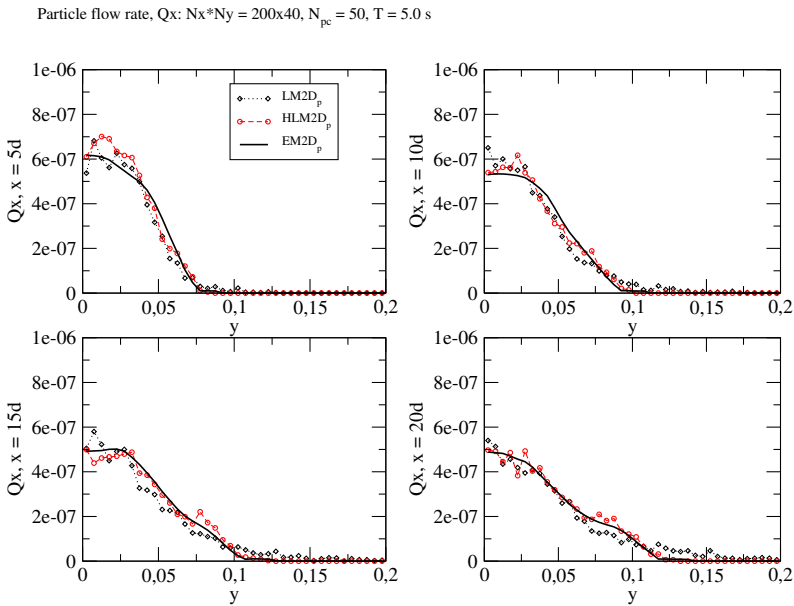


Figure 4.75: Cross-sections of the mean particle flow rate in the longitudinal direction. Comparaison of hybrid simulations $CS_g - HLM2D_p/EM2D_p$ for system (4.1.1)-(4.1.2) with $CS_g - LM2D_p$ for $N_{pc} = 50$ particles per cell on the mesh $N_x \times N_y = 200 \times 40$.

Particle flow rate, Q_y : $N_x \times N_y = 200 \times 40$, $N_{pc} = 50$, $T = 5.0$ s.

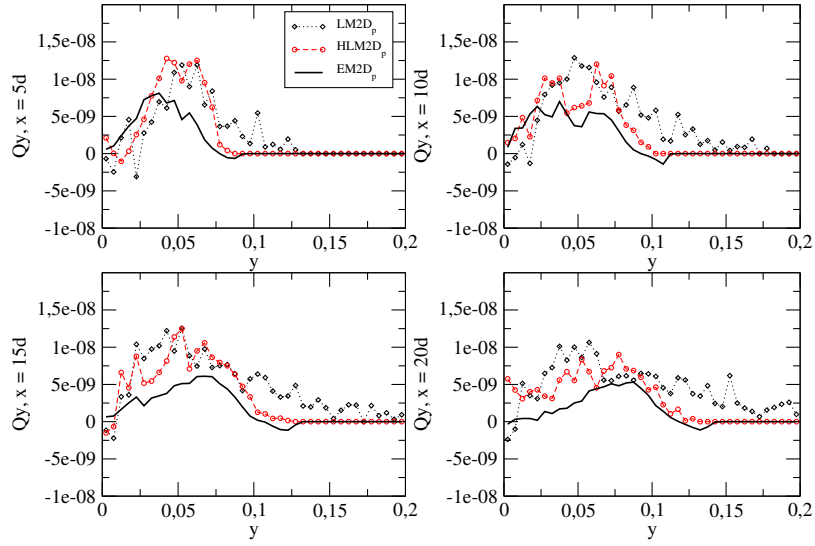


Figure 4.76: Cross-sections of the mean particle flow rate in the transversal direction. Comparaison of hybrid simulations $CS_g - HLM2D_p/EM2D_p$ for system (4.1.1)-(4.1.2) with $CS_g - LM2D_p$ for $N_{pc} = 50$ particles per cell on the mesh $N_x \times N_y = 200 \times 40$.

Particle kinetic tensor, R_{xx} : $N_x \times N_y = 200 \times 40$, $N_{pc} = 50$, $T = 5.0$ s

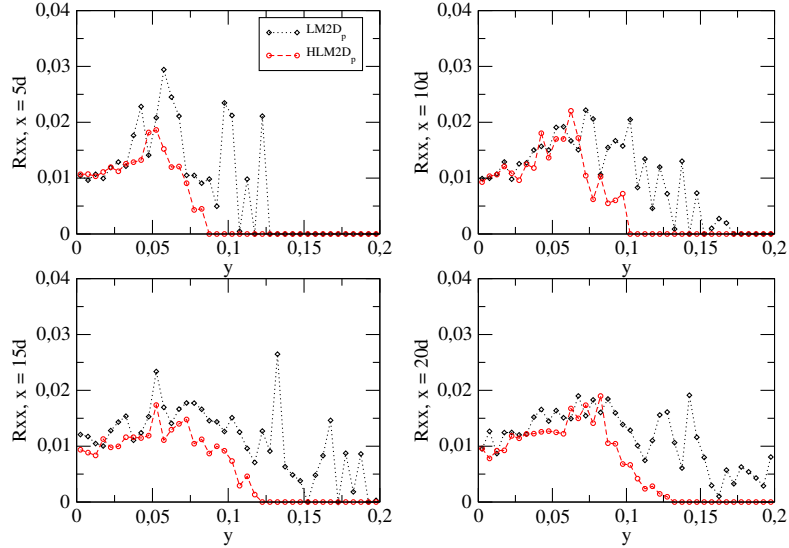


Figure 4.77: Cross-sections of the particle kinetic tensor. Comparaison of hybrid simulations $CS_g - HLM2D_p/EM2D_p$ for system (4.1.1)-(4.1.2) with $CS_g - LM2D_p$ for $N_{pc} = 50$ particles per cell on the mesh $N_x \times N_y = 200 \times 40$.

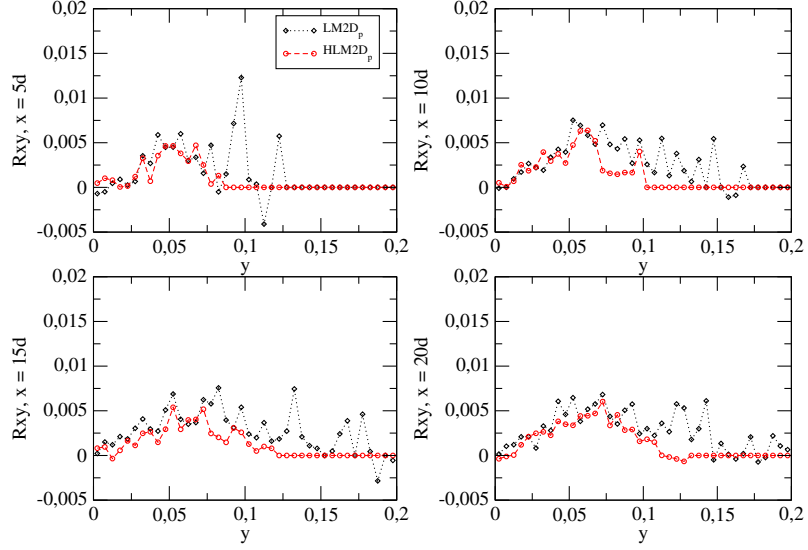
Particle kinetic tensor, R_{xy} : $N_x \times N_y = 200 \times 40$, $N_{pc} = 50$, $T = 5.0$ s

Figure 4.78: Cross-sections of the particle kinetic tensor. Comparaison of hybrid simulations $CS_g - HLM2D_p/EM2D_p$ for system (4.1.1)-(4.1.2) with $CS_g - LM2D_p$ for $N_{pc} = 50$ particles per cell on the mesh $N_x \times N_y = 200 \times 40$.

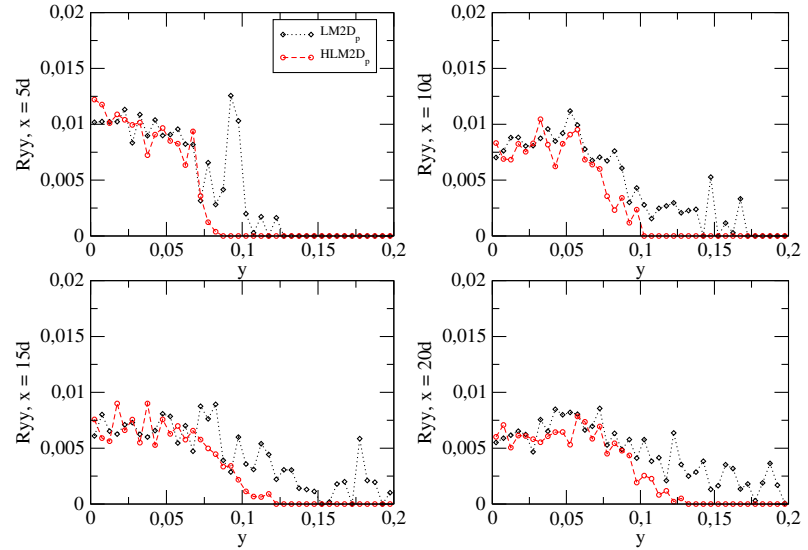
Particle kinetic tensor, R_{yy} : $N_x \times N_y = 200 \times 40$, $N_{pc} = 50$, $T = 5.0$ s

Figure 4.79: Cross-sections of the particle kinetic tensor. Comparaison of hybrid simulations $CS_g - HLM2D_p/EM2D_p$ for system (4.1.1)-(4.1.2) with $CS_g - LM2D_p$ for $N_{pc} = 50$ particles per cell on the mesh $N_x \times N_y = 200 \times 40$.

Bibliography

- [1] Archambeau, F., Mechitoua, N., Sakiz, M.: Code_Saturne: a Finite Volume Code for the Computation of Turbulent Incompressible Flows à Industrial Applications. International Journal on Finite Volumes (2004)
- [2] Buffard, T., Gallouët, T., Hérard, J.M.: A sequel to a Rough Godunov Scheme: Application to Real Gases. Computers and Fluids, **29** (7) 813–847 (2000)
- [3] Chang, G.C.: A Monte-Carlo PDF/Finite-Volume study of turbulent flames. PhD thesis, Cornell University (1996)
- [4] Chibbaro, S., Hérard, J.M., Minier, J.P.: A novel Hybrid Moments/Moments-PDF method for turbulent two-phase flows. Final Technical Report Activity Marie Curie Project. TOK project LANGE Contract MTKD-CT-2004 509849 (2006)
- [5] Chibbaro, S., Minier, J.P.: A note on the consistency of hybrid Eulerian/Lagrangian approach to multiphase flows. International Journal of Multiphase Flow, **37**, 293–297 (2011)
- [6] Clift, R., Grace, J.R., Weber, M.E.: Bubbles, Drops and Particles. Academic Press, New York (1978)
- [7] Degond, P., Dimarco, G., Pareschi, L.: The moment-guided Monte Carlo method. Int. J. for Numerical Methods in Fluids, **67** (2) 189–213 (2011)
- [8] Derevich, I., Zaichik, L.: Precipitation of particles from a turbulent flow. Mekhanika Zhidkosti i Gaza, **5** 96–104 (1988)
- [9] Dorogan, K., Hérard, J.M., Minier, J.P.: Development of a new scheme for hybrid modelling of gas-particle two-phase flows. EDF report H-I81-2010-2352-EN, unpublished, 1–50 (2010)
- [10] Dorogan, K., Guingo, M., Hérard, J.M., Minier, J.P.: A relaxation scheme for hybrid modelling of gas-particle flows. Accepted for publication in Computers and Fluids (2012)
- [11] Dorogan, K., Hérard, J.M., Minier, J.P.: A two-dimensional relaxation scheme for the hybrid modelling of two phase flows. International Conference Finite Volumes for Complex Applications 6, Prague, 6-10 juin 2011. Published in proceedings “Finite Volumes for Complex Applications. Problems and Perspectives”, Springer-Verlag (2011).
- [12] Dreeben, T.D., Pope, S.B.: Wall-function treatment in PDF methods for turbulent flows. Phys. Fluids **9**, 2692 (1997)

- [13] Dreeben, T.D., Pope, S.B.: Probability density function/Monte-Carlo simulation of near-wall turbulent flows. *J. Fluid Mech.* **357**, 141 (1998)
- [14] E, W., Liu, D., Vanden-Eijnden, E.: Analysis of multiscale methods for stochastic differential equations. *Communications on Pure and Applied Mathematics*, John Wiley & Sons, Inc. (2003)
- [15] Gallouët, T., Hérard, J.M., Seguin, N.: A hybrid scheme to compute contact discontinuities in 1D Euler systems. *Mathematical Modelling and Numerical Analysis*, **36**, 1133–1159 (2002)
- [16] Gard, T.C.: *Introduction to Stochastic Differential Equations*. Marcel Dekker, New York Basel (Monographs and Textbooks in Pure and Applied Mathematics, **114**) (1988)
- [17] Gardiner, C.W.: *Handbook of stochastic methods for physics, chemistry and natural sciences*. Springer, Berlin (1990)
- [18] Gatignol, R.: The Faxén formulae for a rigid particle in an unsteady non-uniform Stokes flow. *J. Mec. Théor. Appl.*, **1(2)**, 143–160 (1983)
- [19] Hérard, J.M.: A relaxation tool to compute hybrid Euler-Lagrange compressible models. AIAA paper 2006-2872 (2006) <http://aiaa.org>
- [20] Hérard, J.M., Minier, J.P., Chibbaro, S.: A Finite Volume scheme for hybrid turbulent two-phase flow models. AIAA paper 2007-4587, <http://aiaa.org>
- [21] Hérard, J.M., Uhlmann, M., Van der Velden, D.: Numerical techniques for solving hybrid Eulerian Lagrangian models for particulate flows. EDF report H-I81-2009-3961-EN (2009)
- [22] Hockney, R.W., Eastwood, J.W.: *Computer simulation using particles*. Adam Hilger, New York (1988)
- [23] Kloeden, P.E., Platen, E.: *Numerical solution of stochastic differential equations*. Springer-Verlag, Berlin (1992)
- [24] McKean, H.P.: Lecture Series in Differential Equations 7. Catholic University, Washington D.C. **41** (1967)
- [25] Minier, J.P., Peirano, E.: The pdf approach to polydispersed turbulent two-phase flows. *Physics reports*, **352**, 1–214 (2001)
- [26] Minier, J.P., Peirano, E., Chibbaro, S.: Weak first- and second-order numerical schemes for stochastic differential equations appearing in Lagrangian two-phase flow modelling. *Monte Carlo Methods and Appl.*, **9**, 93–133 (2003)
- [27] Minier, J.P., Pozorski, J.: Wall-boundary conditions in probability density function methods and application to a turbulent channel flow. *Physics of Fluids*, **11**, 2632–2644 (1999)
- [28] Minier, J.P., Pozorski, J.: Derivation of a pdf model for turbulent flows based on principles from statistical physics. *Physics of Fluids*, **9**, 1748–1753 (1997)

- [29] Muradoglu, M., Jenny, P., Pope, S.B., Caughey, D.A.: A consistent hybrid finite-volume/particle method for the pdf equations of turbulent reactive flows. *J. Comp. Phys.*, **154**, 342–371 (1999)
- [30] Øksendal, B.: *Stochastic differential equations. An introduction with applications.* Springer, Berlin (1995)
- [31] Öttinger, H.C.: *Stochastic processes in polymeric fluids. Tools and examples for developing simulation algorithms.* Springer, Berlin (1996)
- [32] Peirano, E., Chibbaro, S., Pozorski, J., Minier, J.P.: Mean-field/PDF numerical approach for polydispersed turbulent two-phase flows. *Prog. Ene. Comb. Sci.*, **32**, 315–371 (2006)
- [33] Pope, S.B.: *Turbulent flows.* Cambridge University Press, Cambridge (2000)
- [34] Pope, S.B.: PDF methods for turbulent reactive flows. *Prog. Energy Combust. Sci.*, **11**, 119–92 (1985)
- [35] Pope, S.B.: Application of the velocity-dissipation probability density function model to inhomogeneous turbulent flows. *Phys. Fluids A*, **3**, 1947 (1991)
- [36] Pope, S.B.: Particle method for turbulent flows: integration of stochastic model equations. *J. Comput. Phys.*, 117:332–49 (1995)
- [37] Pope, S.B., Chen, Y.L.: The velocity-dissipation probability density function model for turbulent flows. *Phys. Fluids A*, **2**, 1437 (1990)
- [38] Pope, S.B.: On the relationship between stochastic Lagrangian models of turbulence and second moment closures. *Phys. Fluids* **6**, 973–985 (1994)
- [39] Pope, S.B.: Lagrangian PDF methods for turbulent flows. *Annu. Rev. Fluid Mech.*, 23–63 (1994)
- [40] Pope, S.B.: Mean Field Equations in PDF Particle Methods for Turbulent Reactive Flows, Technical Report FDA 97-06. Cornell University (1997)
- [41] Pozorski, J., Minier, J.P.: On the Lagrangian turbulent dispersion models based on the Langevin equation. *International Journal of Multiphase Flow*, **24**, 913–945 (1998)
- [42] Reeks, M.W.: On a kinetic equation for the transport of particles in turbulent flows. *Phys. Fluids A*, **3**, 446–456 (1991)
- [43] Simonin, O.: Prediction of the dispersed phase turbulence in particle-laden jets. In: *Gas-Solid Flows 1991*, ASME FED 121, 197–206 (1991)
- [44] Simonin, O., Deutsch, E., Minier, J.P.: Eulerian prediction of the fluid/particle correlated motion in turbulent two-phase flows. *Appl. Sci. Res.*, 51:275–83 (1993)
- [45] Simonin, O.: *Combustion and turbulence in two-phase flows.* Von Karman Institute for Fluid Dynamics, Lecture Series (1996)

- [46] Sommerfeld, M., Kohnen, G., Rüger, M.: Some open questions and inconsistencies of Lagrangian particle dispersion models. In: Proceedings of the Ninth Symposium on Turbulent Shear Flows, Kyoto, Paper 15.1, (1993)
- [47] Sommerfeld, M.: Modeling and calculation of turbulent gas-solid flows with the Euler/Lagrange approach. *KONA (Powder and Particles)*, **16**, 194–206 (1999)
- [48] Talay, D.: in Kree, P., Wedig, W, editors. Simulation of stochastic differential equations, in probabilistic methods in applied physics. Springer, Berlin (1995)
- [49] Xu, J., Pope, S.B.: Source of Bias in Particle-Mesh Methods for PDF Models for Turbulent Flows, Technical Report FDA 97-06. Cornell University (1997)
- [50] Xu, J., Pope, S.B.: Assessment of numerical accuracy of PDF/Monte-Carlo methods for turbulent reacting flows. *J. Comput. Phys.*, 152–192 (1999)

Conclusion & Perspectives

Des écoulements turbulents gaz-particules hors-équilibre thermodynamique (lors de la combustion, des réactions chimiques etc) et dilués en particules sont rencontrés dans de nombreuses situations industrielles et naturelles. Pour une meilleure compréhension et optimisation de tels processus, leur modélisation et simulation numérique s'avèrent nécessaires. Afin d'améliorer la précision des approches Lagrangiennes classiques qui sont bien adaptées à la description de tels écoulements, et notamment pour traduire les phénomènes de polydispersion et prendre en compte les termes sources non-linéaires, on propose une extension de cette méthode suivant les idées présentées dans [4]. Celle-ci consiste en une hybridation locale de deux modèles, Eulerien pour les moments statistiques d'ordre un et Lagrangien stochastique, et vise à réduire l'erreur statistique et le biais propres aux simulations Lagrangiennes "classiques" à coût calcul donné. Cependant, l'implémentation de ce couplage révèle quelques difficultés.

Le premier chapitre présente une méthode Lagrangienne classique appelée méthode Moments/PDF qui utilise une seule description par phase : la phase gaz est décrite par les équations de type RANS (Reynolds Averaged Navier-Stokes) et la phase dispersée - par un système d'équations stochastiques simulant les solutions de l'équation PDF. Cette partie présente essentiellement une synthèse des travaux [32] ainsi qu'une vérification de l'implémentation numérique de cette méthode. A la fin du chapitre, un cas plus réaliste d'un jet diphasique cocourant est étudié afin d'effectuer une comparaison des résultats numériques avec les résultats de référence fournis par *Code-Saturne*. Pour conclure, une nouvelle formulation pour la description des écoulements gaz-particules est proposée et consiste à compléter un système d'équations stochastiques (EDS) pour la phase dispersée par un système Eulerien d'équations aux dérivées partielles pour les moments d'ordre un déduites du système d'EDS. Les deux descriptions sont couplées via les termes d'échange.

La deuxième partie du travail vise à développer un schéma numérique pour la simulation du système Eulerien décrivant les moments statistiques de la phase dispersée sachant que les données statistiques bruitées y sont introduites dû au couplage (le tenseur cinétique et les termes sources non-linéaires). La question de la *stabilité* doit donc être privilégiée. Un schéma Volumes Finis basé sur les techniques de décentrement et de relaxation est proposé et validé dans le cas particulier où le tenseur cinétique est une fonction de la variable du système. Quelques cas-tests concernant le traitement du signal synthétique bruité sont montrés pour évaluer la capacité du schéma à stabiliser les approximations. Dans les chapitre 3, l'extension de ce schéma dans le cadre bi-dimensionnel est proposée et traite notamment du caractère cette fois *fortement anisotrope* du tenseur cinétique.

Dans la dernière partie (chapitre 4), les simulations hybrides sont réalisées pour le cas de jet diphasique cocourant. L'analyse des erreurs numériques est effectuée pour estimer les effets du couplage sur la précision des résultats, notamment en termes de réduction du biais et de l'erreur statistique. Les approximations obtenues semblent converger vers la solution de référence qui est issue des simulations Lagrangiennes "classiques" à convergence. Cependant, un raffinement de maillage supplémentaire est nécessaire pour conclure, car malgré la réduction du biais, une erreur de discréétisation dans les calculs présentés semble être dominante. Une légère réduction de l'erreur statistique dans les approximations "hybrides" est constatée pour un nombre de particules par maille donné. Une extension au cadre tri-dimensionnel pourrait être réalisée sur cette base.

En ce qui concerne les développements ultérieurs souhaitables, la distinction des discrétisations spatiales Eulerienne et Lagrangienne dans la description de la phase dispersée semble nécessaire. En effet, les statistiques fournies par les simulations Monte-Carlo sont essentiellement indépendantes du maillage, donc, en principe, ne nécessitent pas un raffinement supplémentaire, contrairement aux approximations Euleriennes obtenues avec le schéma Volumes Finis, qui sont fortement dépendantes du maillage et nécessitent des discrétisations spatiales et temporelles assez fines.

Une analyse complémentaire concernant la nécessité et la mise en œuvre des relations de consistance (algorithme B dans le chapitre 4) pour les champs approximés par les deux descriptions Eulerienne et Lagrangienne de la phase des particules pourrait être effectuée dans un second temps. Il faudra dans ce cas vérifier la convergence des approximations obtenues vers la solution limite de l'approche Lagrangienne “classique” (en particulier pour ne pas converger vers une autre solution).

Une autre amélioration possible consisterait à étendre le vecteur d'état du modèle Eulerien pour la phase dispersée en y incluant le tenseur cinétique particulaire.

Appendix A. Weak first-order Euler numerical scheme for the time integration of SDEs.

Taken from : “Weak first- and second-order numerical schemes for stochastic differential equations appearing in Lagrangian two-phase flow modelling”, Minier, J.P., Peirano, E., Chibbaro, S.. Monte Carlo Methods and Appl., 9, 93–133 (2003)

Table 4.1: Complete mean-field (RANS)/PDF model.

Mean-field (RANS) equations for the fluid.

Continuity equation:

$$\frac{D}{Dt}(\alpha_f \rho_f) = -\alpha_f \rho_f \frac{\partial \langle U_i \rangle}{\partial x_i}$$

Momentum equation:

$$\frac{D}{Dt} \langle U_i \rangle = -\frac{1}{\rho_f} \frac{\partial \langle P \rangle}{\partial x_i} - \frac{1}{\alpha_f \rho_f} \frac{\partial}{\partial x_j} (\alpha_f \rho_f \langle u_i u_j \rangle)$$

Reynolds stress equation:

$$\frac{D}{Dt} \langle u_i u_j \rangle = -\frac{1}{\alpha_f \rho_f} \frac{\partial}{\partial x_k} (\alpha_f \rho_f \langle u_i u_j u_k \rangle) - \langle u_i u_k \rangle \frac{\partial \langle U_j \rangle}{\partial x_k} - \langle u_j u_k \rangle \frac{\partial \langle U_i \rangle}{\partial x_k}$$

$$+ G_{jk} \langle u_i u_k \rangle + G_{ik} \langle u_j u_k \rangle + C_0 \langle \epsilon \rangle \delta_{ij}$$

$$\text{with } \frac{D}{Dt} = \frac{\partial}{\partial t} + \langle U_k \rangle \frac{\partial}{\partial x_k}$$

SDEs for the discrete particles.

$$\begin{cases} dx_{p,i}(t) = U_{p,i} dt, \\ dU_{p,i}(t) = \frac{U_{s,i} - U_{p,i}}{\tau_p} dt + g_i dt, \\ dU_{s,i}(t) = A_{s,i} dt + B_{s,ij} dW_j(t), \\ A_{s,i} = -\frac{1}{\rho_f} \frac{\partial \langle P \rangle}{\partial x_i} + (\langle U_{p,j} \rangle - \langle U_j \rangle) \frac{\partial \langle U_i \rangle}{\partial x_j} - \frac{1}{T_{L,i}^*} (U_{s,i} - \langle U_i \rangle) \\ B_{s,i}^2 = \langle \epsilon \rangle \left(C_0 b_i \tilde{k}/k + \frac{2}{3} (b_i \tilde{k}/k - 1) \right) \\ T_{L,i}^* = T_L / \sqrt{1 + \beta_i^2 \frac{|\langle \mathbf{U}_r \rangle|^2}{2k/3}}, \quad b_i = T_L / T_{L,i}^*, \quad \tilde{k} = \frac{3}{2} \frac{\sum_{i=1}^3 b_i \langle u_i^2 \rangle}{\sum_{i=1}^3 b_i} \end{cases}$$

Table 4.2: Analytical solutions to system of SDEs (Table 1) for time-independent coefficients. C_i denotes all mean contributions in $A_{s,i}$ above, $T_i = T_{L,i}^*$ and $\check{B}_i^2 = B_{s,i}^2$.

$$\begin{aligned}
 x_{p,i}(t) &= x_{p,i}(t_0) + U_{p,i}(t_0)\tau_p[1 - \exp(-\Delta t/\tau_p)] + U_{s,i}(t_0)\theta_i\{T_i[1 - \exp(-\Delta t/T_i)] \\
 &\quad + \tau_p[\exp(-\Delta t/\tau_p) - 1]\} + [C_i T_i]\{\Delta t - \tau_p[1 - \exp(-\Delta t/\tau_p)] \\
 &\quad - \theta_i(T_i[1 - \exp(-\Delta t/T_i)] + \tau_p[\exp(-\Delta t/\tau_p) - 1])\} \\
 &\quad + g_i\tau_p\{\Delta t - \tau_p[1 - \exp(-\Delta t/\tau_p)]\} + \Omega_i(t) \\
 &\quad \text{with } \theta_i = T_i/(T_i - \tau_p) \quad \text{and } T_i = T_{L,i}^* \\
 U_{p,i}(t) &= U_{p,i}(t_0)\exp(-\Delta t/\tau_p) + U_{s,i}(t_0)\theta_i[\exp(-\Delta t/T_i) - \exp(-\Delta t/\tau_p)] \\
 &\quad + [C_i T_i]\{[1 - \exp(-\Delta t/\tau_p)] - \theta_i[\exp(-\Delta t/T_i) - \exp(-\Delta t/\tau_p)]\} \\
 &\quad + g_i\tau_p[1 - \exp(-\Delta t/\tau_p)] + \Gamma_i(t) \\
 U_{s,i}(t) &= U_{s,i}(t_0)\exp(-\Delta t/T_i) + C_i T_i[1 - \exp(-\Delta t/T_i)] + \gamma_i(t)
 \end{aligned}$$

The stochastic integrals $\gamma_i(t)$, $\Gamma_i(t)$, $\Omega_i(t)$ are given by:

$$\begin{aligned}
 \gamma_i(t) &= \check{B}_i \exp(-t/T_i) \int_{t_0}^t \exp(s/T_i) dW_i(s), \quad \text{where } \check{B}_i^2 = B_{ii}^2 \\
 \Gamma_i(t) &= \frac{1}{\tau_p} \exp(-t/\tau_p) \int_{t_0}^t \exp(s/\tau_p) \gamma_i(s) ds, \\
 \Omega_i(t) &= \int_{t_0}^t \Gamma_i(s) ds.
 \end{aligned}$$

By resorting to stochastic integration by parts, $\gamma_i(t)$, $\Gamma_i(t)$, $\Omega_i(t)$ can be written:

$$\begin{aligned}
 \gamma_i(t) &= \check{B}_i \exp(-t/T_i) I_{1,i}, \\
 \Gamma_i(t) &= \theta_i \check{B}_i [\exp(-t/T_i) I_{1,i} - \exp(-t/\tau_p) I_{2,i}], \\
 \Omega_i(t) &= \theta_i \check{B}_i \{(T_i - \tau_p) I_{3,i} - [T_i \exp(-t/T_i) I_{1,i} - \tau_p \exp(-t/\tau_p) I_{2,i}]\}, \\
 \text{with } I_{1,i} &= \int_{t_0}^t \exp(s/T_i) dW_i(s), \quad I_{2,i} = \int_{t_0}^t \exp(s/\tau_p) dW_i(s), \quad I_{3,i} = \int_{t_0}^t dW_i(s).
 \end{aligned}$$

Table 4.3: Derivation of the covariance matrix for constant coefficients.

$$\langle \gamma_i^2(t) \rangle = \check{B}_i^2 \frac{T_i}{2} [1 - \exp(-2\Delta t/T_i)] \quad \text{where} \quad \check{B}_i^2 = B_{ii}^2$$

$$\begin{aligned} \langle \Gamma_i^2(t) \rangle &= \check{B}_i^2 \theta_i^2 \left\{ \frac{T_i}{2} [1 - \exp(-2\Delta t/T_i)] - \frac{2\tau_p T_i}{T_i + \tau_p} [1 - \exp(-\Delta t/T_i) \exp(-\Delta t/\tau_p)] \right. \\ &\quad \left. + \frac{\tau_p}{2} [1 - \exp(-2\Delta t/\tau_p)] \right\} \end{aligned}$$

$$\begin{aligned} \frac{1}{\check{B}_i^2 \theta_i^2} \langle \Omega_i^2(t) \rangle &= (T_i - \tau_p)^2 \Delta t + \frac{T_i^3}{2} [1 - \exp(-2\Delta t/T_i)] + \frac{\tau_p^3}{2} [1 - \exp(-2\Delta t/\tau_p)] \\ &- 2T_i^2(T_i - \tau_p) [1 - \exp(-\Delta t/T_i)] + 2\tau_p^2(T_i - \tau_p) [1 - \exp(-\Delta t/\tau_p)] \\ &- 2 \frac{T_i^2 \tau_p^2}{T_i + \tau_p} [1 - \exp(-\Delta t/T_i) \exp(-\Delta t/\tau_p)] \end{aligned}$$

$$\langle \gamma_i(t) \Gamma_i(t) \rangle = \check{B}_i^2 \theta_i T_i \left\{ \frac{1}{2} [1 - \exp(-2\Delta t/T_i)] - \frac{\tau_p}{T_i + \tau_p} [1 - \exp(-\Delta t/T_i) \exp(-\Delta t/\tau_p)] \right\}$$

$$\begin{aligned} \langle \gamma_i(t) \Omega_i(t) \rangle &= \check{B}_i^2 \theta_i T_i \left\{ (T_i - \tau_p) [1 - \exp(-\Delta t/T_i)] - \frac{T_i}{2} [1 - \exp(-2\Delta t/T_i)] \right. \\ &\quad \left. + \frac{\tau_p^2}{T_i + \tau_p} [1 - \exp(-\Delta t/T_i) \exp(-\Delta t/\tau_p)] \right\} \end{aligned}$$

$$\begin{aligned} \frac{1}{\check{B}_i^2 \theta_i^2} \langle \Gamma_i(t) \Omega_i(t) \rangle &= (T_i - \tau_p) \{ T_i [1 - \exp(-\Delta t/T_i)] - \tau_p [1 - \exp(-\Delta t/\tau_p)] \} \\ &- \frac{T_i^2}{2} [1 - \exp(-2\Delta t/T_i)] - \frac{\tau_p^2}{2} [1 - \exp(-2\Delta t/\tau_p)] \\ &+ T_i \tau_p [1 - \exp(-\Delta t/T_i) \exp(-\Delta t/\tau_p)] \end{aligned}$$

Table 4.4: Weak first-order Euler scheme

Numerical integration of the system:

$$\begin{aligned}x_{p,i}^{n+1} &= x_{p,i}^n + A_1 U_{p,i}^n + B_1 U_{s,i}^n + C_1 [T_i^n C_i^n] + (\Delta t - A_1) g_i \tau_p^n + \Omega_i^n, \\U_{s,i}^{n+1} &= U_{s,i}^n \exp(-\Delta t/T_i^n) + [T_i^n C_i^n][1 - \exp(-\Delta t/T_i^n)] + \gamma_i^n, \\U_{p,i}^{n+1} &= U_{p,i}^n \exp(-\Delta t/\tau_p^n) + D_1 U_{s,i}^n + [T_i^n C_i^n](E_1 - D_1) + A_1 g_i + \Gamma_i^n.\end{aligned}$$

The coefficients A_1 , B_1 , C_1 , D_1 and E_1 are given by:

$$\begin{aligned}A_1 &= \tau_p^n [1 - \exp(-\Delta t/\tau_p^n)], \\B_1 &= \theta_i^n [T_i^n (1 - \exp(-\Delta t/T_i^n)) - A_1] \quad \text{with} \quad \theta_i^n = T_i^n / (T_i^n - \tau_p^n), \\C_1 &= \Delta t - A_1 - B_1, \\D_1 &= \theta_i^n [\exp(-\Delta t/T_i^n) - \exp(-\Delta t/\tau_p^n)], \\E_1 &= 1 - \exp(-\Delta t/\tau_p^n).\end{aligned}$$

The stochastic integrals γ_i^n , Ω_i^n , Γ_i^n are simulated by:

$$\begin{aligned}\gamma_i^n &= P_{11} \mathcal{G}_{1,i}, \\ \Omega_i^n &= P_{21} \mathcal{G}_{1,i} + P_{22} \mathcal{G}_{2,i} \\ \Gamma_i^n &= P_{31} \mathcal{G}_{1,i} + P_{32} \mathcal{G}_{2,i} + P_{33} \mathcal{G}_{3,i},\end{aligned}$$

where $\mathcal{G}_{1,i}$, $\mathcal{G}_{2,i}$, $\mathcal{G}_{3,i}$ are independent $\mathcal{N}(0, 1)$ random variables.

The coefficients P_{11} , P_{21} , P_{22} , P_{31} , P_{32} , P_{33} are defined as:

$$\begin{aligned}P_{11} &= \sqrt{\langle(\gamma_i^n)^2\rangle}, \\P_{21} &= \frac{\langle\Omega_i^n \gamma_i^n\rangle}{\sqrt{\langle(\gamma_i^n)^2\rangle}}, \quad P_{22} = \sqrt{\langle(\Omega_i^n)^2\rangle - \frac{\langle\Omega_i^n \gamma_i^n\rangle^2}{\langle(\gamma_i^n)^2\rangle}}, \\P_{31} &= \frac{\langle\Gamma_i^n \gamma_i^n\rangle}{\sqrt{\langle(\gamma_i^n)^2\rangle}}, \quad P_{32} = \frac{1}{P_{22}}(\langle\Omega_i^n \Gamma_i^n\rangle - P_{21} P_{31}), \quad P_{33} = \sqrt{\langle(\Gamma_i^n)^2\rangle - P_{31}^2 - P_{32}^2}.\end{aligned}$$
